Middlesex University Research Repository:
an open access repository of
Middlesex University research

http://eprints.mdx.ac.uk

Tizzard, Andrew, 2007. Improving the forward model for electrical impedance tomography of brain function through rapid generation of subject specific finite element models. Available from Middlesex University's Research Repository.

Copyright:

Middlesex University Research Repository makes the University's research available electronically.

Copyright and moral rights to this thesis/research project are retained by the author and/or other copyright owners. The work is supplied on the understanding that any use for commercial gain is strictly forbidden. A copy may be downloaded for personal, non-commercial, research or study without prior permission and without charge. Any use of the thesis/research project for private study or research must be properly acknowledged with reference to the work's full bibliographic details.

This thesis/research project may not be reproduced in any format or medium, or extensive quotations taken from it, or its content changed in any way, without first obtaining permission in writing from the copyright holder(s).

If you believe that any material held in the repository infringes copyright law, please contact the Repository Team at Middlesex University via the following email address:
eprints@mdx.ac.uk

The item will be removed from the repository while any claim is being investigated.

IMPROVING THE FORWARD MODEL FOR ELECTRICAL IMPEDANCE TOMOGRAPHY OF BRAIN FUNCTION THROUGH RAPID GENERATION OF SUBJECT SPECIFIC FINITE ELEMENT MODELS

A thesis submitted to Middlesex University in partial fulfilment of the requirements for the degree of Doctor of Philosophy, July 2007

G. Andrew Tizzard

Director of Studies:	Dr Mehmet Karamanoglu
Supervisors:	Prof. Richard Bayford
	Prof. Anthony White

ABSTRACT

Electrical Impedance Tomography (EIT) is a non-invasive imaging method which allows internal electrical impedance of any conductive object to be imaged by means of current injection and surface voltage measurements through an array of externally applied electrodes. The successful generation of the image requires the simulation of the current injection patterns on either an analytical or a numerical model of the domain under examination, known as the forward model, and using the resulting voltage data in the inverse solution from which images of conductivity changes can be constructed. Recent research strongly indicates that geometric and anatomical conformance of the forward model to the subject under investigation significantly affects the quality of the images. This thesis focuses mainly on EIT of brain function and describes a novel approach for the rapid generation of patient or subject specific finite element models for use as the forward model. After introduction of the topic, methods of generating accurate finite element (FE) models using commercially available Computer-Aided Design (CAD) tools are described and show that such methods, though effective and successful, are inappropriate for time critical clinical use. The feasibility of warping or morphing a finite element mesh as a means of reducing the lead time for model generation is then presented and demonstrated. This leads on to the description of methods of acquiring and utilising known system geometry, namely the positions of electrodes and registration landmarks, to construct an accurate surface of the subject, the results of which are successfully validated. The outcome of this procedure is then used to specify boundary conditions to a mesh warping algorithm based on elastic deformation using well-established continuum mechanics procedures. The algorithm is applied to a range of source models to empirically establish optimum values for the parameters defining the problem which can successfully generate meshes of acceptable quality in terms of discretization errors and which more accurately define the geometry of the target subject. Further validation of the algorithm is performed by comparison of boundary voltages and image reconstructions from simulated and laboratory data to demonstrate that benefits in terms of image artefact reduction and localisation of conductivity changes can be gained. The processes described in the thesis are evaluated and discussed and topics of further work and application are described.

ACKNOWLEDGEMENTS

These are due to my director of studies, Dr Mehmet Karamanoglu and supervisors, Prof. Richard Bayford and Prof. Tony White for their logistical and technical input and support. Thanks are also due to past and present members of the research group at University College, London for technical support and data, most notable of which are Lior Horesh, Rebecca Yerworth, Adam Liston and David Holder.

I also would like to acknowledge the moral, rather than technical, support of my wife and family and their ability to appear more often awed rather than bored by my passion for this work.

To my younger son,

Stephen

TABLE OF CONTENTS

1. INTRODUCTION

1.1. Image Reconstruction Techniques – An Overview

The diagnosis of medical conditions has become increasingly more dependent on imaging modalities in recent years. Pathological studies can reveal the nature and causes of diseases but this is largely through biochemical tests or microscopy; such tests often involve invasive sampling of body tissue or fluids. Medical imaging techniques generally involve physically non-invasive means of ascertaining medical conditions within the body. The oldest and most established technique is the use of X-rays to establish the physical condition of the skeleton and some internal organs. Healthy animal soft tissue is largely transparent to X-ray radiation whereas bone tends to be more opaque. This most basic method of medical imaging demonstrates the fact that if some form of electromagnetic radiation or other medium, such as sound, can be transmitted, absorbed, reflected or otherwise modified in differing degrees by different tissue types, then a means of internal examination can be devised.

Imaging modalities can be classified by various means and cover a wide range of different methodologies. Hornak (1998) has provided a comprehensive review of imaging systems across a range of applications in matrix form. Within this are a number of entries for medical imaging modalities. A basic classification can be implied from this in that an imaging system can be regarded as *probed* or *unprobed*. This basic classification is shown in Table 1.1

Table 1.1: Basic classification of medical imaging modalities

Probed	Unprobed
Computerised Axial Tomography (CAT or CT)	Electroencephalogram (EEG)
Magnetic Resonance Imaging (MRI)	Electrocardiograom (ECG)
Ultrasound	Magnetoencephalogram (MEG)
X-Ray	Nuclear Medical Imaging (NMI)
Endoscopy	Positron Emission Tomography (PET)
	Thermography

Probed methodologies involve the application of some form of probing energy or sub-atomic particle and generally the detection, by some means, of the transmission, reflection or absorption of that energy or particle. With the use of X-radiation as the probing energy; for example, hard tissue is more absorptive in this part of the electromagnetic spectrum and so images of damage to the skeletal structure can be detected on scintillator film. The resultant image is a two-dimensional projection that has a limited range of uses in medical diagnosis.

Endoscopy uses the visible light spectrum as a probing energy and the reflection of that light to produce diagnostic images.

CAT or CT (Computerised Axial Tomography or Computerised Tomography) is a means of generating a three-dimensional view of the area under diagnosis. Using probing energy in the X-ray spectrum, a CT scanner pans a collimated beam of radiation through a full 360^o around the subject. The fanned beam is picked up by a series of detectors diametrically opposite to the source. The detectors measure the attenuation of the beam as it passes through the various tissue densities. From this information a full image of a slice of between 1 mm and 10 mm thick depicting the relative internal absorption of the radiation by the tissue types can be reconstructed. CT scanning is a well-established technology now commonly used in internal diagnosis of a range of disorders. The methodology was introduced in 1972 (Hounsfield, 1973).

Magnetic Resonance Imaging (MRI) or Nuclear Magnetic Resonance Imaging (NMRI) is another well-established imaging modality for the clinical diagnosis of a range of conditions. It is particularly suited for imaging soft tissue as the detected and measured property is the *Nuclear Magnetic Resonance* of hydrogen atoms; a main constituent of soft tissue cells is water (Hornak, 1998). What prompted the development of the use of MRI for medical imaging was the discovery that tumours displayed significantly different MRI to healthy tissue (Damadian, 1971)

Ultrasound utilises acoustic vibrations of frequencies above the limits of human hearing; these being around 3.5 –7 MHz. The imaging technique involves receiving reflections that are detected by piezoelectric sensors and reproduced as a raster image. This is just one example of a modality that does not use electromagnetic radiation as the probing or detected energy.

Positron Emission Tomography (PET), although classified as unprobed in Table 1.1, is activated by the injection of a radio-isotope into the subject. Currently, this is ^{18}F-labeled fluorodeoxyglucose (FDG) which has a half-life of 110 minutes. The principle of operation is based on positron annihilation detection. A positron is an antimatter electron having identical mass to an electron but with a positive charge of the same magnitude. When a positron and electron meet, the mass of each is entirely converted to energy in the form of photons which leave the event in almost opposite directions. It is the incidence of the photons on the detectors in the scanner that is used for image reconstruction. The spatial resolution is around 7 mm for human-sized scanners though the time to acquire images is greater than one hour as this is the minimum time to allow for absorption of the radio-isotope. Another disadvantage of the modality is that with the isotope having a relatively short half-life, manufacture has to be close to or at the clinical site, though more promising isotopes are being developed such as ^{124}I (Iodine) with a half-life of 4.1 days (Walker *et al.* 2004).

1.2. An Overview of Electrical Impedance Tomography (EIT)

Electrical Impedance Tomography is a relatively new, non-invasive imaging method. It enables the internal electrical impedance of any conductive object to be imaged by means of current injection and surface voltage measurements through an array of externally applied electrodes. The resulting aim therefore is to reconstruct a tomograph of electrical conductivity within a body to assist in detection of any anomalies that may be identified from a conductivity, admittivity or impedance change. An alternative terminology which has been coined to describe the process is *Applied Potential Tomography* (APT) but this is in far less common use in recent literature. It has particular advantages over other modalities already discussed in that it is safe, inexpensive and rapid. The equipment is also small and portable (Bayford *et al*, 1996; Metherall, 1998).

1.2.1. Limitations

A major issue that currently limits the use of EIT as a routine technique in biology and medicine is its relatively poor spatial resolution (Barber, 1989; Bayford *et al*, 2001b; Brown *et al*, 1985). The quality of images generated by EIT is influenced by a number of factors that include electrode impedance and measurement errors (Barber and Brown, 1988). The main factor, however, is the algorithm used for reconstruction. A number of studies into the relative accuracy of reconstruction algorithms have been undertaken (Adler and Guardo, 1996; Bayford *et al*, 2001b; Breckon and Pidcock, 1987; Du *et al*, 1998; Jain *et al*, 1997; Olmi *et al*, 2000). Comparisons have also been made of electrode placement and measurement protocols (Avis and Barber, 1994; Boone *et al*, 1994; Boone and Holder, 1996; Booth and Basarab-Horwath, 1996; Cheng *et al*, 1996).

1.2.2. Current Work

EIT has been investigated for a range of applications both within and outside of the clinical medicine field. Blood flow and respiration disorders can be diagnosed within the thorax and a wide range of research activity has taken place in this field (Edic *et al*, 1995; Harris *et al*, 1987; Harris *et al*, 1988; Li *et al*, 1996; Metherall, 1998). The application of EIT on the head, and in particular conductivity distribution within the brain, is the main focus of this work. It has potential clinical benefits in localising epileptic foci during seizures so that corrective surgery can be considered (Boone *et al*, 1994). A resistivity change in the brain during epileptic seizure is brought about by neuronal cell swelling during intense metabolic activity (Hansen and Olsen, 1980; Holder, 1998). Changes in blood flow or depolarisation during epileptic seizure and other brain function also causes resistivity changes (Holder *et al*, 1996) and the rapid reconstruction of EIT images makes it potentially suitable for bedside monitoring (Holder, 1992).

A major problem in attempting to image the brain using electrodes applied externally to the scalp is the reduced levels of current density in the brain brought about by the relatively high resistivity of bone making up the skull. However, it has been identified that the current density within the brain is more uniform because of the presence of the skull (Gamba *et al*, 1999). This reduced current density, however, contributes to ill conditioning in the reconstruction algorithm as will be discussed subsequently.

1.3. Theory of EIT

As previously stated, the underlying principle behind EIT is to determine the conductivity distribution within a medium from a range of voltage measurements taken on the boundary surface under the influence of a range of current injection arrangements. The physical system for EIT involves an array of electrodes placed over the surface of the domain under analysis. For any one measurement, a pair of electrodes is used as a constant current source and sink, whilst a voltage difference is measured via another pair. This measurement procedure is repeated for a range of electrode pairs. There are a number of approaches to reconstructing an image of the resistivity distribution. The method adopted in this work is based on the sensitivity theorem, where the results from the voltage measurements are used to evaluate a *sensitivity matrix*, which is used to solve the relationship:

$$\mathbf{v} = \mathbf{S}\boldsymbol{\sigma} \tag{1.1}$$

where $\mathbf{v}$ is the vector of voltage measurements, $\boldsymbol{\sigma}$ is the vector of the conductivity of elemental volumes or *voxels* and $\mathbf{S}$ the sensitivity matrix. The construction of the sensitivity matrix is by no means trivial as will be seen from the following well-established analysis.

1.3.1. Governing Equations

For the purposes of this analysis, the region under investigation is assumed to be ohmic and isotropic. The interaction between electricity and magnetism can be expressed by Maxwell's equations, and assuming that the magnetic permeability of biological materials is very low, these can be expressed as:

$$\nabla \cdot \mathbf{E} = \frac{\rho}{\varepsilon} \tag{1.2}$$

where $\mathbf{E}$ is the electric field strength, ρ is charge density and ε is the permittivity. This is an expression of the divergence of the vector field, $\mathbf{E}$. It can also be shown that the field is irrotational or:

$$\nabla \times \mathbf{E} = \mathbf{0} \tag{1.3}$$

Ohm's Law for a conductor can be stated for current flow in one dimension as:

$$I = -\sigma A \frac{d\phi}{dx} \tag{1.4}$$

where I is current, σ is conductivity in Siemens/m, A is the cross-sectional area of the conductor and ϕ is the voltage potential across the medium. Defining current density $J = I/A$ and expressing equation (1.4) for a multi-dimensional function $\phi(x, y, z)$, this becomes:

$$\mathbf{J} = -\sigma \nabla \phi \tag{1.5}$$

$\nabla \phi$ is the gradient of the electrical field vector **E** and so equation (1.2) becomes:

$$\nabla^{\mathbf{2}} \phi = -\frac{\rho}{\varepsilon} \tag{1.6}$$

which is *Poisson's equation*. As there are no free charges, $\rho = 0$ and so this becomes *Laplace's equation*:

$$\nabla^{\mathbf{2}} \phi = \mathbf{0} \tag{1.7}$$

There is an infinite number of solutions to this partial differential equation that can only be limited by applying boundary conditions in the form of fixed voltages at defined points on the surface of the domain (*Dirichlet* conditions) or current injections (*Neumann* conditions). Ideally, solutions can be determined analytically for simple boundary conditions and domain geometry and for the sake of accuracy such an approach would be preferred. However, for more complex shapes and loading, this is not feasible and so requires the application of numerical techniques such as the Finite Difference, Finite Element or Boundary Element.

1.3.2. The Forward Solution

The generation of the sensitivity matrix required to solve the conductivity distribution from a set of clinical measurements as described in equation (1.1) would need to be generated from the range of forward solutions for those measurements. Applying a bipolar constant current source and sink to the region under measurement and considering the general statement of Ohm's Law of equation (1.5) that is $\mathbf{J} = -\sigma \nabla \phi$, there is no net outward flux of current from the region and so the divergence of the current vector can be expressed as:

$$\nabla \cdot \mathbf{J} = \mathbf{0} \tag{1.8}$$

This gives rise to the basic Poisson's equation for the forward solution by combining equations (1.5) and (1.8):

$$\nabla \cdot (\sigma \nabla \phi) = \mathbf{0} \tag{1.9}$$

Expanding this divergence gives:

$$\nabla \sigma \cdot \nabla \phi + \sigma \nabla^2 \phi = \mathbf{0} \tag{1.10}$$

or

$$\nabla^2 \phi = -\frac{\nabla \sigma \cdot \nabla \phi}{\sigma}$$

Dimensionally the RHS of equation (1.10) represents an electric field set up by a distribution of current sources and is non-linear, unlike the linear equation (1.5). The distribution of potential is dependent therefore on the boundary condition geometry and the domain geometry (Kiber *et al*, 1990). Analytical solutions are possible provided the domain geometry is simple and a number of such solutions have been carried out. The human head can be approximated as spherical and can be comprised of a sphere to represent the brain and three shells of increasing diameter to represent Cerebro-spinal fluid (CSF), skull and scalp respectively (Liston *et al*, 2001).

Yet, while this idealized geometry can be solved analytically there is an expectation that the results will contain inaccuracies when the inverse solution is applied to measurements from a real human head. These are due to two main contributory factors: one is that the idealized sphere geometry does not take into account the more complex surface features of the head such as skull and jawbone, spinal column, optic foramen and ear canal. The other is that the positional vectors of the electrodes placed on the idealized sphere do not match precisely those on the subject and electrode positioning is a critical factor for accuracy in EIT for static imaging. However, it has been shown that for difference imaging, that is the comparison of one conductivity distribution compared to one previously imaged, electrode placement accuracy is less crucial (Barber and Brown, 1988).

In order that a more reliable sensitivity matrix can be developed, accurate geometric models of the human head are required and the forward solution approximated using continuum mechanics approaches such as the finite difference or volume method, the Finite Element Method (FEM) or the Boundary Element Method (BEM). The method adopted for this work is the FEM as previously discussed and is subject to further treatment later.

1.3.3. The Sensitivity Matrix

The sensitivity matrix of equation (1.1) gives a measure of how surface voltage is affected by distribution of potential within the volume under investigation, for known boundary conditions. Assuming that the surrounding medium of the domain under question has negligible conductance then the only flux of the current density vector field through the surface is at the electrode sites. *Gauss's Divergence Theorem* states that if a vector field, **F**, has continuous first-order partial derivatives at all points in the volume, Ω bounded by surface Γ, then the outward flux of the field from the volume is equal to the total flux over the surface. This can be stated by the equation:

$$\iint_{\Gamma} \mathbf{F}\cdot\mathbf{n}\,dS = \iiint_{\Omega} \nabla\cdot\mathbf{F}\,dV \tag{1.11}$$

where **n** is the unit outward normal and *dS* and *dV* are elements of surface area and volume respectively.

A scalar field, *f*, in a domain will have a normal derivative at any point, *P*, on the surface, Γ, is given by:

$$\frac{\partial f}{\partial n} \equiv \mathbf{n}\cdot\nabla f \tag{1.12}$$

Taking two arbitrary scalar fields Φ and Ψ such that the vector field **F** ≡ Φ ∇Ψ, then the normal derivative at a point on the surface, from equation (1.12) can be expressed as:

$$\mathbf{F}\cdot\mathbf{n} = \Phi\nabla\Psi\cdot\mathbf{n} = \Phi\,\mathbf{n}\cdot\nabla\Psi = \Phi\frac{\partial\Psi}{\partial n} \tag{1.13}$$

and so the divergence statement, equation (1.11) becomes:

$$\iint_{\Gamma} \Phi\frac{\partial\Psi}{\partial n}dS = \iiint_{\Omega} \left(\nabla\Phi\cdot\nabla\Psi + \Phi\nabla^2\Psi\right)dV \tag{1.14}$$

which is a statement of *Green's theorem(first formula)*. Substituting σ∇Ψ for Ψ such that Ψ is a solution of equation (1.9), equation (1.14) becomes:

$$\iint_{\Gamma} \Phi\sigma\frac{\partial\Psi}{\partial n}dS = \iiint_{\Omega} \left(\sigma\nabla\Phi\cdot\nabla\Psi + \Phi\nabla\cdot\nabla(\sigma\Psi)\right)dV \tag{1.15}$$

The second term in the outer brackets of the RHS is equation (1.9), which equates to zero giving:

$$\iint_{\Gamma} \Phi\sigma\frac{\partial\Psi}{\partial n}dS = \iiint_{\Omega} \sigma\nabla\Phi\cdot\nabla\Psi\,dV \tag{1.16}$$

In simple terms, this is merely a statement of the conservation of energy as $\sigma\partial\Psi/\partial n$ is current density in the direction of **n**. Therefore the LHS of equation (1.16) equates to:

$$\iint_{\Gamma} \Phi\sigma\frac{\partial\Psi}{\partial n}dS = I_{\Psi}\left[\Phi\right]_{\Phi_a}^{\Phi_b} = I_{\Psi}\left(\Phi_a - \Phi_b\right) = I_{\Psi}\Phi_{ab} \tag{1.17}$$

for current injection between points *a* and *b* as shown in Figure 1.1.

If Φ and Ψ are interchanged in equation (1.14), a similar treatment leading to equation (1.17) yields:

$$\iint_{\Gamma} \Psi\sigma\frac{\partial\Phi}{\partial n}dS = I_{\Phi}\left[\Psi\right]_{\Psi_c}^{\Psi_d} = I_{\Phi}\left(\Psi_c - \Psi_d\right) = I_{\Phi}\Psi_{cd} \tag{1.18}$$

Assuming $I_{\Psi} = I_{\Phi} = 1$ then we have the statement of reciprocity (Geselowitz, 1971; Lehr, 1972) that states that the voltage difference across electrodes *c-d* resulting from current injection through *a-b* is equal to that across *a-b* resulting from a current injection of the same magnitude through *c-d*. Hence:

$$v = \Phi_{ab} = \Psi_{cd} = \iiint_{\Omega} \sigma\nabla\Phi \bullet \nabla\Psi dV \tag{1.19}$$

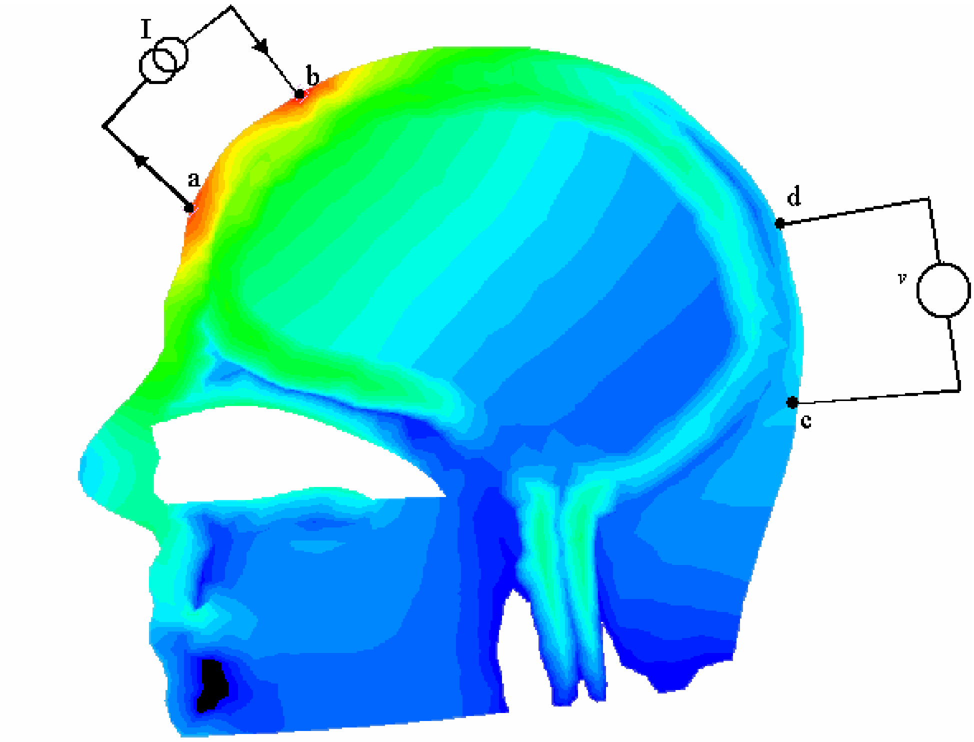

Figure 1.1: Current injected into points a domain at points a–b will give rise to a potential distribution within the volume and over the surface. The potential difference across two other points, c–d, can be measured. It can be shown that the potential difference across a–b is the same when current of the same magnitude is injected into c–d.

This defines the critical relationship between boundary voltages and conductivity distribution as originally proposed in equation (1.1). However, $\nabla\Phi$ and $\nabla\Psi$ are also functions of σ rendering equation (1.19) non-linear; a proposed solution to deriving the sensitivity matrix has been discussed by Metherall (1998) and is included here for completeness. By considering the uniform (subscript u) and perturbed (subscript p) of surface voltage and conductivity, a relationship between perturbed voltage measurements and corresponding perturbations in conductivity can be established. Considering the following relationships to define a conductivity change and hence a voltage measurement change:

$$\sigma = \sigma_u + \sigma_p \tag{1.20}$$

$$v = v_u + v_p \tag{1.21}$$

$$\nabla\Phi = \nabla\Phi_u + \nabla\Phi_p \tag{1.22}$$

$$\nabla\Psi = \nabla\Psi_u + \nabla\Psi_p \tag{1.23}$$

it can be shown that:

$$v_p = -\iiint_{\Omega} \sigma_p \nabla\Phi_u \bullet \nabla\Psi_u dV \tag{1.24}$$

This linearised sensitivity matrix is a statement of how surface voltage measurements change in response to internal conductivity changes. Given a continuum discretised into a number of finite volumes or finite elements, the RHS of equation (1.24) can be evaluated for any known elemental volume, assuming the field gradients to be constant throughout that elemental volume and provided the forward solution has been previously carried out. In this way, equation (1.24) becomes a set of linear algebraic equations based on equation (1.1):

$$\mathbf{v_p} = \mathbf{S}\boldsymbol{\sigma}_\mathbf{p} \tag{1.25}$$

where $\mathbf{v_p}$ is a vector of voltage measurement change, $\boldsymbol{\sigma}_\mathbf{p}$ a vector of elemental conductivity changes and **S** is the sensitivity matrix such that:

$$\mathbf{S_{i,j}} = -\nabla\Phi_{u,j} \bullet \nabla\Psi_{u,j} \Delta V_j \tag{1.26}$$

where i refers to the measurement number, j is the element number and ΔV_j is the volume of the j^{th} element. $\nabla\Phi_{u,j} \bullet \nabla\Psi_{u,j}$ is the cross product of magnitudes of the vector field within element j arising from current injection across *ab* and *cd*. This has been evaluated from the forward solution with boundary conditions relating to the i^{th} current injection and voltage measurement load case. The sensitivity matrix, **S**, is quite commonly referred to as the *Jacobian* and is therefore generally given the symbol, **J**.

1.4. Numerical Methods

In order to evaluate a range of forward solutions to build the sensitivity matrix, a number of different approaches can be adopted. As previously stated, analytical solutions are possible for simple geometry that may not yield the desired accuracy for reasons discussed in §1.3.2 (Liston *et al*, 2001). If accurate geometry is to be utilised then a range of numerical solutions could be used and these include finite volume (FV) (Guoya *et al.*, 2005), finite element (FE) or boundary element (BE) methods. There has also been some work investigating the use of the so called Infinite Element Method (IME). IME is particularly suited to modelling domains where some regions of the model boundary are a relatively large distance from the region of interest or the applied boundary conditions, such as the electrodes in EIT. The method is therefore not suited to modelling the human head but could have a valid application to other geometric forms for example those based on cylinders such as the torso or leg (Vauhkonen *et al*., 2000).

There is a limited range of commercially available solvers for the finite volume and boundary element methods, particularly those that have geometric modelling facilities incorporated within an integrated package. The boundary element method has been used by a number of researchers (de Munck *et al*, 2000; Duraiswami *et al*, 1995; Duraiswami *et al*, 1997; Tarvainen *et al*, 2001). The Finite Element Model has become the most popular approach in applying such continuum mechanics solutions to general engineering problems and many Computer-Aided Engineering packages incorporate finite element pre-processing, solving and post-processing tools. It is also very popular in the application of EIT and a number of researchers have applied the technique to generally simple geometrical models in EIT and EEG (Mengxing *et al*, 1998; Murai and Kagawa, 1985; Pinheiro and Dickin, 1997). In most cases the meshing of the domain has been carried out using semi-automatic or manual methods with solvers generally written in-house. There has yet to emerge a methodology that can automatically generate complex FE meshes of realistic geometry so that the effects of geometric accuracy on reconstructed image quality can be investigated.

There is a number of FE and BE meshes generated for the human head from packages for electroencephalography (EEG) and magnetoencephalography (EMG) source location. MRI scans have been used to generate realistic BE meshes of the human head that included three shells namely: scalp, skull and brain (Yvert *et al*, 1995). Other mesh generation systems include: CURRY (Buchner *et al*, 1997) that produces FE meshes, ASA (www.ant-software.nl) and BESA (www.besa.de) which are BE based. CURRY offers similar quality meshes to I-DEAS, but has limitations on mesh element size. Weinstein *et al* (1995) constructed a number of FE meshes for use in solving the forward problem for EEG and these have, at the time of writing, been expanded upon to provide a mesh with 59,379 nodes and 327,015 elements. Attempts to use this mesh for solving the forward problem for EIT have proved inconclusive as there is a significant number of highly distorted elements and a lack of continuity in areas of the mesh, particularly in the cerebro-spinal fluid (CSF) layer.

The use of a commercial finite element package with automatic mesh generation and integrated solver may provide the means by which realistic FE mesh generation can be accomplished. Packages such as I-DEAS offer a comprehensive range of facilities for building meshes and subsequently checking and improving element quality.

1.4.1. Finite Element Analysis

The general approach to the finite element method is to discretise the domain into a set of regular geometrical shapes such as lines, triangles or tetrahedrons for problems in one, two or three dimensions respectively. These shapes define the finite elements. Alternative geometric element forms include quadrilaterals for two dimensions and hexahedrons for three. Where the edges or surfaces of the element boundaries intersect are called nodes and the edges or surfaces themselves are nodal lines or planes. The governing equations defining the problem are then applied to the elements to generate an approximate solution for how the dependant scalars vary within the elemental area or volume. A full treatment of the finite element method is beyond the scope of this section but the general principle is explained below and expanded in Chapter 5.

By considering a one-dimensional version of the problem defined by equations (1.6) and (1.10), Poisson's equation can be expressed as an ordinary differential equation:

$$\frac{d^2\phi}{dx^2} = -f(x) \tag{1.27}$$

and providing $f(x)$ is known, this can be solved analytically. The numerical method will involve discretising the domain (a straight line) into a number of straight-line elements and approximating the dependent variable within the element. Figure 1.2 shows a simple one-dimensional element consisting of two nodes. Consider any dependent variable, $u(x)$, that satisfies the conditions at the nodes, $u_1=u(x_1)$ and $u_2=u(x_2)$.

Figure 1.2: A one-dimensional linear finite element consisting of two nodes. The interpolation function is a simple linear relationship for the dependent variable along its length.

Approximation using a simple first order polynomial of the form:

$$u(x) = a_0 + a_1 x \tag{1.28}$$

gives relationships for *u(x)* at the nodes:

$$u_1 = a_0 + a_1 x_1$$
$$u_2 = a_0 + a_1 x_2$$

which solve for a_0 and a_1 to give:

$$a_0 = \frac{u_1 x_2 - u_2 x_1}{x_2 - x_1} \text{ and}$$
$$a_1 = \frac{u_2 - u_1}{x_2 - x_1}$$

When substituted into equation (1.28), this gives the approximation in terms of the values of the function at the nodes:

$$u = N_1 u_1 + N_2 u_2 \tag{1.29}$$

where

$$N_1 = \frac{x_2 - x}{x_2 - x_1} \text{ and} \tag{1.30}$$

$$N_2 = \frac{x - x_1}{x_2 - x_1} \tag{1.31}$$

Equation (1.34) is the shape function for the element and N_1 and N_2 are the interpolation functions. It is from these shape functions that individual element equations are built up using a range of techniques such as the *direct approach* or the *method of weighted residuals* (Galerkin's method). These are described in number of texts including Chapra & Canale (1988) and Baker & Pepper (1991). The element equations derived from these methods are built together to form a set of linear algebraic equations of the form:

$$\mathbf{Ku} = \mathbf{F} \tag{1.32}$$

where **K** is the element property matrix (or stiffness matrix in stress and traction analysis), **u** is a vector of unknowns at the nodes and **F** is a vector relating to the boundary conditions of the problem.

For the two dimensional problem, the shape functions are based on the equations:

$$u(x, y) = a_0 + a_1 x + a_2 y \tag{1.33}$$

where *u(x, y)* is the dependent variable. For the three dimensional linear case there will be equations for *u(x,y,z)* containing terms in *x*, *y*, *z*. A two dimensional shape function will be of the form $u = N_1 u_1 + N_2 u_2 + N_3 u_3$.

1.4.2. Meshing Considerations

One problem with the finite element method is that if element geometry deviates too far from an ideal shape then the element equations such as (1.33) contribute to any ill-conditioning of the final stiffness matrix. This can be demonstrated if equation (1.38) were expressed in matrix form:

$$\begin{bmatrix} 1 & x_1 & y_1 \\ 1 & x_2 & y_2 \\ 1 & x_3 & y_3 \end{bmatrix} \begin{bmatrix} a_0 \\ a_1 \\ a_2 \end{bmatrix} = \begin{bmatrix} u_1 \\ u_2 \\ u_3 \end{bmatrix} \tag{1.34}$$

or $$\mathbf{EA} = \mathbf{u}$$

The values of the coefficients can then be solved using standard methods. Inaccuracies will occur if the determinant, **|E|,** is small and it can be shown that this is twice the elemental area. Thus if the area of a triangular element is small compared to the length of the largest side then ill-conditioning will be introduced to the element matrix which will then contribute to the final stiffness or global matrix for the whole model. For three-dimensional elements, it is the ratio of volume to element edge length that is critical.

For complex models with many thousands of elements, it would be too much to expect that there will be none with unacceptable distortion levels, but it is a primary aim in creating a mesh to minimise element distortion. Commercial finite element packages contain a range of functions for determining and reducing element distortion. I-DEAS has automatic meshing provision that attempts to limit the extent of element distortion during mesh creation and a set of tools to evaluate and improve mesh quality thereafter.

There are many ways to specify element distortion, or deviation from an ideal geometry. The simplest measure offered is the ratio of the maximum to minimum element edge length or the *Aspect Ratio* of the element. The value for a regular ideal element will be unity and any values above 5 may indicate unacceptable element geometry (Mottram and Shaw, 1996) though this guideline cannot be considered entirely reliable, as it does not take into account the whole of the element's geometry. Element *distortion* in I-DEAS is evaluated by mapping the actual element geometry to that of an ideal or parent element (cube or regular tetrahedron); the determinant of the Jacobian (matrix of partial derivatives) is multiplied by the ratio of the volumes (or areas) of the actual to parent elements. Most analysts consider values above 0.7 to be acceptable and negative values are impermissible.

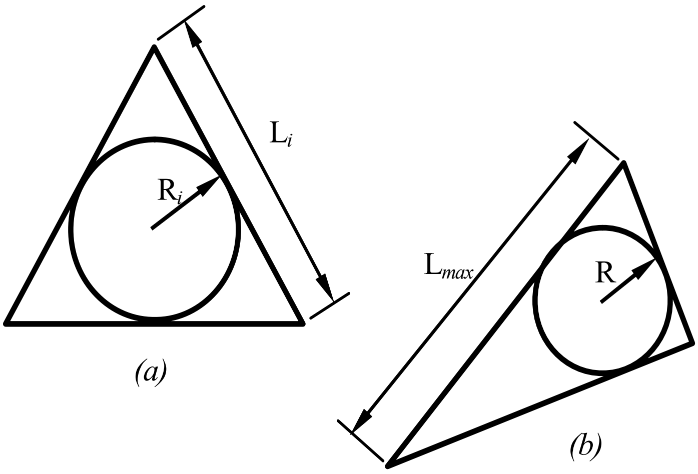

Figure 1.3: Principle of measuring the stretch of a two dimensional element: the ratio of the radius of the inscribed circle to the length of longest side is compared to that of an ideal element.

Many analysts use the measure of *Stretch* to quantify element quality. Stretch gives a comparative ratio of the regularity of an element to its ideal geometry. Figure 1.3 shows an ideal 2D triangular and a distorted 2D element to demonstrate procedure for evaluating stretch. For the equilateral (ideal) triangle in Figure 1.3(a) the ratio of the radius of the inscribed circle to the length of one side is:

$$\frac{R_i}{L_i} = \frac{\mathbf{1}}{\mathbf{2}}\mathbf{\tan 30}^\circ = \frac{\mathbf{1}}{\mathbf{2\sqrt{3}}} = \frac{\mathbf{1}}{\mathbf{\sqrt{12}}} \tag{1.35}$$

The ratio of the value $R/L_{\max}$ for the actual element in Figure 1.3(b) to that of the ideal element is the stretch value, S, which is given by:

$$S = \mathbf{\sqrt{12}}\frac{R}{L_{\mathbf{max}}} \tag{1.36}$$

For a three-dimensional tetrahedral element the stretch value is the ratio of inscribed sphere radius to maximum edge length multiplied by √24. I-DEAS documentation states that most analysts will consider stretch values of greater than 0.05 acceptable for tetrahedral elements. The tools provided in I-DEAS for mesh quality checking allow a histogram of a range of quality measures to be displayed. These include element distortion, aspect ratio, stretch and minimum or maximum included angle. In determining the quality of any one mesh it is desirable to ensure that a high percentile (>95%) of elements do not possess a stretch of less than 0.05 for a three-dimensional model (EDS, 2003), provided that they are not in the region of interest.

1.5. Reconstruction and the Inverse Solution

In the work undertaken for this thesis, a linearised sensitivity approach defined in equation (1.30) is used with the inverse solution based on *Singular Value Decomposition* (SVD). There has, however, been a significant amount of work undertaken in developing algorithms for EIT reconstruction. Initial work by the Sheffield group utilised back-projection methods (Barber and Seagar, 1987; Brown *et al.*, 1985; Brown and Barber, 1983; Guardo *et al.*, 1991; Metherall, 1998) and is now considered a well established reconstruction technique. The main approach is back-projection between equi-potential lines as the change in resistivity of the area between two equi-potential lines is considered as being proportional to the change in voltage difference on the boundary. An alternative approach to this is the so-called *perturbation* method (Kim et al, 1987; Kim and Woo, 1987) in which the resistivity of one element is increased by a known factor and the change in boundary measurements evaluated. In the initial studies for this approach voltage was applied to the domain and current measured, though it is well understood now that current injection generates better results. Other methods include layer stripping (Somersalo et al, 1991) and more recently the d-bar method (Isaacson et al, 2004; Isaacson et al, 2006).

All these methods rely on linear approximation in that any change in the boundary value measurement, whether it be voltage or current, is assumed to represent a proportional change in resistivity within the domain. This is clearly not the case, particularly for large changes of resistivity or conductivity, though many researchers apply the assumption to perturbations of up to 50% (Bayford, 2006). Therefore, it is only possible to carry out difference or dynamic imaging where only changes over time are evaluated compared to a fixed reference or base-line. Static imaging requires the use of a non-linear algorithm utilising iteration towards the solution such as the Newton-Raphson method (Breckon and Pidcock, 1987; Yorkey and Webster, 1987). Such an approach requires the re-evaluation of the sensitivity matrix – a lengthy and computationally demanding task – at each iteration. Another issue arising in static imaging is that in clinical use there can be no guarantee of the uniformity of contact impedance across the electrode set, whereas difference imaging cancels out this problem. However, for many applications, the approach is seen to be the only way forward and many investigators have worked to improve non-linear algorithms, for example Horesh et al (2004).

1.5.1. EIT of Brain Function

The main problem associated with the inverse problem in EIT is the fact that one is attempting to solve a large number of unknowns with a relatively small number of equations. The data acquired in EIT of brain function by this research group consists of 258 current injections and corresponding boundary voltage measurements. Figure 1.4 shows a schematic of the head net used for the EIT measurements described in this thesis. It is based on the standard EEG positions with an additional four sites making a total of 31 electrodes.

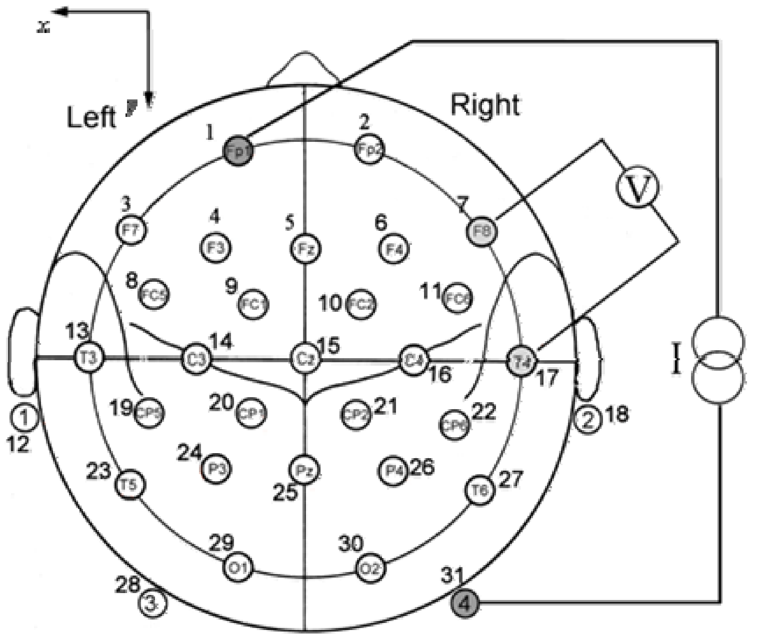

Figure 1.4: The relative positions of the electrode sites on the head-net for EIT measurement. The system is based on EEG 10-20 positions plus four additional electrodes.

Current is injected through opposite electrodes and boundary voltages measured from a combination of adjacent electrodes. For example, if current is injected through electrodes 1 and 30, voltage measurements are taken from a number of adjacent pairs such as [2 7], [7 17], [17 27] … and so on for a comprehensive range of current injection pairs to define one image time frame. The process is reasonably quick; for example the UCLH Mark 1b Electrical Impedance Tomography System is capable of performing more than 600 measurements per second which equates to nearly three images per second for the 258 measurements (Yerworth *et al*, 2002). In reality the current injected is AC and the frequency chosen to accentuate the difference in reactance of the tissue types and the perturbations to be imaged. The choice is made with reference to published sources of the impedance of the tissue ($Z = R + jX$) often presented as a Cole-Cole plot (Cole and Cole, 1941), which is a graph on the imaginary plane of the real versus the imaginary component of the tissue. The curve is an arc segment starting and finishing on the horizontal real axis centre below the real axis and proceeding anti-clockwise with increasing frequency.

For the linearised sensitivity approach, the EIT measurement process begins with one or more reference frames before the expected onset of perturbations leading to impedance change within the brain. The difference between the perturbed voltage measurements and the reference are then used in the solution of equation (1.30). The problem is therefore reduced to the inversion of the sensitivity matrix or *Jacobian*, **J**. There are a number of methods described in the literature for the inverse solution and reconstruction of EIT images and a comprehensive review is given by Liston (2003) in his thesis. In this work, reconstruction is carried out using the schema adopted and mostly used by the research group, the details of which are beyond the scope of this thesis but are briefly reviewed here for completeness.

1.5.2. Data Normalisation

In practice, the sensitivity matrix is normalised prior to inversion which is a two stage process: data (or row) normalisation followed by a voxel or element (column) normalisation. Row normalisation has the effect of reducing geometry and electrode position errors. Column normalisation compensates for the large variation of sensitivity between regions near the electrodes and those more remote from them.

Row normalisation is carried out by pre-multiplying the sensitivity matrix, **J**, with a diagonal matrix **R** where

$$\mathbf{V}^{norm} = \mathbf{J}\boldsymbol{\sigma}^{prior} \qquad (1.37)$$

$$\mathbf{R}_{ii} = \frac{1}{\mathbf{V}_i^{norm}}$$

where $\boldsymbol{\sigma}^{prior}$ define the conductivity priors for all elements.

Column normalisation is achieved by post-multiplying by a diagonal matrix, **C**, the diagonal elements of which are the reciprocals of the root mean square of the columns of the sensitivity matrix, thus:

$$\mathbf{A} = \mathbf{RJC} \qquad (1.38)$$

to define **A** as the normalised sensitivity matrix.

1.5.3. Singular Value Decomposition

The inversion method adopted is a *Truncated Singular Value Decomposition* (TSVD or SVD). SVD is a well established, robust method for solving ill-conditioned systems of equations and is based on the premise that a matrix, **A**, can be decomposed into:

$$\mathbf{A} = \mathbf{UWV}^{\mathrm{T}} \qquad (1.39)$$

Where **U** and **V** are orthonormal vectors and **W**, a diagonal matrix where the elements w_{ii} are the reciprocal of the *singular values* or *eigenvalues* of **A** in decreasing order. The inversion of this matrix, therefore, is simply:

$$\mathbf{A}^{-1} = \mathbf{VW}^{-1}\mathbf{U}^{\mathrm{T}} \qquad (1.40)$$

$\mathbf{W}^{-1}$ is evaluated easily from the reciprocal of the diagonal elements of **W**.

1.5.4. Inversion

The issue with EIT, as previously mentioned, is that a large number of unknowns need to be evaluated from a significantly lower number of equations, in other words the system is underdetermined. For this reason the matrix is better conditioned such that a square matrix $\mathbf{A}^+$ is inverted where $\mathbf{A}^+ = \mathbf{A}\mathbf{A}^\mathbf{T}$. The inverse is then pre-multiplied by $\mathbf{A}^\mathbf{T}$ to achieve the final inverse of correct dimensions.

As the singular values in **W** in equation 1.39 are in decreasing order of magnitude it is possible to establish a threshold where they are so small that, upon inversion, they will introduce unacceptable errors into the solution. In practice this is carried out either by deciding upon a ratio of maximum to minimum singular value that is acceptable, or by directly specifying the number of singular values to retain in the solution. Having established a point at which to truncate the singular values, all corresponding values in $\mathbf{W}^{-1}$ are set to zero. This method is often referred to as *Penrose-Moore pseudo inversion*.

1.6. Scope of Thesis

The research groups at University College London (UCL) and Middlesex University have been developing the use of EIT for imaging brain function pertinent to a number of clinical applications. As discussed in §1.2.2, these include the use of EIT for localising epileptic foci and also for establishing the presence of haemorrhage in stroke. Impedance changes in the brain can occur as a result in the change in blood volume, blood having significantly lower impedance than brain. Lack of blood to a region, or *ischaemia*, starves the tissue of oxygen resulting in cell death – a common indicator in stroke – which will cause increases in impedance. Haemorrhagic stroke as well as localised increased blood flow during epilepsy as a result of repetitive neuronal activity during a seizure will result in a measurable decrease in impedance (Bayford, 2006; Clay and Ferree, 2002; Holder *et al*, 1996; Holder, 1998).

1.6.1. Rationale

If EIT is to have significant clinical advantages in these areas, then image quality is essential. It is now well known that the use of anatomically and geometrically accurate forward models in EIT confers significant benefits as regards to the quality of reconstructed images. Many of the arguments presented in the literature that support this are derived from experiments that use some of the outcomes of this thesis. In the Chapters that follow, the historic progress of the work is described which describes a number of original contributions to the effort of generating accurate finite element models of the human head. The initial development work in this area is described in Chapter 2. This represents an important contribution to investigations carried out by the groups at UCL and Middlesex University as it provides a ready basis to generate meshes, based on any one solid model, with a range of resolutions and with relative ease. The approach used took a departure from automatic and semi-automatic segmentation approaches for the sake of geometric accuracy. Not only did the underlying geometry exhibit a high degree of accuracy, but the method also allowed finite element meshes with acceptable element geometry to be created. Still relying on the acquisition of MRI or CT datasets, the approach is inappropriate for time-critical issues in clinical use, an example of which is stroke diagnosis. For this example thrombolytic (clot-busting) therapy has been shown to improve outcome, but must be administered within three hours. However, Neuroimaging must be performed first to ascertain the cause, as such medication cannot be administered if the cause is a haemorrhage. In practice, CT cannot usually be performed and reported this soon, but EIT systems could be deployed in casualty departments and in theory could provide a rapid distinction between haemorrhage and infarction. In addition to the need for image acquisition, however, the manual segmentation methods deployed which take advantage of the precision of modern surface and solid modelling Computer-Aided Design tools are even more time consuming.

With the issues relating to the need for timely mesh generation in mind, the hypothesis to examine and test is that of whether subject- or patient-specific forward models can be generated by warping an existing accurate finite element model. The issues to examine are whether a finite element mesh can be warped without adversely affecting mesh quality and still produce acceptable images. Chapter 3 begins to explore this by applying simple affine warping of spheres to generate ellipsoids and report the effects on element geometry and localisation of simulated EIT data of known conductivity perturbations.

The initial stages of the process of more accurate warping is addressed in Chapter 4, which demonstrates a method of utilising the electrode positions used in EIT, which are based on the standard EEG configuration, to define a B-Spline surface patch more closely matching that of the subject or target. This relatively rapid and novel process is shown to generate a surface accurate to within more than acceptable tolerance, which can be used to define boundary conditions for elastic warping of head models.

The development of the algorithm for elastic warping is set out in Chapter 5. Though based on well-known methods, it represents a novel application of such techniques, particularly in respect of shelled models and the need to maintain geometrical integrity. The algorithm is optimised for this geometrical integrity, element quality and solution times. Validation of the algorithm is provided in Chapter 6 using both simulated and laboratory data to demonstrate its effect on image quality and localisation of perturbed conductivity changes.

1.6.2. Summary of Aims

Thus the issues to be addressed and demonstrated can be summarised:

- That Electrical Impedance Tomography of brain function will benefit from the creation and use of geometrically and anatomically accurate forward models of a subject.

- That Computer-Aided Design techniques such as those found in state-of-the-art commercial surface and solid modelling packages are an effective means of generating accurate models but would be themselves inappropriate for time-critical clinical use.

- That warping an existing finite element mesh is a viable and rapid means of improving geometric accuracy of the forward model without degradation to its numerical integrity and that the existing configuration of the system, such as electrode positions and known landmarks, can provide sufficient geometric data for warping.

- That established continuum mechanics methods can be adapted, applied and optimised to carry out timely finite element mesh warping whilst maintaining the geometric relationship between anatomical features and that the quality and accuracy of reconstructed images generated using such forward models is maintained or improved.

2. GENERATING FINITE ELEMENT MESHES OF THE HUMAN HEAD MODELS

A number of finite element models of the human head for these investigations have been generated using I-DEAS. These have ranged from simple hemispherical and spherical four-shell models to a complete model exhibiting significant geometrical integrity to a real head. The latter offers a high degree of precision regarding the geometry of the skull. The spherical models were simply generated from a partitioned solid model of four spheres each defining the main compartments of the human head, namely: Scalp, Skull, Cerebro-spinal fluid and brain. These simple models were used to test the feasibility of using a sphere as the underlying geometry for modelling the human head. The method and results of these investigations are described and discussed by Bagshaw *et al*. (2003). This work also discusses the feasibility of using these simple spherical models for the reconstruction algorithm by evaluation against more realistic head shaped models and a tank phantom. The realistic head models have been developed over time and the remainder of this Chapter describes the historical development of the construction of the underlying geometry and finite element models.

2.1. Initial Modelling Investigations

An initial model was constructed to test the process of mesh generation and was produced semi-automatically from segmented MRI scans. This initial model has been described by Bayford *et al.* (2001b) and has been used to investigate the current flow and density within the brain under a number of conditions (Bayford *et al*, 2000). In all cases, the actual geometric and finite element modelling was carried out by this author and is described in more detail below.

Construction of solid models from a series of cross-sectional slices is relatively straightforward in any solid or surface modeller, though to generate complex models from a large number of slices can be tedious. Many commercial feature-based modelling packages provide both solid and surface modelling functionality though few allow the existence of solids and surfaces together in the same part. I-DEAS is one system that does provide such an environment and this is of particular benefit in the modelling of the human head. This is because complex surface structures can be built piecewise and then subsequently associated with the solid model. A solid model is a highly comprehensive representation of a component, part or artefact as it models edges, surfaces and material direction for those surfaces. The solid model, therefore, is the intersection of the extrusion of the surfaces in the material direction. A surface model does not normally exhibit material direction and therefore represents an infinitesimally thin shell bound by its edges (Corney and Lim, 2001; Tizzard, 1994). For FE modelling, a solid model of the geometry to be meshed is required to ensure that elements are generated within the solid material of the model and can, if necessary, adopt the material properties of the solid. Without the material direction aspects of a solid model, the FE mesh generator cannot determine the volume to be considered. BE modelling, by its very nature, can use a surface model as the basis for mesh generation; it can also use the surface information implicit in a solid model.

2.1.1. Construction

The MRI datasets used for the initial model were imported into a graphics processing software package and the main elements of the cross section profiled or segmented; this is shown in Figure 2.1. Accurate cross-sectional curves defining scalp and brain were generated for a high percentage of the head and sufficient information for the skull was extracted to enable a solid model to be created. In the initial model, the curves created from the segmentation process were written out to a DXF (Drawing Exchange Format) file which is a widely used graphics exchange format with origins in Computer-Aided Design. I-DEAS can import DXF files into its native two-dimensional drawing application that can then, in turn, be transferred to the three-dimensional modelling domain.

The curves imported were not, in themselves, suitable for generating a three-dimensional solid model as they were made up from a large number of straight-line segments. In order that a geometrically acceptable model was generated, each curve needed to be recast as a Non-Uniform Rational B-Spline (NURBS) using the appropriate tool in I-DEAS. This was done using the original DXF imported curves as templates; once created, the curves were positioned appropriately in the z-axis to create the framework to generate the solid. The B-spline fitting procedure is depicted in Figure 2.1(b). In order to simplify the initial modelling, symmetry was assumed throughout and so only one half of the MRI scan was considered and the end tangents for the NURBS were set to a horizontal vector to ensure smooth blending with the mirrored half. Non-uniform rational B-Splines are commonly used in solid and surface modelling systems as they offer the ability to be fitted to complex profiles with a great deal of flexibility. They can be defined in a range of degrees of order from third (cubic) up to ninth in many modellers. An n^{th} order spline allows blending to the $(n-1)^{\text{th}}$ derivative and so a cubic spline allows blending between two curves or surfaces such that gradient and curvature match - the minimum requirement for visual smoothness. Higher order splines allow a high level of shape control though a similar degree of flexibility can be achieved with lower order NURBS that have more than one span. I-DEAS produces multi-span degree five NURBS that allow a high degree of shape control and blending.

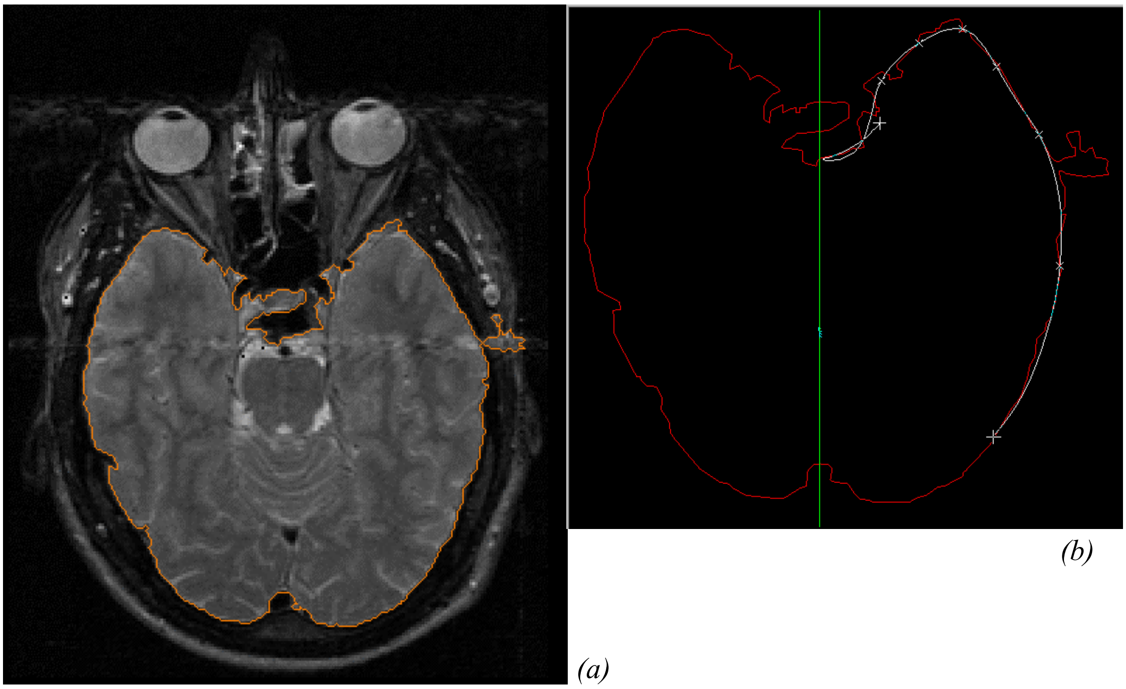

(b)

(a)

Figure 2.1: The MRI slices were segmented and imported to I-DEAS. (a) A typical MRI slice is segmented in a graphics-processing package. In this example, the boundary of the brain region has been determined. (b) The imported profile is used as a template to generate the NURBS curves.

Once the curves for each cross-section are generated and positioned, the solid model can be created using a surface loft utility. This generates the outer and the planar (symmetry) surfaces and optionally the end caps, which can be seen in Figure 2.2 as the top and bottom sections. If end caps are specified then a solid model is generated which can be reflected about the plane of symmetry to create the full head shown in Figure 2.3. The lofted model produced required little adjustment to create the model except that a number of connecting lines needed positional adjustment. Connecting lines in I-DEAS are isoparms or lines on the resulting surface that link points of equal parametric position on the individual cross-sectional curves.

A similar approach was taken to generate the skull and the brain though the segmented MRI data lacked the same degree of clarity that was prevalent in the scalp profiles. This is not an uncommon issue with manual segmentation of MR images (Meier *et al*, 1998). Whilst it was possible to create a sufficiently accurate model of the brain, the skull lacked some of lower features such as the upper and lower jaw structures. The CSF was considered as a shell of uniform thickness around the geometry of the brain and so the brain and the CSF combined were cut from the solid model of the skull to generate the cranial cavity. The skull was cut from the whole head to produce a solid model of the scalp and regions normally comprising the lower jaw. Consequently there was no modelling of the nasal cavity and eye-sockets and ear pinnae were removed from the head profiles to reduce overall complexity.

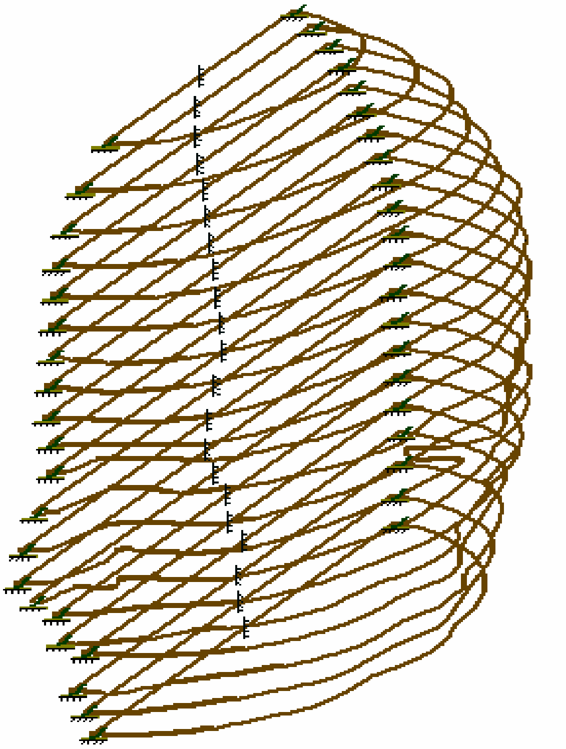

Figure 2.2: NURBS curves are fitted to the imported curves. Symmetry is assumed and each NURB is appropriately positioned in the z – axis ready for lofting into a solid.

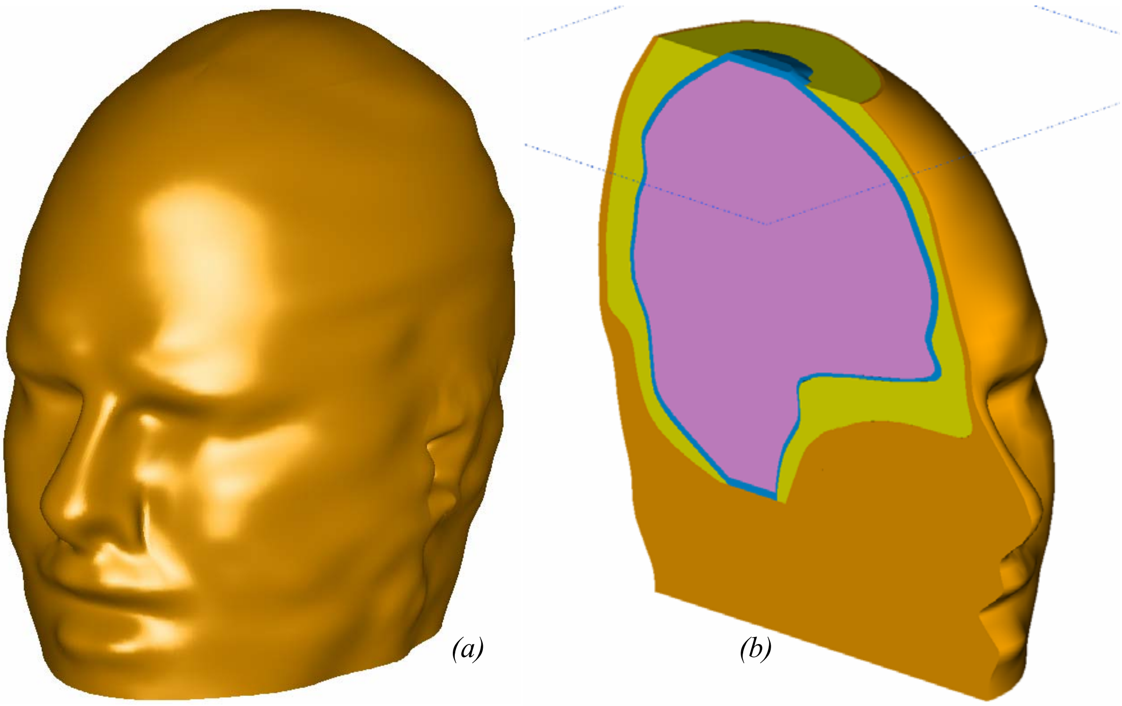
(a)
(b)

Figure 2.3:(a) the full head is created by lofting the profiles and reflecting about the plane of symmetry. (b) the skull and brain are created in a similar way and the CSF is a shell of even thickness around the brain. Boolean subtraction was used to fit the components together.

2.1.2. Meshing

The main incentive for using I-DEAS for this work is that it is known to have robust and well-developed meshing tools. Other software packages are available to carry out the meshing such as NETGEN (Schoberl, 1997) which is freely available as a binary executable and as source code. This package would be suitable if a homogeneous mesh were to be generated but, as in this case, where different anatomical regions are defined by discrete boundaries within the model, it has proven to be unsuitable.

A number of strategies can be adopted for meshing a solid in I-DEAS. I-DEAS is a comprehensive design tool incorporating not only feature-based solid modelling of individual parts or components but also the ability to constrain parts together into an assembly. The initial model of the head used this approach to generate a complete assembly containing all four anatomical elements. The FE application can process assemblies as well as individual parts and so by meshing individual components, a complete FE model can be built by bringing together the individual meshes. The nodes and elements are renumbered in the process enabling the final mesh to be presented so that the nodes and elements of the individual components can be identified. The original rationale to this approach was that each component could be meshed with the relevant material properties; the final assembled mesh would then represent a non-homogeneous model.

The problem with this strategy, however, was that there would be no guarantee that nodes would coincide on the scalp - skull, skull - CSF and CSF - brain boundaries. A tool exists in the software to identify and rationalise coincident nodes to ensure that the flow of current (heat) is modelled across the boundaries. The tool requires the user to input a maximum distance between nodes to define coincidence but there is considerable uncertainty that all nodes on the boundary of one component will be sufficiently close to those on the corresponding boundary on its adjacent component. This will give rise to areas of discontinuity in the mesh making the results questionable. This problem did not however detract from the original purpose of creating the model, which was to investigate the software's ability for solving the forward problem for EIT. In other words, to show that:

1. MRI data can be extracted and imported into the software and used as templates for creating accurate profiles for each cross-section.

2. These cross-sections can be used to generate solid models of the anatomical components of the human head.

3. The solid models can be meshed using three-dimensional finite elements and individual component meshes can be assembled together.

4. The final mesh can be solved and give an indication of the effects of the highly resistive skull tissue on the current density in the brain.
5. The model can be exported for use with existing algorithms for solving the inverse problem.

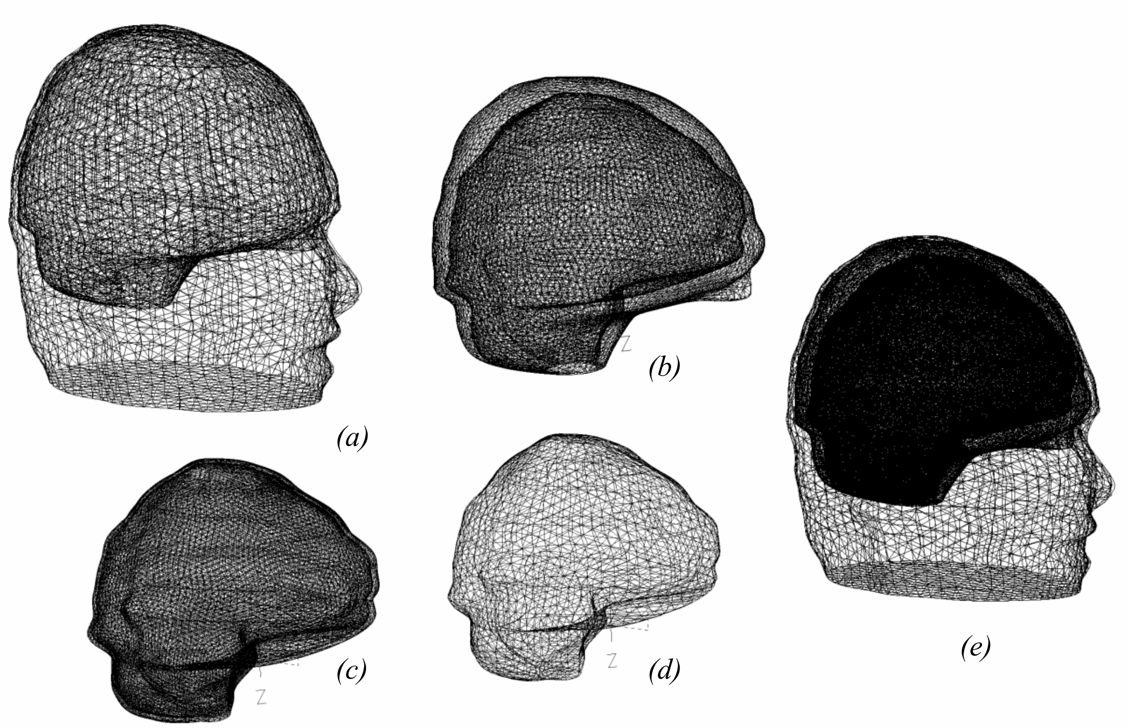

Figure 2.4:Finite element meshes of all the components and the complete assembly: (a) scalp, (b) skull, (c) CSF, (d) brain and (e) complete assembly. Global element size was set to around 8 to 10 mm, tetrahedral, linear elements and moderate advancing front.

The FE meshes for all of the components and the whole assembly are shown in Figure 2.4. The maximum time to mesh each component of the head required was approximately 30 s on an Intel Pentium III 500 MHz with 128 MB RAM under Windows NT 4.0 (SP6).

The release of I-DEAS (Master Series 8) used for this initial work incorporates a number of automatic meshing strategies. For three-dimensional meshing, the surfaces are meshed first and then the volume is filled using the nodes and element boundaries on the surfaces as a starting point. Any surface is meshed using one of two methods: Parameter Space or Maximum Area Plane (EDS, 2003; Lawry, 1999). The overall surface form of a solid model may be made up from a number of discrete surfaces that blend together in such a way as to ensure continuity. This means that at all points along the boundary between the surfaces the gradient and curvature of both surfaces are equal.

In parameter space, the software maps any curved surface to a normalised two-dimensional planar surface extending from 0, 0 to 1, 1 in the *s* and *t* directions (Figure 2.5). The mapped edges of the unit square are then divided up according to the selected global element length for nodal placement and then nodes are positioned and spaced on the plane which is also governed by the global length. When the planar surface is mapped back to the original, the nodal positions thus created form the vertices of the newly created elements. Parameter space has a number of limitations that exclude certain surface forms from being meshed in this way. The most significant of these is when a surface contains a pole such as one produced by a solid of revolution where the curve revolved touches that axis of revolution. In this case the resulting surface cannot be successfully mapped to a 2D planar surface.

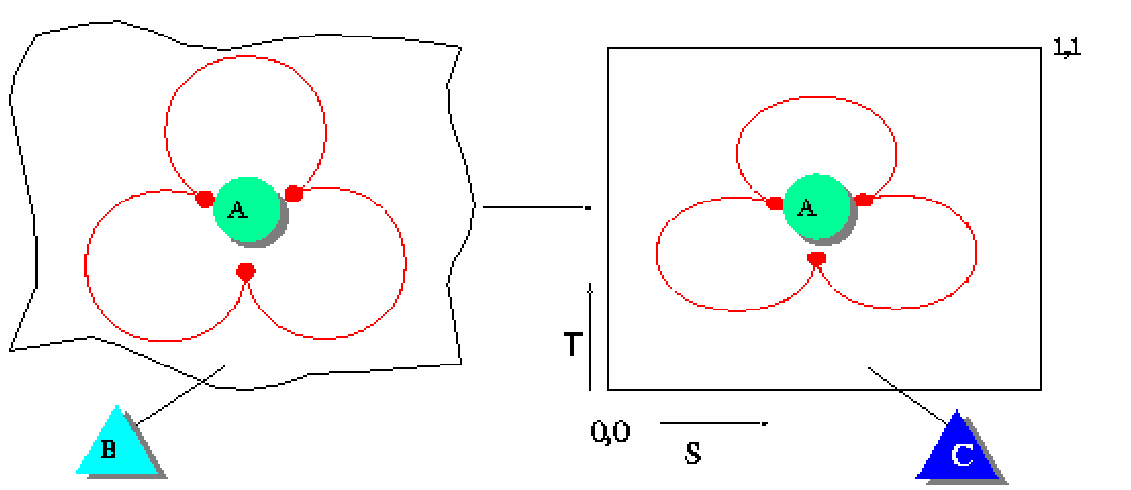

Figure 2.5: Surface mapped to parameter space. A is the planar surface, B is the underlying model space geometry and C is the underlying parameter space geometry. From EDS(2003), © Structural Dynamics Research Corporation, 2003.

In situations where parameter space cannot successfully create a surface mesh, Maximum Area Plane meshing may be used. In this case the surface is projected onto a plane along a vector which ensures that the resulting planar outline has the maximum area. The projection vector and the plane are thus orthogonal. The outline is then used as the underlying geometry to generate the surface mesh and then the inverse projection matrix is used to compute the nodal positions back to the original surface. The limitation for this method is that every point on the surface to be projected must have a unique point on the maximum area plane. If this is not the case then the surface must be split or partitioned into two or more surfaces that are more planar in form. This is illustrated in Figure 2.6.

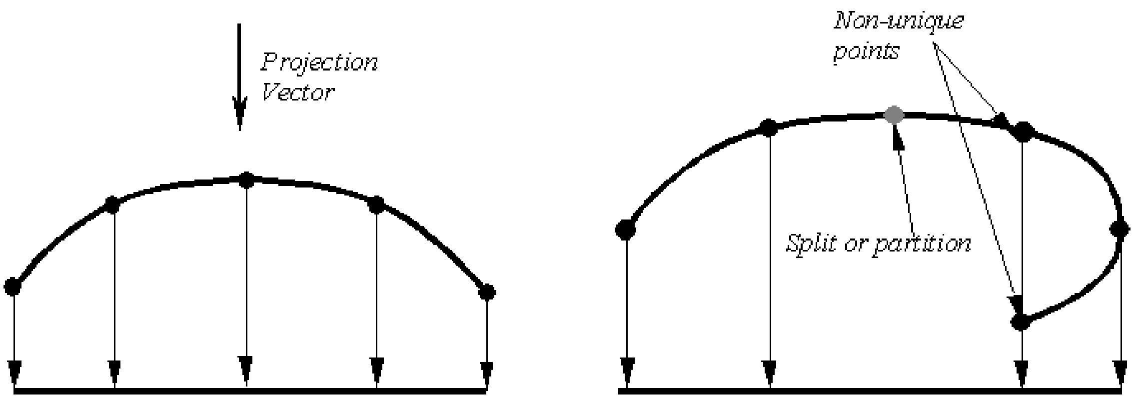

(a) (b)

Figure 2.6: Maximum Area Plane maps a surface to a plane by projection along the vector that creates an outline of maximum area. This is successful in (a) but unsuccessful in (b) where the projection yields non-unique points. If the surface is split or partitioned then the resulting surfaces may yield successful results along different projection vectors.

Once all surfaces are populated with elements and nodes, the three-dimensional elements are built into the solid material, starting from the surfaces and working in. Three algorithms exist for this. The first, *TriquaMesh*, is a traditional recursive sub-division of the volume, the second is a more recently developed *Advancing Front* algorithm and the third is *Delaunay*. Advancing front builds the mesh in layers from the outer surfaces inwards and can change the size the element with each successive layer. Parameters can be set to specify at which layer element growth begins and at what rate the elements in each successive layer grow. The method optionally allows the mesh of a large interior to be coarser towards the centre than at the outer edges and thus reduce mesh population and solution time for large bodies. The resulting mesh is particularly useful in stress analysis where mean stresses in the interior of a body have lower gradients compared to those exhibited at corners and edges. This may present an advantage in this study where the rapidly varying gradients of current density through the relatively thin skull region need a finer mesh than the more distributed values observed in the larger brain region (Gamba *et al*, 1999). On the other hand a coarser mesh within the brain region may provide insufficient sensitivity for the inverse problem. The Delaunay method is an improved advancing front algorithm with unity interior growth.

Prior to generating the mesh in each of the component part of the head, the relevant material for the solid models needed to be set so that the elements generated adopted their properties. The provision for heat transfer modelling in I-DEAS is suitable for solving an EIT forward problem, as the governing equations are similar as previously discussed. In order that meaningful numerical data can be extracted, the analogy between thermal and electrical systems needs to be compared and quantities mapped. Upon examination of the two systems it can be seen that voltage maps to temperature and charge to energy (§1.3.2); time and length remain unchanged in the mapping. Table 2.1 shows a comprehensive listing of the quantitative mapping between the thermal and electrical systems with dimensional analysis.

Table 2.1: Comparison of units and dimensions between electrical and thermal models

Electrical		Thermal	
Quantity	Dimensions	Quantity	Dimensions
Coulomb	C	Joule	$M L^2 T^{-1}$
Amp (C/s)	$C T^{-1}$	Watt (J/s)	$M L^2 T^{-2}$
Volt (J/C)	$M L^2 T^{-1} C^{-1}$	K	K
Ohm (V/A)	$M L^2 C^{-2}$	Thermal Resistance (K/W)	$K M^{-1} L^{-2} T^2$
Siemens/m (A/mV)	$M^{-1} L^{-2} C^2$	Conductivity (W/mK)	$M L^1 T^{-2} K^{-1}$

By default, the basic units in I-DEAS are for length – mm, mass – kg and force – mN. The relevant material property to be set for the head components, and hence the elements, is that for thermal conductivity (mW m^{-1} K^{-1} or μW mm^{-1} K^{-1} in I-DEAS) which maps to electrical conductivity (mA m^{-1} V^{-1} or mS m^{-1}). The electrical conductivity values chosen for the model are listed in Table 2.2 along with their respective values in I-DEAS.

Table 2.2: Conductivity values for different tissue types with I-DEAS equivalent values and sources

Tissue type	σ_{elec}(S m^{-1})	σ_{therm}(mW m^{-1} K^{-1})	Reference for σ
Brain	0.25	250	Geddes and Baker (1967)
CSF	1.79	1790	Baumann (1997)
Skull	0.018	18.0	Law (1993)
Scalp	0.44	440	Burger and Milaan (1943)

The number of elements generated for all of the components was 23219, 63982, 47140 and 21574 for scalp, skull, CSF and brain respectively. Figure 2.7 shows the distribution of stretch for all elements in the assembled model comprising over 155000 elements. The mean stretch is a little under 0.7 and a very low percentage is below the stated threshold of 0.3. Taking into account the premise that any value over 0.05 is acceptable it is clear that there is almost 100% acceptability in the quality of the mesh.

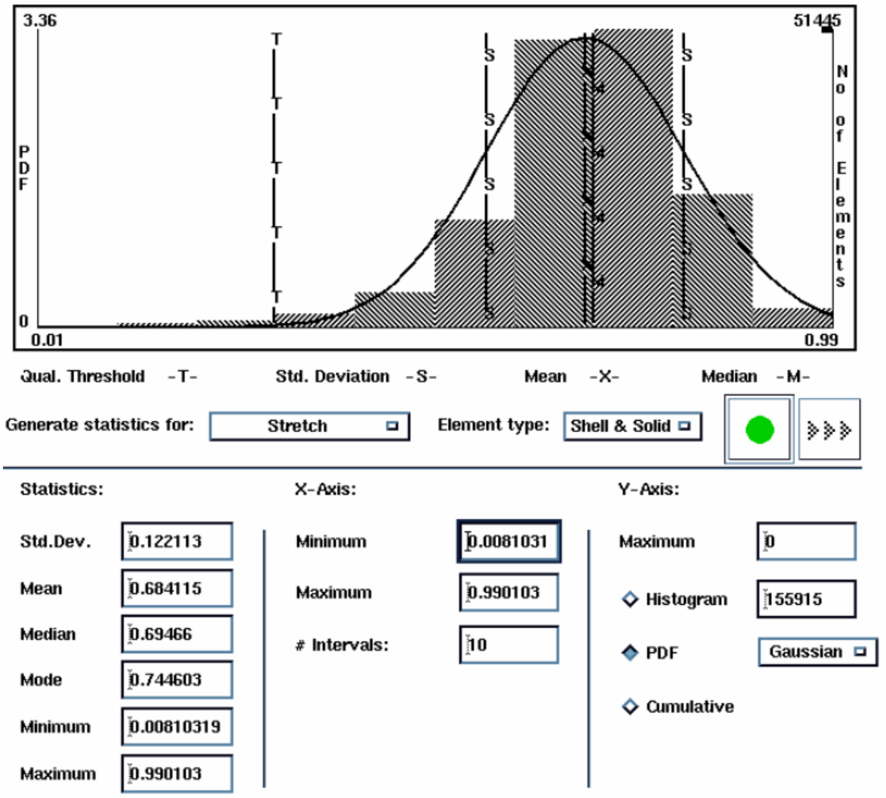

Generate statistics for: Stretch

Element type: Shell & Solid

Statistics:

Std.Dev. 0.122113

Mean 0.684115

Median 0.69466

Mode 0.744603

Minimum 0.00810319

Maximum 0.990103

X-Axis:

Minimum 0.0081031

Maximum 0.990103

Intervals: 10

Y-Axis:

Maximum 0

◇ Histogram 155915

◆ PDF Gaussian

◇ Cumulative

Figure 2.7: Stretch statistics for the final assembled mesh. The threshold value (T) is 0.3 and the distribution shows that a small percentile of elements falls below this criterion. The minimum stretch value of 0.008 is poor but there are very few elements with this value.

2.1.3. Initial Results

An example of the solution for the head model with a single source and sink is shown in Figure 2.8. Current, in the form of a heat source of ± 1 mW (1000 μW) equivalent to ± 1 mA, was injected to the front and back of the head model using single nodes to simulate a polar drive. The solution required approximately 2 minutes to complete on a PC with an Intel Pentium III 500 MHz processor with 128 MB RAM running under Microsoft Windows NT 4 (SP6).

It has already been recognised, for reasons stated above, that the results of the forward solution could not be relied upon entirely for purposes of inverse modelling. However, it can be seen from the plot of Figure 2.8(a) that the CSF plays a critical part in determining the pattern of current density within the brain. This is owing to the relatively high conductivity of the layer compared to skull and brain. The CSF layer is over 7 times more conductive than the brain and around 100 times more so than the skull. This means that the current has a tendency to shunt around the CSF layer rather than transverse across and this is even more evident from the results depicted in Figure 2.8(b).

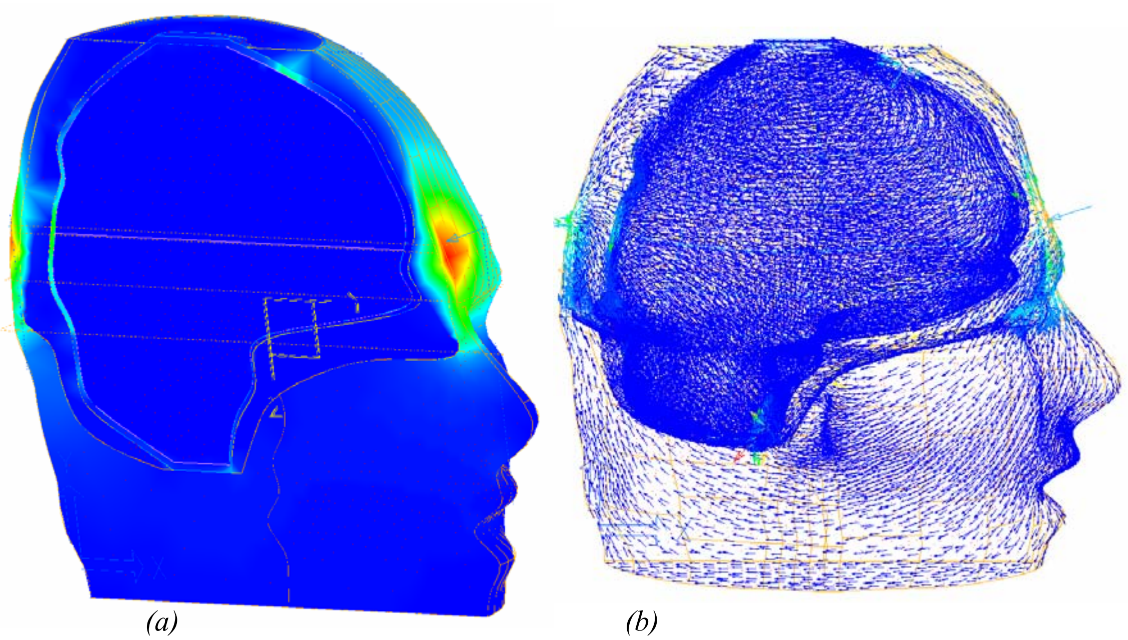
(a) *(b)*

Figure 2.8: Results from a forward solution for a current injection of 1 mA, source at the front and sink at the back of the head. The magnitude of the current density is colour coded in (a) and direction of current flow in (b).

It is quite clear from this initial study that the role of the CSF needs further investigation using a model in which there is a greater degree of confidence that the forward solution is reliable. The need for a more geometrically refined model has been identified, where there are little or no coincident nodes on the component boundaries and which has more accurately defined anatomical features such as lower jaw and nasal cavity. Even further refinement may include optic foramen features as there is likelihood that current will shunt along the more conductive optic nerve via the eye and generate higher current density around the frontal region of the CSF and thalamus in the brain.

2.2. Model Improvement and Refinement

A number of commercially available surface modelling software packages exist to enable this. These tools include *Alias-Wavefront Studio Tools* (www.alias.com), as used for this work and *Rhinoceros* (www.rhino3d.com). Surface modelling is a common technique in current use in engineering and product design. A significant proportion of modern consumer and specialised products from aerospace through automobile design to personal accessories such as cellular phones are modelled in this way for manufacture. The current view of the market for products (product semantics) is that users are attracted by aesthetics as much as function and modern surface modelling techniques such as the use of Non-Uniform Rational B-Splines allow the more organic forms required by the market to be generated. Thus the same software techniques are uniquely suited to the modelling of human anatomy.

Although I-DEAS has substantial surface modelling capability, its strengths in engineering design centre mainly on feature-based solid modelling, mechanism design and analysis, manufacturing and finite element stress and thermal analysis. For this reason it is considered as being an excellent tool for generating good finite element meshes but additional tools are required to assist in the surface modelling. The standard head model was therefore created using Alias|Wavefront Studio Tools. The surface models created were exported to I-DEAS using IGES (Initial Graphics Exchange Specification) so that they could be appropriately prepared and finite element models generated. IGES is a well-established format for transferring geometry of wide-ranging complexity from simple lines and arcs to high order NURBS. The transfer is precise and loss-less provided that both modellers, namely Studio Tools and I-DEAS, are correctly configured with appropriate IGES flavours. This is a process easily achieved within the software packages.

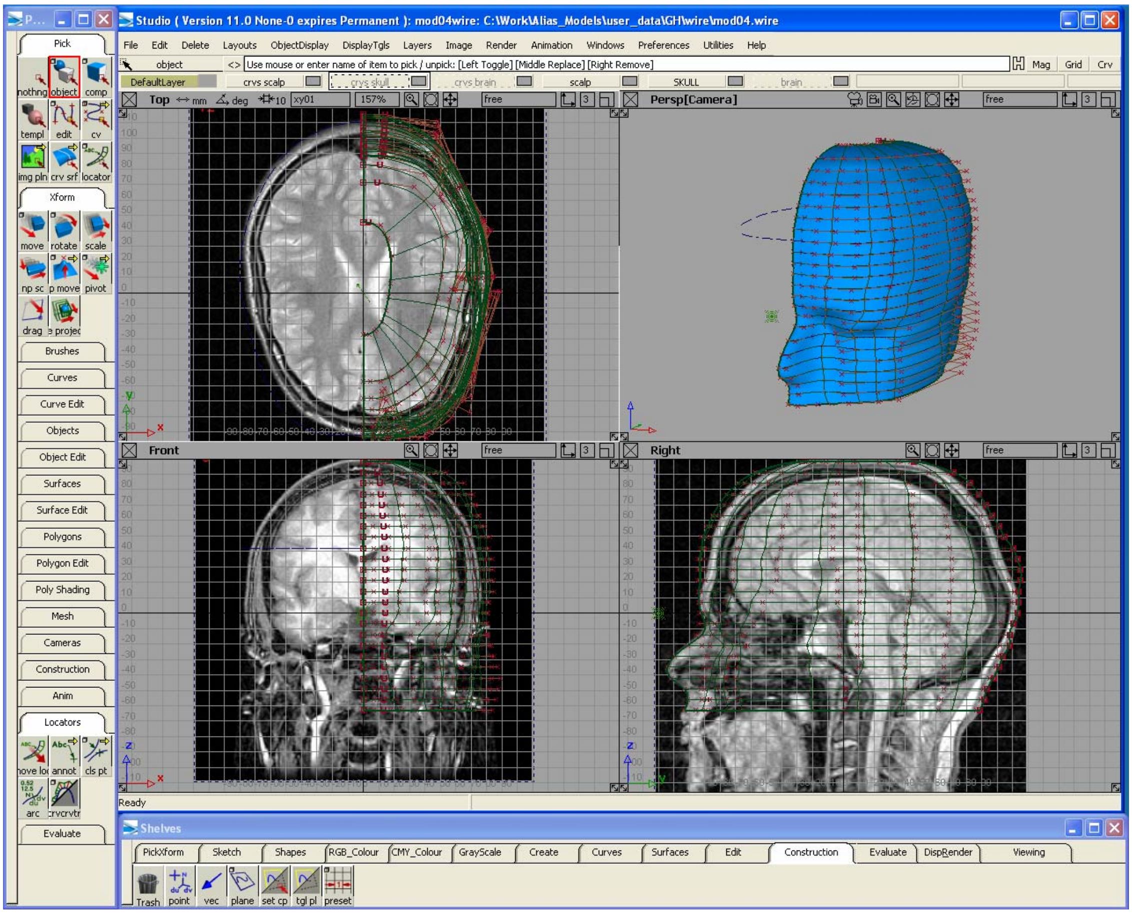

Studio (Version 11.0 None-0 expires Permanent): mod04wire: C:\Work\Alias_Models\user_data\GH\wire\mod04.wire

Use mouse or enter name of item to pick / unpick: [Left Toggle] [Middle Replace] [Right Remove]

Ready

Figure 2.9: Screen image of Alias|Wavefront Studio Tools. The MRI slices are cast as image layers in the xy, yz and zx planes. Individual layers can be accessed in plane so that NURBS curves can be modelled around the features. The surface constructed from the curves can also be seen the in the perspective view.

Another advantage of using a dedicated surface modeller such as Studio Tools over that of using I-DEAS for the geometric modelling is that such packages normally allow bitmap images to be cast as background planes to the modelling surface. These images, when correctly scaled and positioned, can then be used as templates for sculpting the curves defining the surfaces. They can be in two forms: the first is the image plane upon which a single image may be placed and the second type is known as image layers or paint layers. The latter can hold a series of images such as that retrieved from an MRI or CT scan; individual layers can be turned on or off so that all the slices can be individually modelled. A screen image of the surface modeller is shown in Figure 2.9, which illustrates the placement of image and the initial process of modelling the scalp.

2.2.1. The Standardised Head Model

An anatomical model of the skull was photographed to generate three orthographic views so that the images could be cast as image planes (paint layers) onto the modelling surface of the software. A photograph of the anatomical model used for this model is shown in Figure 2.10. In addition to these, further images were acquired from the MRI dataset used in the initial model and photographs from the Visible Human Project; typical images are shown in Figure 2.11 (www.nlm.nih.gov/research/visible/visible_human.html). The combination of these data facilitated the understanding of the surface forms to be modelled and their geometric relationship with each other. The functions in the software generate and manipulate NURBS to provide precise control over curve form and these were used to contour the slice images from the MRI datasets and photographs. Five separate surface models were generated, namely scalp, external skull, jaw bone, internal skull (to define the CSF) and external brain.

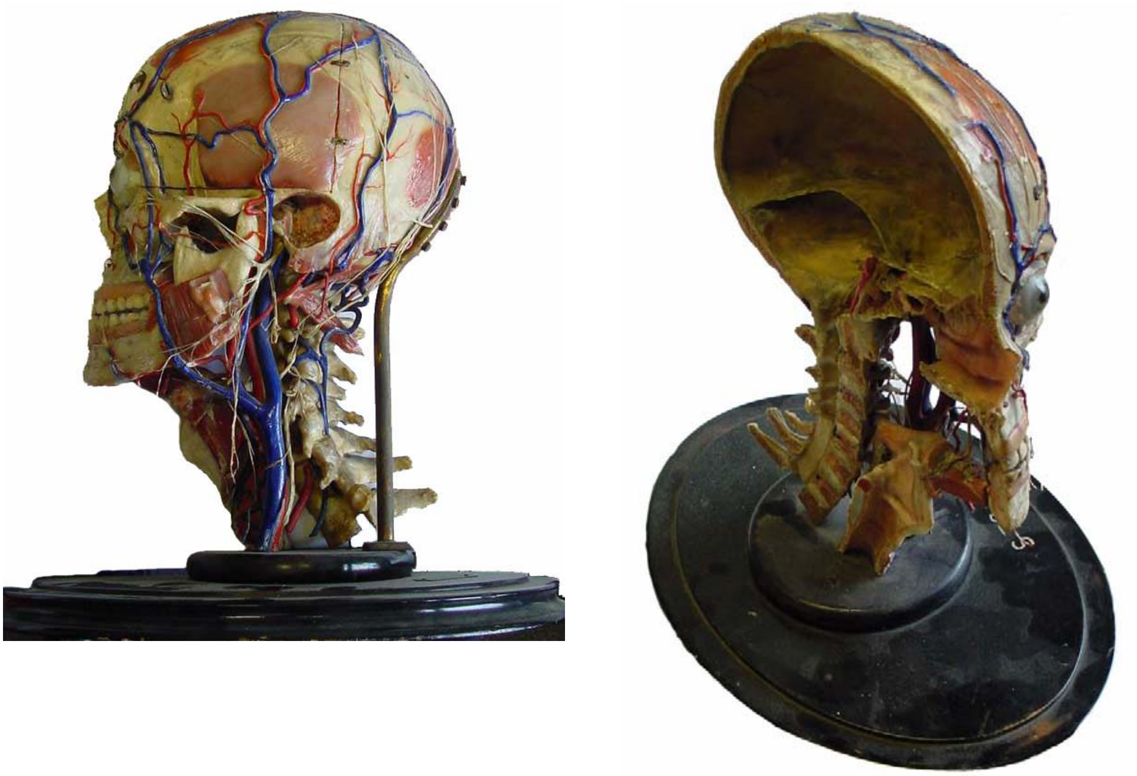

Figure 2.10: Photographs of the anatomical model of the skull used for the standardised head model

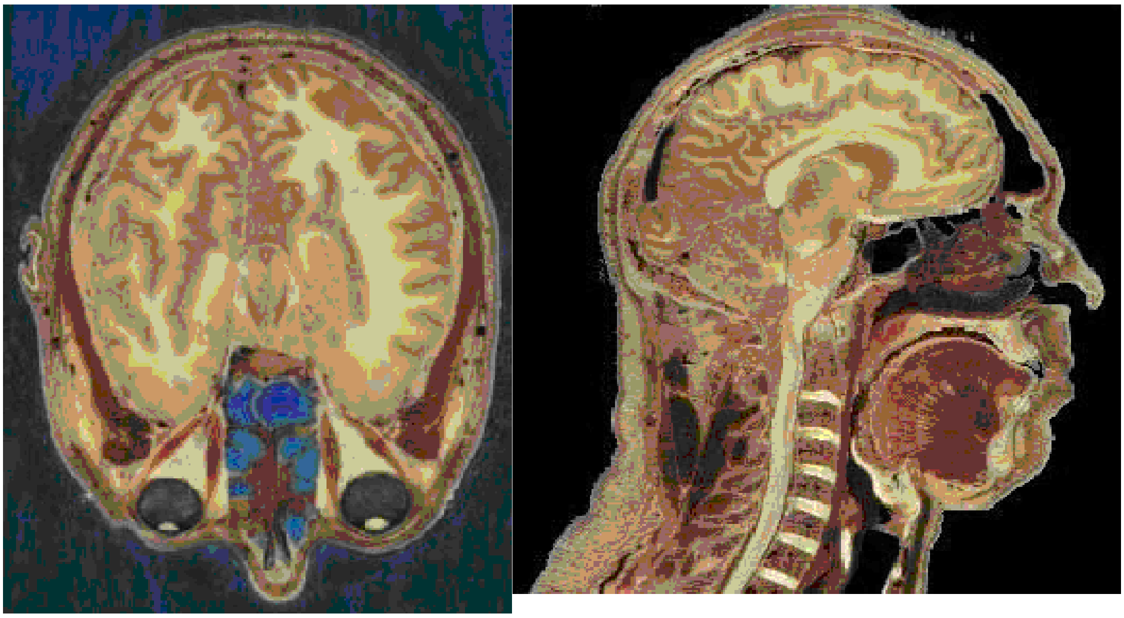

Figure 2.11: Samples from the photographic dataset taken from the Visible Human Project

The scalp was created from the MRI dataset by profiling NURBS curves to form an interpolated fit to the scalp form at each slice. In other words, the section was manually segmented with a continuous curve of high degree. A sufficient number of slices are used, normally spaced between five and seven mm apart depending on the resolution of the MRI. The slice images were parallel to the modeller's XY plane which corresponds to the transverse plane of the scan. A typical curve fitted to a scalp profile is shown in Figure 2.12(a). From this, it can be seen that symmetry is reasonably assumed; the dashed line showing the mirror image of the actual curve modelled. NURBS provide for a significant degree of control over the shape of the curve. The shape is finely and locally controlled by manipulating the positions of the control vertices (CVs), which are shown as crosses in Figure 2.12(a).

The curve is initially created by placing the edit points or knots – shown as squares in Figure 2.12(a) – at a number of positions around the profiles. Sufficient edit points were used to accurately profile the most geometrically complex cross-section or slice in the dataset and the same number of knots were placed in each slice at approximately similar positions. This ensured that the final surface generated, when the curves are skinned or blended together, has acceptable simplicity whilst maintaining accuracy of form. In order to achieve this, once the most complex curve had been created (generally level with the tip of the nose for the scalp), subsequent curves were copied to the new z-ordinate and carefully manipulated to fit the relevant image using the CVs.

In order that the two halves of the model blend at the plane of symmetry, the first two CVs at each end of the curve must lie on the same horizontal axis. The direction vector between the first two CVs in a curve defines the end gradient and the radius of arc that passes through the first three points defines the end curvature. Thus, with the CVs lying on the same horizontal axis, and with an exact mirror copy, the blend between the two halves agrees in gradient and curvature.

The skull was generated using a variety of surface modelling techniques. The main cranial structure was created using the techniques described above and other regions such as the nasal features, eye sockets and spinal column were modelled separately and the surfaces trimmed so that they blended in with the overall model. The jaw was also modelled separately using the anatomical model to inform the surface design. The internal skull and external brain models were generated from the physical human body photographic slice data and appropriately registered scaled to match and fit the skull manually. Images showing the historical development of the model are shown in Figure 2.13.

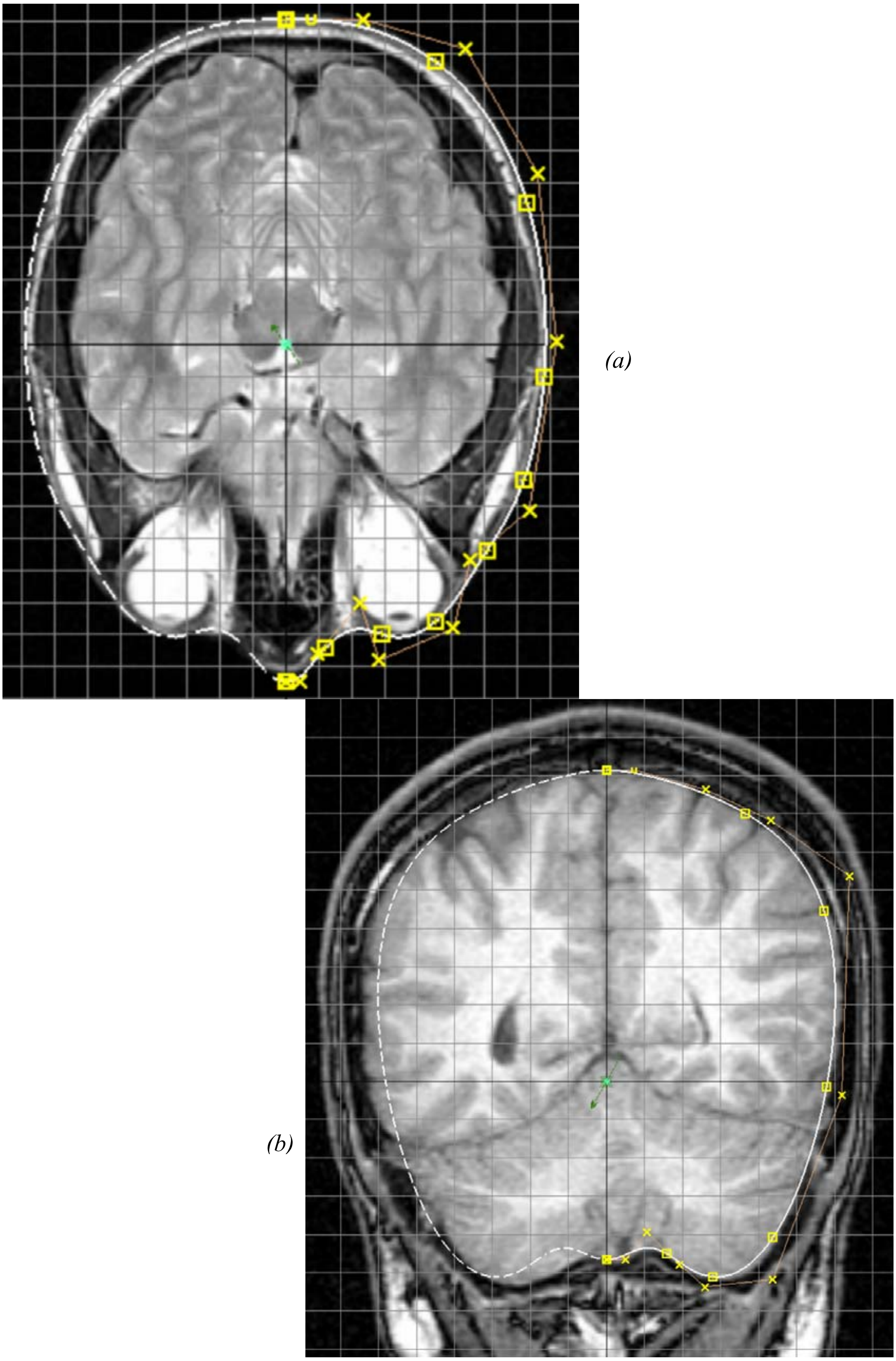

Figure 2.12: Typical curve fitting of (a) the scalp and (b) brain using MRI slice data. The NURB curve is manipulated using the CVs (shown as crosses) and is interpolated through the knots (squares). A higher density of knots in the anterior region indicated more complex surface definition. Symmetry is assumed (shown dashed). The scalp modelling is more appropriately achieved using transverse sections whereas the brain geometry lends itself better to being modelled using coronal slices.

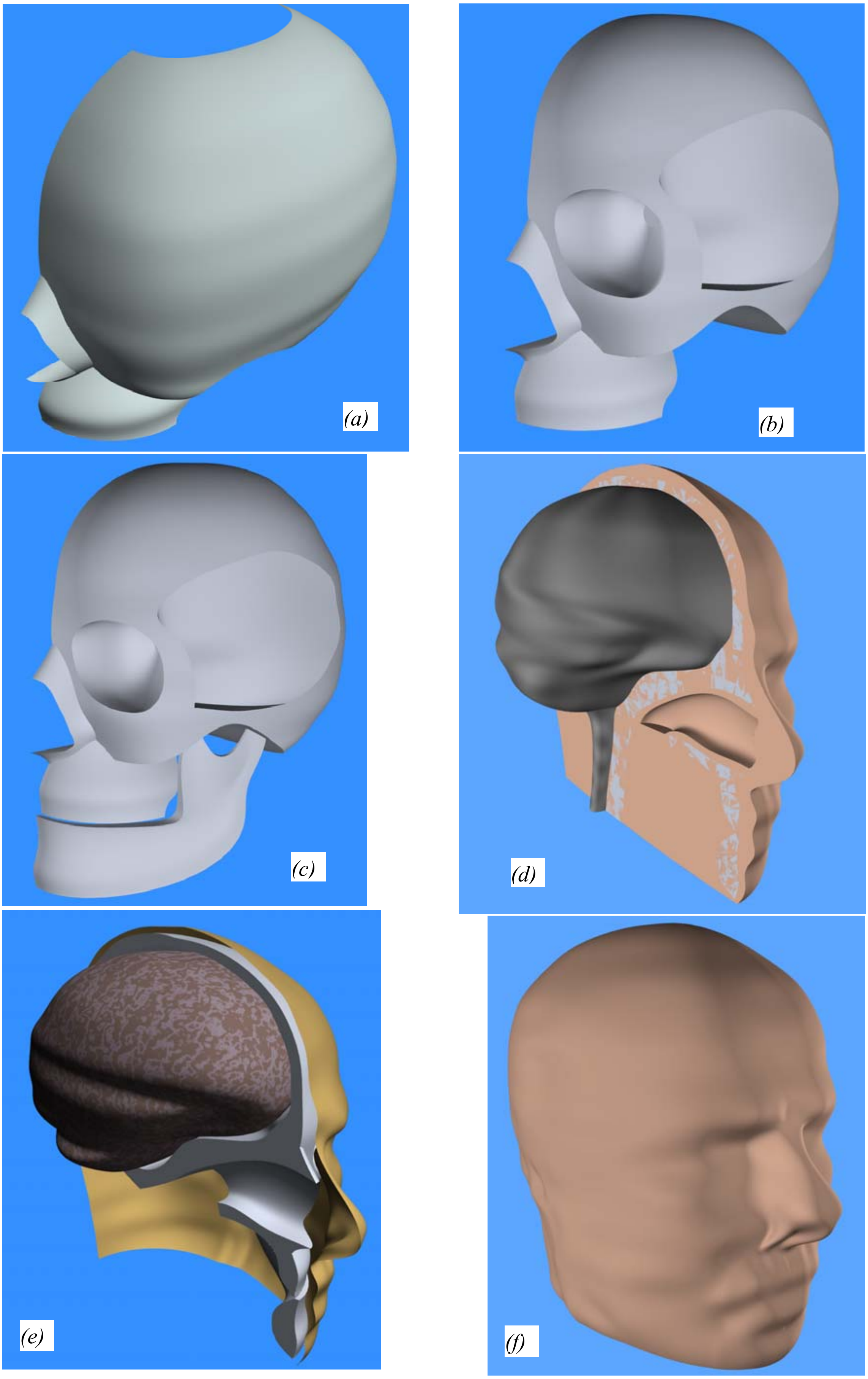

Figure 2.13: Stages in the generation of the realistic standard head model (a) initial cranial and nasal features, (b) additional features modelled, (c) jaw bone in position, (d) inner skull (CSF) (e) brain and (f) the final head model.

2.2.2. Patient and Tank Specific Models

Underlying solid models from which patient specific meshes were generated were also produced using the surface modeller. Slices were extracted from an MRI dataset for the subjects under investigation and the bitmaps were cast as image planes (paint layers) onto the surface modelling screen.

The specific models described here are: a neonate created from a MRI dataset, two epilepsy patients as discussed by Bagshaw *et al.* (2003) and latex tank containing a real human skull. The neonate model (Figure 2.14) was created from 25 transverse slices spaced a five mm intervals. Again, symmetry was assumed and once all curves for each layer were defined, the surfaces were created using the skin facility (surface loft) to generate a degree three blended surface through the slices. The surface models were then capped off at the top and the bottom to form a closed object. As the available anatomical data was limited to the MRI only, it was not possible to model certain skull features accurately. Eye sockets were possible but the lower skull regions and the jaw bone were to some extent idealised by the process.

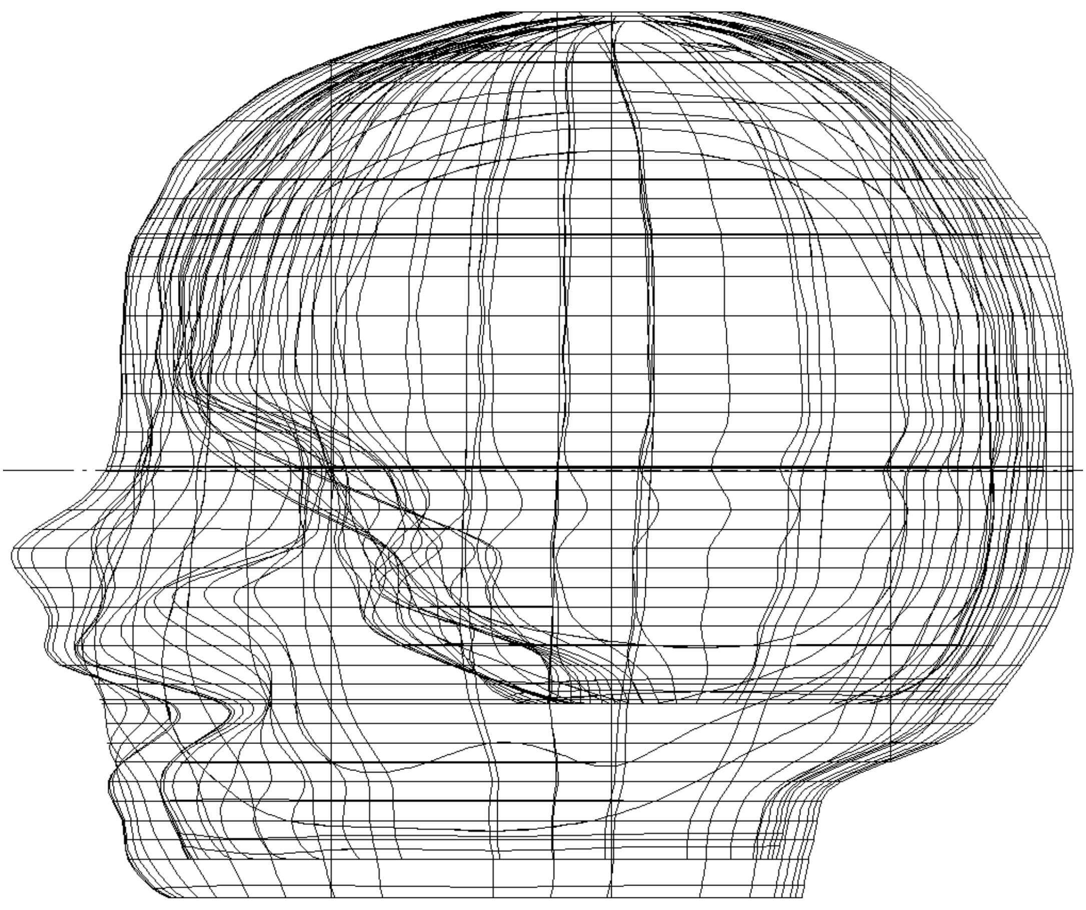

Figure 2.14: The neonate model showing internal surfaces. The modelling of the jaw bone and lower features of the skull is idealised by the simplified process

For the epilepsy patients, images of slices spaced seven mm apart were used in the XY plane (transverse) so that curves could be defined for the scalp and skull profiles, and images spaced six mm apart from the ZX plane (coronal) allowed the brain and CSF surfaces to be generated. The use of transverse slices for the scalp and skull provided the best information as certain features such as eye sockets could be readily modelled. Coronal images allowed better control over modelling the brain, CSF and internal skull features as illustrated in Figure 2.12(b). Again, symmetry has been assumed though it is confirmed from this illustration that this assumption does not fully hold for the form of the brain. As for the neonate, the surfaces were capped and the plane of symmetry defined so that a closed surface model could be produced; this facilitated the creation of a solid model when transferred to I-DEAS for meshing.

The tank model was generated in a similar manner but using a Computerised Tomography dataset. Symmetry could be reasonably assumed for the internal features but not for the scalp. The scalp representation in the tank was modelled around the skull by hand and exhibited too much asymmetry to justify the assumption. Thus, both halves were modelled separately and the curves for each half blended together using the tools in the surface modeller that allows curvature blending between two NURBS.

2.2.3. Meshing the Head Models

Once in I-DEAS, the four regions of scalp, skull, inner skull (CSF) and brain were merged together into a partitioned solid so that all regions were defined for meshing. The internal regions of skull, CSF and brain were thus represented as internal surfaces in the enclosed solid head. This approach is far more effective than the use of assembly modelling of defining the separate regions as I-DEAS will place nodes on any internal surface that partitions the solid. Further subdivision of surfaces was required to ensure that element surfaces could be generated using either the *parameter space* or *maximum area plane* techniques used by the meshing algorithm as described in §2.1.2. This subdivision was carried with the *split surface* utility in I-DEAS using a set of planar surfaces that divided the model's surfaces in a polar array perpendicular to the XY plane and also a linear array parallel to the XY plane. The polar array was equally spaced at 60^o. The linear array was spaced such that the resulting split surfaces represented suitably small surface patches, and also that the spherical form of the eye sockets and the tip of the nose were equally split. The aim of the surface splitting process is therefore to attempt to achieve a situation where most of the surface patches thus produced could be meshed using the *maximum area plane* method. These planar surfaces and their geometrical relationship to the standardised head are illustrated in Figure 2.15; a similar approach to surface splitting was carried out on all models.

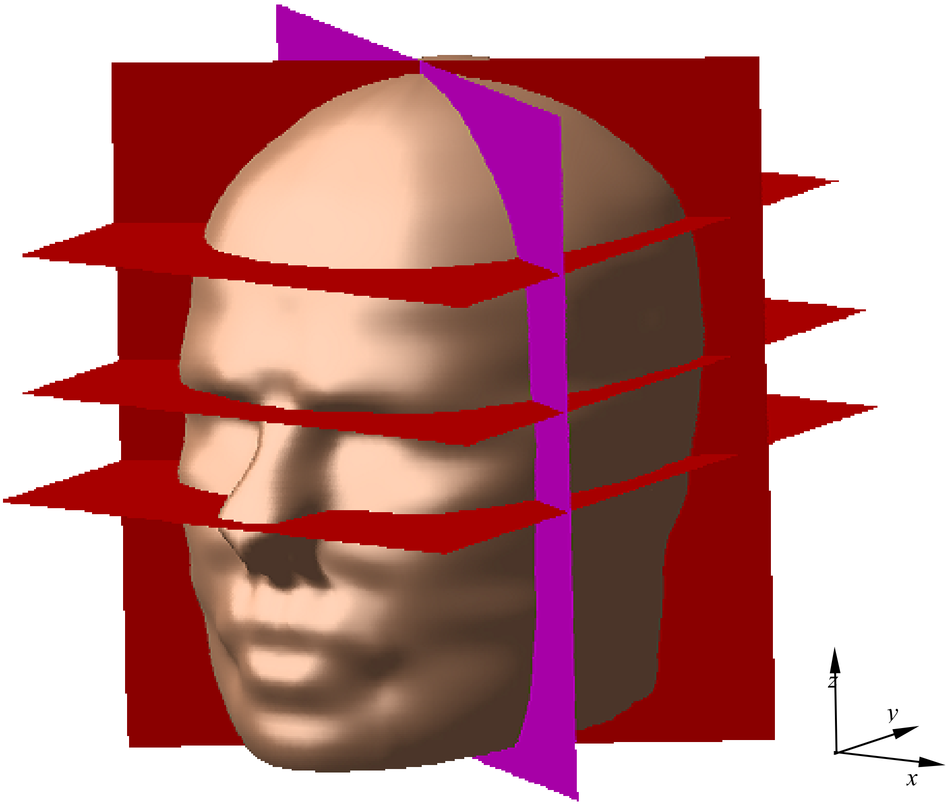

Figure 2.15: The planar surfaces used to split the standardised head model are so defined as to minimise surface area of the resulting patches thus facilitating maximum area plane meshing for most of the model. The vertical planes are equi-spaced at 120^o *angles taking into account that a split line already exists at the plane of symmetry. The horizontal planes (parallel to xy) are spaced to ensure certain complex features (e.g. eye sockets) are suitably split.*

Mesh density was controlled by specifying a global element size and the mesh previewed before final generation to ensure that an appropriate number of elements would be generated. As stated previously, three methods exist in I-DEAS to populate the volumes with elements and these are termed in the documentation as: TriQuaMesh, Advancing Front and Delaunay. TriQuaMesh appears from a historical perspective to be the oldest method used in earlier versions of the software. The Advancing Front method is described as Advancing Front with Local Reconnection (AFLR). It is beyond the scope of this thesis to describe the various advancing front approaches that have been presented in the literature which a numerous, for example: Schoberl (1997), Frey *et al.* (1998) and Radovitzky *et al.* (2000). The advancing front method in I-DEAS allows a growth rate and initial layer to be defined. The growth rate defines a factor by which element length will grow for each front as it advances into the volume of the domain. The initial layers value specifies from which front (layer) this growth factor begins to take effect. The documentation states that the Delaunay method is initially identical to the AFLR technique but once the surface mesh has been generated, it is checked for quality and refined, after which it is frozen. The differences, therefore, between the latter two methods are small except that it is reported that the Delaunay method has improved speed of mesh generation. From experience of generating meshes using both methods, the Delaunay method tends to be more robust for shelled models though no quantitative tests have been carried out to support this.

Tools exist in I-DEAS to separate the elements within the regions into groups so that they can be specifically selected for the application of prior conductivity values required for the forward model. This separation is relatively straightforward: the partitions for scalp, skull, CSF and brain become defined in I-DEAS as volumes and the element grouping tools allow elements to be selected that relate to those volumes. Once grouped into volumes, the elements in each group can be selectively displayed, visually identified and then the groups renamed accordingly.

2.2.4. Using the Meshed Models

While it is possible to carry out a single forward solution using I-DEAS thermal analysis as described in §2.1.3, a significant number of forward solutions with different boundary conditions will need to carried out and voltage gradients for each element extracted in order to build the sensitivity matrix. This process would not be the most efficient means of carrying out a reconstruction as other means exist to do this. The facility used in these investigations to perform forward and inverse solutions is EIDORS, a software suite written in MatLab (www.mathworks.com) and described by Polydorides *et al.* (2002). Therefore a means of exporting the meshes generated by I-DEAS in the appropriate format is required.

I-DEAS can export the meshes as *Universal Files*; these are text-based files specific to the software that can easily be parsed to extract nodal positions (vertices) and elemental connectivity (simplices) as well as the location of the elements within any of the considered regions, namely scalp, skull, cerebro-spinal fluid (CSF) and brain. A software facility has been written by the author in C++ that can parse I-DEAS Universal Files. This package has been given the working title GraphEIT (pronounced *Graphite*) and provides a graphical user interface with a number of functions to assist in visualising the meshes and utilising the EIDORS suite. Among the features available in the software are:

1. the means to define perturbations and generate simulated data using the EIDORS forward solver

2. menu access to the EIDORS routines that generate the Sensitivity matrix (Jacobian) and save this to a project folder

3. the ability to load and invert the sensitivity matrix using Truncated Singular Value Decomposition algorithm (Penrose-Moore pseudo inversion)

4. functions to carry out affine registration and deformation on the finite element mesh (see Chapter 3)

2.3. Results

Results evaluating a range of meshes generated on the geometry of the models described are given in Table 2.3. All five geometric models are shown each with a number of meshes of different densities defined by the number of nodes and elements in the model. The range of stretch for each mesh is given as a minimum and a maximum along with the mean and standard deviation of that stretch range. The number of elements with a stretch below 0.1 and the corresponding percentage of elements in that category are given.

Table 2.3: Analysis of FE Models

			Stretch Statistics					
Model	Nodes	Elements	Minimum	Maximum	Mean	Std dev	< 0.1	%
Standard	5939	31111	0.026	0.977	0.661	0.150	36	0.116
	24688	131672	0.105	0.990	0.679	0.110	0	0.000
Patient 1	6935	37062	0.014	0.970	0.601	0.166	184	0.496
	9025	48424	0.025	0.974	0.590	0.167	142	0.293
	27959	151797	0.006	0.984	0.635	0.152	384	0.253
	29891	162753	0.022	0.991	0.638	0.148	320	0.197
Patient 2	9062	47547	0.022	0.980	0.634	0.145	39	0.082
	9663	51043	0.053	0.989	0.639	0.145	57	0.112
	27078	145778	0.029	0.982	0.663	0.121	43	0.029
	30799	165344	0.056	0.989	0.665	0.120	22	0.013
Neonate	8703	45702	0.024	0.982	0.643	0.128	33	0.072
	26586	142654	0.033	0.988	0.686	0.111	34	0.024
Tank	4882	24722	0.024	0.960	0.576	0.162	120	0.485
	9959	52327	0.012	0.978	0.629	0.154	347	0.663

2.4. Discussion

The qualities of all the meshes shown in Table 2.3 are generally good. Although there are elements in most of them with stretch values below 0.05, the percentage of these is small and no mesh has elements with stretch values below 0.1 that are greater in number than 0.7% of the total element count. Denser meshes, or those with more elements, tend to exhibit better overall quality. This is largely because the elements with poorer stretch values are concentrated in the thinner shells of the model such as the CSF and thinner scalp areas. Larger elements in these regions tend to have poorer aspect ratios because of the low thickness. It is, at present, still unclear what bearing discretization quality has on image reconstruction in EIT. Many more investigations need to be carried out on both phantom tank models and human subjects for both linear and non-linear algorithms. Another source of error, which may be of significance, is the assumption made on the symmetry of the geometric models. In many cases, visual inspection of the MRI images used allowed a reasonable assumption of symmetry, though this is clearly an issue of further investigation. The tank model, which was segmented for a CT scan, clearly showed that this assumption was tenuous and was treated accordingly. The use of MRI images in itself presents a problem as MRI images could be distorted up to 5 mm (Grabowski *et al*, 1998; Maurer, Jr. *et al*, 1996).

The time taken to generate the models, and hence the meshes, has a significant bearing on any eventual clinical use. If quality of EIT imaging is highly dependant on the fact that the geometry underlying the forward model is close to that of the specific patient, then the methods described here will not be of value in the time-critical clinical application of stroke diagnosis. This application cannot be undertaken using a linearised sensitivity approach as an absolute image is required of the admitted patient and linear methods show relative conductivity changes. For the non-linear approach thus required for stroke diagnosis, positional accuracy of electrode placement on the forward model relative to that on the patient must be high; a requirement not critical in a linear solution (Barber and Brown, 1988). Thus the electrode positions must be accurately defined on the mesh used, and therefore at least the surface geometry and nodal positions on the scalp must be accurate. The standard head model was the most time intensive to create as it contained the most precise detail of anatomical features. The other models were more idealized and could take anything up to twenty hours to produce by an experienced modeler, including meshing.

3. RATIONALE FOR AND EFFECTS OF WARPING FINITE ELEMENT MESHES

The methods detailed in the previous Chapter describe effective methods for generating patient-specific finite element meshes for the forward model in EIT. It has been concluded, however, that such methods of carrying out registration of MR or CT data with surface models are inappropriate for time-critical clinical use. The level of human intervention required to generate the surface models is far too prohibitive for the applications of stroke diagnosis or even epilepsy foci localisation as discussed in §2.4. The amount of time to segment the volumetric images and then to generate the meshes can be in the order of twenty hours or more. When a stroke diagnosis indicating a condition of ischemia or haemorrhage is required within a few hours of onset, this is clearly unacceptable.

Therefore, a methodology has yet to emerge that can automatically and rapidly generate complex Finite Element meshes of realistic patient-specific geometry for solving the forward model in EIT. The proposal presented here is that if a library of geometrically robust FE meshes exists as a set of *a priori* data, then any one model can be selected as a close match to a patient and subsequently warped to fit a limited number of registration points or dimensions measured from that patient. These registration points will consist of known anatomical landmarks and the electrode positions. There is evidence to show that the integrity of the FE model and its underlying geometry has significant and measurable effects on the quality of reconstructed images (Bagshaw *et al*, 2003; Liston *et al*, 2003). However, it is not yet clear how important accurate representation of the complex geometry of a specific patient's head shape is on image quality. As already discussed in §1.4, systems for acquiring patient-specific geometry for mesh generation from MR or CT datasets do exist as part of software for inverse source modelling of the Electroencephalogram (EEG), namely: BESA, ASA and CURRY. Meshes generated in this way do not normally account for the layer of cerebro-spinal fluid (CSF). It is possible that these tools and the meshes generated could be used for Electrical Impedance Tomography though the main focus for current investigations is to establish the relationship between boundary form and EIT image quality; it is still unclear how boundary form and discretization errors affect the inverse solution from both linearised and non-linear algorithms. Inconsistencies in boundary forms between the subject and the underlying geometry of the forward model appear to be a significant source of image artefacts in EIT (Soleimani *et al*, 2004).

3.1. Previous Work

There has been some research activity towards generating patient-specific models of the human head, though the work has been generally confined to the fields of EEG and MEG. An exception to this is that presented by Gibson *et al*. (Gibson *et al*, 2003). They have proposed a method specifically for optical tomography where a surface from the adult head described in §2.2.1 of this thesis is warped to fit a set of points measured from a neonatal head surface using a thin plate spline. The new surface is then used as the underlying geometry for a mesh generated using NETGEN (Schoberl, 1997). Thus, a new homogeneous mesh is regenerated for each patient though no account is taken for the other regions in the domain such as skull, CSF and brain. The requirement for the work of this thesis is to generate patient-specific meshes with a non-homogeneous structure and, as already discussed in §2.1.2, NETGEN has not proven to be suitable for producing such a mesh. Also, the time taken to regenerate a new mesh would increase the overall time to produce a forward model for an individual patient. This fact supports the proposal to develop a means of warping a complete and geometrically acceptable FE mesh to produce a more accurate forward model for each subject.

Registration of volumetric medical images to existing geometrical models has been utilised by many researchers mainly for EEG and MEG analysis. A number of the methods currently used in these fields is reviewed and evaluated by Koikkalainen and Lotjonen (2004). These methods include point-based registration where corresponding points are taken from a volumetric image of a subject (the target) and an *a priori* model (the source) so that affine transformations can be applied to the model to provide a close fit to the target. The points used for registration can be a substantial set of known positions, such as electrode sites or data otherwise digitised from a laser scan. They can also be a simple dataset consisting of know landmarks such as nasion, inion and the two periauricular (pre-auricualr) points.

Affine transformations can be defined by seven or nine parameters. The seven parameters are translation in x, y or z, rotation about x, y or z and an isotropic scale factor. Nine parameter transformations will include translation, rotation and anisotropic scaling or stretch with respect to three dimensions. In addition to this type of registration, non-rigid transformation is also used and again these are discussed by Koikkalainen and Lotjonen (2004). The more interesting and relevant of these methods to this study are those registration techniques that use a triangulated surface model as the source and a MR, CT or, more importantly, a digitised surface point (DSP) datasets as the target. Non-rigid registration generally involves a free-from deformation (FFD) of the nodes in the TSM to the edges extracted from an MR or CT scan. It is reported that this can often produce undesirable results if the *a priori* TSM is not initialised to be close enough in geometric form to the target and so techniques of model selection are used to obtain a close match from a library of database of models.

Whilst any of the methods can be used as a basis for warping a head model to match the geometric form of a patient for EIT, they generally do not involve the use of a finite element model and hence the effect that the deformation of the model has on the integrity of the elements is not reported. Apart from the method proposed by Gibson *et al.* (2003) discussed above, Grabowski et al (1998) have presented a method using non-homogeneous finite element models. The method involves projecting the surface nodes on boundaries in the source model to corresponding surfaces extracted from the target MRI and then applying a relaxation to the elements thus distorted. Little detail is given about the solution for the relaxation problem except to say that it can be reduced to an Eigenvalue problem.

3.2. Mesh Warping Investigation

Therefore a method for warping a finite element model of a standard head, or one extracted from a library, to match specific and relevant target geometry for use as a basis for the forward model in EIT needs to be devised. The processes that make up this method may consist of an initial affine transformation of the source finite element model to that of the target. The target needs to be simply and rapidly defined for time-critical clinical use by the application of some normal anatomical landmarks as discussed previously. The next stage in the procedure is to carry out a free-form deformation of the surface nodes to match the positions of the electrodes. This is by no means a trivial process as the relatively small number of electrodes provides a basis only for a very coarse TSM and so the alternative is to adopt a scheme similar to that of Gibson *et al.* (2003) to define a surface through the electrode positions. The methods for this are the subject of the following Chapter where the electrode positions are analysed and a scheme for fitting a bi-cubic B-Spline patch through the electrodes is described. Having deformed the surface nodes in this manner then a means of maintaining the geometric integrity of the elements within the shells needs to be considered and this will be discussed in Chapter 5.

The effects of warping the finite element model either by affine transformation or FFD also need to be considered and the remainder of this Chapter is devoted to this investigation. In order to achieve this, simulated data from conductivity changes at various positions in meshed ellipsoids were generated. These were then used to reconstruct images, using a linear truncated Singular Value Decomposition (SVD) algorithm, with FE meshes of spheres that have been warped to the same dimensions as the original meshed ellipsoids as the forward model and subsequent reconstruction.

3.3. Simulated Data for Mesh Warping Investigation

For the purposes of investigating the effects of large scale warping of a finite element mesh, simulated data were generated from FE meshes of an ellipsoid. A solid model of an ellipsoid was created using I-DEAS master modeller by generating a solid of revolution of a semi-ellipse. The dimensions of the ellipsoid were chosen to match the aspect ratio of the standard accurate head model described in §2.2.1; these being: 150 mm in the x-direction, 190 mm in the y-direction and 200 mm in the z-direction. These sizes were determined and rounded to the nearest 10 mm from measurements taken from the model as shown in Figure 3.1.

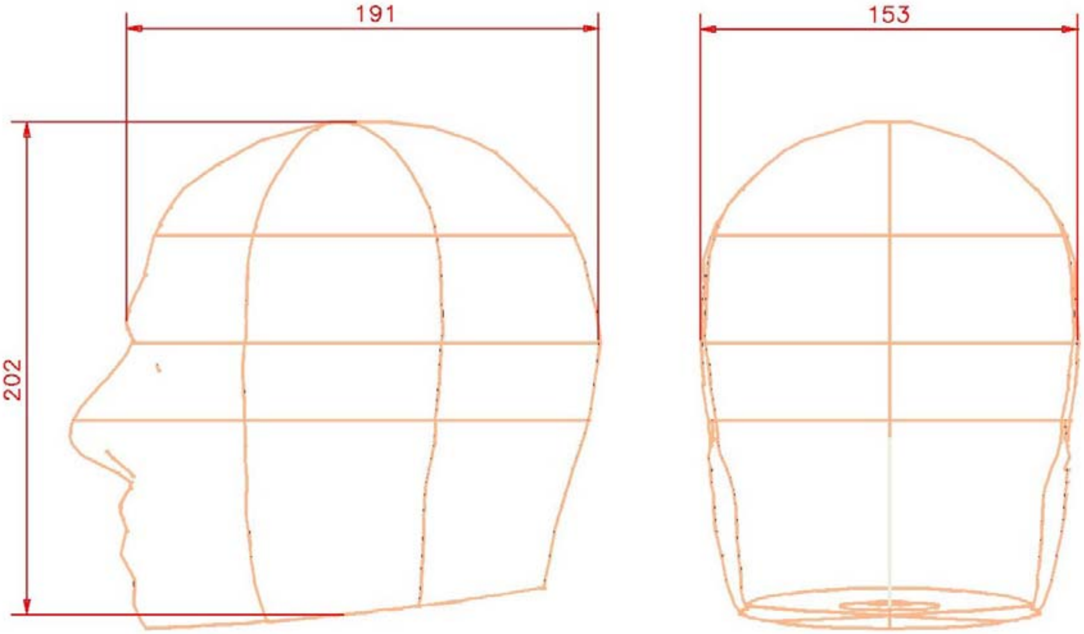

Figure 3.1: Orthographic drawing of the standardised head model showing approximate dimensions in x (153 mm), y (191 mm) and z (202 mm). These values are rounded to 150, 190 and 200 mm respectively for the purposes of modelling the ellipsoid.

Two FE models were created: a homogeneous model consisting of 11820 elements and 2387 nodes and a four-shell model consisting of 13985 elements and 2662 nodes. The four-shell model was separated into regions representing brain containing 5020 elements, CSF with 2693 elements, skull with 2972 elements and scalp with 3300 elements. The internal regions were also generated using revolved semi-ellipses, the relative geometrical radii of which were for brain 85%, CSF 3% and skull 9%. These three internal solids were partitioned into the main scalp solid model to generate the internal surfaces required to segregate the elements within each region. The number of elements, and hence the global element length, chosen for each model is such that the time taken for generating simulated data would be around 40s per forward solve on a Pentium 4 3.0GHz using EIDORS whilst ensuring an acceptable level of accuracy of the boundary voltages at the electrodes. For the shelled model, the elements generated for each region were separated into groups in I-DEAS and named according to their affiliation, that is: ELEMENTS – SCALP, ELEMENTS – SKULL, ELEMENTS – CSF and ELEMENTS – BRAIN. The FE models were exported as I-DEAS Universal Files complete with the group information.

The software utility, *GraphEIT*, previously described in §2.2.4 has functionality to define ideal perturbation positions, sizes and conductivities and report back actual position and size having established the nearest elements to the ideal. It can then perform a forward solve for each perturbation using imported files defining electrode positions and the current injection and voltage measurement protocol. The forward solution is generated by communication with the MATLAB engine and execution of the relevant modified EIDORS routines. Boundary voltage data can then be saved for use in the inverse solution to generate the images. The Universal Files for both the homogeneous and shelled ellipsoid models were imported into *GraphEIT* so that perturbations could be defined and simulated data generated. Materials can also be defined in *GraphEIT* and these are assigned to each element depending on the region in which it lies. The material property for each element is extracted from the Universal file by name for matching with the pre-defined material in *GraphEIT*. Five materials are pre-defined, namely: Homogeneous, Scalp, Skull, CSF and Brain; these were assigned the values of 1.0, 0.44, 0.018, 1.79 and 0.25 S/m respectively. Any element without a material definition in the Universal file is automatically assigned to the Homogenous material.

For the homogeneous model, conductivity perturbations were simulated and these were localised at approximately –50 to +50 mm along the x-axis and -70 to +70 mm along the y-axis in steps of 10 mm for each axis. The radius of the perturbations was set such that the resulting radius was of the order of 10 to 15 mm; the actual values achieved were 12.6 mm with a standard deviation of 0.9 mm. This value was calculated by summing the volume of the elements making up the perturbation and reporting the radius of the equivalent sphere of that volume. A total of 26 perturbations were therefore simulated for the ellipsoid model with conductivity perturbations representing a 10% change. To achieve this, new material was created in *GraphEIT* (named "Increase) and given the conductivity of 1.1 S/m.

The shelled model was similarly prepared and simulated data generated using 26 similar perturbations. The mean radius of the perturbations was 12.9 ± 1.1 mm. It was noted in this case that the perturbations at the extremes of the positions stated above, that is $x = -50$, $x = +50$, $y = -70$ and $y = +70$, that the perturbations also occupied the CSF region of the model. Therefore, the majority of the perturbations were positioned wholly within the brain region of the model and were assigned a conductivity value of 0.3 S/m, representing a 20% increase in brain conductivity. The whole procedure is depicted in Figure 3.2.

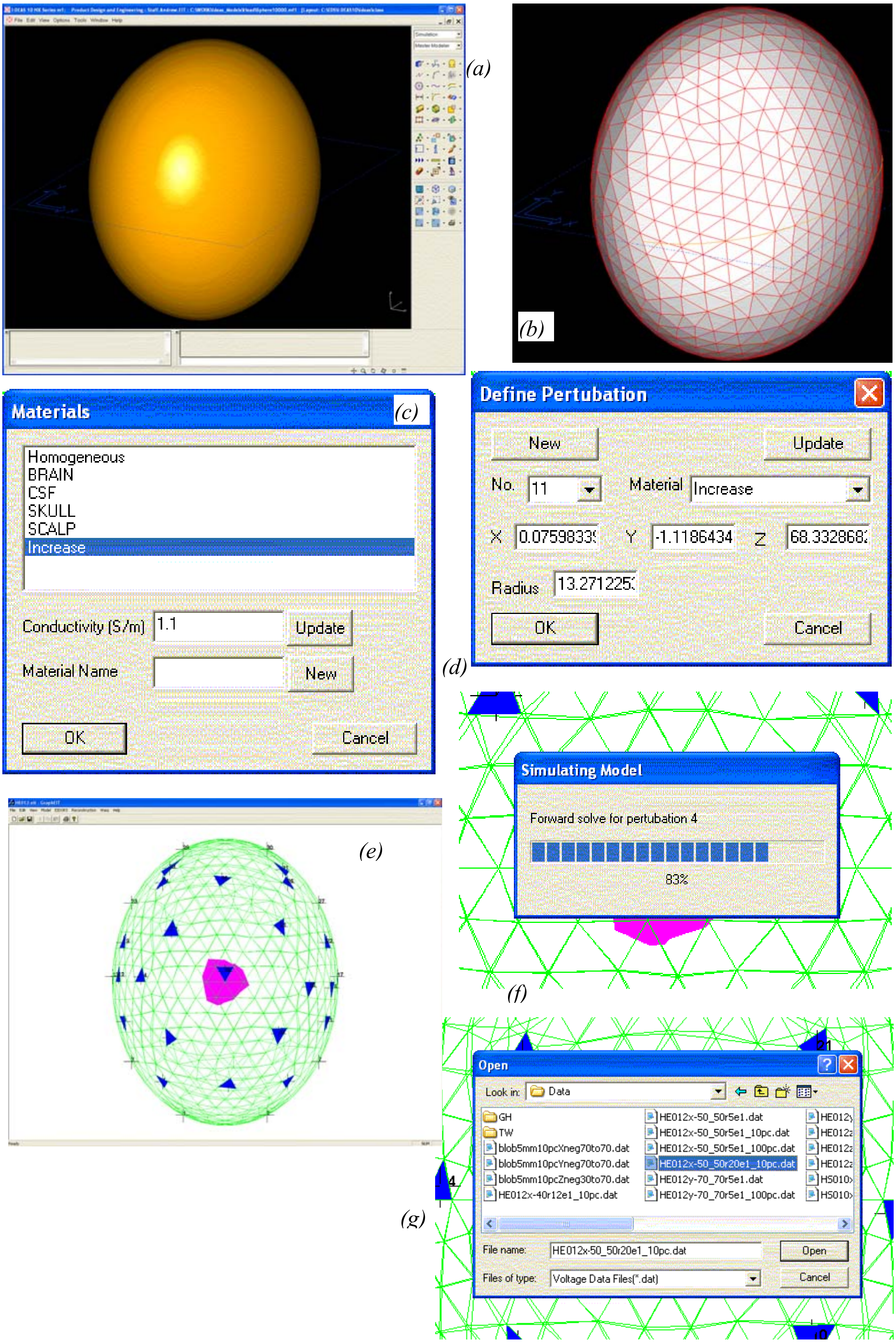

Materials

Homogeneous
BRAIN
CSF
SKULL
SCALP
Increase

Conductivity (S/m): 1.1

Material Name:

Define Pertubation

No.: 11
Material: Increase
X: 0.0759833
Y: -1.1186434
Z: 68.332868
Radius: 13.271225

Simulating Model

Forward solve for pertubation 4

83%

Open

Look in: Data

GH
TW
blob5mm10pcXneg70to70.dat
blob5mm10pcYneg70to70.dat
blob5mm10pcZneg30to70.dat
HE012x-40r12e1_10pc.dat
HE012x-50_50r5e1.dat
HE012x-50_50r5e1_10pc.dat
HE012x-50_50r5e1_100pc.dat
HE012x-50_50r20e1_10pc.dat
HE012y-70_70r5e1.dat
HE012y-70_70r5e1_100pc.dat

File name: HE012x-50_50r20e1_10pc.dat
Files of type: Voltage Data Files(*.dat)

Figure 3.2:The procedure for generating simulated data. (a) The ellipsoid is created in I-DEAS and then (b) meshed. (c) Materials can be created and modified in GraphEIT. (d) Perturbations can be defined, imported and edited, actual positions and sizes are reported and (e) displayed. (f) Forward solve can be carried out with communication to Matlab engine using the EIDORS suite to generate and (g) save the boundary voltage measurements.

3.4. Mesh Warping and the Forward Model

The main emphasis of this work is to determine the effects of warping a Finite Element model so that its underlying geometry matches that from which an EIT data set as taken. Two FE models were constructed for warping, both of which were generated from solid spheres of 200mm diameter in I-DEAS. The first was a homogeneous spherical mesh of 29435 elements, 6135 nodes. The second was a shelled mesh of 29832 elements and 5586 nodes, again partitioned into four compartments or regions and with the same ratios for the radii used for the ellipsoids from which simulated data was generated. The final mesh contained, in each region, 12554 elements in the brain, 5079 elements in the CSF, 5825 elements in the skull and 6374 elements in the scalp. A function exists in *GraphEIT* to apply affine transformations on the mesh with up to 6 parameters, namely translation in three dimensions and three anisotropic scaling factors. Anisotropic scaling was used to warp the meshes such that the underlying geometry was the same as the ellipsoids used for generating the simulated data described above. Thus, the scale factors applied were 0.75 in the x direction, 0.95 in y and 1.0 in z.

The distribution of elemental volume and element stretch were evaluated before and after warping to establish its effects on mesh quality and integrity. *GraphEIT* can analyse the meshes to show distribution of stretch and element volumes throughout the domain. The Stretch statistics can be displayed as a histogram in the same way that they can in I-DEAS as shown in §2.1.2 along with the minimum, maximum, mean, median and standard deviation. Element volume data can be shown as a scatter diagram depicting the values of volume plotted against the radial position of the element from the model global origin as well as a histogram. The spread of elemental volume throughout the model gives an indication of the variation of resolution of the sensitivity matrix. The sensitivity coefficient for each element is directly proportional to the volume as indicated in equation (1.31).

Electrode placement was based on EEG 10/20 positions resulting in a total of 31 electrodes and a protocol used involving opposite current injection resulting in a total of 258 measurements. Electrode diameter was approximated to 10 mm and this resulted in each electrode occupying five element faces on the outer surface of the homogeneous model and two faces for the shelled. The sensitivity matrix was generated using modified EIDORS routines by passing the relevant matrices from *GraphEIT* to the MATLAB engine. This is then saved to a file for subsequent normalisation and inversion.

3.5. Reconstruction on Warped Meshes

The methodology used to reconstruct data was based on the linearised sensitivity approach described in §1.3.3. The sensitivity matrix was inverted using Singular Value Decomposition (SVD), truncated to 70 values to correspond with the schema used by Bagshaw *et al* (2003).

Prior to inversion the sensitivity matrix was row and column normalised and the resulting inverse Jacobian matrix was transferred back to GraphEIT for application of the simulated data and display using a slicer-plot showing unsmoothed images of conductivity changes. Facilities for analysing the images include a peak conductivity search and a means of determining the mean centre and size of a region of interest based on conductivity values lying in a given percentage of the peak conductivity. Setting this deviation to 50% allows a full-width at half maximum (FWHM) to be evaluated; an example of one view of the image is shown in Figure 3.3.

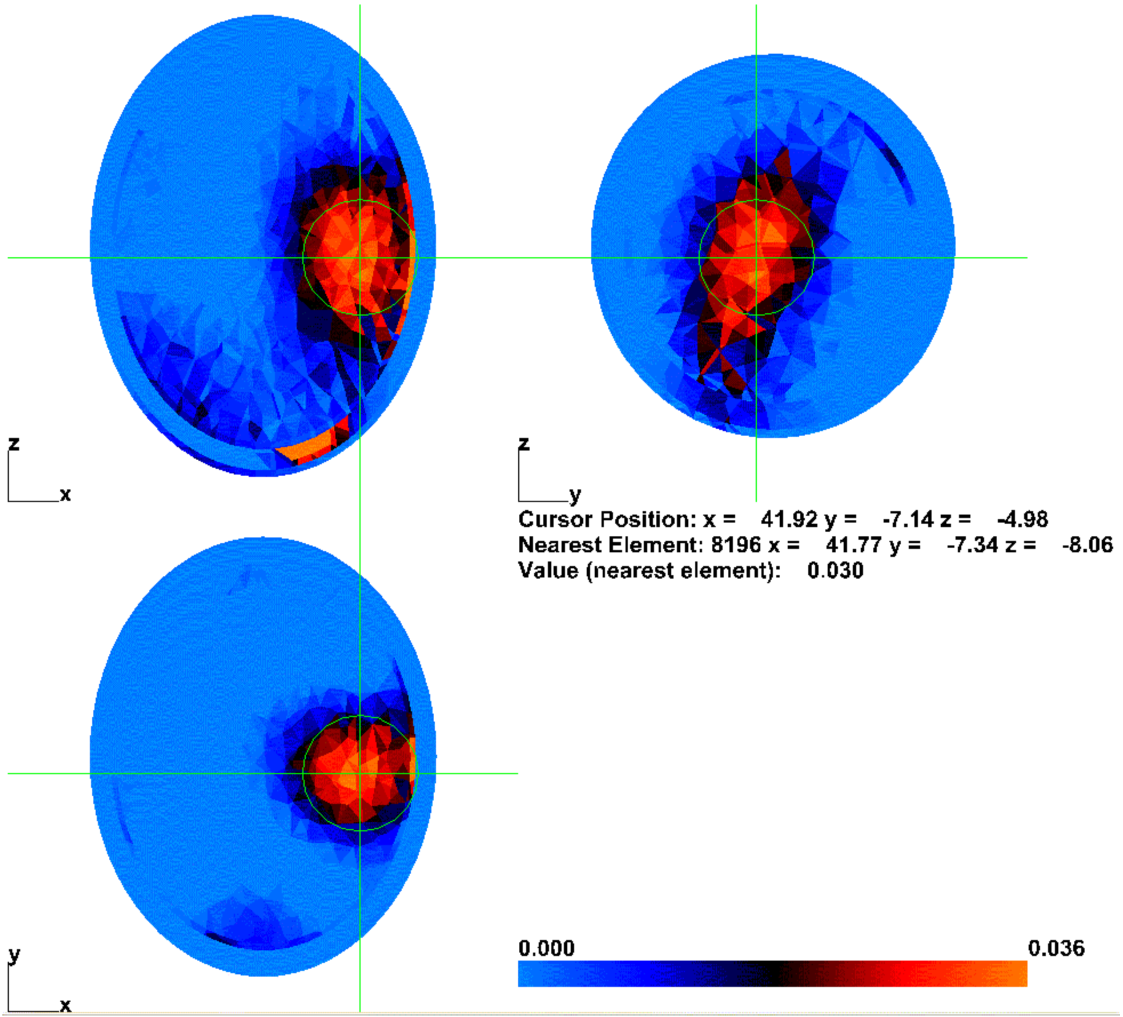

Cursor Position: x = 41.92 y = -7.14 z = -4.98
Nearest Element: 8196 x = 41.77 y = -7.34 z = -8.06
Value (nearest element): 0.030

Figure 3.3: Example of image generated from the slicer plot in GraphEIT. The cursor is centred on a positive conductivity change and the circular aperture is sized to show the boundary of a 50% decrease from the peak conductivity found within the region. Colour-bar units represent actual conductivity increases having been truncated to filter out any artefactual conductivity decreases.

3.6. Results

The results from this investigation that have significance in determining the effects of mesh warping are the change in mesh quality and integrity and the localisation of the perturbations simulated in the modelled ellipsoids on the warped spheres.

3.6.1. Mesh Quality and Integrity

The quantitative changes in element volume were as predicted. The ratio of the volume of the ellipsoid to that of the sphere is the product of the anisotropic scaling factors in all three directions which is 0.75 × 0.95 × 1 = 0.7125. The ratios of the minimum, median, maximum, mean and standard deviation of elemental volumes in both the homogeneous and shelled models before and after warping agreed precisely with this prediction. A qualitative change, however, can be seen in Figure 3.4.

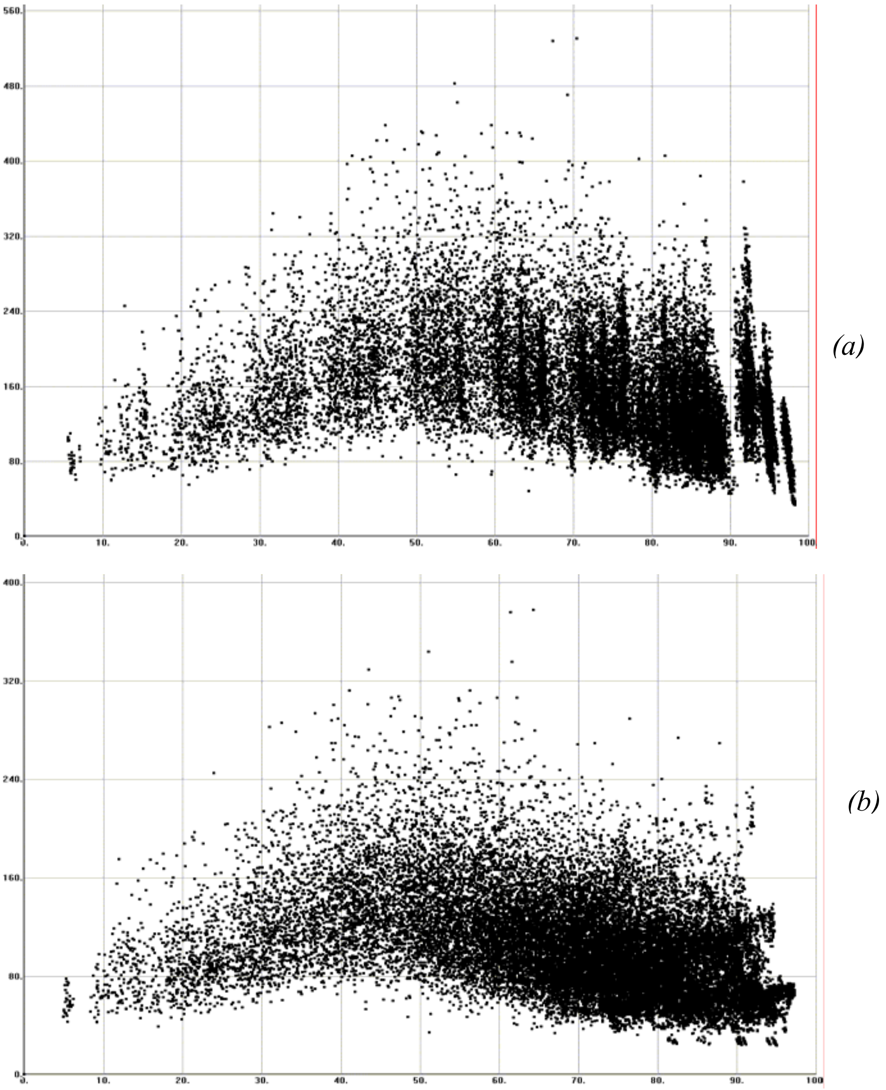

Figure 3.4: Scatter diagrams of element volume for the homogeneous sphere. The horizontal axis is radial distance of the element from the global (world) origin and the vertical axis is element volume in mm^3. (a) Element volumes for the sphere before warping and (b) for the resulting ellipsoid after warping.

The change in stretch is somewhat less predictable as the value for each element is dependant upon the pre-warped stretch and the element's orientation. The stretch statistics for both the homogeneous and shelled spheres before and after warping are summarised in Table 3.1.

Table 3.1: Changes in stretch statistics as a result of warping

Model		Stretch Statistics			
		Minimum	Maximum	Mean	Standard deviation
Homogeneous	Before	0.344	0.986	0.681	0.098
	After	0.318	0.965	0.653	0.104
% change		-7.6	-2.1	-4.1	6.1
Shelled	Before	0.134	0.986	0.639	0.151
	After	0.102	0.966	0.615	0.150
% change		-31.4	-2.0	-3.8	-0.7

3.6.2. Localisation of Simulated Perturbations

In the reconstruction of simulated data from the homogeneous and shelled models, images of significant conductivity increase could be seen in most of the slices observed. For perturbations varied in position long the x axis (right to left), the localisation of the conductivity increases were generally clearly observed with those towards the centre being less well defined. This is demonstrated in Figure 3.5, where unprocessed images are shown at $x \approx -40$ and $x \approx 0$ for both homogeneous and shelled ellipsoids. For perturbations that varied in position along the y axis (anterior to posterior), conductivity increases were also generally quite clearly seen though with far less definition for those from the anterior to the centre of the models. This region is subject to poorer sensitivity owing to the lower density of electrodes.

By truncating the display and colour bar, and hence filtering out all negative artefacts, the conductivity increases could be more clearly seen and localised. The positions of the increases were relatively easy to localise in the x and y directions but, in many cases, they penetrated the model in the $-z$ direction. The information in the sensitivity matrix in the lower hemisphere of the models is limited owing to the distance from the electrodes. Truncated reconstructions of the models are shown in Figure 3.6 for both the homogeneous and shelled ellipsoids. To establish position in these cases, therefore, the centre of the increase in x and y was evaluated with the cursor as close to $z = 0$ as possible.

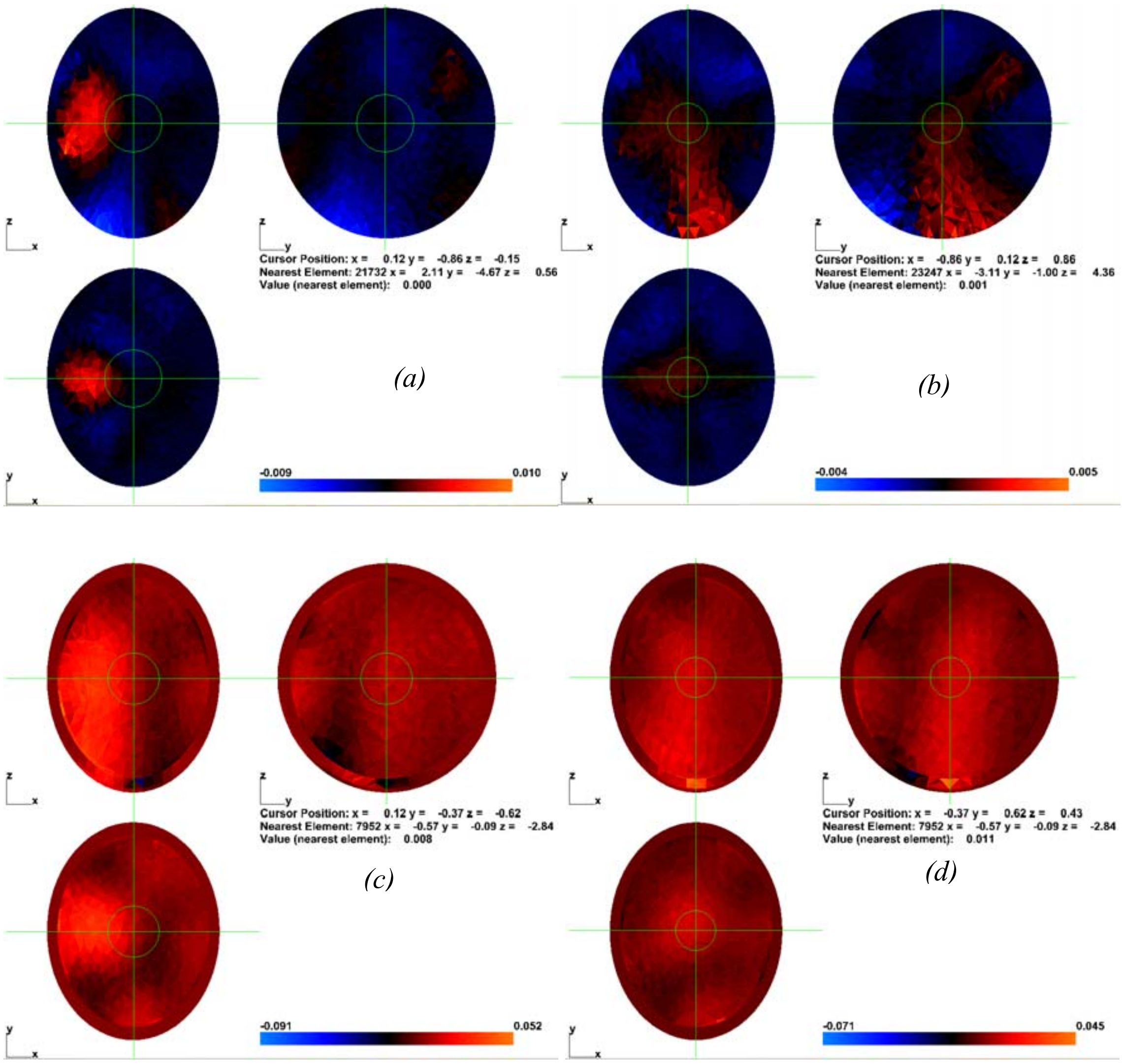

Figure 3.5: Unprocessed slicer plots of reconstruction of simulated data for (a) homogeneous x ≈ -40, (b) homogeneous x ≈ 0, (c) shelled x ≈ -40 and (d) shelled x ≈ 0. Conductivity increases are generally clearly seen where perturbations are nearer the outer boundary of the ellipsoid. Colour bar units are actual increases.

The localisation error is defined as the difference between the geometric centre of the original perturbation in the simulated data and its corresponding position in the reconstruction along the direction of perturbation movement. Another useful measure is the magnitude of the difference in both *x* and *y* directions between the actual and reconstructed perturbations, ignoring the z deviation as discussed above.

For the homogeneous sphere the mean and standard deviation of the absolute differences for the perturbations varied in the *x* direction was 3.6 ± 2.9 mm for the *x* values only and 4.3 ± 3.0 mm for the magnitude of the *xy* differences. For the perturbation positions varied along the y axis, these values were 2.7 ± 2.7 mm and 3.4 ± 2.4 mm respectively. The overall variation of magnitude for both sets of perturbations was 3.7 ± 2.6 mm. The range of variation is shown in

Figure 3.7(a) where actual position is plotted against the reconstructed position and compared to the ideal.

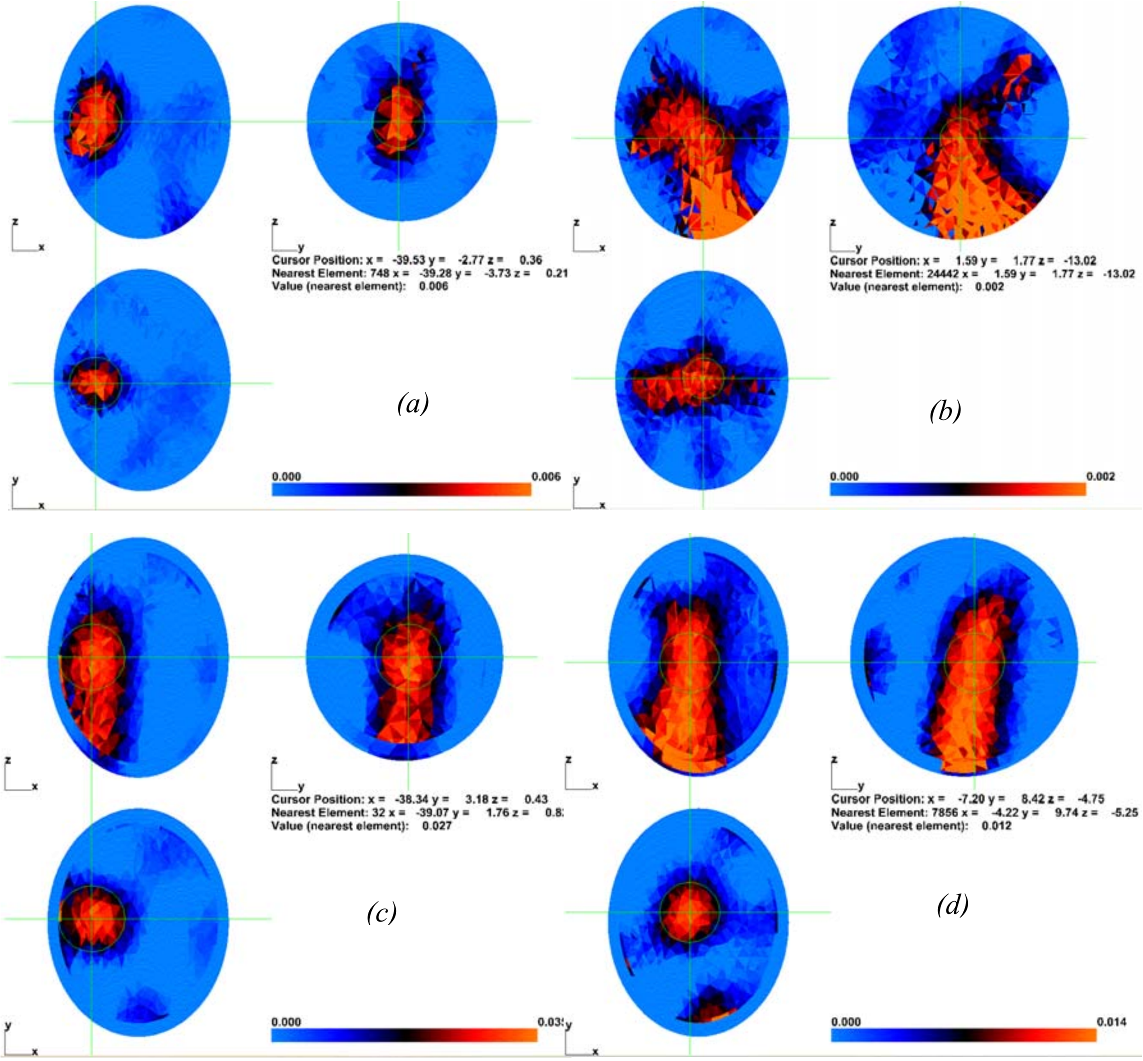

Figure 3.6: Truncated slicer plots of reconstruction of simulated data for (a) homogeneous x ≈ -40, (b) homogeneous x ≈ 0, (c) shelled x ≈ -40 and (d) shelled x ≈ 0. Decreases in conductivity are truncated to display only positive increases. There is a significant difficulty in determining the z position of the reconstructed perturbations, particularly in the shelled model.

Similar results for the shelled ellipsoids can be seen in Figure 3.7(b). Here the mean and standard deviation of the absolute differences for the perturbations was 3.6 ± 2.9 mm for the *x* values only and 7.1 ± 4.0 mm for the magnitude of the *xy* differences. For the perturbation positions varied along the y axis, these values were 4.9 ± 4.7 mm and 6.8 ± 5.9 mm respectively. The overall variation of magnitude for both sets of perturbations was 6.9 ± 5.1 mm.

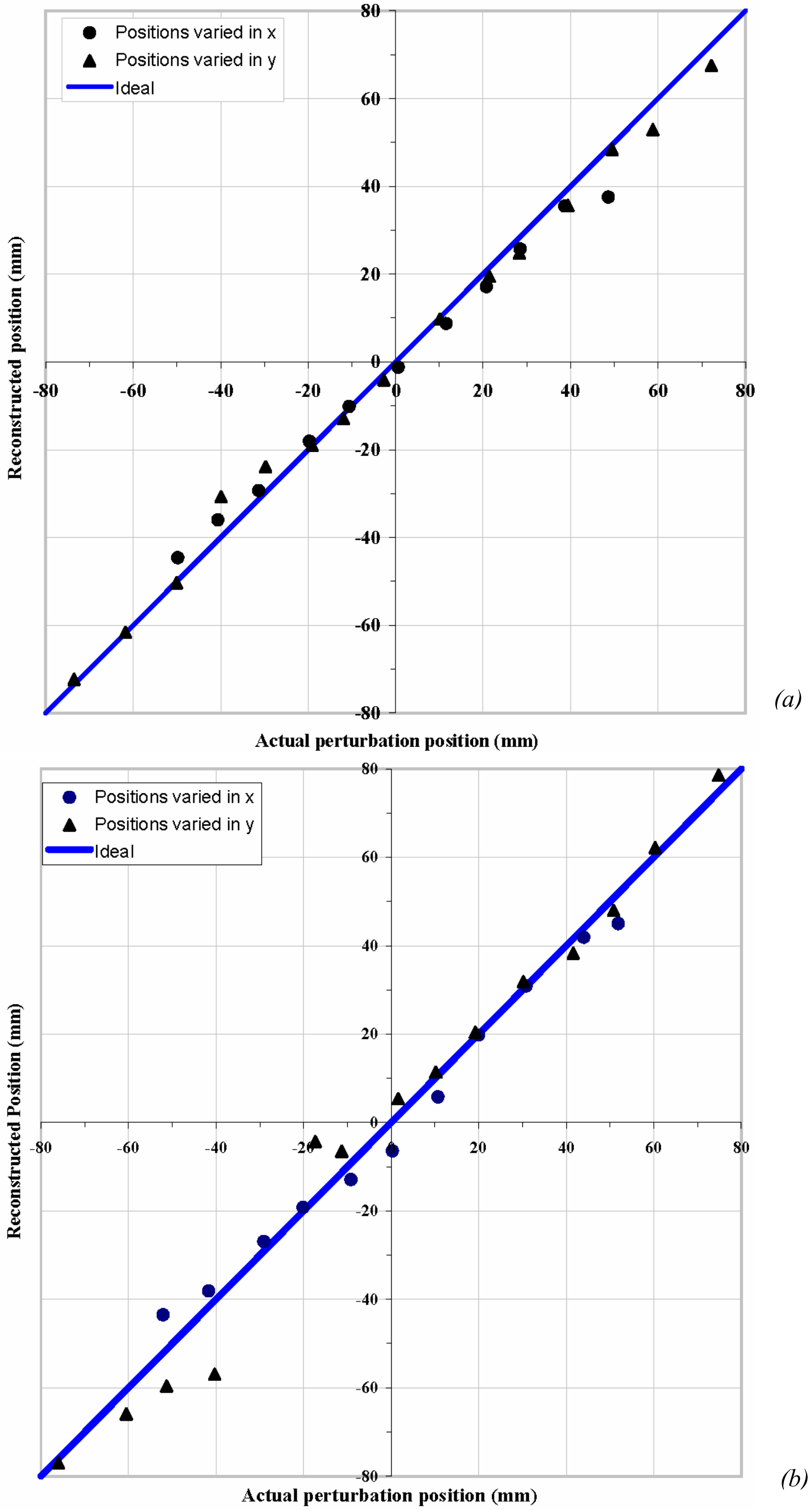

Figure 3.7: Graph of actual perturbation positions versus the positions of the reconstructed conductivity increases for (a) the homogeneous and (b) the shelled ellipsoids. The values plotted show the deviations from the ideal in the direction of the positional variation of the perturbations.

3.7. Discussion, Conclusions and Further Work

The procedures and the results described above have provided a useful insight into the effects of warping finite elements models of spheres into ellipsoids. The warping of the shapes is far more extreme than that expected if a standard finite element model of the human head is to be warped to that of a known patient. The mesh quality degradation for both homogeneous and shelled models is minimal and result in meshes with acceptable element quality. Localisation errors are within the accepted ranges for this type of linearised sensitivity matrix reconstruction algorithm.

Thus the rationalisation and justification of developing a scheme to warp a finite element model is confirmed. This work leads on to a number of activities for further investigation, which are the focus of the following Chapters. As already stated, standard FE meshes of the adult human head will require minimal warping to achieve a close geometric match to a specific patient and so there is a reasonable expectation that element quality will be marginally affected by this process. From previous discussion in the introduction to this Chapter, it can also be hypothesised that image quality and localisation could be improved. Subsequent discussion therefore describes the approach of acquiring key registration points from the heads of a number of subjects. Among these registration points are the actual electrode positions plus additional orientation points defined by nasion and inion and left and right pre-auricular positions. The standard head mesh can undergo affine registration to these latter positions and the mesh warped, i.e. non-rigidly registered, to fit the electrode positions. This could result in a final model where electrode positions are accurately defined allowing non-linear reconstruction techniques to be adopted. Non-linear reconstruction relies heavily upon accurate electrode positioning and is necessary for the absolute imaging requirements of stroke patients.

4. SURFACE FITTING TECHNIQUES

For rapid generation of FE meshes for specific patients within a time-critical clinical environment, a number of prior measurements of the subject need to be taken. With EIT imaging of brain function, the electrode arrangement is based on the EEG 10/20 configuration (Binnie *et al*, 1982; Malvimuo and Plonsey, 1995) and the positions of these electrodes could be the basis of the prior information in defining patient geometry. In this case, only the area under the electrodes could undergo any non-rigid registration, though the remainder of the model may be shaped to a reasonable level of accuracy by affine transformation based on that registration. The mesh warping proposed in this work uses this hypothesis as a basis for generating patient specific forward models. Additional data could easily be acquired by suitable design of the electrode cap or by some other means to include the positions of known registration points such as nasion, inion, and the left and right pre-auricular (periauricular) points. The nasion position can be quite accurately determined though the pre-auricular and the inion positions are more subject to error owing to the variation of geometry in those regions between individuals. The use of electrode positions to redefine head surface geometry has been tried, for example Gibson *et al.* (2003) used optode positions to redefine a surface for re-meshing a neonate head using a thin plate spline. Lamm *et al.* (2001) used spline interpolation of electrode positions to co-register EEG and MRI data to some degree of accuracy. Cohen *et al.* (2000) have presented a method for the ordering and parameterisation of a large number (>9,000) of scattered points obtained from a human head so that B-Spline and NURBS surfaces could be approximated. The generation of B-Spline surfaces from a point dataset is widely presented in literature prompted largely by the need for reverse engineering of surface forms in design and manufacturing (Eck and Hoppe, 1996; Hoppe, 1994; Maekawa and Ko, 2003; Pottmann and Leopoldseder, 2003). The problem to be solved for this work is to construct a surface through a relatively small number (31) points that are already reasonably well-ordered.

This Chapter outlines the methods used to define a bi-cubic B-Spline surface patch that interpolates all the electrode positions currently used for EIT of brain function, thereby defining a surface which matches that of the subject to within accuracy of 0.1 mm, or better, of the measured electrode positions. Surfaces for eight human subjects and one phantom model have been produced. For the human subjects, the electrode measurements are taken prior to routine EIT measurements using a *Microscribe* probe (www.immersion.com/digitizer/) with a manufacturer's reported positional resolution of 0.13 mm and accuracy of 0.38 mm. The phantom model is the latex tank containing a real human skull as discussed in §2.2.2 which was subject to CT scanning. The electrode positions were determined directly from the CT scan to within 1 mm accuracy.

4.1. B-Spline Interpolation

The B-Spline method of interpolating curves and surfaces is a well established standard for geometric modelling in most modern Computer-Aided Design packages as previously discussed in Chapter 2. The mathematical basis of the B-Spline is the subject of many texts in Computer Graphics and Computer-Aided Design, for example Foley & Van Dam (1982), Onwubiko (1989), Anand (1993), mathworld (mathworld.wolfram.com/B-Spline.html) and many others. The basic parametric form of a B-Spline curve is a piecewise polynomial of the form given by:

$$C(u) = \sum_{i=1}^{n} V_i N_{i,k}(u) \tag{4.1}$$

where $C(u)$ is a point (x, y, z) on the resulting B-Spline curve, V_i is the i^{th} control vertex and $N_{i,k}(u)$ is the B-Spline basis function.

This is essentially a generalisation of the Bezier curve and uses the principle of divided difference to establish the curve from the control vertices. The basis function is derived by establishing a knot vector $\mathbf{T} = \{t_1, t_2, \ldots t_m\}$ which is non-decreasing. These define the control vertices $\mathbf{V} = \{V_1 \ldots . V_n\}$ of the spline with order, k and degree, d where $d=k-1$ and $m=n+k$. If the B-Spline is normalised then the knots are evaluated by:

$$t_i = \begin{cases} 0, & i \le k \\ \dfrac{i-k}{n-k+1}, & k < i \le n \\ 1, & i > n \end{cases} \tag{4.2}$$

The B-Spline basis function, $N_{i,k}(u)$, for degree k, at parametric point u ($0 \le u \le 1$) along the curve is given by:

$$N_{i,1} = \begin{cases} 1, & t_i < t_{i+1} \text{ and } t_i \le u \le t_{i+1} \\ 0, & \text{otherwise} \end{cases} \tag{4.3}$$

and recursively by:

$$N_{i,k}(u) = \frac{u - t_i}{t_{i+k-1} - t_i} N_{i,k-1}(u) + \frac{t_{i+k} - u}{t_{i+k} - t_{i+1}} N_{i+1,k-1}(u) \tag{4.4}$$

However, for the application proposed here, the control polygon defined by V is unknown and the curve points C, for known values of u, are. Equation (4.1) can be expressed in matrix form as:

$$\mathbf{C} = \mathbf{NV} \tag{4.5}$$

Where **N** is a $n \times n$ matrix, each row of which is the result of the basis function for each value of u in **C**. Thus if **C** is known then the control polygon can be evaluated from:

$$\mathbf{V} = \mathbf{N}^{-1}\mathbf{C} \tag{4.6}$$

The values of u are derived from linear interpolation of the distances between the points in **C**.

The approach above can be extended to define a B-Spline surface expressed parametrically in two directions, u and v by the tensor product:

$$C(u,v) = \sum_{i=1}^{m}\sum_{j=1}^{n} N_{i,k}(u) N_{j,l}(v) V_{i,j} \tag{4.7}$$

In this case, V defines a control net of $m \times n$ points; the degree of the surface is k in the u direction and l in the v direction, or in matrix form:

$$\mathbf{C} = \mathbf{N}_v \mathbf{V} \mathbf{N}_u^{\mathbf{T}} \tag{4.8}$$

4.2. Interpolation of Electrode Positions

The electrode head-net used for EIT has been adapted from that used in EEG recording with additional electrode sites to make the number up to a total of 31. This is illustrated in Figure 4.1, which shows the positions of the EEG electrodes and the additional sites relative to the *xy* or transverse plane. The whole array of electrodes is renumbered for EIT purposes. The current injection and voltage measurement process is also illustrated.

4.2.1. Registration of Electrode Positions

As previously discussed, the positions of all 31 electrodes plus the four registration points were acquired from the human subjects prior to an EIT measurement. The range of subjects comprised volunteers and patients under ethical approval. A head net was applied to each subject and the hair and skin prepared beneath each electrode site. The *microscribe* was then used to record the three-dimensional Cartesian position for the centre of each electrode on the scalp, prior to electrode insertion, as well as the nasion, inion and left and right periauricular points. Throughout the measurement process, it was essential that the subject underwent minimal movement in order to reduce measurement error. This would be very difficult to achieve in practice and therefore constitutes the most significant source of error in the study.

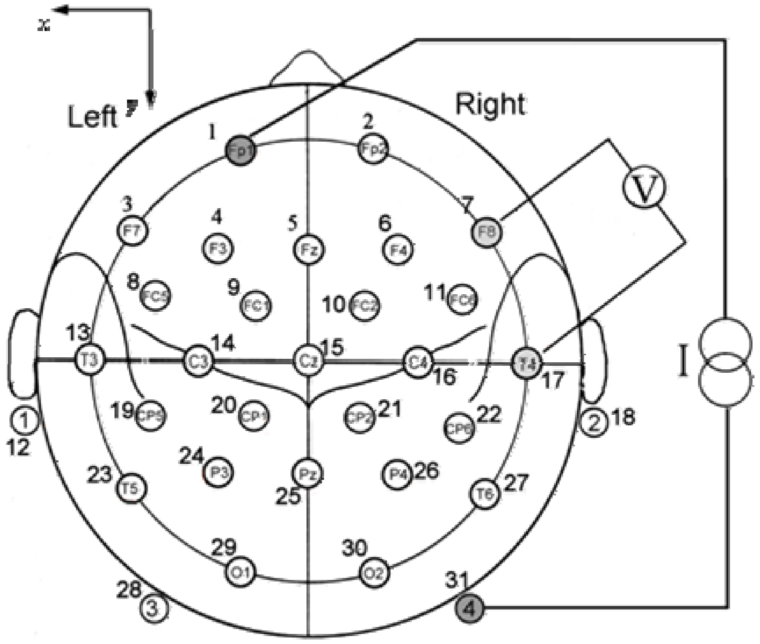

Figure 4.1: The relative positions of the electrode sites on the head-net for EIT measurement. The system is based on EEG 10-20 positions, electrodes standardized by the American Electroencephalographic Society plus four additional electrodes. They are all renumbered for EIT purposes. Current injection and voltage measurement is also illustrated.

The origin position and axis orientation of the measurements thus taken were relatively arbitrary and so subsequent analysis was necessary to perform the registration to the standard head mesh for which the positions of the four registration points were known. A procedure was then established to align the electrode position measurements to the coordinate system for the standard head as indicated in Figure 4.1, that is right to left in the positive x direction, nasion to inion in the positive y direction with the head orientated upright in the positive z direction. The electrode and registration positions were stored in a *patient position file* (ppf) that could be read into a MATLAB (www.mathworks.com) array of dimensions 35 by 3 in the order: Nasion, Inion, Right, Left, electrode 1, electrode 2, … electrode 31. The alignment procedure is defined as follows:

1. Normalise all positions to the nasion position in the ppf.

2. Establish the approximate direction of the z axis using electrode 15 and one other electrode lower in the z direction, e.g. electrode 11. If $z_{15} < z_{11}$ then rotate the ppf 180° about the current x axis. That is, for all i:

$$
\begin{aligned}
y_i' &= -y_i \text{ and} \\
z_i' &= -z_i
\end{aligned}
\tag{4.9}
$$

3. Establish a rotation matrix, $\mathbf{R}_z$, using the Nasion and Inion points as reference to align these points parallel to positive y axis with reference to the xy plane. The angle, θ_z, is defined as:

$$\sin\theta_z = \frac{-x_I}{\sqrt{x_I^2 + y_I^2}} \text{ and} \tag{4.10}$$

$$\cos\theta_z = \frac{y_I}{\sqrt{x_I^2 + y_I^2}}$$

4. Establish a rotation matrix, $\mathbf{R}_x$, to rotate the dataset such that the Nasion and Inion are precisely aligned with the positive y axis. The angle, θ_x , is defined as:

$$\sin\theta_x = \frac{-z_I}{\sqrt{x_I^2 + y_I^2 + z_I^2}} \text{ and} \tag{4.11}$$

$$\cos\theta_x = \frac{y_I}{\sqrt{x_I^2 + y_I^2 + z_I^2}}$$

5. Check that the positions are not mirror-imaged about the *yz* plane, that is, if electrode positions $x_2 > x_1$ then change the sign of all x values.

6. Establish a rotation matrix, $\mathbf{R}_y$, to either precisely align the left and right pre-auricular points parallel to the x axis or to align the vertex electrode, 15, such that it lies on the *yz* plane. The accuracy of the measured positions of the pre-auricular points could be perceived to be subject to greater error than that of the vertex electrode; an experienced EEG technician is more likely to position the vertex electrode with greater position on the *yz* plane. To align the pre-auricular points the angle of rotation is defined by:

$$\sin\theta_y = \frac{z_R - z_L}{\sqrt{(x_R - x_L)^2 + (y_R - y_L)^2 + (z_R - z_L)^2}} \text{ and} \tag{4.12}$$

$$\cos\theta_y = \frac{x_L - x_R}{\sqrt{(x_R - x_L)^2 + (y_R - y_L)^2 + (z_R - z_L)^2}}$$

7. For the vertex electrode:

$$\sin\theta_y = \frac{x_{15}}{\sqrt{x_{15}^2 + z_{15}^2}} \text{ and} \tag{4.13}$$

$$\cos\theta_y = \frac{z_{15}}{\sqrt{x_{15}^2 + z_{15}^2}}$$

8. Establish a rotation matrix, $\mathbf{R}_x$, that will align the nasion-inion vector parallel to that of the reference standard mesh using:

$$\sin\theta_x = \frac{z_N^{ref} - z_I^{ref}}{\sqrt{\left(y_N^{ref} - y_I^{ref}\right)^2 + \left(z_N^{ref} - z_I^{ref}\right)^2}} \text{ and} \tag{4.14}$$

$$\cos\theta_x = \frac{y_I^{ref} - y_N^{ref}}{\sqrt{\left(y_N^{ref} - y_I^{ref}\right)^2 + \left(z_N^{ref} - z_I^{ref}\right)^2}}$$

9. Translate the ppf to align the mean of the registration points to the equivalent position derived from the reference mesh.

For each of the rotational transformations defined above the positions are modified using standard rotational transformation matrices **R**. For counter clockwise rotation these are defined for rotation about *x*:

$$\mathbf{R}_x = \begin{bmatrix} 1 & 0 & 0 \\ 0 & \cos\theta_x & \sin\theta_x \\ 0 & -\sin\theta_x & \cos\theta_x \end{bmatrix} \tag{4.15}$$

For rotation about y:

$$\mathbf{R}_y = \begin{bmatrix} \cos\theta_y & 0 & -\sin\theta_y \\ 0 & 1 & 0 \\ \sin\theta_y & 0 & \cos\theta_y \end{bmatrix} \tag{4.16}$$

and about z:

$$\mathbf{R}_z = \begin{bmatrix} \cos\theta_z & \sin\theta_z & 0 \\ -\sin\theta_z & \cos\theta_z & 0 \\ 0 & 0 & 1 \end{bmatrix} \tag{4.17}$$

4.2.2. Parameterisation of Electrode Positions

In order to define a surface that interpolates all these points, their positions in the parameter space of the resulting surface needs to be established. If a B-spline surface is to fit through the points then some or all of them will need to lie on a regular, uniform and rectangular parametric grid.

The 10-20 positions are named such as to suggest a parameterisation of the electrode positions as illustrated in Figure 4.2, which is taken from Malvimuo and Plonsey (1995). The additional electrodes standardized by the American Electroencephalographic Society occupy positions mid-way between the international 10-20 standard positions. Therefore a parametric grid of 10 by 10 spans is indicated, though this needs re-evaluation as the EIT arrangement does not include the landmarks comprising nasion, inion and pre-auricular positions as electrode sites and the four additional EIT specific sites will further modify the parameterisation. Removal of the landmarks from the parameterisation therefore indicates a grid of 8 by 8 spans or 9 by 9 points.

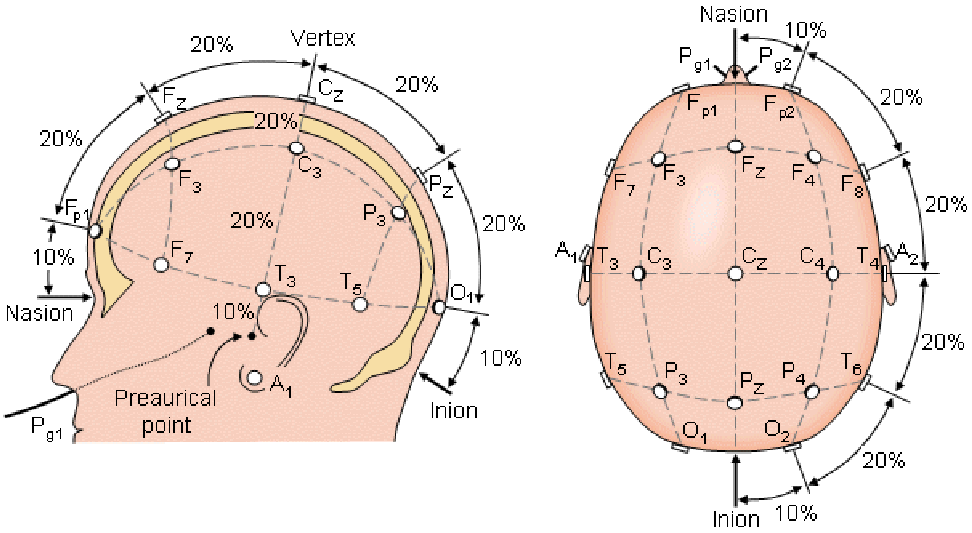

Figure 4.2: The relative positions of the electrode sites on the EEG 10-20 system taken from Malvimuo and Plonsey (1995). Additional positions standardized by the American Electroencephalographic Society indicate a 10 by 10 grid (11 by 11 points). Exclusion of nasion, inion and pre-auricular points and additional EIT positions will modify this parameterisation.

The boundary points from Figure 4.1 are clear; these being electrode numbers [1 2 7 17 18 31 30 29 28 12 13 3] working clockwise. A clearer view of this can be seen in Figure 4.3, which shows the electrode positions positioned approximately on the standard head model created in I-DEAS. Also shown in this illustration are the four points used for registration of the electrode positions measured from the subjects: nasion, inion, left pre-auricular point and the right pre-auricular point. The B-Spline surface, being quadrilateral in parameter space, needs to be a standard four-sided patch. The four sides can be defined, therefore, by the boundary electrode positions: [3 1 2 7], [7 17 18 31], [31 30 29 28] and [28 12 13 3]. These can be renamed to denote their parametric position on the surface patch as $\boldsymbol{u}_{0.0}$, $\boldsymbol{v}_{0.0}$, $\boldsymbol{u}_{1.0}$ and $\boldsymbol{v}_{1.0}$ respectively.

It can be seen from Figure 4.2 that EEG electrodes, if mounted correctly on a subject, are generally uniformly spaced with sets of electrodes lying on clearly identifiable curves. The directions of these curves are generally in the x and y directions which correspond to the parametric directions u and v respectively. In the u direction these are the boundary curves: $\boldsymbol{u}_{0.0}$ and $\boldsymbol{u}_{1.0}$ as well as five additional curves defined by electrodes: [3 4 5 6 7], [8 9 10 11], [13 14 15 16 17], [19 20 21 22] and [12 23 24 25 26 27 18].

In order to examine the curves defined by the positions of the electrodes and to build an infrastructure upon which the curve and surface reconstruction could be built, equations (4.2) to

(4.6) were implemented in MATLAB (www.mathworks.com). Although MATLAB has an integrated spline toolbox with some B-Spline functionality, the transparency and control of the functions are not readily apparent and so a number of functions were generated to achieve this. These are *bsknots* which returns the knot vector **T** given the number of edit points, n, and the required degree, d; *bsbasis* returns the B-Spline basis vector **N** for any given value of u, **T** and d. A function *bsinterpolate* uses these two functions to implement equation (4.6) and return a curve data structure from three vectors C_x, C_y, C_z being the x, y and z values of the known edit points on the curve. The data structure comprises two variables and five vectors. The variables are the number of edit points, n and the degree of the curve, d; the vectors are the parametric positions of the edit points, **U**, the knot vector, **T** and three vectors $\mathbf{V}_x$, $\mathbf{V}_y$, $\mathbf{V}_z$ being the x, y and z values of the control vertices defining the B-Spline.

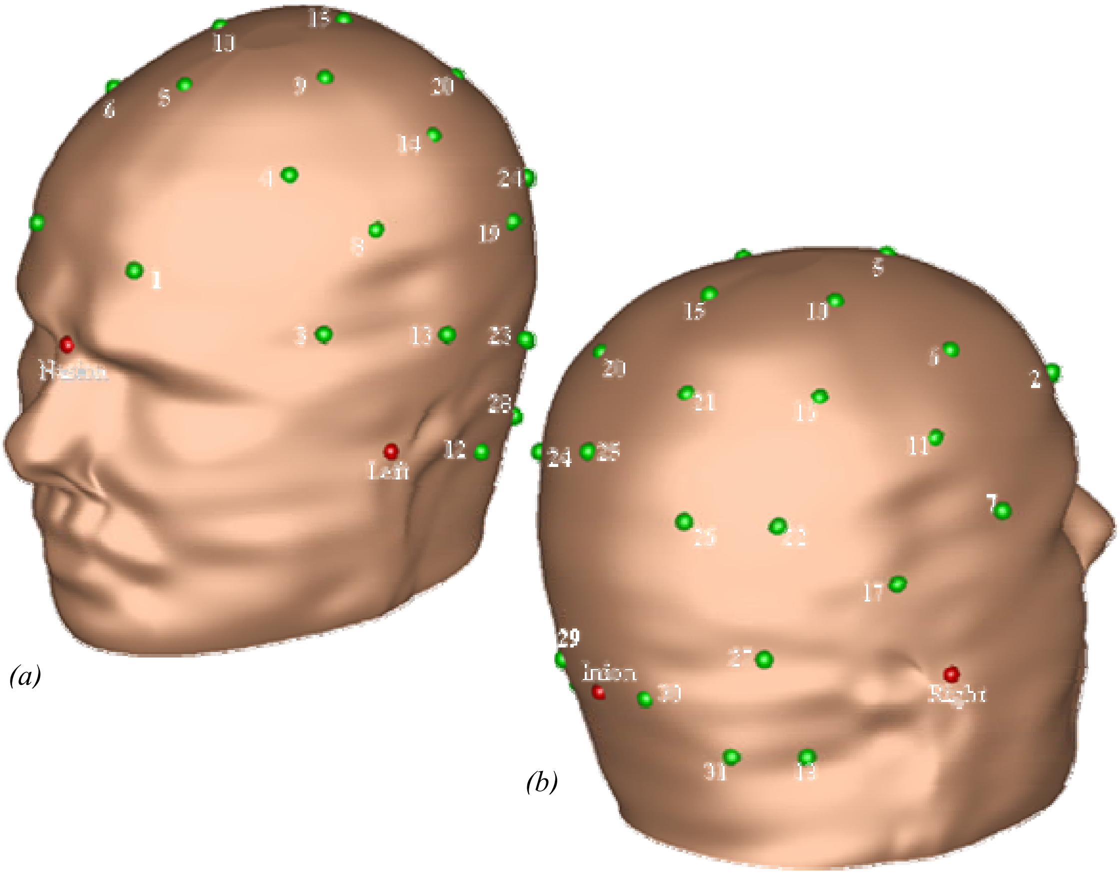

Figure 4.3: The relative positions of the electrode sites shown as approximate locations on the standard head. (a) is a view of anterior-left and (b) posterior-right. Also shown are the four registration points, namely: nasion, inion and left and right periauricular points.

These are shown plotted in Figure 4.4 where it is clear that the curves that do not intersect the boundary curves will need to be extended to points interpolated on those boundary curves. Also, the curve defined by [3 4 5 6 7] intersects the patch boundary at the corner making that particular spline non-isoparametric.

However, a simplification of the surface patch boundary could be implemented; the lengths of the curves defined by electrodes [28 12 13 3] and [7 17 18 31] are equal whereas those defined by [3 1 2 7] and [31 30 29 28], i.e. $\boldsymbol{u}_{0.0}$ and $\boldsymbol{u}_{1.0}$, are not. The longer of the two latter curves is $\boldsymbol{u}_{0.0}$ and this can be truncated by interpolation to match the length of $\boldsymbol{u}_{1.0}$.

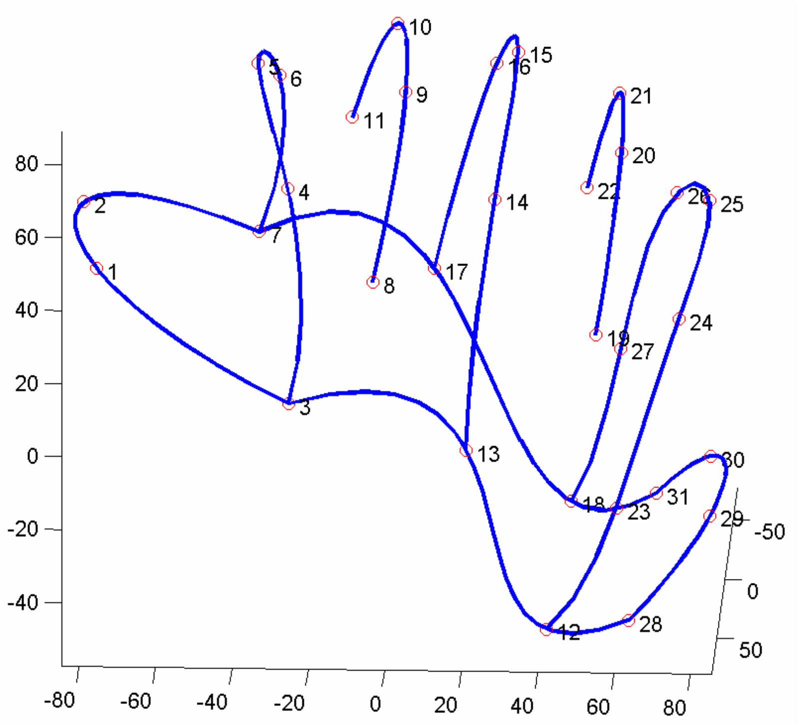

Figure 4.4: The curves in the u direction for the measured electrode positions for a typical subject. The curves that meet the boundaries could potentially be used to define surface edit points. For the others, some scheme of interpolation is needed.

The length of a B-Spline curve can be numerically evaluated relatively quickly and accurately by the application of equations (4.1) and (4.5). The new end points for curve $\boldsymbol{u}_{0.0}$ can be evaluated from the same equations for:

$$v_{0.0} = 0.5 + \frac{L_{1.0}}{2L_{0.0}} \tag{4.18}$$

and

$$v_{1.0} = 0.5 - \frac{L_{1.0}}{2L_{0.0}}$$

where $L_{0.0}$ is the length of $\boldsymbol{u}_{0.0}$ and $L_{1.0}$ that of $\boldsymbol{u}_{1.0}$. This yields two more points to be considered in the surface patch boundary: 32 and 33, which will further modify the parameterisation indicated by the standards previously discussed. Thus $\boldsymbol{u}_{0.0}$ is now defined by points [33 2 1 32], $\boldsymbol{v}_{0.0}$ by [33 7 17 18 31] and $\boldsymbol{v}_{1.0}$ by [32 3 13 12 28]; $\boldsymbol{u}_{1.0}$ remains unchanged.

An alternative, and perhaps more correct, means of determining the interpolated points 32 and 33, is to consider the fact that point 32 lies parametrically mid-way between points 1 and 3 and similarly, point 33 between electrodes 2 and 7. This essentially divides the curve defined by points [33 2 1 32] into sixths if the midway point between electrodes 1 and 2 is included. Therefore points 33 and 32 can be evaluated from the original curve by interpolating the points at $u = {}^1/_6$ and $u = {}^5/_6$ respectively.

Examination of the parametric position of the electrodes and interpolated points on these newly defined curves yields that they divide the curves up into approximate quarters or factors thereof as indicated by standard 10-20 positions. For curve $\boldsymbol{u}_{0.0}$ the mean position of points 3 and 2 of all subjects is v=0.25 and v=0.70 respectively and these values vary only marginally if points 33 and 32 are derived from the one-sixth interpolation described in the previous paragraph as opposed to making curve $\boldsymbol{u}_{0.0}$ the same length as curve $\boldsymbol{u}_{1.0}$. For the equivalent points, 30 and 29 on curve $\boldsymbol{u}_{1.0}$, these values are v=0.28 and v=0.73, which in both cases equate approximately to v=0.25 and v=0.75. The same holds true to a reasonable level of approximation for the curves $\boldsymbol{v}_{0.0}$ and $\boldsymbol{v}_{1.0}$. The points 7, 17 and 18 on $\boldsymbol{v}_{0.0}$ yield mean parametric positions of 0.19, 0.46 and 0.77 respectively; for $\boldsymbol{t}_{1.0}$ the points 3, 13 and 12, these values are 0.20, 0.46 and 0.78 respectively.

A similar analysis can be carried out on the other curves in the u direction that meet the boundary curves as illustrated in Figure 4.4. These can now be nominated as $\boldsymbol{u}_{0.25}$, $\boldsymbol{u}_{0.5}$ and $\boldsymbol{u}_{0.75}$ comprising points [3 4 5 6 7], [13 14 15 16 17] and [12 23 24 25 26 27 18] respectively. The mean parametric positions of points 6, 5 and 4 are 0.25, 0.49 and 0.75; for points 16, 15 and 14 they are 0.26, 0.50 and 0.74. These values show a conclusive division into quarters though the points 23, 24, 25, 26 and 27 on curve $\boldsymbol{u}_{0.75}$ yield values of 0.16, 0.33, 0.50, 0.67 and 0.85 respectively. These values indicate more a division of the curve into sixths as would be expected.

It is not possible to establish similar values for the curves spanning electrodes [8 9 10 11] and [19 20 21 22] without resorting to interpolating points on $\boldsymbol{v}_{0.0}$ and $\boldsymbol{v}_{1.0}$, on the understanding that they lie equally between the points [3 4 5 6 7] and [13 14 15 16 17]. Assuming that these curves do in fact lie on the surface at values v=0.375 and v=0.625 respectively, points can be interpolated on $\boldsymbol{v}_{0.0}$ and $\boldsymbol{v}_{1.0}$ to complete them and generate tentative curves $\boldsymbol{u}_{0.375}$ and $\boldsymbol{u}_{0.625}$. Consequently, the mean parametric values of points 11, 10, 9 and 8 become 0.14, 0.38, 0.62 and 0.86 respectively and this indicates that these positions lie on the one-eighth divisions of 0.125, 0.375, 0.625 and 0.875. For the points on $\boldsymbol{u}_{0.625}$, namely 22, 21, 20 and 19 these values are 0.21, 0.40, 0.60 and 0.79 which, although they correspond to the implied standard spacing, could be approximate to the one-eighth and one-quarter positions of 0.25, 0.375, 0.625 and 0.75.

Thus the implication that the surface through the electrodes could be defined as a parametric grid of 8 by 8 spans could be drawn. This would generate a B-Spline control net of 9 by 9 vertices most of which would correspond to the approximate parametric positions of the electrodes. The exceptions would be that no electrodes or additional points would lie on the isoparametric curves v=0.125($\boldsymbol{u}_{0.125}$) and v=0.875 ($\boldsymbol{u}_{0.875}$); there would also be more significant mismatch between the control vertices where v=0.75 and the underlying electrodes defined by $\boldsymbol{u}_{0.75}$. A 9 by 9 B-Spline patch of this nature is relatively easy to generate from equation (4.8) which could be rewritten as:

$$\mathbf{C} = \mathbf{N}\mathbf{V}\mathbf{N}^{\mathbf{T}} \tag{4.19}$$

as the B-Spline basis array, **N**, will be the same for both u and v for all subjects. In this case the edit points, C, are known and so the positions of the vertices on the control net, V, can be evaluated from:

$$\mathbf{V} = \mathbf{N}^{-1}\mathbf{C}\left(\mathbf{N}^{\mathbf{T}}\right)^{-1} \tag{4.20}$$

The B-Spline basis array, **N**, is:

$$\mathbf{N} = \begin{bmatrix} 1 & 0 & 0 & 0 & 0 & 0 & 0 & 0 & 0 \\ 0.015625 & 0.457031 & 0.457031 & 0.070313 & 0 & 0 & 0 & 0 & 0 \\ 0 & 0.031250 & 0.468750 & 0.479167 & 0.020833 & 0 & 0 & 0 & 0 \\ 0 & 0 & 0.070313 & 0.611979 & 0.315104 & 0.002604 & 0 & 0 & 0 \\ 0 & 0 & 0 & 0.166667 & 0.666667 & 0.166667 & 0 & 0 & 0 \\ 0 & 0 & 0 & 0.002604 & 0.315104 & 0.611979 & 0.070313 & 0 & 0 \\ 0 & 0 & 0 & 0 & 0.020833 & 0.479167 & 0.468750 & 0.031250 & 0 \\ 0 & 0 & 0 & 0 & 0 & 0.070313 & 0.457031 & 0.457031 & 0.015625 \\ 0 & 0 & 0 & 0 & 0 & 0 & 0 & 0 & 1 \end{bmatrix} \tag{4.21}$$

Using the curves $\boldsymbol{u}_{0.25}$, $\boldsymbol{u}_{0.5}$ and $\boldsymbol{u}_{0.75}$ and the boundary curves $\boldsymbol{u}_{0.0}$, $\boldsymbol{v}_{0.0}$, $\boldsymbol{u}_{0.0}$ and $\boldsymbol{v}_{1.0}$ as an infrastructure a bi-cubic B-Spline patch can be defined using the following procedure:

1. Define the boundary curves $\boldsymbol{u}_{0.0}$, $\boldsymbol{u}_{1.0}$, $\boldsymbol{v}_{0.0}$ and $\boldsymbol{v}_{1.0}$ and truncate $\boldsymbol{u}_{0.0}$ either to the same length as $\boldsymbol{u}_{1.0}$ or by interpolating $u = {}^{1}/_{6}$ and $u = {}^{5}/_{6}$.

2. Define the quartile curves in the u direction $\boldsymbol{u}_{0.25}$, $\boldsymbol{u}_{0.5}$ and $\boldsymbol{u}_{0.75}$ to define the surface infrastructure using existing electrode points.

3. Interpolate nine equally spaced points on each of the curves in the u direction namely $\boldsymbol{u}_{0.0}$, $\boldsymbol{u}_{0.25}$, $\boldsymbol{u}_{0.5}$, $\boldsymbol{u}_{0.75}$ and $\boldsymbol{u}_{1.0}$ to define 35 additional points.

4. Generate B-Spline curves through these additional points in the v direction to generate 7 B-Spline curves.

5. Interpolate nine equally spaced points on each of these new curves and the boundary curves $\boldsymbol{v}_{0.0}$ and $\boldsymbol{v}_{1.0}$ to define a total of 81 edit-points to define the surface. These are arranged such that columns are points in the *v* direction and rows in the *u* direction.

6. Build the B-Spline basis matrix, **N**, using equations (4.2) to (4.4) with parameter spacing, 1/(*n*-1), where n is the number of edit points in each direction which, for this case, is nine.

7. Apply equation (4.18) to generate the control net, **V**.

The procedure has been implemented in a MATLAB procedure with the original electrode positions, the surface degree, *d*, and the number of edit points in each direction, *n*, as input variables to return a surface data structure. In a similar manner to the curve data structure described above, the surface structure comprises two variables *n* and *d*, the knot vector, **T**, and three matrices of size *n* by *n* denoted $\mathbf{V}_x$, $\mathbf{V}_y$ and $\mathbf{V}_z$ defining the positions of the control vertices. The procedure is illustrated pictorially in Figure 4.5. In Figure 4.5(d), the additional points generated in step 3 in the above procedure are numbered from 34 and it is apparent that many of the electrode positions are close to these points or the curves defined by them. The next stage of the process is to establish a procedure or algorithm that can manipulate this approximate surface to ensure that it interpolates all the electrode positions accurately and this is described in the next section.

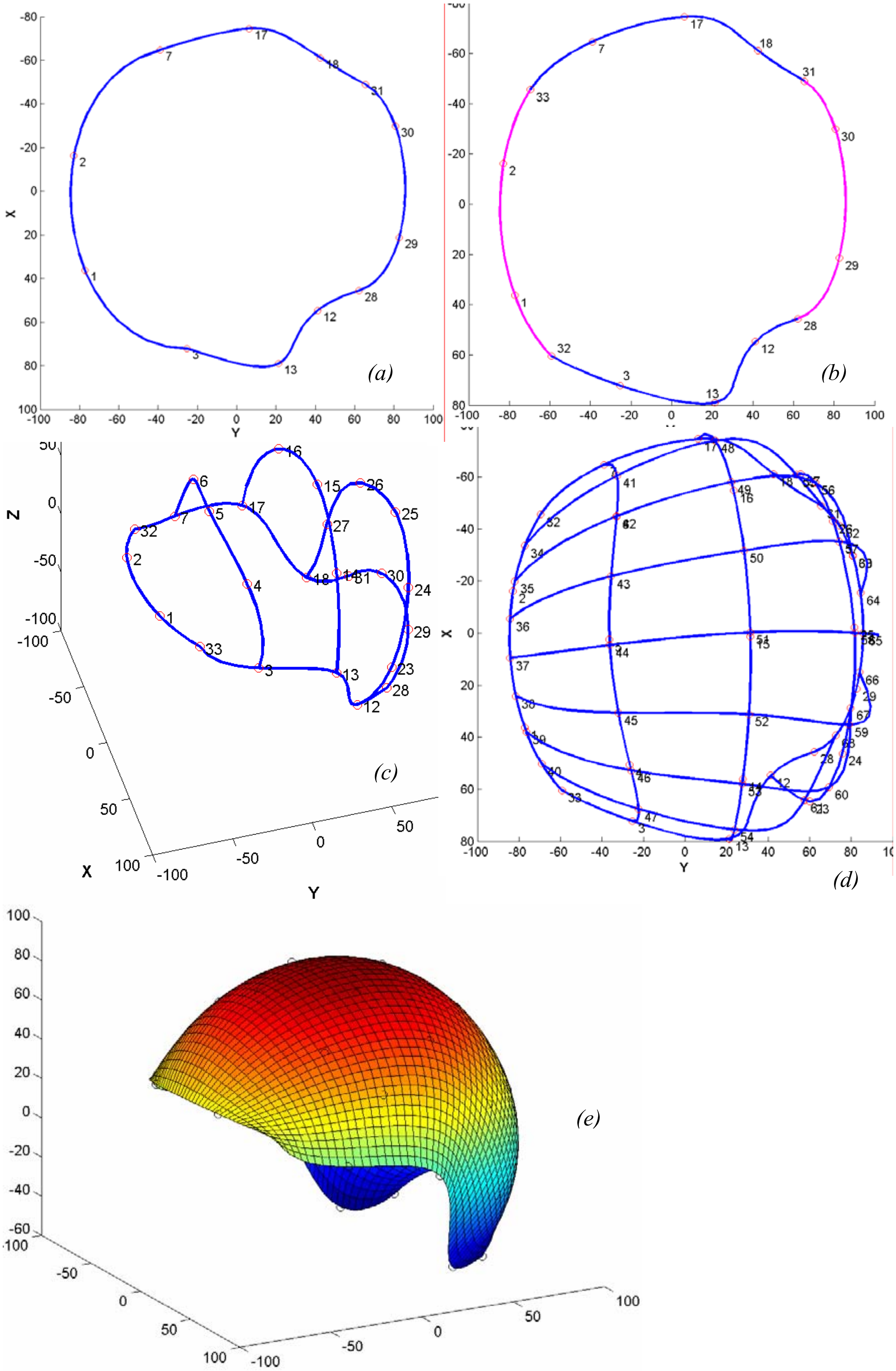

Figure 4.5: The initial approximate surface interpolation procedure. Boundary curves are generated in (a) and the u=0 curve truncated in (b). Additional curves are generated in (c) to provide an infrastructure so that nine (or n) curves can be defined in (d). These are equally divided to define the surface patch shown in (e).

4.3. Surface Manipulation

The surface defined by the procedure laid out in the previous section is an approximation of that which ideally fits through all the electrode positions. In order to achieve the best fit, the surface must be manipulated. The method to achieve this manually in commercial surface modelling software is to modify the position of the control vertices or edit points. In this case, an automatic method is proposed that iteratively modifies the control net to minimise the distance of the electrodes from the surface.

4.3.1. Orthogonal Point Projection

The first requirement for such automated surface manipulation is that the distance of each electrode from the B-Spline surface be known and this can be achieved by establishing the orthogonal projection of the point to the surface. This is a process covered by a number of authors as discussed by Hu and Wallner (2005) who present the established first order method and also propose a second order algorithm. For simplicity, the first order algorithm is used in subsequent analysis in this work and it is presented here for completeness.

Given the point to project, **p**, an initial guess for its projection onto the surface, $\mathbf{p}_0$, can be made by finding the nearest control vertex to that point. As the parametric position, (u, v), is known for this point it can be evaluated. A new point forming the basis of the next guess is found by projecting **p** onto the tangent plane at $\mathbf{p}_0$ to obtain $\mathbf{p}_1$. The plane is found by evaluating the partial derivatives, $(\mathbf{g}_u, \mathbf{g}_v)$ of the surface at $\mathbf{p}_0$ and the outward normal, $\mathbf{n}=(\mathbf{g}_u \times \mathbf{g}_v)$. New values for (u, v) can be evaluated $(u+\Delta u, v+\Delta v)$ where:

$$\mathbf{p_1} - \mathbf{p_0} = \mathbf{g}_u \, \Delta u + \mathbf{g}_v \, \Delta v \tag{4.22}$$

Multiplying through by $\mathbf{g}_u$ and $\mathbf{g}_v$ yields:

$$\mathbf{g}_u \cdot \mathbf{g}_u \Delta v + \mathbf{g}_v \cdot \mathbf{g}_u \Delta v = (\mathbf{p_1} - \mathbf{p_0}) \cdot \mathbf{g}_u \tag{4.23}$$

and

$$\mathbf{g}_u \cdot \mathbf{g}_v \Delta u + \mathbf{g}_v \cdot \mathbf{g}_v \Delta v = (\mathbf{p_1} - \mathbf{p_0}) \cdot \mathbf{g}_v \tag{4.24}$$

Equations (4.20) and (4.21) represent a system of linear equations that can be solved for Δu and Δv. The above procedure can be repeated for $\mathbf{p}_0 = \mathbf{p}_1$ until Δu and Δv fall below an acceptable tolerance or until the angle between the plane tangential to the surface and the vector between $\mathbf{p}_1$ and **p** is close to 90°. The resulting values of u and v represent the parametric position of the orthogonally projected point to the surface, $\mathbf{p}_0$.

The partial derivatives of a B-Spline surface are relatively easily evaluated and is discussed by a number of sources e.g. Shene (www.cs.mtu.edu/~shene/COURSES/cs3621/NOTES). The derivative of a B-Spline curve of order, k, is another B-Spline of order k-1 based on a new set of control vertices, Q, defined by:

$$Q_i = \frac{k}{T_{i+k+1} - T_{i+1}} \left(V_{i+1} - V_i \right) \tag{4.25}$$

The derivative of the B-Spline curve is then evaluated using a basis function derived from a knot sequence reduced from the original by removing the first and last knots to give $\mathbf{T} = \{t_2, t_3, \ldots, t_{m-1}\}$ and the derivative is defined as:

$$\frac{\mathrm{d}}{\mathrm{d}u} C(u) = C'(u) = \sum_{i=1}^{n-1} Q_i N_{i,k-1}(u) \tag{4.26}$$

For a surface, the partial derivatives $\partial C(u,v)/\partial u$ and $\partial C(u,v)/\partial v$ can be evaluated. By combining equations (4.5) and (4.8), the control vertices for the curve in the u direction at v can be evaluated from:

$$\mathbf{V}_v = \mathbf{N}_v \mathbf{V} \tag{4.27}$$

This can be applied to equations (4.25) and (4.26) for u to yield $\partial C(u,v)/\partial u$ ($\mathbf{g}_u$). Similarly the control vertices for the curve in the v direction at u can be evaluated from:

$$\mathbf{V}_u = \mathbf{V} \mathbf{N}_u^{\mathbf{T}} \tag{4.28}$$

to yield the partial derivative $\partial C(u,v)/\partial v$ ($\mathbf{g}_v$).

4.3.2. Initial Results

The approximate surface built from the boundary curves and the three additional curves in the u direction as described in §4.2.2 is likely to form a close fit to up to 18 of the electrode positions. These positions being those on the patch boundary plus the two curves $\boldsymbol{u}_{0.25}$ and $\boldsymbol{u}_{0.5}$ as, in general, their parameterisation matches closely that of the resulting equi-spaced grid of 9 by 9 points. The electrodes on curve $\boldsymbol{u}_{0.75}$ comprising [23 24 25 26 27] may show up some more significant positional errors because the parameterisation does not conform to the 9 by 9 grid. Also the electrodes [8 9 10 11] and [19 20 21 22] (curves $\boldsymbol{u}_{0.375}$ and $\boldsymbol{u}_{0.625}$) will also be subject to significant positional errors. Therefore there are potentially 13 electrodes that may exhibit significant positional errors. A MATLAB function, *bsptonsrf_res*, was implemented to establish the orthogonal project of a point to the surface. This function takes a point vector, a surface data structure and desired precision as input and returns the parametric values, u and v, the point on the surface, the distance of the original point from the surface and the outward normal. This function, when applied to all electrode positions, can produce relevant data for all points. This was carried out for all subjects to generate a list of electrodes whose distance from the surface was greater than 0.1 mm. A summary of this is given in Table 4.1, showing the minimum, maximum, mean and standard deviation of those points. In addition, it lists the number of points in the list and the electrode number with the greatest positional error, e_{max}.

Table 4.1: Summary of positional errors > 0.1 mm for approximate surface for all subjects

subject	minimum	maximum	mean	Standard deviation	Count of electrodes	e_{max}
1	0.1162	2.8110	0.8901	0.9799	10	8
2	0.1190	3.4800	2.0793	1.2249	9	21
3	0.1108	6.3400	2.0740	2.1959	9	10
4	0.2086	3.1781	1.7628	0.9639	10	9
5	0.1528	3.4184	1.6568	1.0066	10	10
6	0.1021	2.9142	1.3853	0.8208	10	9
7	0.6651	4.5544	2.4232	1.3905	8	22
8	0.2692	4.1650	1.6319	1.5154	8	10
9	0.1813	4.1028	1.4575	1.1086	11	19
mean	0.21	3.88	1.71			
Std dev	0.18	1.09	0.45			

The results show that no subject exhibited more than the predicted 13 electrodes with significant error. In all cases, the maximum error was associated with an electrode on the curves predicted to contain them, namely $\boldsymbol{u}_{0.375}$ and $\boldsymbol{u}_{0.625}$. Examination of all electrodes for all subjects revealed that the listed points came entirely from those curves plus up to three from curve $\boldsymbol{u}_{0.75}$.

4.3.3. Control Net Manipulation

A particular advantage of a B-Spline surface is its ability to provide local shape control within the vicinity of a control vertex. With this in mind, it is reasonable to predict that if a control vertex closest to an electrode with significant error is manipulated appropriately, the surface can be shaped to reduce the error to within a desired degree of accuracy. Considering the definition of the B-Spline surface in equation (4.7):

$$C(u,v) = \sum_{i=1}^{m}\sum_{j=1}^{n} N_{i,k}(u)N_{j,l}(v)V_{i,j}$$

and if the control net, V, was modified by ΔV such that $V_1 = \mathrm{V} + \Delta V$ then a correspond change would take place in $C(u,v)$, that is:

$$C(u,v)+\Delta C(u,v)=\sum_{i=1}^{m}\sum_{j=1}^{n}N_{i,k}(u)N_{j,l}(v)\left(V_{i,j}+\Delta V_{i,j}\right) \tag{4.29}$$

$$=\sum_{i=1}^{m}\sum_{j=1}^{n}N_{i,k}(u)N_{j,l}(v)V_{i,j}+\sum_{i=1}^{m}\sum_{j=1}^{n}N_{i,k}(u)N_{j,l}(v)\Delta V_{i,j}$$

and therefore:

$$\Delta C(u,v)=\sum_{i=1}^{m}\sum_{j=1}^{n}N_{i,k}(u)N_{j,l}(v)\Delta V_{i,j} \tag{4.30}$$

Relating this to equation (4.19) for a regular 9 by 9 grid:

$$\mathbf{C}=\mathbf{N}\mathbf{V}\mathbf{N}^{\mathbf{T}}$$

a positional change $\Delta V_{p,q}$ to a control vertex $V_{p,q}$ parametrically closest to an electrode off the surface at $C_{u,v}$ will result in a localised surface reshaping such that:

$$\Delta\mathbf{C}_{u,v}\approx\mathbf{N}_{p,p}\Delta\mathbf{V}_{p,q}\mathbf{N}_{q,q} \tag{4.31}$$

For a change in surface position at (u,v), the required change in the control vertex position is therefore given by:

$$\Delta\mathbf{V}_{p,q}\approx\frac{\Delta\mathbf{C}_{u,v}}{\mathbf{N}_{p,p}\mathbf{N}_{q,q}} \tag{4.32}$$

where p is the row and q the column of the 9 by 9 B-Spline basis array, **N**, given in equation (4.21). While the shape control is localised, there will be minor, though possibly significant, changes to the surface form at the electrode positions within the immediate vicinity. Therefore a re-evaluation of the positional errors for all electrodes will need to take place and the shaping procedure reiterated. The value of $\Delta\mathbf{C}_{u,v}$ is that determined from the process described in §4.3.2 and the algorithm to iteratively manipulate the control vertices is as follows.

1. Generate a table of all electrodes off the surface by the desired positional accuracy and evaluate $\Delta\mathbf{C}_{u,v}$ for each.

2. For all such electrodes, establish the nearest control vertex, $\mathbf{V}_{p,q}$, to the electrode. For a surface defined by a grid of m by n points, the value p=round(u(n-1))+1 and q=round(v(m-1))+1. In the case currently considered here m=n=9.

3. For the same electrodes, evaluate $\Delta\mathbf{V}_{p,q}$ from equation (4.32).

4. Evaluate a new control vertex array as $\mathbf{V}=\mathbf{V}+\Delta\mathbf{V}$.

5. Repeat from step 1 until all electrodes are within the desired tolerance of the surface.

4.3.4. Surface Fitting Results

The above procedure was applied to all subjects to achieve electrode positional tolerances of 0.1 mm and 0.05 mm to establish speed of convergence. To achieve an electrode position of 0.1 mm, the number of iterations ranged from 5 to 19 with the mean between 8 and 9 and a mode of 6. After manipulation of the control net, the maximum deviation of the electrode positions averaged 0.089 mm with a standard deviation of 0.007 mm. Halving the desired tolerance to 0.05 mm increased the number of iterations by an average of 20%, the range being between 6 and 24 with a mean of around 10 and mode of 8 iterations. The maximum deviation of the electrode positions from the final surface averaged 0.045 mm with a standard deviation of 0.005 mm.

Figure 4.6 shows examples of how the maximum electrode positional error converged for two examples. These are the fastest and slowest converging subjects alongside which are shown the final manipulated surface for a desired tolerance of 0.1 mm.

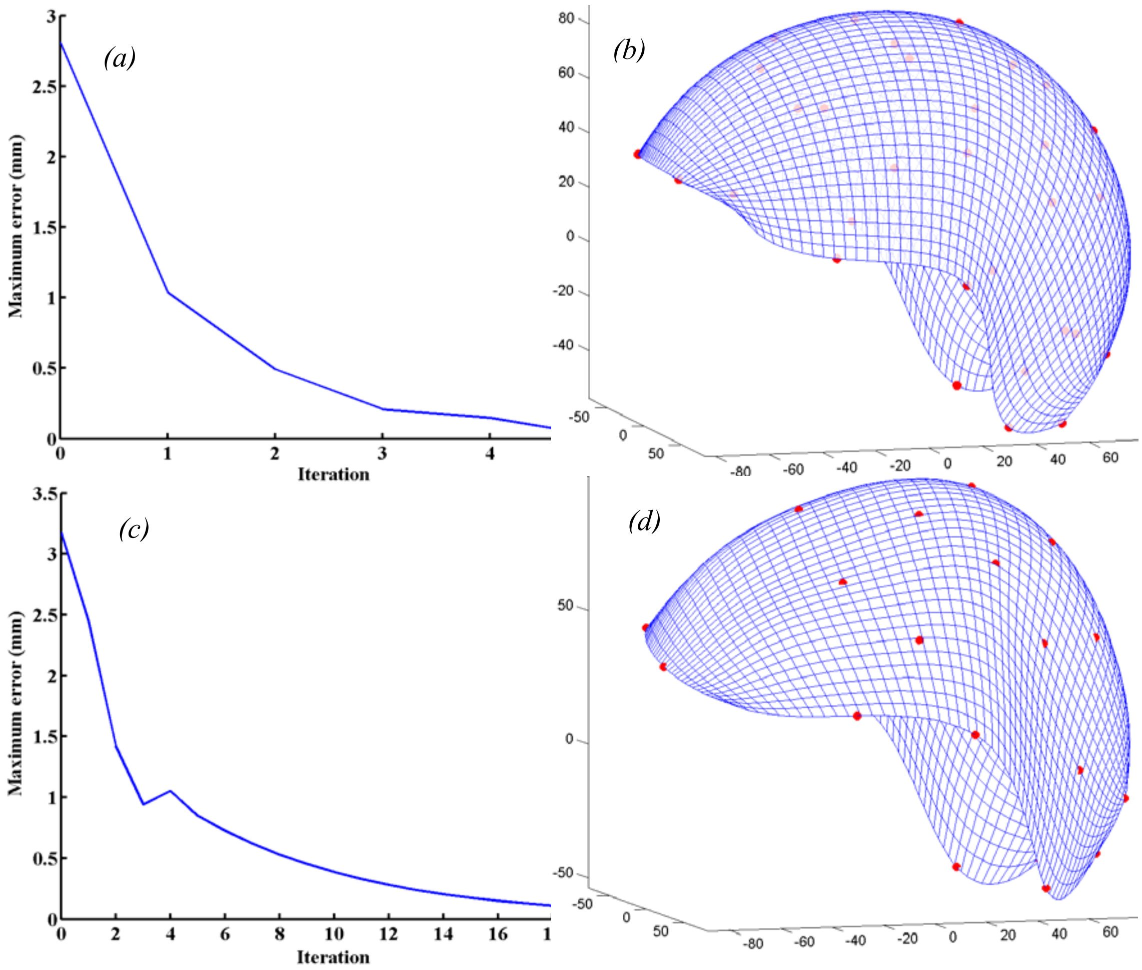

Figure 4.6: Results of the surface manipulation for the fastest and slowest convergence of maximum error among the subjects. The fastest convergence (a) was 5 iterations with final surface in (b). The slowest (c) was 19 iterations giving rise to the final surface in (d).

4.4. Surface Quality Evaluation

In order to evaluate the performance of the methodology described above, the surfaces generated through the electrodes need to be compared to the actual geometric form of the subject. This requires that a surface model of the subject, with which a comparison is made, needs to be built and meshed using the techniques described in §2.2.2 and §2.2.3 so that the deviation of the nodes on the surface of the Finite Element model from the surface through the electrodes can be established. MRI datasets of usable quality were not available for any of the human subjects used for the investigation described above, though the CT scan for the tank phantom provides a valuable source of data for making this comparison.

4.4.1. Tank Mesh Comparison

As previously stated, the electrode and landmark positions for the tank phantom were derived from the CT scan itself and the accuracy of the resulting positions was no better than 1 mm, this being the resolution of the CT image data. Moreover, the surface model generated from the dataset, as described in §2.2.2, would suffer similar inaccuracies. Additional concerns were also noted with the tank model in that the parameterisation of the electrodes on the surface boundaries did not conform well to the expected values indicated by normal 10-20 positions. The reason for this became apparent from examination of the B-Spline surface and the CT scan images; electrodes 12 and 18 were positioned too high and more towards the anterior than usual. These two electrodes should be positioned on the Mastoid Process, where in the tank model they were placed over a position corresponding nearer to the External Auditory Meatus.

To overcome this problem, positions were obtained from the CT scan that corresponded more accurately to the correct position of electrodes 12 and 18 and the surface built from this data. The two tank meshes described in §2.2.2 were then used to evaluate the quality of the surface. These meshes consisted of 24722 elements and 52327 elements from which the boundary nodes were extracted and the orthogonal distances from those nodes and the B-Spline surface calculated. An acceptable result would be that a significant majority of the nodes would be within 2 mm of the surface.

An even more accurate evaluation would result from aligning the surface more precisely with the mesh. As the accuracy of the landmark positions taken from the CT scan suffer the same inaccuracy of 1 mm, then it would be reasonable to assume that the surface could be undergo affine linear transformation such that the distances of the nodes from the surface is minimised. In order to achieve this, a Newton-Raphson algorithm (secant method) was implemented that modified the position of the surface in relation to the meshes such that the sum of the distances, for x, y and z, was minimised. Again the distances from the nodes to the surface could be calculated and the procedure also results in providing an indication of inaccuracy in measuring the landmarks from the CT scan.

4.4.2. Results

A total of eight results of the analysis described above were obtained and these are summarised in Table 4.2 and Table 4.3. Table 4.2 shows results for the mesh consisting of 24722 elements for surfaces created both by truncating the curve $\boldsymbol{u}_{0.0}$ by making it equal in length to $\boldsymbol{u}_{1.0}$ and by interpolating points at $v = {}^1/_6$ and $v = {}^5/_6$. For each of these surfaces the mean and standard deviation of the distances of the nodes under the surface are given for each of the conditions where the surface is kept in its natural position, and where it is translated to minimise the sum of the distances.

Table 4.2: Summary of electrode B-Spline surface quality for 24722 element mesh

Truncation	Surface position	Mean (mm)	Std (mm)	< 1 mm (%)	< 2 mm (%)	< 3 mm (%)	Δx (mm)	Δy (mm)	Δz (mm)
equal	Natural	1.15	0.90	55.0	83.7	95.0			
	Translated	1.05	0.81	55.4	89.0	97.5	-0.367	-1.054	0.571
${}^1/_6, {}^5/_6$	Natural	1.15	0.87	55.1	83.9	95.3			
	Translated	1.03	0.78	57.3	89.9	97.7	-0.356	-1.056	-0.568

Table 4.3 shows the equivalent results for the mesh consisting of 52327 elements.

Table 4.3: Summary of electrode B-Spline surface quality for 52327 element mesh

Truncation	Surface position	Mean (mm)	Std (mm)	< 1 mm (%)	< 2 mm (%)	< 3 mm (%)	Δx (mm)	Δy (mm)	Δz (mm)
equal	Natural	1.20	0.96	55.0	82.1	94.0			
	Translated	1.12	0.91	52.7	86.0	96.2	-0.308	-0.907	-0.468
${}^1/_6, {}^5/_6$	Natural	1.18	0.92	55.2	82.4	94.5			
	Translated	1.08	0.86	55.8	88.3	96.6	-0.320	-0.927	-0.463

Each table also gives a statistical breakdown of the error analysis showing the percentage of nodes that are within 1, 2 and 3 mm of the surface. Where the surfaces have been translated, the tables also show that translation in the x, y and z directions. Figure 4.7 shows the statistical distribution of errors for the 24722 element mesh where the surface through the electrodes has been translated to minimise the sum of the errors. Also inset in this illustration is an image of the mesh in relation to the surface. The larger errors can be visually observed around the electrodes 12, 18, 28 and 30; the positions of electrodes 12 and 18 have already been modified to accommodate poor parameterisation along the left and right boundaries.

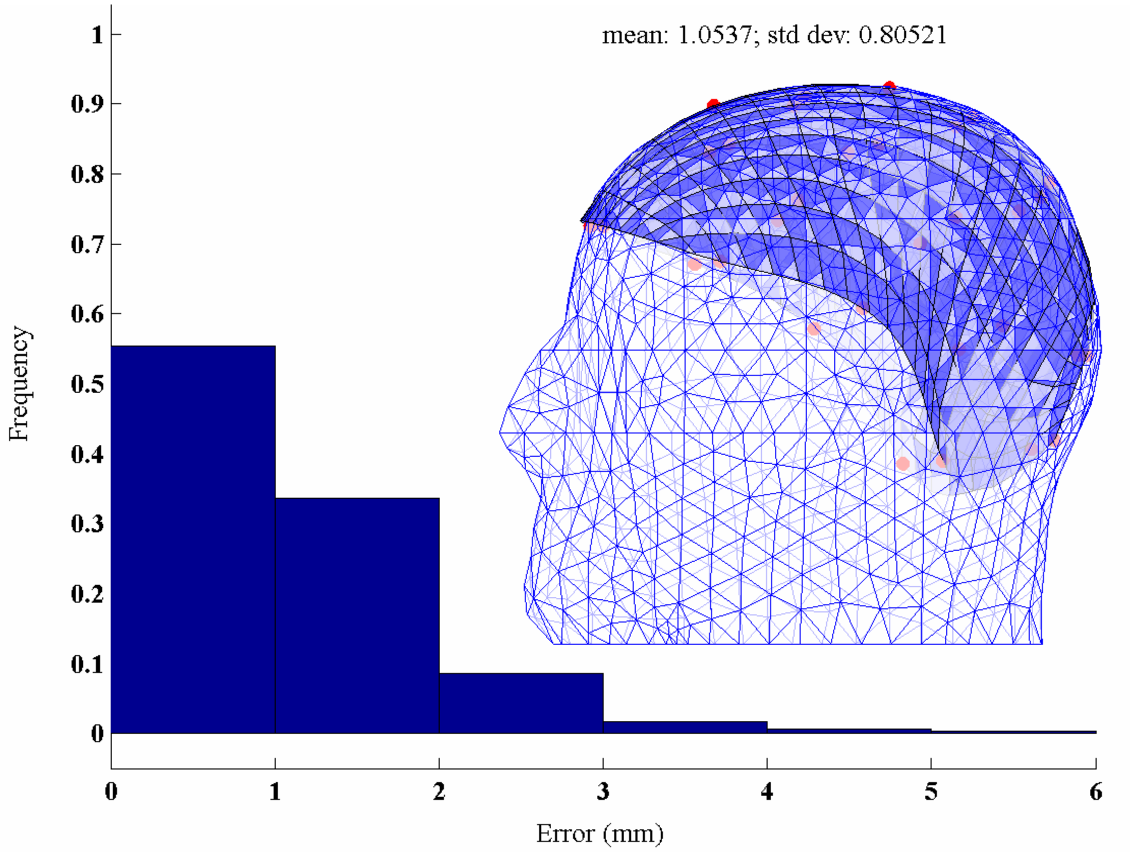

Figure 4.7: The statistical distribution of error between the surface through the electrodes and the 24722 element mesh of the tank phantom. The surface aligned to the mesh is also shown inset. The distribution is exponentially distributed with 89% of nodes having less than 2 mm error and 97.5% less than 3 mm. The largest errors can be observed near the surface boundary around electrodes 12, 18, 28 and 31 which could be accounted for by the poor parameterisation of the boundary electrodes in the model.

4.5. Discussion and Conclusions

It has been demonstrated that a bi-cubic B-Spline patch, through measured electrode positions, can be approximated in the first instance, and then subsequently manipulated to achieve an accurate outcome. A relatively few number of iterations are required to manipulate individual control vertices such that positional errors between the electrode positions and the surface are reduced to as little as 0.1 mm. A marginal increase in the number of iterations is required to halve this error value.

However, little value is gained from attempting to achieve too high a precision with the experimental data presented here. This is because electrode positions were obtained with an accuracy no better than 0.38 mm with the *microscribe* device used. This value is the best case as further inaccuracies would have been incurred from subject movement during the measurement procedure. Furthermore, the landmark registration sites are also difficult to establish accurately, particularly the inion and pre-auricular points owing to variation in subject anatomy. Another, perhaps significant, source of error arises from the electrode placement itself. Though an experienced EEG technician can site electrodes with a reasonable level of consistency, there will still be an expectation that the parametric positions would be subject to errors that would be difficult to quantify. It is likely that the accumulation of these factors have had a bearing on the speed with which the surface manipulation algorithm converged as well as on the visual quality of the final surfaces generated. Improvements to the surface generation are possible and would include engaging in the design of a more suitable head net and the use of Non-Uniform Rational B-Splines (NURBS). The latter is an extension of the B-Spline that applies weights to the control vertices to alter the locality of the control of surface form when manipulating a control vertex. More detailed discussion of such improvements is confined to Chapter 8.

The results obtained from the analysis of the tank phantom surface and meshes are encouraging in that they show good conformity between a bi-cubic B-Spline surface fitted and manipulated through the measured electrode positions and the actual subject-specific finite element mesh and the surface nodes of that mesh. The latter surface model, being manually segmented from the CT scan of the tank phantom, will be subject to the errors already discussed regarding this type of modelling. The expectation that the maximum errors between the actual surface defined by the nodes of the FE model and that derived from electrode positions for this case would be in the region of 2 mm has been reasonably demonstrated.

In all cases presented in §4.4.2, more than 80% of the nodes are within 2 mm of the surface and more that 94% are within 3 mm. Significant improvements in the measured accuracy are observed when the surface is translated to minimise the sum of the errors in x, y and z. Marginal improvements are also observed if the anterior curve $\boldsymbol{u}_{0.0}$ is truncated by interpolating points $^1/_6$ and $^5/_6$ along the length of the original (Figure 4.5). For these latter cases with both meshes and where the surfaces are translated, more than 88% of the nodes are within 2 mm of the surfaces and more than 96% are within 3 mm.

There is a general conformity across the results regarding the amount of translation the surfaces need to undergo in order to minimise the errors. The assertion that these values indicate the positional error in measuring the landmark and electrode positions from the CT scan is well supported by the data; the maximum movement in any one direction being in the region of the expected 1 mm predicted error.

5. ALGORITHMS FOR WARPING FINITE ELEMENT MESHES OF THE HUMAN HEAD

The methodology described in the previous Chapter establishes the initial stages of generating subject-specific finite element meshes for use in the forward model for EIT. The ability to accurately model the surface under the electrodes can potentially allow the mesh to be reshaped or warped to match the geometry in that area. This Chapter discusses the next stage of the process, which is to warp the mesh to the specific geometry whilst maintaining an acceptable level of element quality and anatomical accuracy within the whole model. Previous work in this area has already been discussed (Cohen *et al*, 2000; Gibson *et al*, 2003; Lamm *et al*, 2001). Other work has also been undertaken in the area of modifying FE meshes such that they conform to patient-specific geometry. In the field of biomechanics, Couteau *et al.* (2000) have introduced a *Mesh-Matching* algorithm based on Octree Splines. This method is applied to homogeneous meshes and is demonstrated on a model of the upper femur. Points extracted from CT scans of patients' femurs are used to warp an existing FE mesh. No surfaces are built during this process but instead a substantial dataset of points is used. For medical image co-registration, methods to modify template images to subject specific target images using elastic warping techniques similar to those described here have been demonstrated (Bowden *et al*, 1998; Christensen *et al*, 1996).

This thesis proposes a technique that uses the methods described in Chapter 4 to generate the B-Spline surface patch under the electrodes upon which to project the nodes on the mesh surface beneath the patch. The displacements of these nodes will serve as the initial boundary conditions for a deformation of the whole mesh using established stress analysis techniques. Unlike the method previously discussed (Couteau *et al*, 2000), the process attempts to warp the whole mesh using only a relatively small area of the target surface while also maintaining an acceptable geometric form for the whole head surface. Also, the relative thicknesses of the layers making up the anatomical features of scalp, skull, CSF and brain need to be maintained after warping as does the overall mesh quality quantified by element stretch. A similar approach has been adopted for simulation of deformation of the brain during Neurosurgery (Warfield *et al*, 2000) but as yet the author is unaware of any application of such a technique to the warping of a non-homogeneous domain for the purpose of anatomical matching for use in EIT. The following section reviews the fundamentals of Finite Element Stress Analysis that will be applied to the problem.

5.1. Stress Analysis Techniques

The behaviour of elastic bodies under applied forces or deformation is well known and has particular relevance to the problem of warping the head mesh such that it more closely conforms to patient specific geometry. The fundamentals of stress analysis has been published widely in the form of text books (Dally and Riley, 1978; Benham and Warnock, 1979) and is briefly reviewed here to establish context.

5.1.1. Fundamentals

The tensile stress in a bar, or the one dimensional case, is given by the relationship:

$$\sigma_x = E\varepsilon_x \tag{5.1}$$

where E is the modulus of elasticity (*Young's modulus*) and ε the strain, or for an extension in the x direction $\varepsilon_x = du/dx$. A lateral contraction also occurs in the bar in the form of strains in the y and z directions:

$$\varepsilon_y = \varepsilon_z = -\nu\varepsilon_x = -\nu\frac{\sigma_x}{E} \tag{5.2}$$

where ν is *Poisson's ratio* which for a wide range of elastic materials is in the range of 0.25 – 0.35. For a block undergoing shear deformation, shear stress, τ, is defined as the shear force divided by unit area and its relationship to shear strain, γ, is:

$$\tau_{xy} = G\gamma_{xy} \tag{5.3}$$

In this relationship, G is the shear modulus and is directly related to Young's modulus and Poisson's ratio such that:

$$G = \frac{E}{2(1+\nu)} \tag{5.4}$$

In three dimensions, a complex system of stresses on an elastic body consists of six stress components ($\sigma_x, \sigma_y, \sigma_z, \tau_{xy}, \tau_{yz}, \tau_{zx}$) and their corresponding strains ($\varepsilon_x, \varepsilon_y, \varepsilon_z, \gamma_{xy}, \gamma_{yz}, \gamma_{zx}$). The development of the relationship between the stresses and strains is explained by a number of authors as previously stated, for example Dally (1978). The relationship between stress and strain can be expressed in matrix notation:

$$\boldsymbol{\sigma} = \mathbf{D}\boldsymbol{\varepsilon} \tag{5.5}$$

The vectors $\boldsymbol{\sigma}=[\sigma_x, \sigma_y, \sigma_z, \tau_{xy}, \tau_{yz}, \tau_{zx}]^T$ and $\boldsymbol{\varepsilon} = [\varepsilon_x, \varepsilon_y, \varepsilon_z, \gamma_{xy}, \gamma_{yz}, \gamma_{zx}]^T$ and the *elastic stiffness* or *material property* matrix is defined as:

$$\mathbf{D}=\frac{E}{(1+\nu)(1-2\nu)}\begin{bmatrix} 1-\nu & \nu & \nu & & & \\ \nu & 1-\nu & \nu & 0 & 0 & 0 \\ \nu & \nu & 1-\nu & 0 & 0 & 0 \\ 0 & 0 & 0 & \frac{1-2\nu}{2} & 0 & 0 \\ 0 & 0 & 0 & 0 & \frac{1-2\nu}{2} & 0 \\ 0 & 0 & 0 & 0 & 0 & \frac{1-2\nu}{2} \end{bmatrix} \tag{5.6}$$

The stress-strain relationship of equations (5.5) and (5.6) is a pivotal component in the formulation of finite element stress analysis.

5.1.2. Potential Energy

The principle of minimum potential energy, combined with the Rayleigh-Ritz method forms the basis of finite element stress analysis. A structure loaded by external forces or, as is the case for this work, subjected to a known deformation will be storing energy in the form of the internal strain energy. This is balanced with the potential energy of the internal body forces due to the mass of the structure under gravity and the applied external loads on the structure. Thus, the total potential energy, Π, is equal to the strain energy, U, minus the potential energy of the applied loads and body forces combined, W:

$$\mathbf{\Pi}=\mathbf{U}-\mathbf{W} \tag{5.7}$$

Strain energy is defined as one half the product of stress and strain per unit volume, i.e.:

$$\mathbf{U}=\frac{\mathbf{1}}{\mathbf{2}}\int_V \boldsymbol{\sigma}^{\mathrm{T}}\boldsymbol{\varepsilon}\, dV \tag{5.8}$$

and

$$\mathbf{W}=\int_V \mathbf{u}^{\mathrm{T}}\mathbf{X}dV+\int_S \mathbf{u}^{\mathrm{T}}\mathbf{T}_{\mathrm{S}}dS \tag{5.9}$$

where $\mathbf{u}^{\mathrm{T}}$ are the displacement components throughout the body, **X** the body forces per unit volume and $\mathbf{T}_{\mathrm{S}}$ are the surface tractions or surface forces per unit area.

Thus an expression for potential energy can be defined which relates applied forces to displacements and material properties.

$$\mathbf{\Pi}=\frac{\mathbf{1}}{\mathbf{2}}\int_V \boldsymbol{\sigma}^{\mathrm{T}}\boldsymbol{\varepsilon}\, dV-\int_V \mathbf{u}^{\mathrm{T}}\mathbf{X}dV-\int_S \mathbf{u}^{\mathrm{T}}\mathbf{T}_{\mathrm{S}}dS \tag{5.10}$$

5.1.3. Application to Finite Elements

Shape functions are derived from element geometry as shown in equations (1.33) to (1.39) which can be expanded to three dimensions and is covered by a range of finite element texts, for example Baker & Pepper (1991). If the displacement vector anywhere within a tetrahedral element with no mid-side nodes is $\mathbf{u}(x,y,z)$ and $\mathbf{d} = [u_1, v_1, w_1, u_2, v_2, w_2, u_3, v_3, w_3, u_4, v_4, w_4]^{\mathrm{T}}$, being the displacements of the nodes in x, y and z, then:

$$\mathbf{u} = \mathbf{N}\mathbf{d} \tag{5.11}$$

where:

$$\mathbf{N}(\xi_i) = \begin{Bmatrix} \xi_1 \\ \xi_2 \\ \xi_3 \\ \xi_4 \end{Bmatrix} = \frac{1}{6V_e} \begin{Bmatrix} a_1 + b_1 x + c_1 y + d_1 z \\ -(a_2 + b_2 x + c_2 y + d_2 z) \\ a_3 + b_3 x + c_3 y + d_3 z \\ -(a_4 + b_4 x + c_4 y + d_4 z) \end{Bmatrix} \tag{5.12}$$

V_e is the volume of the element and is related to the coordinates of the nodes such that:

$$V_e = \frac{1}{6} \det \begin{bmatrix} 1 & X_1 & Y_1 & Z_1 \\ 1 & X_2 & Y_2 & Z_2 \\ 1 & X_3 & Y_3 & Z_3 \\ 1 & X_4 & Y_4 & Z_4 \end{bmatrix}_e \tag{5.13}$$

The coefficients in equation (5.12) are also defined:

$$a_i \equiv \det \begin{bmatrix} X_j & Y_j & Z_j \\ X_m & Y_m & Z_m \\ X_p & Y_p & Z_p \end{bmatrix}_e \tag{5.14}$$

$$b_i \equiv -\det \begin{bmatrix} 1 & Y_j & Z_j \\ 1 & Y_m & Z_m \\ 1 & Y_p & Z_p \end{bmatrix}_e$$

$$c_i \equiv \det \begin{bmatrix} X_j & 1 & Z_j \\ X_m & 1 & Z_m \\ X_p & 1 & Z_p \end{bmatrix}_e$$

$$d_i \equiv -\det \begin{bmatrix} X_j & Y_j & 1 \\ X_m & Y_m & 1 \\ X_p & Y_p & 1 \end{bmatrix}_e$$

Here, the indices (i ,j, m, p) relate to the node numbers (1, 2, 3, 4) to establish all the coefficients a_i to d_i.

Strain is related to displacement through first order partial differentiation:

$$\varepsilon_x = \frac{\partial u}{\partial x};\ \varepsilon_y = \frac{\partial v}{\partial y};\ \varepsilon_z = \frac{\partial w}{\partial z} \tag{5.15}$$

$$\gamma_{xy} = \frac{\partial u}{\partial y} + \frac{\partial v}{\partial x}; \gamma_{yz} = \frac{\partial v}{\partial z} + \frac{\partial w}{\partial y}; \gamma_{xz} = \frac{\partial u}{\partial z} + \frac{\partial w}{\partial x}$$

and hence:

$$\boldsymbol{\varepsilon} = \partial \mathbf{u} \tag{5.16}$$

where

$$\partial = \begin{bmatrix} \frac{\partial}{\partial x} & 0 & 0 \\ 0 & \frac{\partial}{\partial y} & 0 \\ 0 & 0 & \frac{\partial}{\partial z} \\ \frac{\partial}{\partial y} & \frac{\partial}{\partial x} & 0 \\ 0 & \frac{\partial}{\partial z} & \frac{\partial}{\partial y} \\ \frac{\partial}{\partial z} & 0 & \frac{\partial}{\partial x} \end{bmatrix}$$

Combining equations (5.11) and (5.16) yields:

$$\begin{aligned} \boldsymbol{\varepsilon} &= (\partial \mathbf{N})\mathbf{d} \\ &= \mathbf{Bd} \end{aligned} \tag{5.17}$$

Substituting equation (5.12) and using the chain rule, for example:

$$\frac{\partial N}{\partial x} = \frac{\partial N}{\partial \xi_i}\frac{\partial \xi_i}{\partial x} \tag{5.18}$$

gives:

$$\mathbf{B} = \frac{1}{6V_e}\begin{bmatrix} b_1 & 0 & 0 & b_2 & 0 & 0 & b_3 & 0 & 0 & b_4 & 0 & 0 \\ 0 & c_1 & 0 & 0 & c_2 & 0 & 0 & c_3 & 0 & 0 & c_4 & 0 \\ 0 & 0 & d_1 & 0 & 0 & d_2 & 0 & 0 & d_3 & 0 & 0 & d_4 \\ c_1 & b_1 & 0 & c_2 & b_2 & 0 & c_3 & b_3 & 0 & c_4 & b_4 & 0 \\ 0 & d_1 & c_1 & 0 & d_2 & c_2 & 0 & d_3 & c_3 & 0 & d_4 & c_4 \\ d_1 & 0 & b_1 & d_2 & 0 & b_2 & d_3 & 0 & b_3 & d_4 & 0 & b_4 \end{bmatrix} \tag{5.19}$$

Combining equations (5.5) and (5.17) gives:

$$\boldsymbol{\sigma} = \mathbf{DBd} \tag{5.20}$$

Substituting this and equation (5.11) into (5.10) for an individual element yields:

$$
\begin{aligned}
\boldsymbol{\Pi}_e &\approx \frac{\mathbf{1}}{\mathbf{2}}\int_{V^e}(\mathbf{DBd})^{\mathrm{T}}(\mathbf{Bd})\,dV - \int_{V^e}(\mathbf{Nd})^{\mathrm{T}}\mathbf{X}dV - \int_{S^e}(\mathbf{Nd})^{\mathrm{T}}\mathbf{T}_{\mathbf{S}}dS \\
&= \frac{\mathbf{1}}{\mathbf{2}}\mathbf{d}^{\mathrm{T}}\left(\int_{V^e}\mathbf{B}^{\mathrm{T}}\mathbf{DB}\,dV\right)\mathbf{d} - \mathbf{d}^{\mathrm{T}}\left(\int_{V^e}\mathbf{N}^{\mathrm{T}}\mathbf{X}dV + \int_{S^e}\mathbf{N}^{\mathrm{T}}\mathbf{T}_{\mathbf{S}}dS\right) \\
&= \frac{\mathbf{1}}{\mathbf{2}}\mathbf{d}^{\mathrm{T}}\mathbf{K}_{\mathbf{e}}\mathbf{d} - \mathbf{d}^{\mathrm{T}}\mathbf{F}_{\mathbf{e}}
\end{aligned}
\tag{5.21}
$$

Applying the principal of minimum potential energy where:

$$
\frac{\partial \Pi_e}{\partial \mathbf{d}} = \mathbf{K}_{\mathbf{e}}\mathbf{d} - \mathbf{F}_{\mathbf{E}} = 0
\tag{5.22}
$$

yields a statement of Hooke's law for the element, $\mathbf{K_e d} = \mathbf{f}$. Therefore a stiffness matrix for each element can be derived from equation (5.12):

$$
\mathbf{K}_{\mathbf{e}} = \int_{V^e}\mathbf{B}^{\mathrm{T}}\mathbf{DB}\,dV
\tag{5.23}
$$

It is assumed that the elastic moduli are constant inside the element and **B** is constant, therefore:

$$
\mathbf{K}_{\mathbf{e}} = V_e\mathbf{B}^{\mathrm{T}}\mathbf{DB}
\tag{5.24}
$$

This is a 12 by 12 matrix for a linear tetrahedral element.

5.2. Warping Algorithm development

The foregoing, well-established analysis serves as a basis for the warping algorithm. The method can be used to apply geometric warping to a mesh provided a number of surface displacements are known. These are initially defined as the orthogonal projection of the surface nodes immediately under the B-Spline patch fitted through the electrode positions. A global stiffness matrix needs to be built to define equation (5.22) for the whole mesh, which is an assembly of the individual stiffness matrices for the elements based on their interconnectivity.

5.2.1. The Global Stiffness Matrix

The assembly of the global stiffness matrix is relatively straightforward but by no means trivial if it is to be achieved efficiently. For this work, the code used in the MATLAB *bld_master* function in EIDORS (Polydorides and Lionheart, 2002) has been adapted. This code uses a highly efficient method of evaluating the shape function $\mathbf{N}\{\zeta\}$ using equations (5.12) to (5.14). The modification into a new MATLAB function *bld_stiffness* is relatively straightforward using the method to evaluate the coefficients, (a_i, b_i, c_i *and* d_i) in equations (5.12) and (5.13) to build the matrix, **B**, using equation (5.19). The code returns the sparse stiffness matrix, **K**, from the array of node coordinates, an array of the element connectivity indexed to the node array and a vector of the values of Young's modulus, *E*, for each element and Poisson's ratio, *v*, for the materials.

The global stiffness matrix is assembled by summing the terms in the individual element stiffness matrices that correspond to a common node shared by a number of elements. The result being, for a mesh consisting of *n* nodes, a square matrix of dimensions 3*n* such that:

$$\mathbf{Kd} = \mathbf{F} \tag{5.25}$$

The vector, **d**, in equation (5.25) also has a length 3*n* defining the displacement of each node in each of the three orthogonal Cartesian directions. This is also the case for the force vector, **F**, defining the directional components of applied or reaction forces at each node. In the warping case, **F** is derived from the final term in equation (5.10) as the effects of gravity and mass are ignored. All the terms in **F** corresponding to a node not subject to a given displacement are known and zero; the displacements of the projected boundary nodes are the only known terms in **d**.

5.2.2. Solution

The displacements of all nodes as a result of warping is calculated from the solution of the system of equations in equation (5.25) which needs to be rearranged to evaluate all the unknowns as discussed above. Equation (5.25) can be re-written:

$$\left[\begin{array}{c|c} \mathbf{K}_{11} & \mathbf{K}_{12} \\ \hline \mathbf{K}_{21} & \mathbf{K}_{22} \end{array}\right] \left[\begin{array}{c} \mathbf{d}_1 \\ \hline \mathbf{d}_2 \end{array}\right] = \left[\begin{array}{c} \mathbf{F}_1 \\ \hline \mathbf{F}_2 \end{array}\right] \tag{5.26}$$

In this representation $\mathbf{d_1}$ is a vector of known displacements, that is those of the nodes projected to the B-Spline surface and those fully restrained – the boundary conditions of the problem. The vector, $\mathbf{d_2}$, contains the unknown displacement of all other nodes. $\mathbf{F_1}$ is therefore a vector of all unknown reaction forces arising from the displacement boundary conditions, while $\mathbf{F_2}$ is a vector of all the known reaction forces at the nodes where displacements are originally unknown. To comply with the principles of static equilibrium, the values in $\mathbf{F_2}$ are all zero. Expanding equation (5.26):

$$\begin{aligned} \mathbf{K}_{11}\mathbf{d}_1 + \mathbf{K}_{12}\mathbf{d}_2 &= \mathbf{F}_1 \\ \mathbf{K}_{21}\mathbf{d}_1 + \mathbf{K}_{22}\mathbf{d}_2 &= \mathbf{F}_2 = \{0\} \end{aligned} \tag{5.27}$$

From which the solution for evaluating unknown displacements, $\mathbf{d_2}$, can be readily derived:

$$\begin{aligned} \mathbf{K}_{22}\mathbf{d}_2 &= -\mathbf{K}_{21}\mathbf{d}_1 \\ \mathbf{d}_2 &= -\mathbf{K}_{22}^{-1}\left(\mathbf{K}_{21}\mathbf{d}_1\right) \end{aligned} \tag{5.28}$$

Initial warping tests were carried out using the above methodology. Prior to application of the algorithm, the mesh to be warped must undergo the affine registration described in §4.2.1 and then additionally be scaled relative to all three Cartesian directions such that the registration points in the *source* mesh (the mesh to be warped) align with the associated *target* or subject-specific patient position file.

Equation (5.28) could be solved using any iterative method supplied in MATLAB. One would expect little difference in the final results whatever method is selected and the main criterion for choice would be the time it takes to carry out the solution. The main choices are minimum residual norm (*minres*), symmetric LQ (*symmlq*) or preconditioned conjugate gradients (*pcg*). The latter requires that the matrix be factorised and is used in the forward solver for EIDORS with incomplete Cholesky decomposition (*cholinc*) as the pre-conditioner. Initial tests on the algorithm support the assertion that there is little difference in the results when using any of these methods, though it was noted that the solution took two to three times longer with preconditioned conjugate gradients when a drop tolerance of 0.01 was used with incomplete Cholesky decomposition. Very little time difference was observed between all three when the drop tolerance was increased to 0.1. For the purposes of initially testing and evaluating the algorithm, the minimum residual norm method has been selected though it is clear that further work is needed in establishing the most suitable and is the subject of later discussion.

5.3. Optimisation

As stated above, the boundary conditions for the warping algorithm are made up primarily from the displacements of the nodes on the surface of the source mesh that are orthogonally projected onto the source B-Spline patch generated from the target electrode positions. The method for accomplishing this is described in full in §4.3. In addition, there must be a set of nodes that are fully restrained or where the displacements are set to zero. Furthermore, material properties also need to be established and optimised. The values for Young's modulus and Poisson's ratio may have a bearing on the performance of the algorithm. It was predicted that the relative stiffness of the three thin shells: Scalp, Skull and CSF, need to be significantly higher than that of the brain to ensure that the thickness of each is maintained to a reasonable margin of error. Little is known about the variation of these layers from subject to subject and so the assumption made in this work is that it is minimal. It may be that Poisson's ratio will also have a significant effect and tests need to be carried out to establish its effects on the performance of the algorithm.

A series of tests were performed using the algorithm on two meshes of similar resolution; a shelled sphere designated SS040 comprising 40,001 elements and 7,311 nodes and a meshed adult head designated SA049 comprising 49,172 elements and 9,142 nodes. The object of the tests were to warp these target meshes to the target phantom tank using the B-Spline surface cast through the electrode positions and registration points measured from the CT scan described in Chapter 4, and to evaluate the performance as measured by the change in specific quality criteria before and after warping. Very little is known about the difference between the source and the target models not covered by the patch. All that is known is the positions of the registration points for the Nasion, Inion and left and right pre-auricular points. For the initial tests carried out on the spherical, shelled sphere the registration points were defined as being the closest nodes to the positions of the registration points in the adult human head solid model described in §2.2.1.

5.3.1. Performance Criteria

The criteria used to evaluate performance were the change in element stretch and the depths of the Scalp, Skull and CSF surfaces from the mesh surface under the B-Spline patch. These two criteria were measured before and after warping. Element stretch values give a key indication of mesh quality. The mean of stretch values has some significance as it gives an overall picture of the change in mesh quality. More important than this, however, is the value of minimum stretch as a significant number of elements with a value of less than 0.05 has potential to introduce errors in the forward solution used in EIT reconstruction as discussed in Chapter 2. The change thicknesses or depths of the anatomical features comprising the boundaries between scalp and skull, skull and CSF and CSF and brain also give an indication of the distortion of these layers as a result of warping. The ideal, in the absence of any meaningful anthropometric data, would be to minimise the change in the thickness of these features. These values can be established relatively easily before and after warping by determining the orthogonal distances of the nodes on the boundaries to the surface mesh beneath the B-Spline patch. This section of the surface mesh can be built once all surface nodes that can be orthogonally projected to the B-Spline patch have been identified. The orthogonal distance of any point to a given triangle can be established by evaluating the coefficients of the equation of the plane that passes through all three vertices. This is a well established methodology covered by a number of authors such as Foley and Van Dam (1982) and Anand (1993). Orthogonality can be established by testing whether the projected point lies within the triangle boundaries by checking that the sum of the areas of the three triangles formed from the vertices and the projected point is not greater than that of the original triangle. Thus the nodes that lie on the outer boundaries of the Skull, CSF and Brain are individually subjected to this process; any nodes that cannot be orthogonally projected are rejected and the distances of those that can recorded. This is carried out using a MATLAB function, *layerthicks,* which returns an array containing the minimum, maximum, median, mean and standard deviations of the depths of all three layers.

An additional criterion to assess the algorithm is the forward solution time of equations (5.26) to (5.28). As discussed above, the minimum residual norm method is used for comparison and tests were carried out on a Intel Pentium 4 based Personal Computer, running at 3 GHz with 1 GB of RAM. The final, more subjective criterion is a visual check of the final warped surface.

5.3.2. Material Properties

The material properties that can be varied to establish appropriate values are Young's Modulus, E, and Poisson's ratio, v. It would be logical to assume that to ensure that the relative deformations of the scalp, skull and CSF regions of the model were to be minimal, then the ratio of the stiffness of these areas to that of the brain region should be high. The initial tests carried out on the two models specified above were to warp the model varying this ratio. The stiffness of the three regions were kept the same in the tests but were varied so that they were stiffer than that of the brain by ratios of increasing orders of magnitude from 1 to 10^4. For these tests, Poisson's ratio was set to 0.3 for all regions, this being typical for a wide range of elastic materials. Additionally all mesh surface nodes that were greater than 80 mm (d_0) from the triangulated surface under the B-Spline patch were fully restrained.

Similar tests were carried out varying Poisson's ratio, v, with values of 0 to 0.4 in steps of 0.1 and additionally with $v = 0.45$. Equation (5.6) determines that v should be less than 0.5, otherwise stress will be undefined. Again for these tests $d_0 = 80$, and the ratio of Young's Modulus of the three shell features to that of brain (R_E) was set to 10.

5.3.3. Boundary Conditions

The nodes projected to the B-Spline patch form the basis for the displacement boundary conditions for the warping algorithm. Additional nodes on the surface boundary are fully restrained and the selection of these needs to be varied to determine the performance under these conditions. For the above tests all nodes greater than a distance $d_0 = 80$ mm were selected. A further set of results was therefore obtained by varying d_0 from 20 mm to 100 mm in steps of 20. It is also conceivable that the mesh would warp successfully under a minimum restraint condition, specifically if only one node, the furthest from the triangulated surface beneath the B-Spline patch, were restrained. The distance of this node from the surface was recorded and included in the data.

5.4. Optimisation Results

5.4.1. Material Properties

For both the shelled sphere, SS040, and the adult head, SA049, the ratio of material stiffness, R_E, for the shelled regions had a significant effect on element quality for $R_E = 1$. Little difference in the minimum stretch was observed for values of $R_E \geq 10$ as can be seen in Figure 5.2. Much the same trend can be seen when warping the adult head to the tank patient position dataset. The shell depth criterion is shown in Figure 5.3 as a percentage change in the mean depths of the inner surfaces of scalp, skull and CSF from the outer surface of the scalp beneath the B-Spline patch. In both cases, there is minimal change in the mean values for $R_E > 100$, though it is clear that there is evidence to assume that there is no change in layer depths after warping for $R_E \approx 10$ for scalp and skull in SS040 and for $R_E \approx 3$ in SA049. The CSF depth is a summation of all three shell thicknesses and this exhibits around 1% change in depth for $R_E = 10$ in both cases which changes marginally for higher values in SS040 and improves significantly in SA049. The solution time criterion is summarised in Figure 5.4 where marked increases in computation time and hence reductions in algorithm efficiency are observed for higher stiffness ratios.

Figure 5.1 shows a view of the warped sphere, SS040, with $d_0 = 80$ mm and $R_E = 10$.

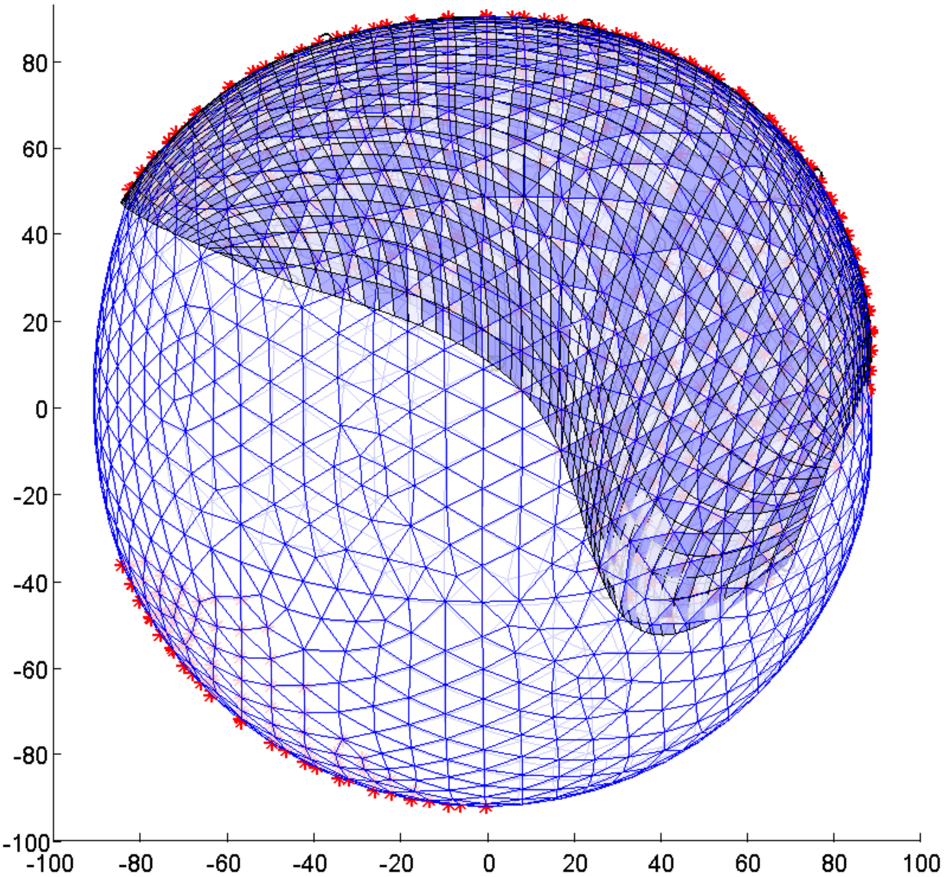

Figure 5.1: Lateral view after warping the 40001 (SS040) element sphere. The nodes coloured red indicate the boundary conditions being all beneath the B-Spline patch and those in the lower left corner. $d_0 = 80$ *mm and* $R_E = 10$*.*

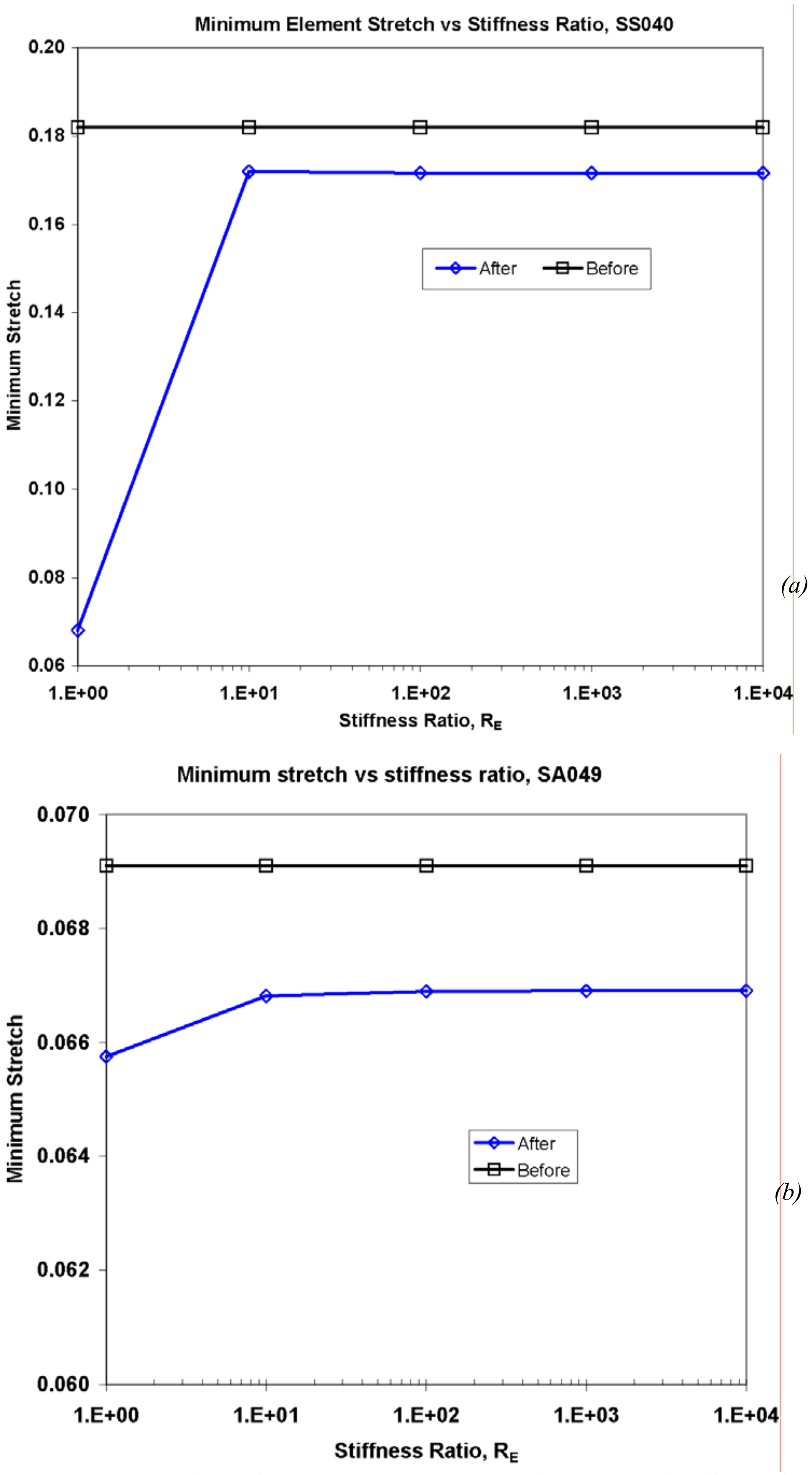

Figure 5.2: The relationship between the ratio, R_E, of the material stiffness of Scalp, Skull and CSF to Brain and minimum element stretch compared to that before warping (a) the 40001 element sphere and (b) the 49172 element adult head. Little improvement can be gained in minimum stretch for values of $R_E > 10$ in either case.

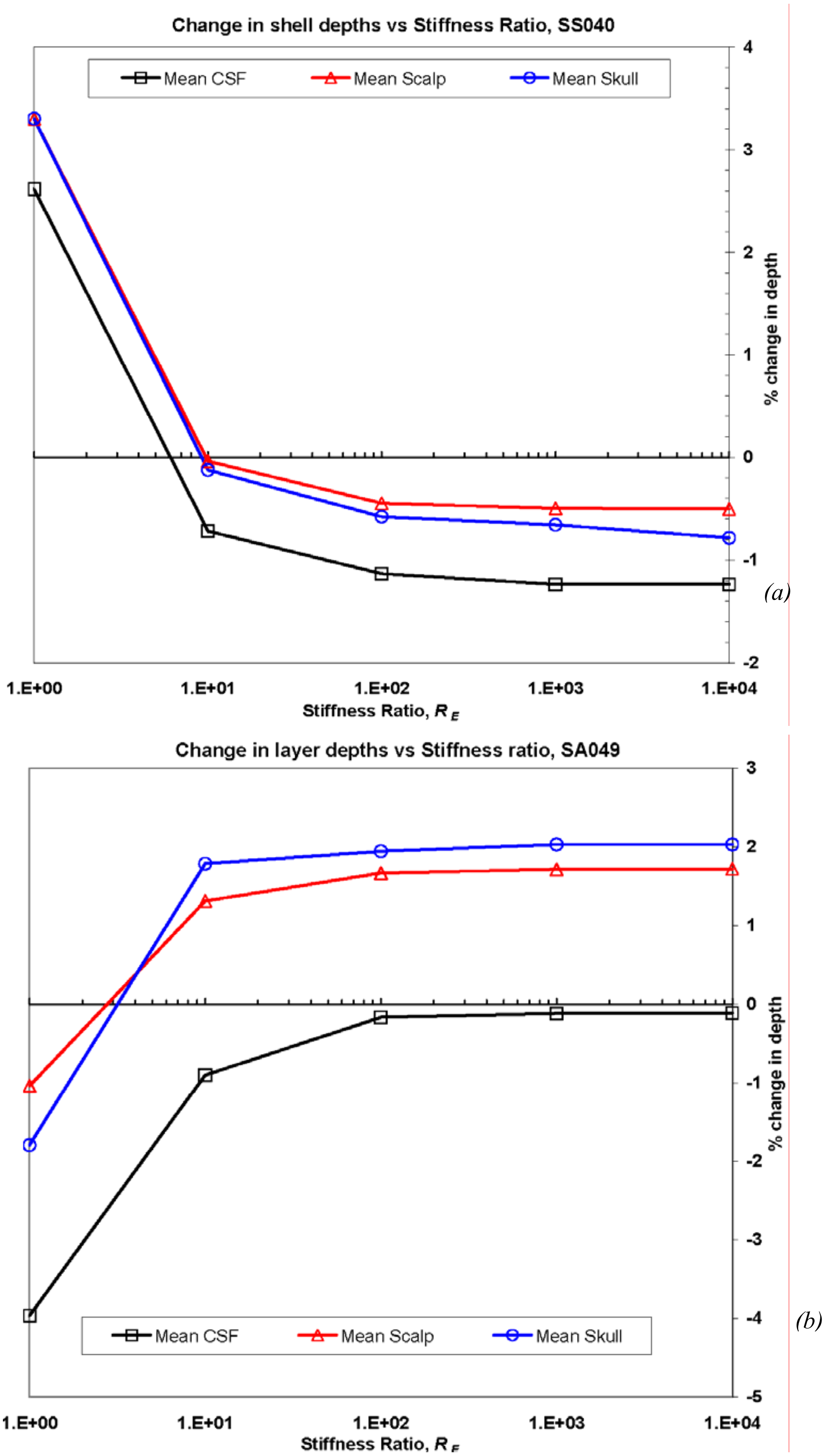

Figure 5.3: The relationship between the ratio, R_E, of the material stiffness of Scalp, Skull and CSF to Brain and change in mean layer depths after warping (a) the 40001 element sphere and (b) the 49172 element adult head. Little improvement can be gained in for values of $R_E > 100$ in either case. For SS040, there is a clear optimum for $R_E \approx 10$

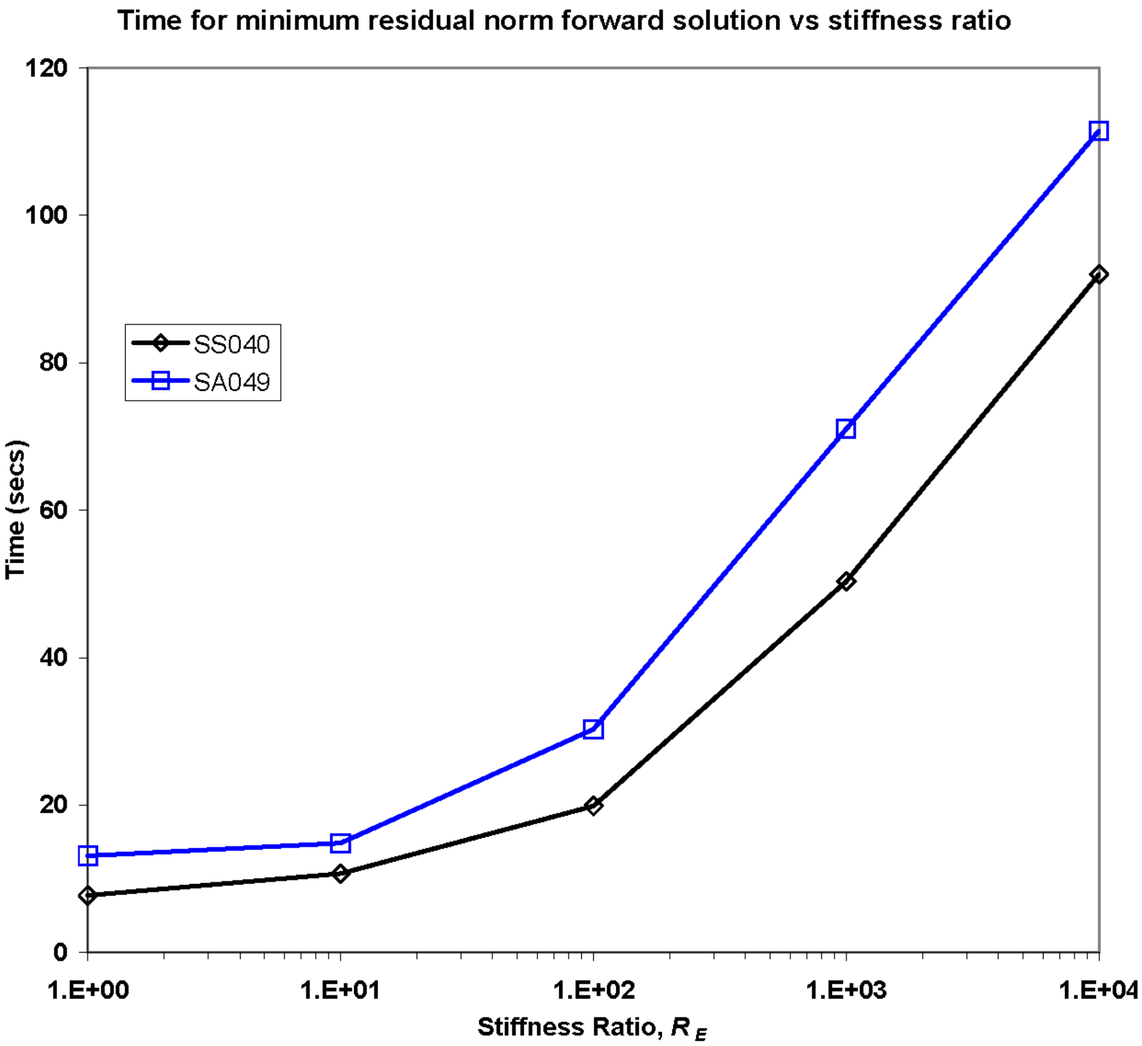

Figure 5.4: The relationship between the ratio, R_E, and forward solution time compared to that before warping the 40001 (SS040) element sphere and the 49172 (SA049) element adult head. Significant increases in computation times are experiences for $R_E > 10$.

Varying Poisson's ratio for all materials does have a significant effect of minimum stretch and layer depths. Figure 5.5 shows the variation of minimum stretch against Poisson's ratio for the meshes before and after warping. The results indicate strongly that the choice for $v = 0.3$ is justified for the algorithm; although for SS040 an optimum appears to be in the region of 0.35 to 0.4. However, little improvement is gained compared to the original choice which is borne out by examination of the change in layer depths as depicted in Figure 5.6.

For SS040, there is a clear optimum for skull and scalp layer depths at $v = 0.3$, with only around 1% change for the CSF layer. The choice of this value for SA049 is still acceptable with changes in region of 2% or less.

There is little in the way of change to solution time across the range of Poisson's ratio for both models. For SS040, the minimum solution time is around 9 s at $v = 0$ with only a slight increase to 10.5 s at $v = 0.3$. The equivalent values for SA049 are around 11 s and 14 s respectively.

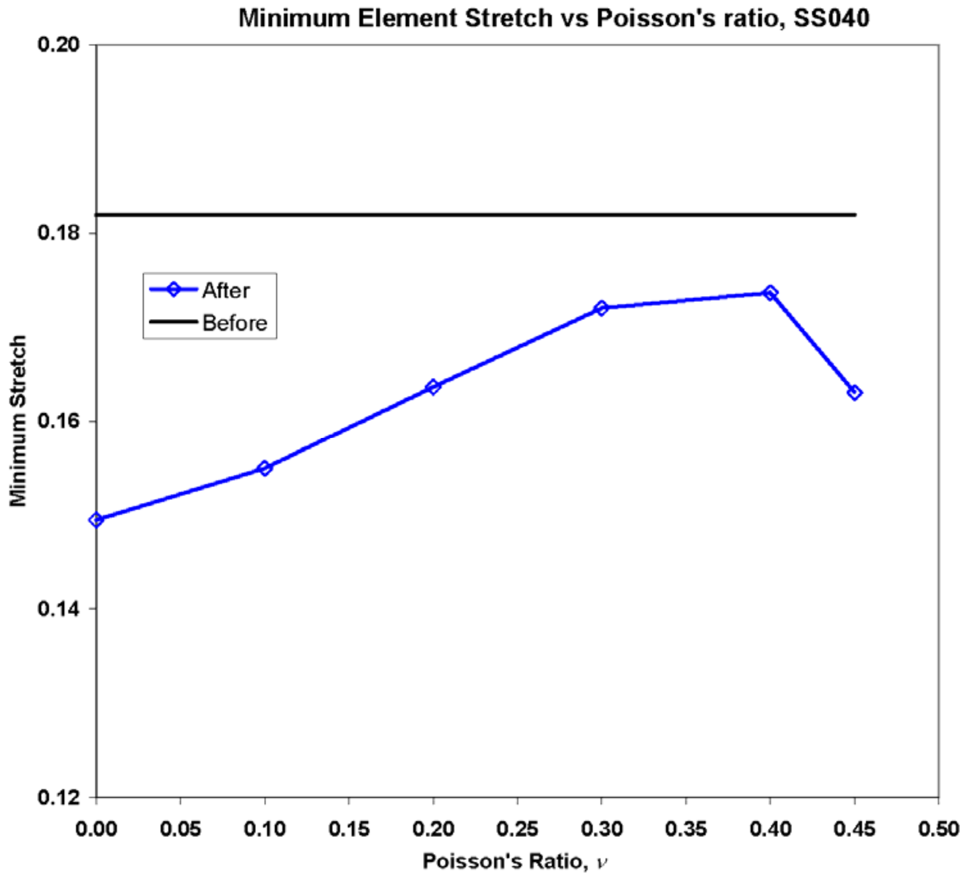

(a)

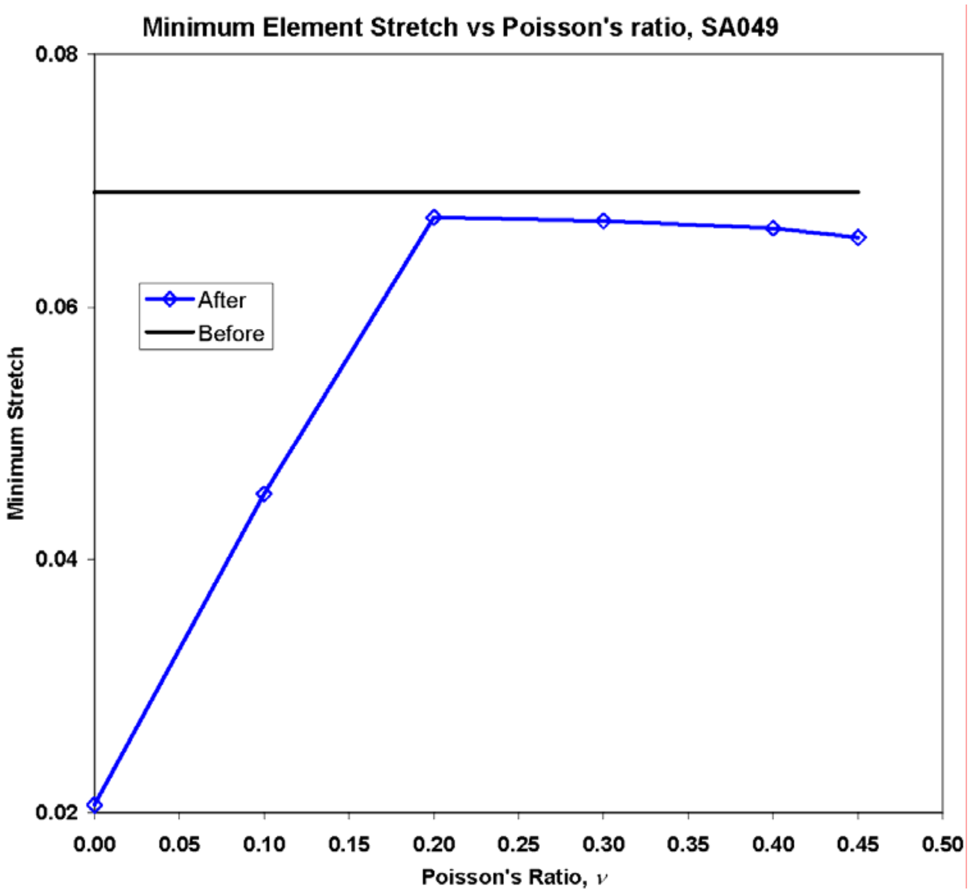

(b)

Figure 5.5: The relationship between Poisson's ratio, v, of all the materials and minimum element stretch before and after warping (a) the 40001 element sphere and (b) the 49172 element adult head. Values below 0.2 perform poorly compared to those in the range 0.3 – 0.4

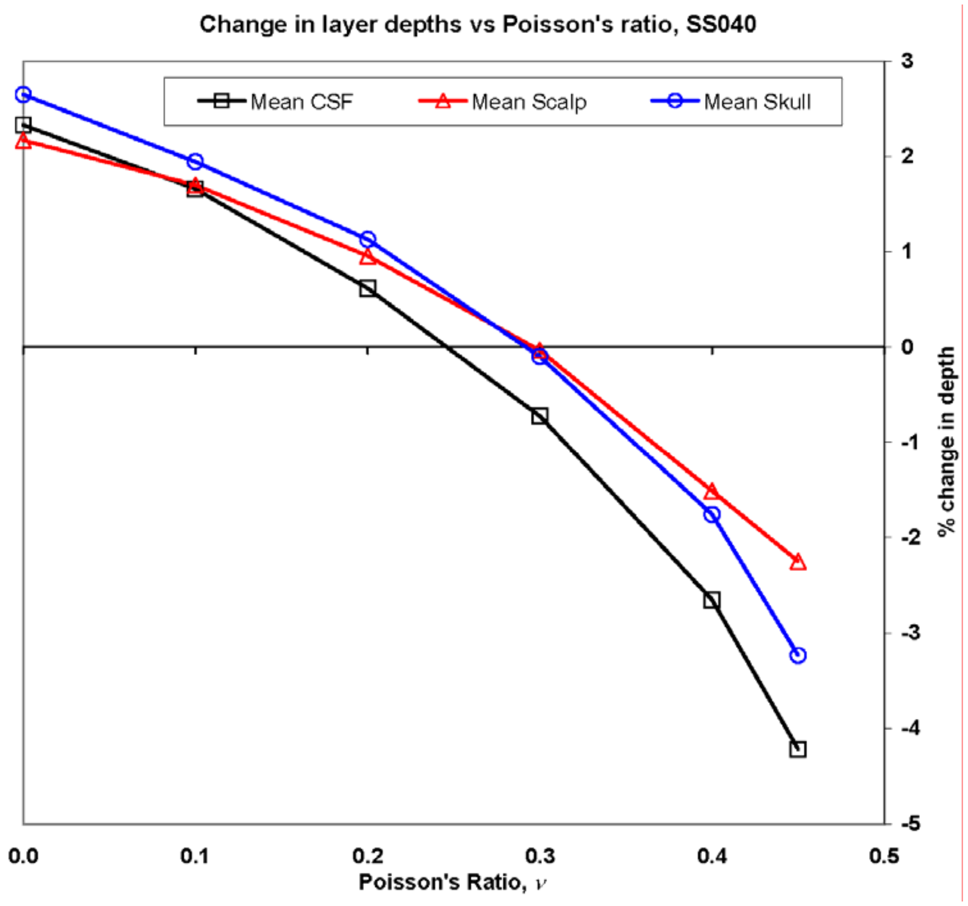

(a)

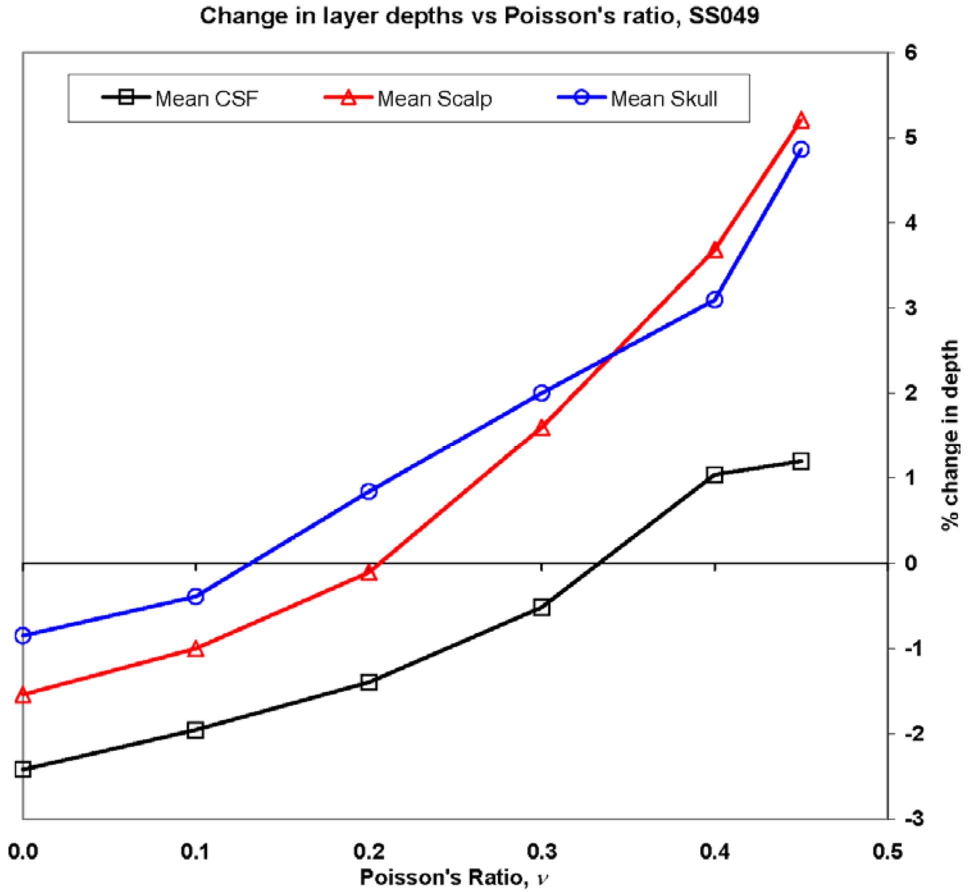

(b)

Figure 5.6: The relationship between Poisson's ratio, v, of all the materials and mean layer depths after warping (a) the 40001 element sphere and (b) the 49172 element adult head. The choice of the value of 0.3 is borne out.

5.4.2. Boundary Conditions

The results obtained by varying d_0 from 20 mm to 100 mm in steps of 20 are recorded along with the selection of one unique node being the furthest distance from the triangulated surface beneath the B-Spline patch. The effect of this on minimum element stretch is shown in Figure 5.7 as a comparison between the values before and after warping. In both cases, there is clear improvement in value of minimum stretch for $d_0 \geq 40$ mm. For the shelled sphere there is continued marginal improvement until $d_0 \geq 60$ mm. For the adult head a peak is indicated, within the limitations of the results, at around $d_0 = 40$, though there is marginal degradation in performance for values greater than this and appears to level off towards the maximum distance of 148.76 mm.

Mean shell depths show no particular trend across the range for either mesh. For the sphere, changes are within 0.9% for all layers and for the adult head they are within 2% for all layers. Solution times for both models are shown by the graph in Figure 5.8; the trend is a linear relationship between d_0 and solution time, though the change in time from $d_0 = 20$ to the maximum for the adult head is around 14 s and somewhat less for the shelled sphere. As this does not represent a significant degradation in performance, it is difficult to evaluate the optimum for this parameter. Thus further tests were carried out to assess the performance of the algorithm for different size meshes for varying values of d_0, these being the two extremes of mesh resolution or system size. The first was a low resolution shelled sphere comprising 8,439 elements and 1,610 nodes (SS008), the second being the adult head meshed to 131,672 elements and 24,688 nodes (SA132). Lateral views of SA132 before and after warping are shown in Figure 5.9 with d_0 set to maximum and $R_E = 10$. The minimum stretch results for both meshes are summarised by the graphs in Figure 5.10.

In both cases, improved minimum stretch values were observed for higher values of d_0. For SS008, little improvement was observed for $d_0 \geq 60$ but for SA132 there was a linear trend of improvement towards the maximum value of d_0. Furthermore, for values of d_0 less than around 67 mm, the minimum stretch was negative. Negative stretch values indicate an inversion or collapse of elements and hence an unacceptable distortion of the mesh geometry. These latter results are important in deciding the design criteria for the generic warping algorithm as they indicate that it is more advantageous from an element geometry standpoint to set d_0 to its maximum in all cases.

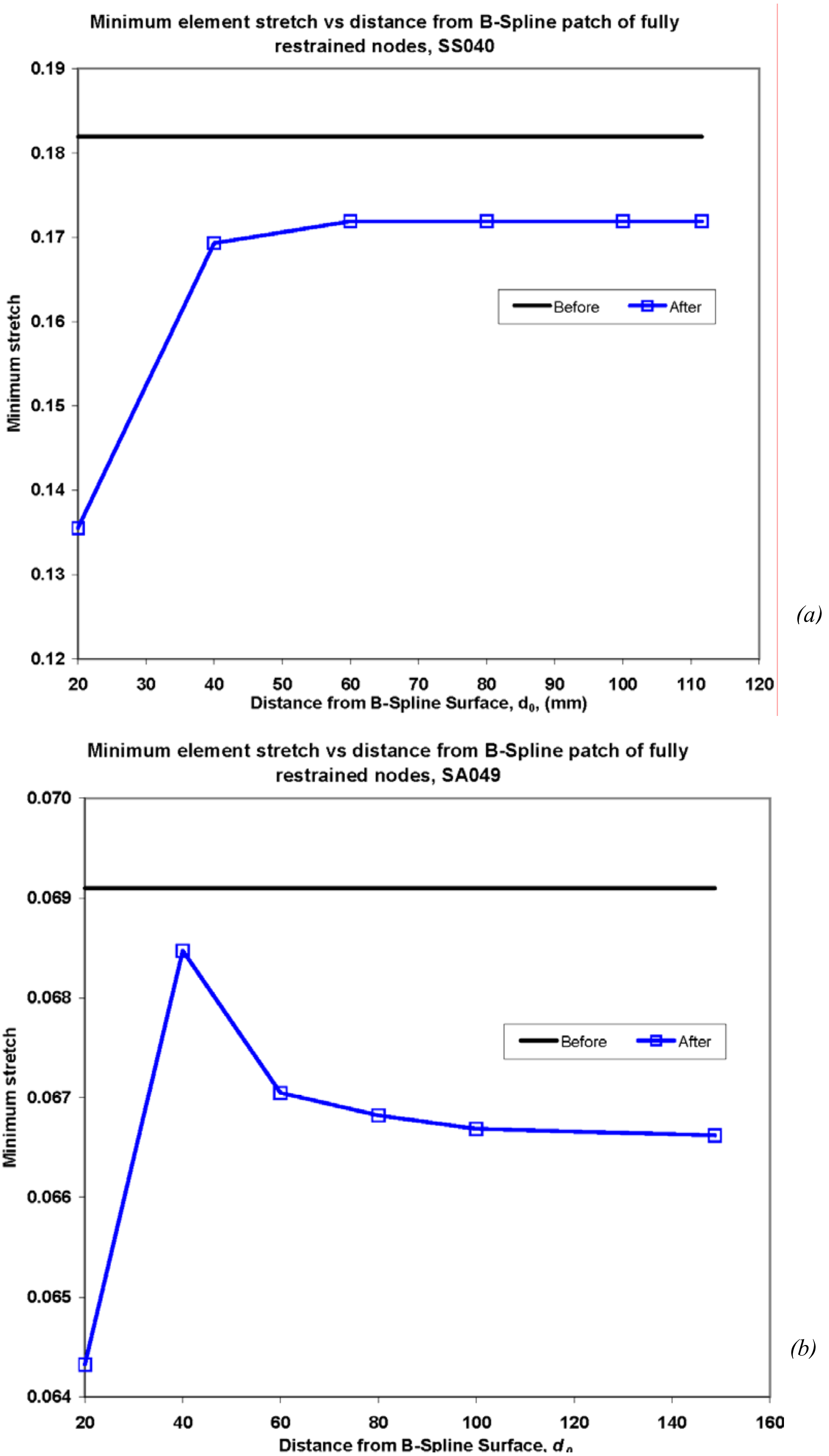

Figure 5.7: The relationship between distance between fully constrained nodes and the mesh surface beneath the B-Spline patch, d_0, and minimum element stretch before and after warping (a) the 40001 element sphere and (b) the 49172 element adult head.

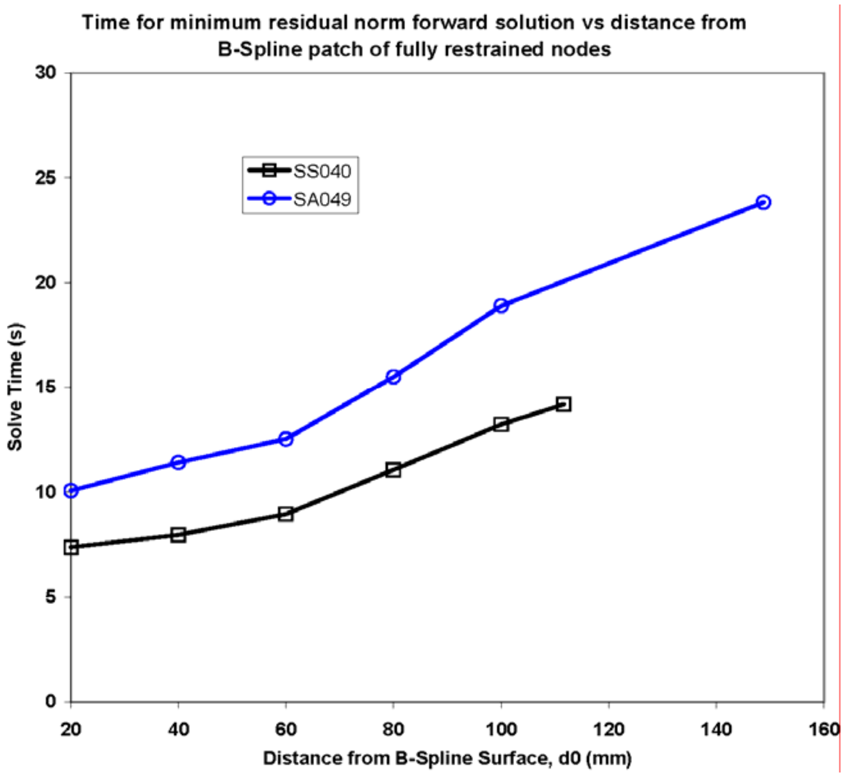

Figure 5.8: The relationship between the distance between fully constrained nodes and the mesh surface beneath the B-Spline patch, d_0, and forward solution time compared to that before warping the 40001 (SS040) element sphere and the 49172 (SA049) element adult head. The trend indicates a linear relationship.

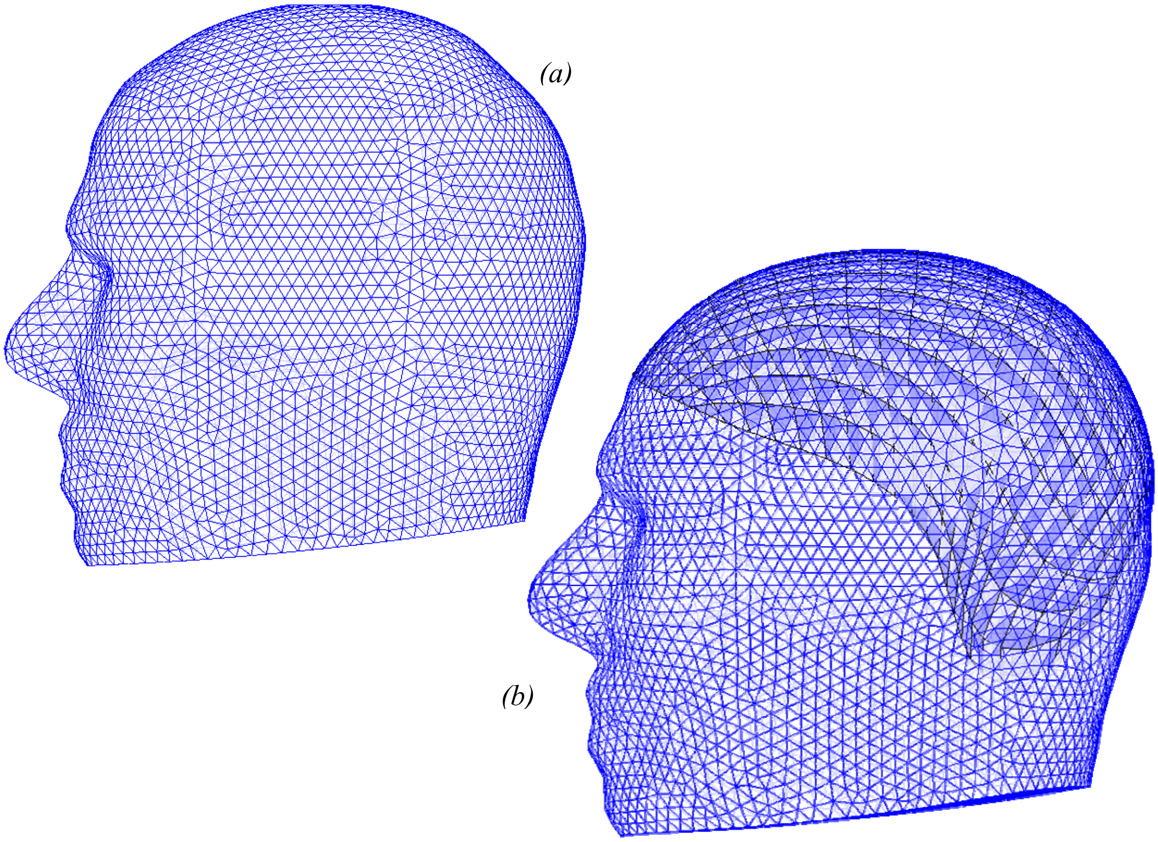

Figure 5.9: Side views of SA132 (a) before and (b) after warping with R_E = 10 and d_0 set to maximum.

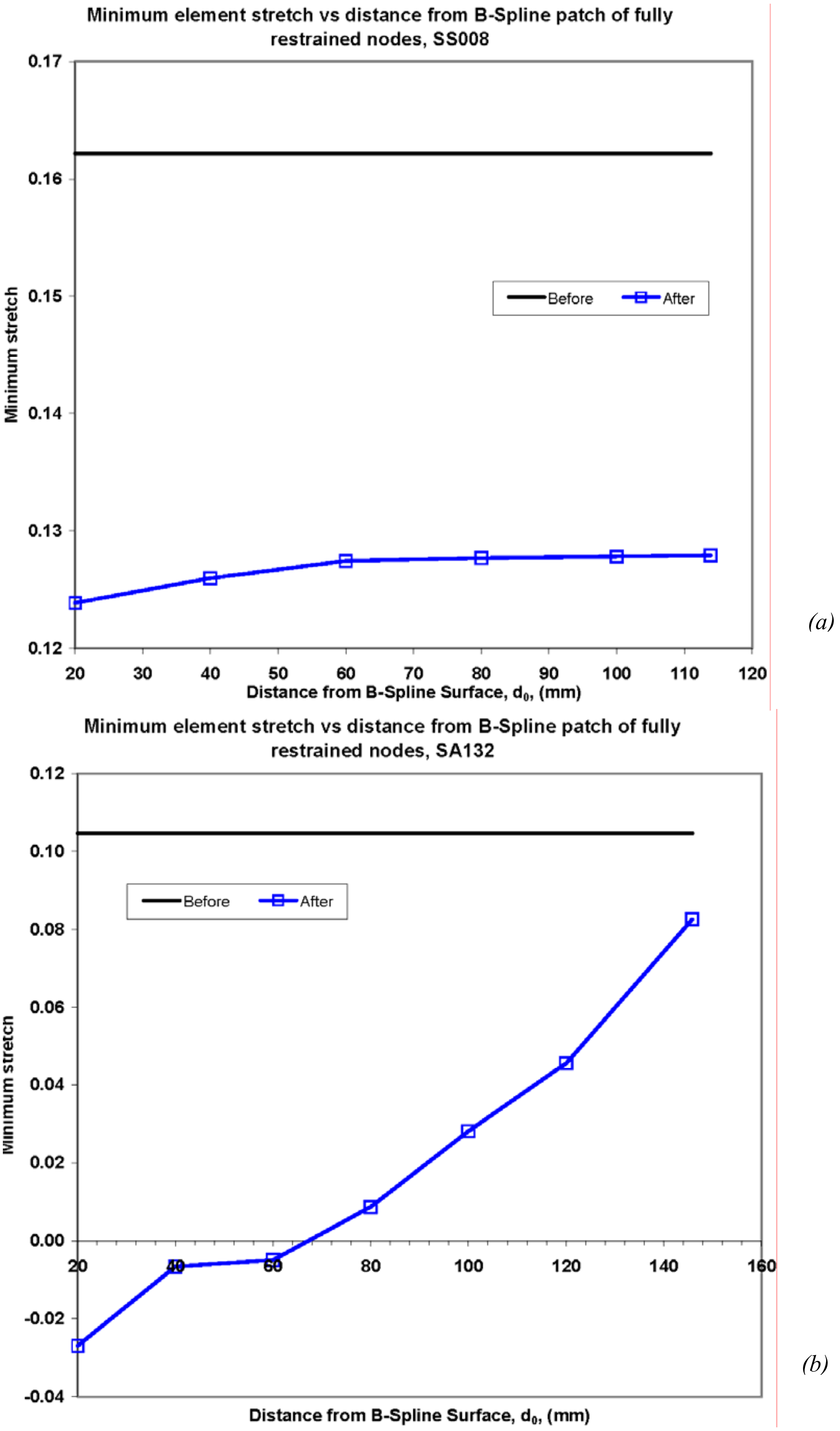

Figure 5.10: The relationship between distance between fully constrained nodes and the mesh surface beneath the B-Spline patch, d_0, and minimum element stretch before and after warping (a) the 8,439 element sphere and (b) the 131,672 element adult head. Values of $d_0 < 67$ show negative minimum stretch in the high resolution mesh.

5.4.3. Discussion of Optimum Values

The above results indicate that there are specific values of the parameters discussed in §5.3 that give optimum performance of the algorithm for minimum element stretch, layer depth change and solution time. Although it might be logical to assume that relatively higher stiffness values in the thin shells defining scalp, skull and CSF compared to that of brain would produce lower element distortions and smaller changes in layer thickness in the warped model, the results indicate that only marginal, if any, improvements are gained at the expense of significant increase in solution time. In fact, there is evidence to indicate that layer depth change is minimised with a stiffness ratio of around 10:1 and a value of Young's modulus of 0.3 for all materials gives satisfactory results. It is interesting to note the difference in trends in Figure 5.6 for how layer depths vary with Poisson's ratio for the warped sphere (SS040) and the adult head (SA049). There can be no conclusive explanation for this except to speculate that it is due to the thickness of the layers in the sphere being uniform by design whereas the thicknesses of the scalp, skull and CSF in the adult head models are non-uniform.

The results pertaining to the choice of the boundary condition scheme seem to favour one where the only fully restrained node is that furthest from the triangulated surface defined by the nodes orthogonally projected to the B-Spline patch. While it could be argued that minimum stretch is optimised for both SS040 and SA049 at around d_0 = 60 mm for solution time, further investigation across a range of mesh sizes indicate that there are significant improvements to be gained for choosing the unique furthest node criterion. This is particularly so for the high resolution shelled adult head that was tested where severe element collapse and inversion occurs, as indicated by negative minimum stretch values, with lower values of d_0.

Thus a summary of preferred values of algorithm parameters can be stated and in shown in Table 5.1.

Table 5.1: Summary of warping algorithm parameters

Parameter	Description	Value
R_E	Ratio of Young's modulus of scalp, skull and CSF to brain	10
v	Poisson's ratio	0.3
d_0	Minimum distance of surface nodes from deformed nodes to be fully restrained	Unique node at maximum distance

The results obtained are largely limited to the particular meshes of the sphere and adult head used for the tests. These have a fairly high resolution of around 40,000 to 50,000 elements though it would not be unreasonable to assume that the results are typical across a range of mesh resolutions. The fact that the tests using a low resolution sphere and a high resolution adult head produced satisfactory results support this assumption.

5.5. Geometric Evaluation

Having established a generic set of optimum parameters for the algorithm, the evaluation of the geometric performance can be tested. This section describes further tests carried out using these values on a range of shelled sphere and adult head meshes of varying resolutions.

5.5.1. Evaluation Meshes

A number of meshes of different resolutions were generated in I-DEAS for both the shelled sphere and shelled adult head. The number of elements and nodes generated in a finite element mesh can be controlled relatively easily in I-DEAS by adjusting the global element length parameter prior to meshing. An example of this effect can be seen in Table 5.2 which lists the shelled sphere meshes generated along with the global element length, element stretch characteristics and the identification of the resulting mesh.

Table 5.2: Summary of shelled sphere meshes

Global Element length (mm)	No. Elements	No. Nodes	Stretch					Model Identification
			Min	Max	Median	Mean	Standard deviation	
20	8439	1530	0.151	0.955	0.515	0.484	0.199	SS008
16	13881	2548	0.199	0.961	0.607	0.560	0.192	SS014
14	17604	3217	0.204	0.958	0.606	0.578	0.178	SS018
12	25898	4767	0.236	0.969	0.620	0.611	0.153	SS026
10	40001	7311	0.182	0.972	0.631	0.638	0.126	SS040
8	63370	11714	0.138	0.977	0.658	0.669	0.096	SS063
7.5	78951	14395	0.226	0.986	0.673	0.681	0.099	SS079

In addition to these models, that described and used in §3.4, SS030, comprising 29832 element and 5586 nodes can be added to the list.

A series of meshed shelled adult heads has also been generated as summarise in Table 5.3. Because of the increased complexity of geometry in the human head solid model, it is not possible to produce viable meshes with less than around 27,000 elements. This is demonstrated by the fact that the minimum stretch for SA028 is very low at 0.0018 and there are more than 100 elements with a stretch value less than 0.1. It could be argued that this mesh is bordering on unacceptable with quality statistics of this nature, though many more tests will need to carried out with EIT reconstruction to assess the extent of the effects of this. For the remainder of the meshes, there are less than 40 elements with stretch below 0.1 with quality increasing with system size.

Table 5.3: Summary of shelled adult head meshes

No. Elements	No. Nodes	Stretch			Model Identification
		Min	Max	Mean	
27684	5226	0.0018	0.9641	0.6025	SA028
31111	5939	0.0257	0.9770	0.6605	SA031
35073	6556	0.0254	0.9781	0.6310	SA035
49172	9142	0.0691	0.9815	0.6572	SA049
77196	14188	0.0570	0.9869	0.6752	SA077
131672	24688	0.1046	0.9896	0.6794	SA132

5.5.2. Method

The above meshes were subjected to warping, using the phantom tank patient position file as the target with the parameters listed in Table 5.1. The values recorded before and after warping were: minimum, maximum and mean stretch; quantity of elements with stretch values below 0.1, 0.2, 0.3 0.4 0.5 and 0.6; mean layer depths for scalp, skull and CSF orthogonally beneath the B-Spline patch; execution times for projecting nodes to the B-Spline patch, building the stiffness matrix (§5.2.1) and forward solution for minimum residual norm. The meshes for spheres and adult head were dealt with separately.

5.5.3. Results and Discussion of Geometric Evaluation

The effect on minimum stretch for the shelled sphere meshes is depicted in Figure 5.11(a) as minimum stretch versus number of elements before and after applying the warping algorithm. While no perceivable trend is noted it can be seen that the change in minimum stretch across the range represents a minimal degradation of element quality resulting from the warping process. The average change in mean stretch across the whole range represents a drop of 4.2% with a range from 4.0% to 4.5%. This compares quite favourably with the result recorded in §3.6.1 for warping a shelled sphere to an ellipsoid – a drop of 3.8%. As the shelled spheres in this set of experiments were affinely scaled to ellipsoids before projecting surface nodes to the B-Spline patch and warping, the actual warping process contributes very little to mean stretch change.

A similar set of results for the adult head meshes is depicted in Figure 5.11(b). There is a trend here that minimum stretch generally improves with system size, as would be expected. The elements with small stretch values in the adult head are likely to be in the areas where geometry detail is fine and shell thicknesses small. Meshing more finely in these areas is likely to generate elements with better geometry. Minimum values after warping the adult head meshes indicate no significant change in element quality; in fact, for a few cases, there is a small improvement in the value of minimum stretch.

The above results are borne out by examination of the change of the profile or distribution of stretch values across the range of models. The change in the frequency of elements with a stretch below 0.6 for both classes of model, and all values up to 0.6 in steps of 0.1, is displayed in Figure 5.12. The benefit of such a set of results is to indicate what quantity of elements, as a proportion of the mesh, degrades in quality. The mean stretch for meshed spheres ranges from 0.48 to 0.68 and the trend is that it increases logarithmically with system size (number of elements). For the adult head the range is much smaller being from 0.60 to 0.68 with no specific trend arising from the range of system sizes used. Therefore the increased frequency of a model's elements with stretch below 0.6 gives an indication of the degradation in quality throughout the whole finite element mesh.

For the spheres, it can be seen that there is a significant increase of greater than 5% of the model's elements to stretch values less than 0.3 for the lower resolution meshes and to less than 0.5 for those of higher resolutions. This demonstrates the effects of the more severe deformation undertaken to warp a sphere to the shape of a human head. Nevertheless, the outcome is a set of meshes whose stretch profiles are still of an acceptable level of quality as witnessed by the minimum stretch value and the fact that even in the worst case of the lowest resolution, SS008, no elements are distorted to stretch value of less than 0.1.

The results for the adult head meshes show that the change in stretch distribution profile is modest in all cases, the worst case being less than 3% of a model's elements being degraded to a value of less than 0.6. On the whole there is very little degradation of mesh quality, as indicated by a decrease in mean stretch of around 1.2% for SA031 and less than 0.7% for all other models. This can be readily explained by the fact that the deformation is far less severe when warping from a model already human head-shaped to another of roughly similar geometry.

Execution times for both sets of results are shown in Figure 5.13. The interesting detail to note from these results, for which no explanation is forthcoming, is that for the spheres, the trend is that execution times are linear with system size whereas for the adult head models, it is exponential with a low power index of around 1.6×10^{-5}. However, execution times across the whole set of meshes are not excessive and some savings could be made by reducing overheads due to results gathering or by improvements to the forward solution method used.

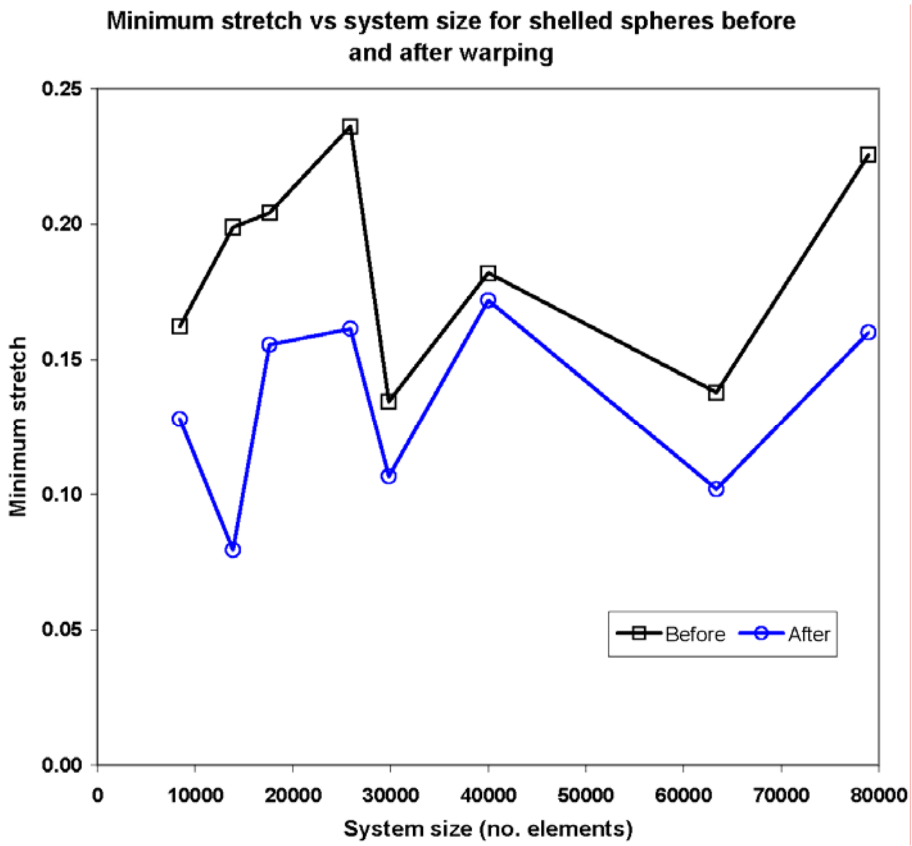

(a)

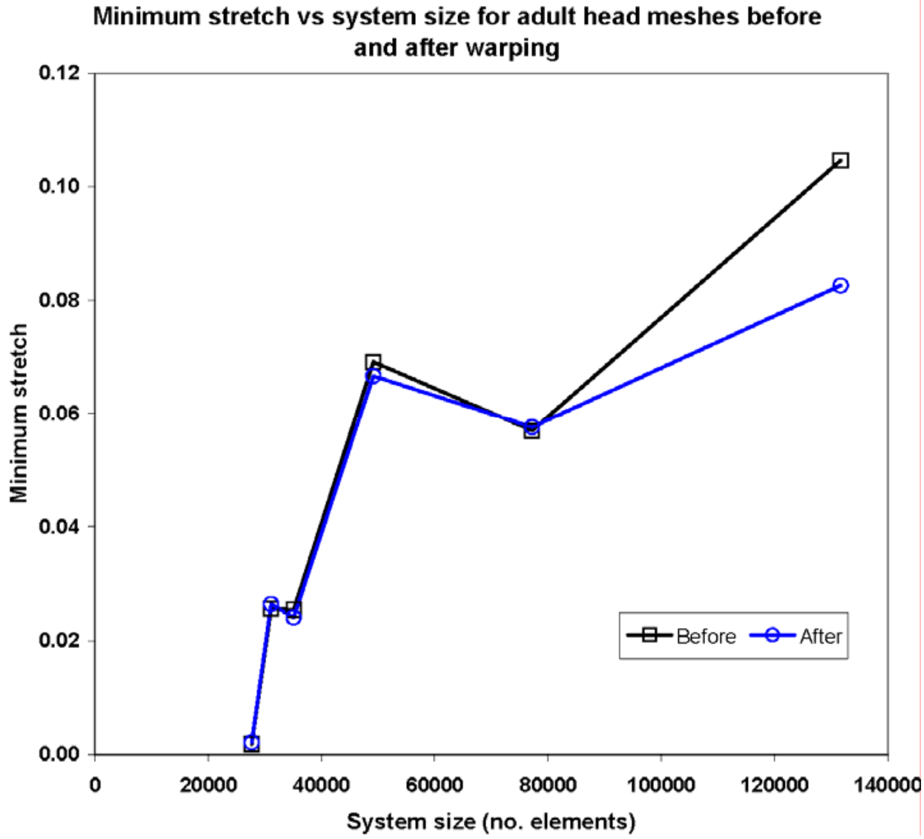

(b)

Figure 5.11: The relationship between minimum stretch and system size after (a) warping the shelled spheres and (b) the adult head models. There is no perceivable trend for the spheres though the degradation of minimum element quality is minimal. There is an expected increase of mesh quality for higher resolution adult head meshes and changes in minimum stretch represent very little in the way of quality degradation through warping.

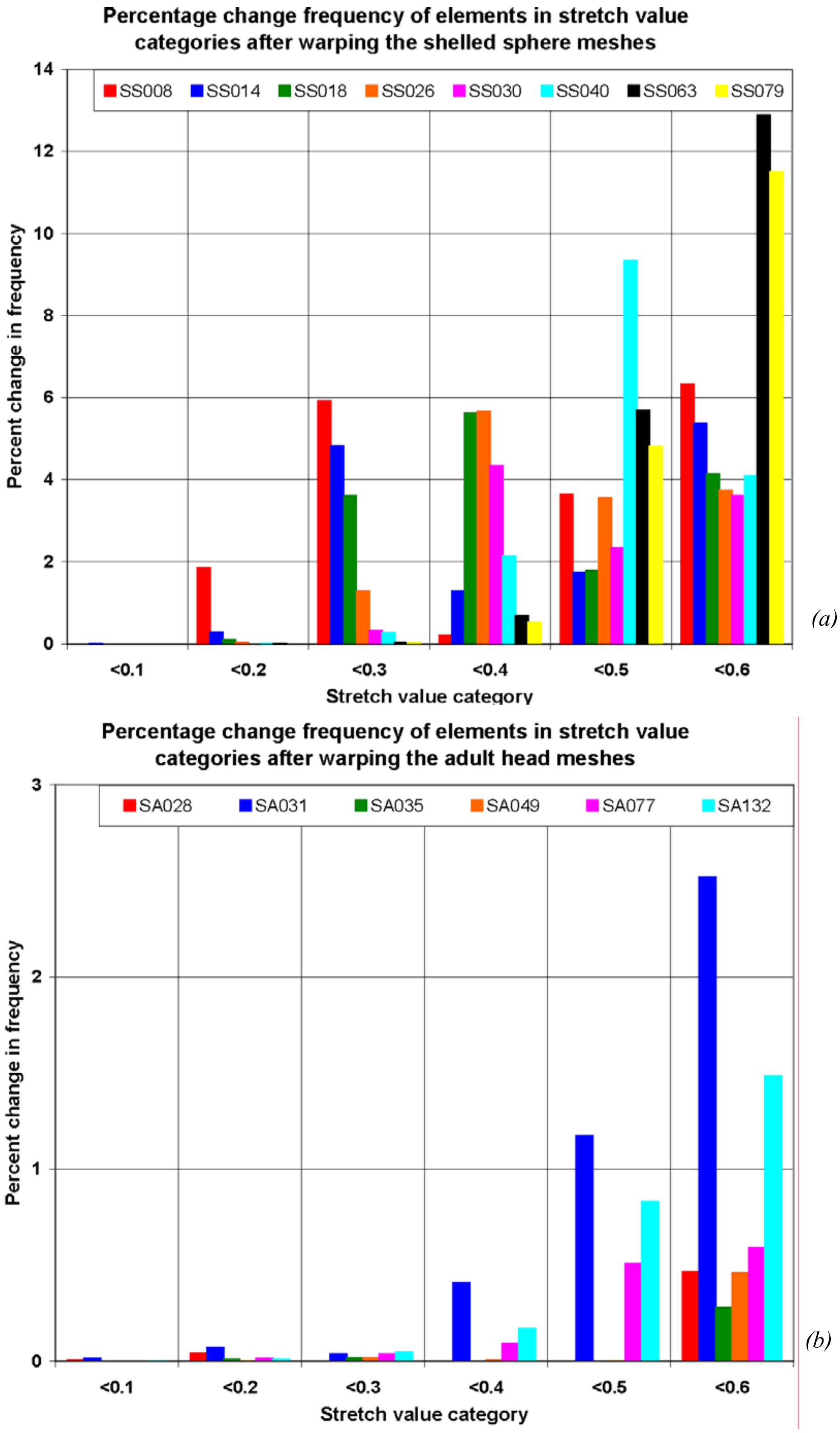

Figure 5.12: The change in stretch profiles after (a) warping the shelled spheres and (b) the adult head models. A significant change in the profile is noted for the spheres though very little for the adult head models.

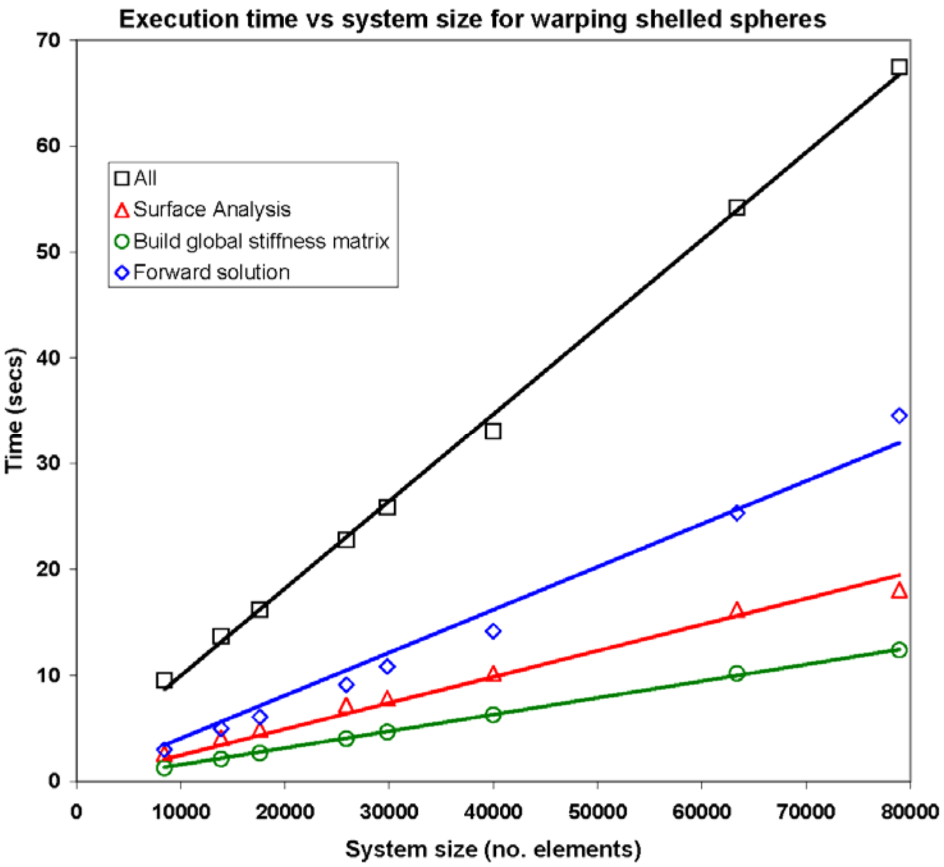

(a)

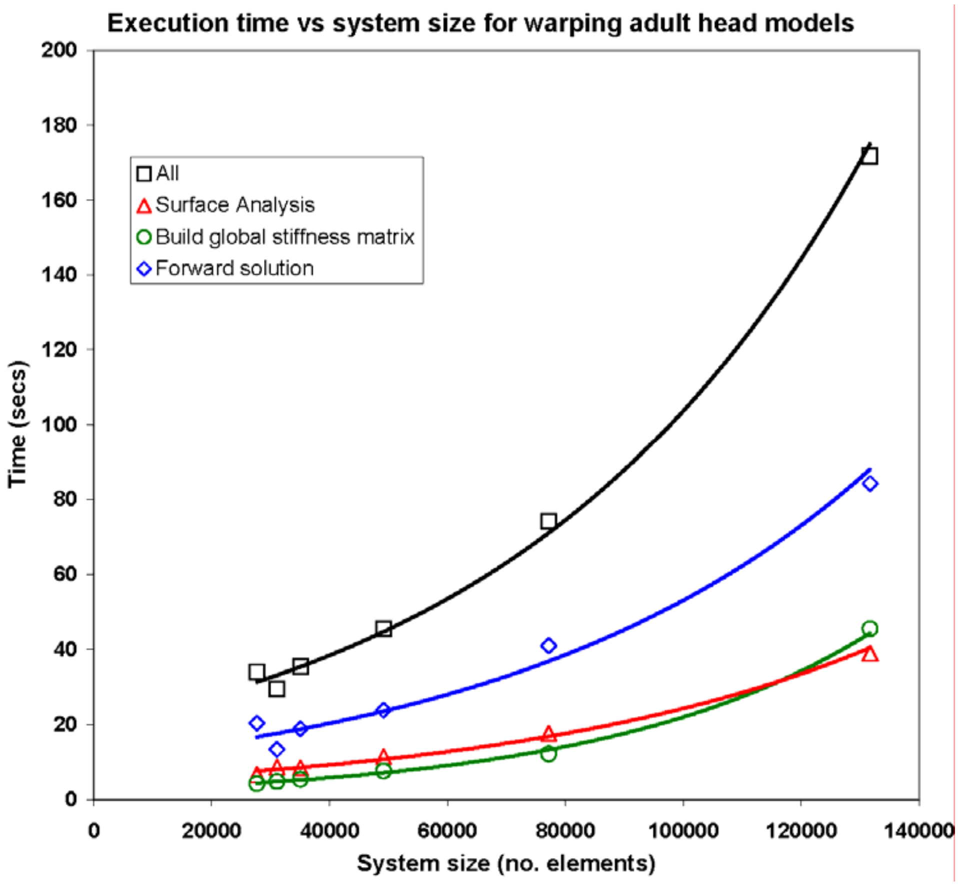

(b)

Figure 5.13: Execution times overall and for various stages of (a) warping the shelled spheres and (b) the adult head models. Execution times are not excessive though improvements, particularly for the forward solution, could be investigated.

5.6. General Discussion and Conclusions

The foregoing analysis and experimentation has demonstrated that it is possible to deform a finite element model of the human head such that the surface under the electrodes is geometrically similar, to within the accuracy of the surface generation techniques, to a target subject. While the approach used to achieve the warping of the whole model is based on well established methods, it represents a novel application of the techniques.

5.6.1. Justification of Approach

In terms of classical stress analysis, such a method would not be used where such relatively large deformations are applied. The methods are only valid for evaluating stresses and displacements of a model where such displacements, and hence strains, are small. This is because the stiffness matrices for the individual elements, which are subsequently assembled into the global stiffness matrix, are based upon the shape functions, which are in turn based upon element geometry. Large displacement, and hence possibly significant element deformation, will result in a new element geometry that will render the original shape functions invalid. Such a condition of large displacement requires the application of a non-linear solution approach (Adams and Askenazi, 1999) involving iterative steps towards a final solution. The facts that, in this case, the boundary conditions comprise displacements as opposed to loads and that evaluation and significance of internal stresses is unimportant validate the use of a linear solver for the warping algorithm.

It is also well known that the use of linear tetrahedral elements for stress analysis is prone to significant errors in the results (Mottram and Shaw, 1996) and quadratic elements with mid-side nodes are normally recommended. Such treatment leads to large global stiffness matrices (equation (5.25)) and is unnecessary for the purpose of mesh warping as accurate evaluation of internal stresses is unimportant. The above results show that the use of the linear tetrahedral structure generated for normal EIT reconstruction produces acceptable results from a purely geometric point of view.

The results of the evaluation in the previous section support these assertions. Warping the shelled spheres represent a more severe case of deformation than for the adult head and so the outcome results in greater degradation of mesh quality in terms of minimum and mean stretch as well as the reduction in stretch across the whole mesh. Even so, for the most part, the warped shelled sphere models comprise element quality characteristics well within acceptable bounds.

5.6.2. Improving Execution Time

Execution time of the algorithm is also acceptable and there is a general conformity between the two model types. The major contributor to the overall execution time is the forward solution for which the minimum residual norm method has been chosen in this case. It could be argued that the only criterion for the selection of matrix inversion technique for the solution of equation 5.25 is the execution time. As previously indicated in §5.2.2, little difference in time or relative residual was noted between using the minimum residual norm, symmetric LQ and preconditioned conjugate gradients with incomplete Cholesky factorisation. Horesh *et al* (2005b) have carried out tests on using a number of methods for the forward solution in EIT and optical tomography and have noted that significant improvements in computational demand can be made by using a multi-level inverse based incomplete LU preconditioner to a simplified quasi minimum residual solver. It is also suggested that for this type of solution incorporating the use of real values only, benefits could also be reaped from using Algebraic Multi-Grid (AMG) preconditioners (Soleimani *et al*, 2005).

5.6.3. Procedure Summary

The complete warping process can be summarised as follows:

The warping function coded in MATLAB (*Warper*) takes a series of parameters as input: the list of node coordinates and elemental connectivity list of the source mesh, the patient position file (coordinates of registration points and electrodes) of the target mesh, the list of coordinates of registration points for the source mesh, a structure defining material properties of the elements in the mesh and the minimum restrained node distance d_0 (§5.3.3), which for maximum distance criteria is set to -1. The procedure undertaken is then:

1. Align the electrodes in the patient position file with the registration points of the source according to §4.2.1

2. Parameterise the electrode positions as described in §4.2.2, and generate the B-Spline surface patch to within a tolerance of 0.1 mm (§4.3).

3. If required for testing and evaluation purposes, evaluate the stretch characteristics for the mesh prior to the warping phases.

4. Analyse the interaction of the B-Spline surface patch and the source mesh by projecting mesh surface nodes to the patch. Isolate those surface nodes that project orthogonally to the patch to generate a triangulated surface section of the mesh. Prior to this the mesh is affinely scaled such that the source and target registration points are aligned.

5. If required for testing and evaluation purposes, evaluate the layer depths of nodes that can be orthogonally projected to the triangulated surface mesh beneath the B-Spline patch.

6. Define the boundary conditions to include those nodes isolated in (4) plus those that meet the distance criterion to be designated as fully restrained.

7. Build the stiffness matrix, define and solve equation (5.28). This yields the evaluation of all nodal displacements, **d**, which are added to the coordinates of the nodes of the source mesh to generate the warped mesh.

8. If required for testing and evaluation purposes, evaluate the stretch characteristics and the layer depths for the warped mesh.

9. Display the results if required.

6. VALIDATION OF WARPING ALGORITHM

The algorithm described in the previous Chapters successfully modifies finite element models such that the boundary surface defined by the electrode array closely conforms to that of the target subject. Optimising the parameters for the warping algorithm generates meshes of equally good quality whilst maintaining the geometric integrity of the target's anatomical detail to within acceptable bounds. The true test of the success of this approach is whether the forward solution of the warped model and reconstruction of conductivity changes within it correlate to those of the target. This Chapter describes tests undertaken to carry out this comparison and the results of those tests, leading into a more detailed evaluation, discussion and conclusions in the next Chapter.

The validation requires the acquisition of data from conductivity changes within a model of the human head to establish a number of criteria. It is hypothesised that more accurate boundary geometry will improve reconstruction image quality and localisation of conductivity changes within the domain. Data were acquired from two sources. Simulated data were generated from forward modelling conductivity perturbations within a finite element model of the head-shaped phantom as well as data acquired in the laboratory from a similar experiment using the actual phantom. This latter dataset was the same used in previous work carried out by the group at UCL and presented by Liston (2003) and Bagshaw *et al.* (2003).

6.1. Methods

6.1.1. Simulated Data

The generation of the surface model of the head-shaped tank is described in §2.2.2. This model was further modified by defining the actual electrode positions acquired from the CT scan described in §4.4. Cylinders were generated, centred to the electrode positions and orientated such that their axes were normal to the head surface at each electrode site. The cylindrical surface geometry was then used to split the scalp surface in I-DEAS. This had the effect that when the model was meshed, the electrode sites were separately triangulated resulting in more accurate electrode position and geometry. As with all previous FE models, meshes were exported as universal files and imported to *GraphEIT* where electrode faces were added and access to all relevant EIDORS tools made available. Figure 6.1 shows a mesh generated in this manner consisting of 30650 elements and 6030 nodes and designated TA031EL. Internal geometry is defined to represent the skull and the saline solution consisting of 8130 and 22520 elements respectively.

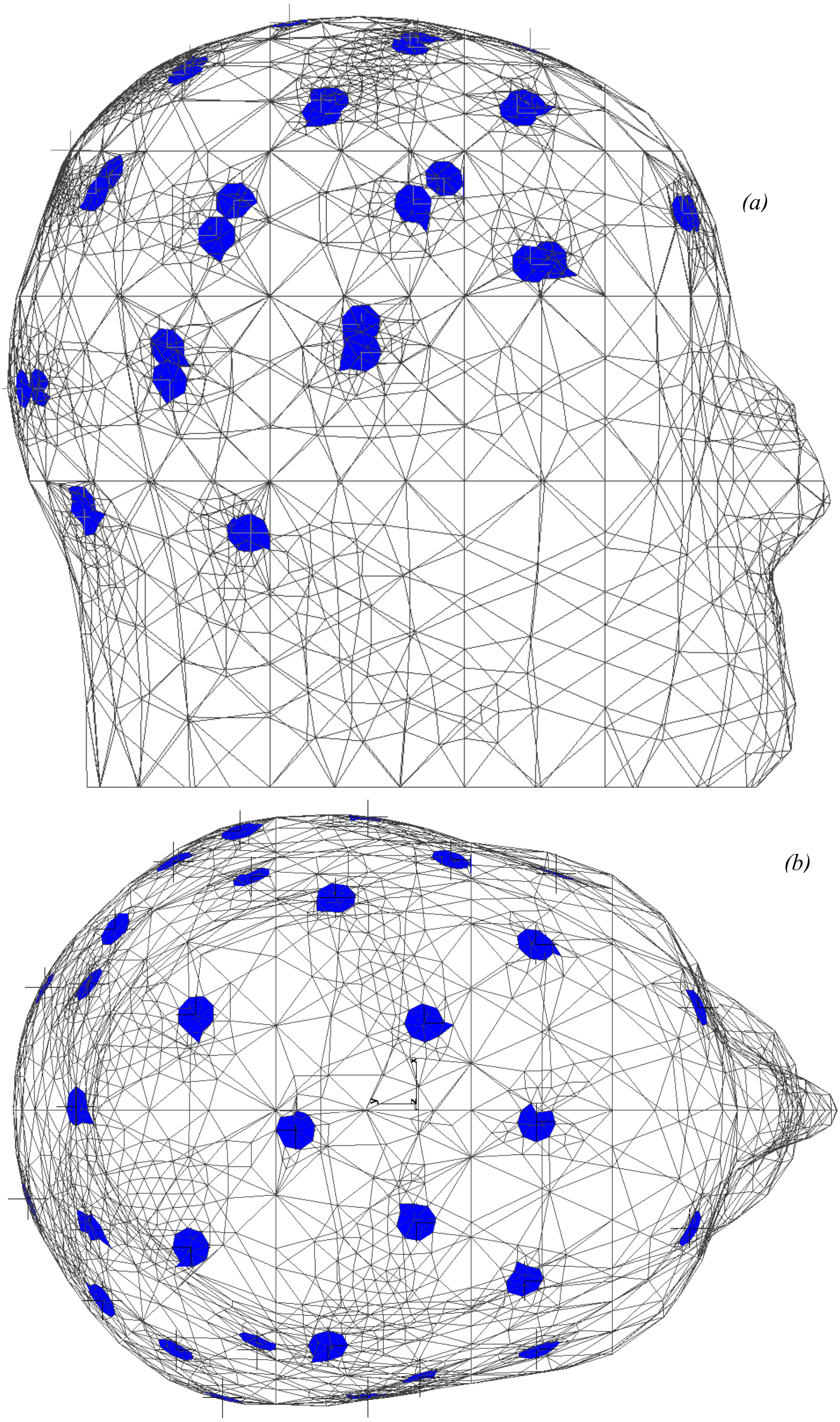

Figure 6.1: Wireframe images of the finite element model of the tank phantom with electrodes: (a) right view and (b) top view.

Conductivity perturbations were defined in the model in the same manner as described in §3.3 in the horizontal *x* direction from -50 mm to + 50 mm in steps of 10 mm with both the *y* and *z* values set to +20 mm. Being roughly spherical, the radii of the perturbations were set to ensure that they were volumetrically equivalent to around 10 mm. In fact the mean value of the eleven radii was 9.9 ± 0.7 mm. The actual coordinate positions of the centres are recorded in Table 6.1.

Table 6.1: Summary of perturbation positions in TA031EL

	Actual Positions		
Desired *x* position	*x*	*y*	*z*
-50	-44.6	19.7	19.0
-40	-39.2	18.9	18.8
-30	-27.1	18.7	21.2
-20	-21.1	15.3	18.8
-10	-10.5	14.9	19.4
0	3.7	15.5	21.7
10	9.2	16.5	22.7
20	24.2	17.2	22.2
30	29.3	18.6	22.1
40	36.6	19.4	21.2
50	46.0	18.3	17.8
Mean		*17.5*	*20.4*
Standard Deviation		*1.7*	*1.7*

The conductivity of the perturbations was set to match that of an insulator such as Perspex (10^{-5} Sm^{-1}) so that the experiment would numerically match that of the head-shaped phantom. The conductivity priors were also set to match the same phantom as reported by Liston (2003) and Tidswell *et al.* (2001) to be 208 ± 2.1 Ωm for the skull, evaluating to 0.0048 Sm^{-1}, and 2.37 ± 0.02 Ωm for the remainder of the model, evaluating to 0.422 Sm^{-1}. The latter was the measured conductivity of the saline solution used in the tank experiments.

6.1.2. Head-Shaped Phantom Tank Data

The data from the head-shaped tank was the same used by Adam Liston in his thesis cited above. A narrow piece of doweling was inserted through the foramen magnum (Figure 6.2) from which was suspended a cylinder of Perspex measuring 20 mm in length and diameter to model conductivity perturbations at various positions. Data were measured using a Hewlett-Packard 4284A-based EIT system delivering a current of 1-3 mA at 10 kHz using a baseline/stimulus/baseline paradigm (Tidswell *et al*, 2001). A number of experiments were carried out for each position of the Perspex cylinder and the mean baseline and stimulus boundary voltages evaluated. Any channels with high levels of noise or drift were set to zero and the doweling was present throughout the baseline and stimulus epochs.

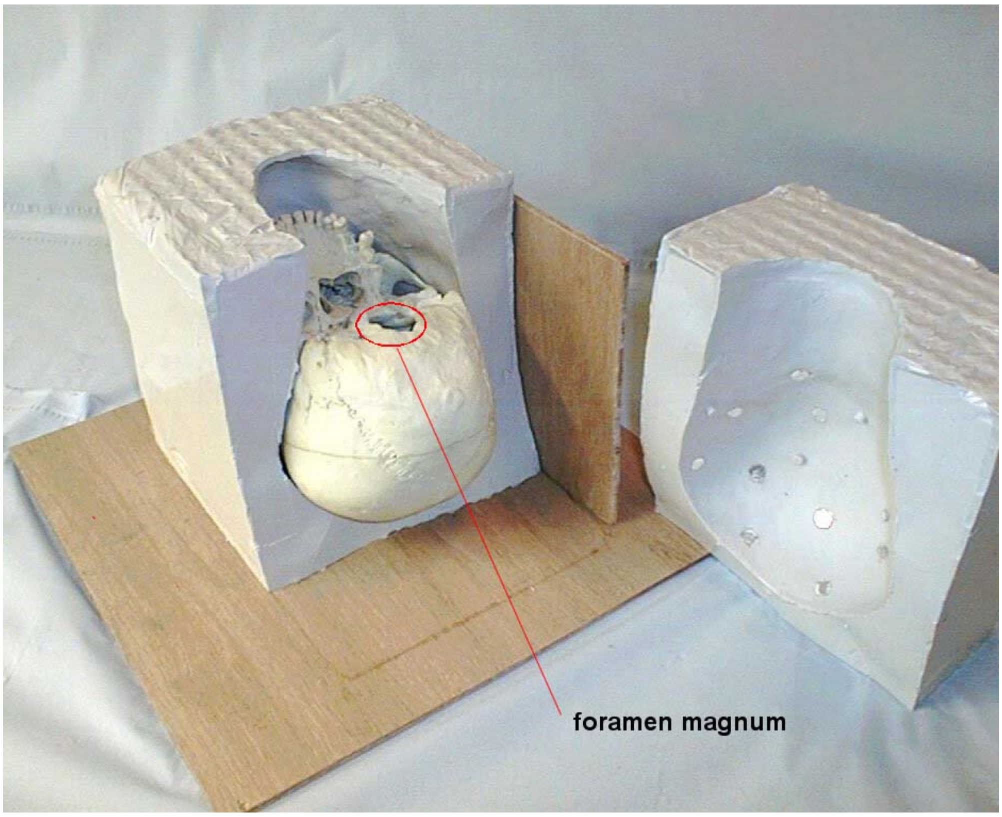

Figure 6.2: The head shaped tank phantom shown with the two halves separated and a human skull inside.

The cylinder was centred at positions in x from -45 mm to + 45 mm in steps of 10 mm with y = 43 mm and z = 2 mm relative to electrodes 13 and 17: a total of 10 positions. This equates to approximately y = 55 mm and z = -6.4 mm for the finite element models used and in the x direction, the difference between the origins of the tank and the FE models is around 1 mm. Typical noise was measured to be 0.04 % or a signal to noise ratio (SNR) of around 70dB.

6.1.3. Target Models

For both the simulated and tank data the target models represented a range to investigate the effectiveness of the warping algorithm. Four base models are summarised in Table 6.2: a tank model with accurate electrodes, a tank model without specific electrode modelling, a shelled sphere and a shelled adult head. The sphere and the adult head were both used with a simple affine warping to the basic dimensions of the tank and with elastic warping using the algorithm described in the previous Chapter. The reconstruction of the simulated data on the first mesh represents an *inverse crime* (Colton and Kress, 1998), which is the use of the exact same model for forward and inverse solutions. It is included for completeness and should give a basis of comparison for the other reconstructions.

Table 6.2: Summary of target meshes

No. Elements	No. Nodes	No. Elements in Skull	Model Identification	Description
30650	6030	8130	TA031EL	Tank with accurate electrode positions and size
41314	7384	11201	TA041	Tank without accurate electrodes
40001	7391	8467	SS040w	Shelled sphere affinely warped to tank dimensions
			SS040e	Shelled sphere elastically warped to tank
35073	6556	9152	SA035	Shelled adult head not warped
			SA035w	Shelled adult head affinely warped to tank dimensions
			SA035e	Shelled adult head elastically warped to tank

6.1.4. Boundary Voltage Data

For all of the models, a forward solution at baseline was carried out. For TA031EL, this was a consequence of generating the simulated data as the first measurement cycle is always the baseline for linear solutions. For the other meshes a baseline measurement was generated in all warped states. The boundary voltages for the latter were normalised to those of TA031EL by offsetting by the differences in the least squares fit through the data and scaling. The point of the exercise was to give a comparative measure of the correlation of the boundary voltages before and after warping.

6.1.5. Reconstruction of Conductivity Perturbations

The images were reconstructed for both simulated and tank data on all models using the slicer plot in *GraphEIT* described in Chapter 3. For the reconstructions of all models a sensitivity matrix was generated and inverted using singular value decomposition truncated to 40 values. For all models, this evaluated to a ratio of 0.2 % to 0.4 % of the smallest to the largest value; the only exception being for TA041 where the ratio was 0.05 %.

Image quality was noted from a purely subjective point of view. A number of criteria could be considered important the most important of which are the clarity of the reconstructed perturbation and the presence of artefacts in the brain region of the image. It is expected that there would be some significant noise outside the brain region, particularly in the lower regions of the models which are remote from the electrodes. Bagshaw *et al.* (2003) describe a method of evaluating reconstructed images based on the subjective judgement of two assessors based on knowledge of the perturbation position and the level of noise in the image. The evaluation here is based on a largely similar subjective approach, though the method of generating images is somewhat different and the subsequent analysis reduced to that of the author. The images generated in this thesis are the raw slicer plots as described in Chapter 3 whereas in the work previously cited, the images are generated using a MATLAB utility, *nim*, written by Dr Tom Tidswell of the UCL group. In *nim*, the images are rasterized from the domain volume and subjected to a polynomial smoothing. The purpose of carrying out any image quality analysis for this thesis is to establish whether elastic warping has a visible effect on image integrity.

Also localisations of the conductivity decreases caused by the Perspex were measured and checked against the ideal positions. Depending on the target used, there was a range of difficulty in establishing the position and so a consistent approach was adopted to ensure a valid comparison across the models. For each image the colour bar resolution was set so that a clear volume of conductivity decrease could be identified and the aperture size set so that the approximate centre of the area could be established as illustrated in Figure 6.3.

For most images a colour bar resolution of five was most appropriate. The aperture was then set to 30 mm so that the nearest local peak to within 15 mm of this approximate centre could be identified. This initial aperture size represents around two to three element widths for the range of mesh resolutions used. Upon finding the local peak, *GraphEIT* truncates the image so that the colour bar range lies between the peak conductivity found and zero. For the conductivity decreases expected from the experiments, the range was from a negative value to zero as seen in Figure 6.4. The aperture can then be positioned to identify the centre of the volume shown and adjusted in size so that encompasses the area to within 50% of the peak in the *xy* plane thereby giving the full-width half-maximum (FWHM).

To quantify the accuracy of the localisation of the perturbed volumes, measured position is correlated to actual position in the *x* direction to establish a least squares correlation. An additional measure used is to evaluate the mean absolute deviation of the measured position to that of the actual perturbation in all three orthogonal directions.

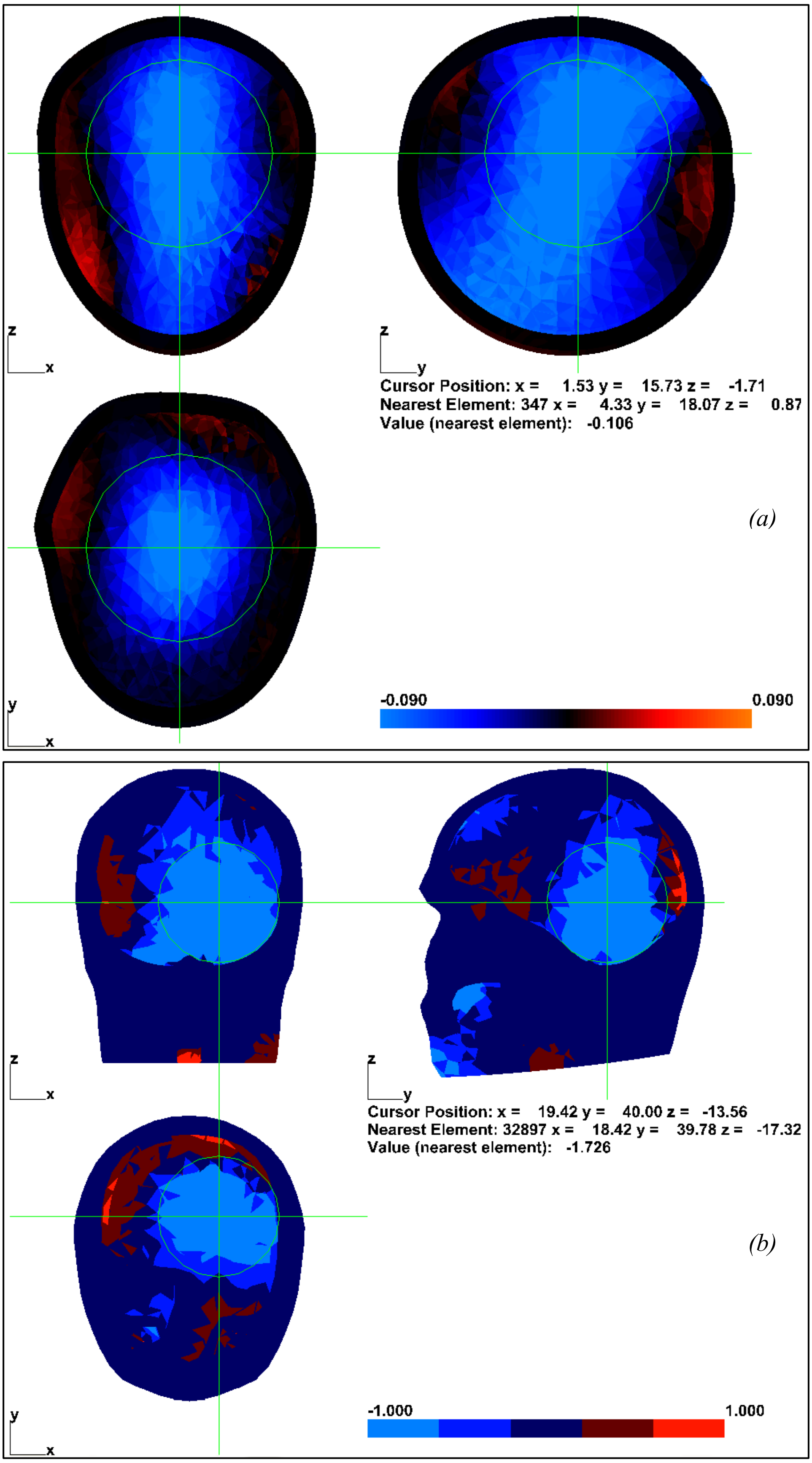

Figure 6.3: Raw images of perturbation 7 for (a) simulated data on SS040e and (b) tank data on SA035. Colour bar resolution is set so a clear area of conductivity decrease could be identified and the aperture set so that an approximate centre could be established. Aperture was then decreased so that the nearest peak to within 15 mm could be localised.

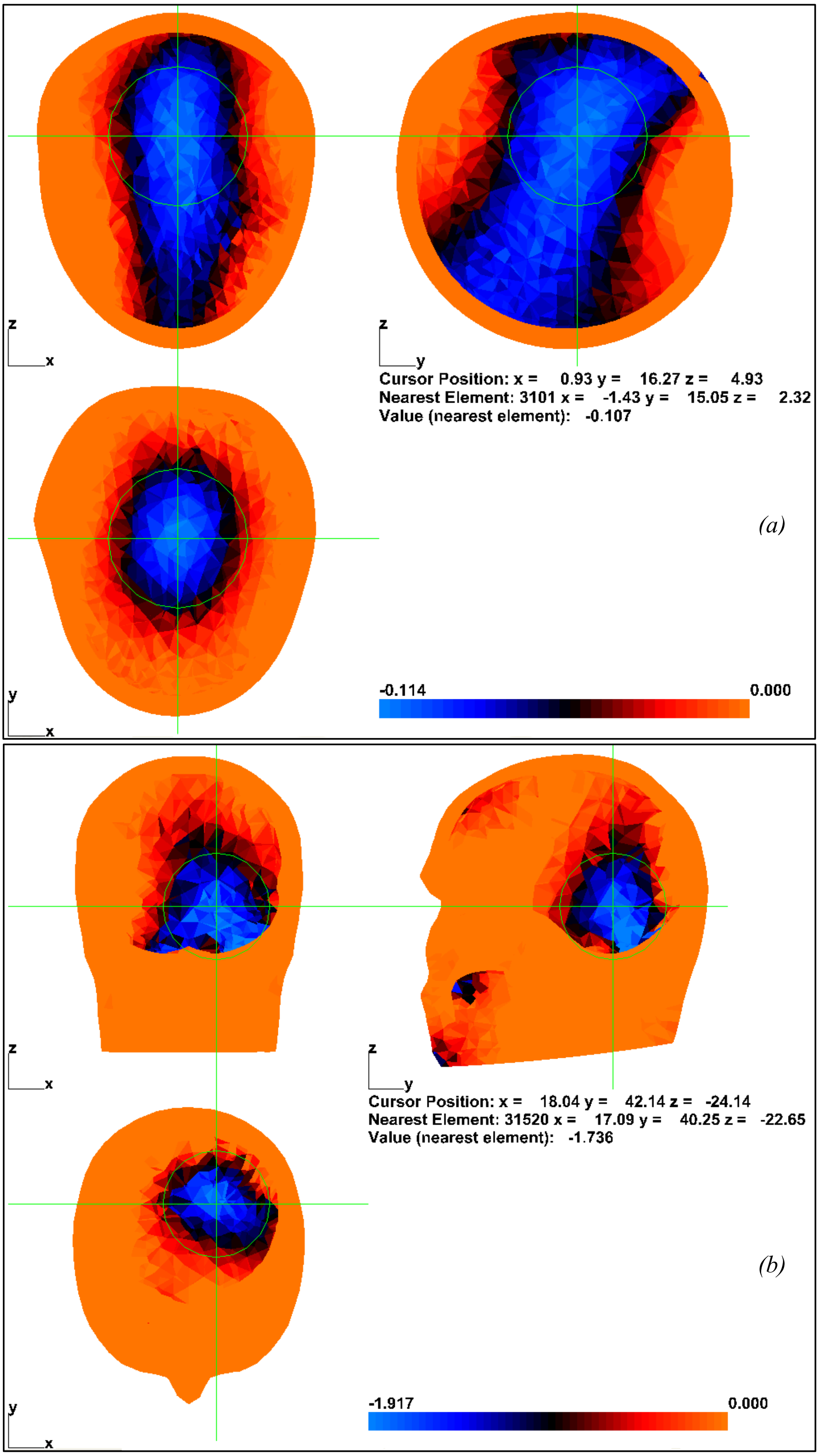

Figure 6.4: Truncated images of perturbation 7 for (a) simulated data on SS040e and (b) tank data on SA035. Aperture position is adjusted so that it is centred on the perturbation and sized to encompass the FWHM in the xy plane.

6.2. Results and Discussion

6.2.1. Boundary Voltage Data

A plot of baseline or reference boundary voltages for all 258 measurements for the target models and tank data normalised to the simulated source data from TA031EL is shown in Figure 6.5. These show an acceptable correlation for all models which can be further demonstrated by examining the least squares correlation of the data in Table 6.3.

Table 6.3: Correlation of target model reference boundary voltages to simulated and tank sources

Model	Least Squares Correlation to TA031EL	Least Squares Correlation to Tank
TA031EL	*1.000*	0.950
TA041	0.985	0.938
SS040w	0.976	0.951
SS040e	0.976	0.957
SA035	0.945	0.920
SA035w	0.941	0.907
SA035e	0.943	0.910
Phantom Tank with Skull	0.950	*1.000*

However, there is no conclusive indication that the elastically warped meshes improve the correlation over that of one that is not warped, as is the case with SA035. In fact, the affinely warped SA035w and the elastically warped SA035e show a decreased correlation compared to the non-warped mesh, albeit insignificant. For the shelled sphere models based on SS040, there is no substantial measurable difference between the elastically and affinely warped versions. The best correlation arises from the model with identical underlying geometry to that of the source, TA041, and any deviation from the ideal could be attributed to inaccuracies in electrode position and geometry in the target.

There might be an expectation that the head-shaped model, namely SA035 and its derivatives, would provide a better correlation than the sphere-based targets. The fact that this is not the case is likely to point to the additional complexity in the underlying geometry of the shelled adult head. The latter contains anatomical features closely approximating the upper portion of the spinal column, a feature not present in the original tank phantom and its geometric model. In fact the tank phantom is a significantly simplified model more in keeping with that of the shelled sphere and this could be a plausible explanation of improved boundary voltage simulation from the sphere-based models. This fact is supported by the improved correlation of the real data from the phantom over that of SA035 and its derivatives.

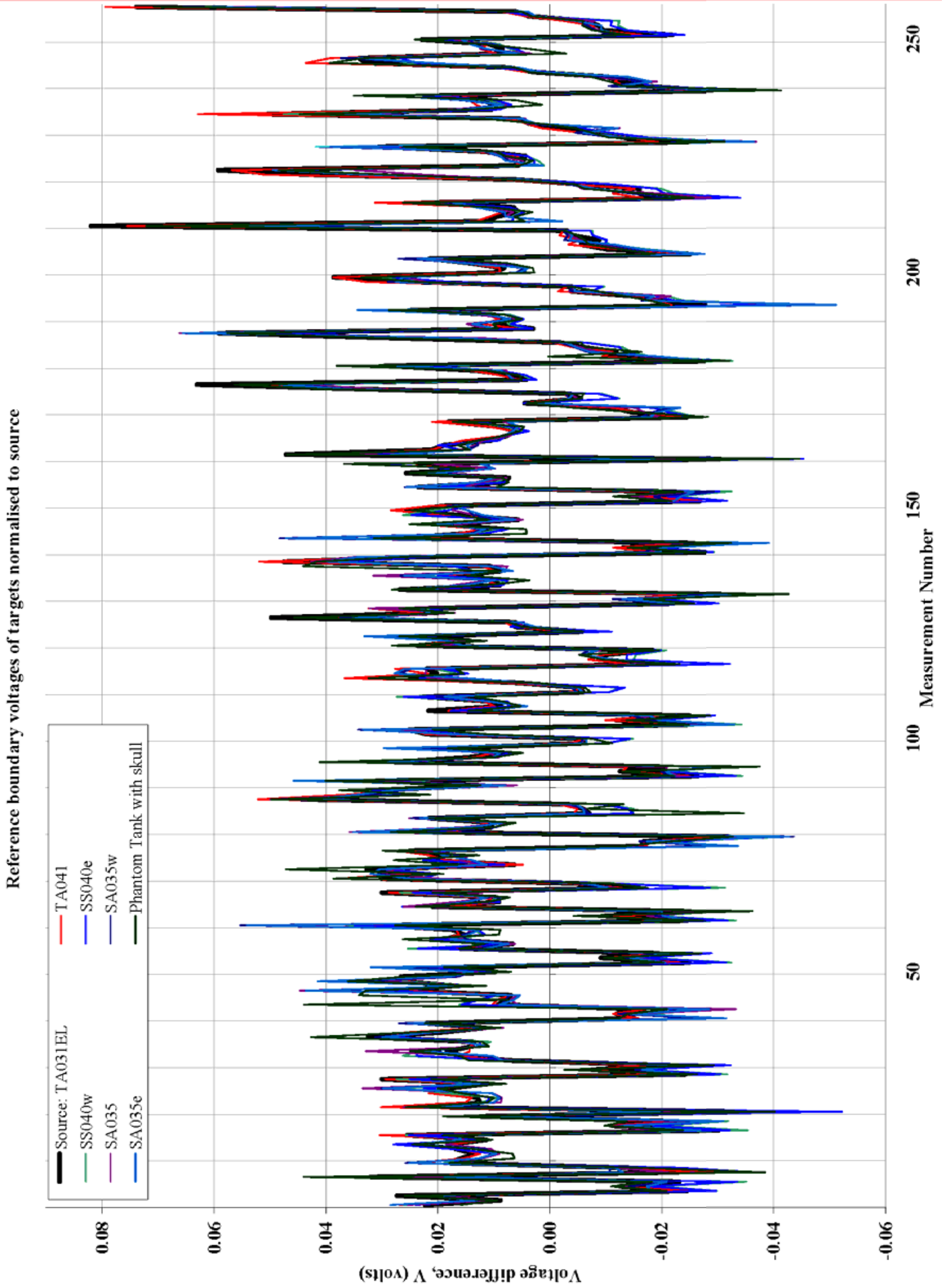

Figure 6.5: Reference of baseline boundary voltages for the target models and tank data normalised to the simulated reference from TA031EL.

6.2.2. Image Quality

Figure 6.6 and Figure 6.7 show samples of reconstructed tank phantom data on TA031EL as a reference for comparison for image quality for warped meshes. These samples are chosen for illustration as they represent perturbations well within the brain region but not closest to the centre. There is an expectation that perturbations towards the outer boundary of the brain may reconstruct better where sensitivity is better and those towards the centre would be less clear owing to significantly reduced sensitivity in this region. As TA031EL is an accurate model of the tank phantom, both in anatomical and electrode geometries, it would be expected that this would represent a reasonable reference for comparison of the other meshes. Noise is evident in the brain region for the images shown though it is minor and the conductivity perturbations can be seen to be approximately in the correct positions.

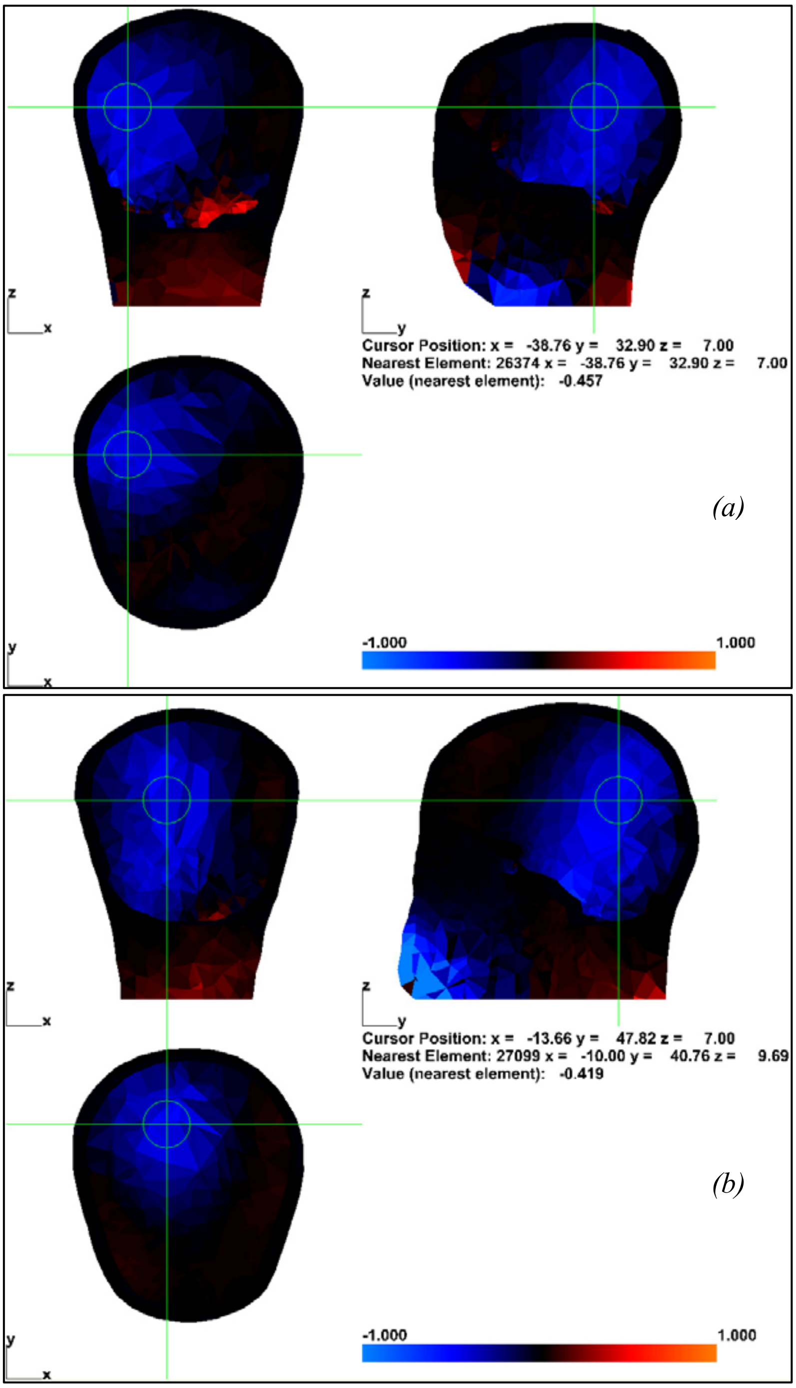

Figure 6.6: Raw images tank phantom data for perturbations at (a) x ≈ -35mm and (b) x ≈ -15 mm reconstructed on TA031EL.

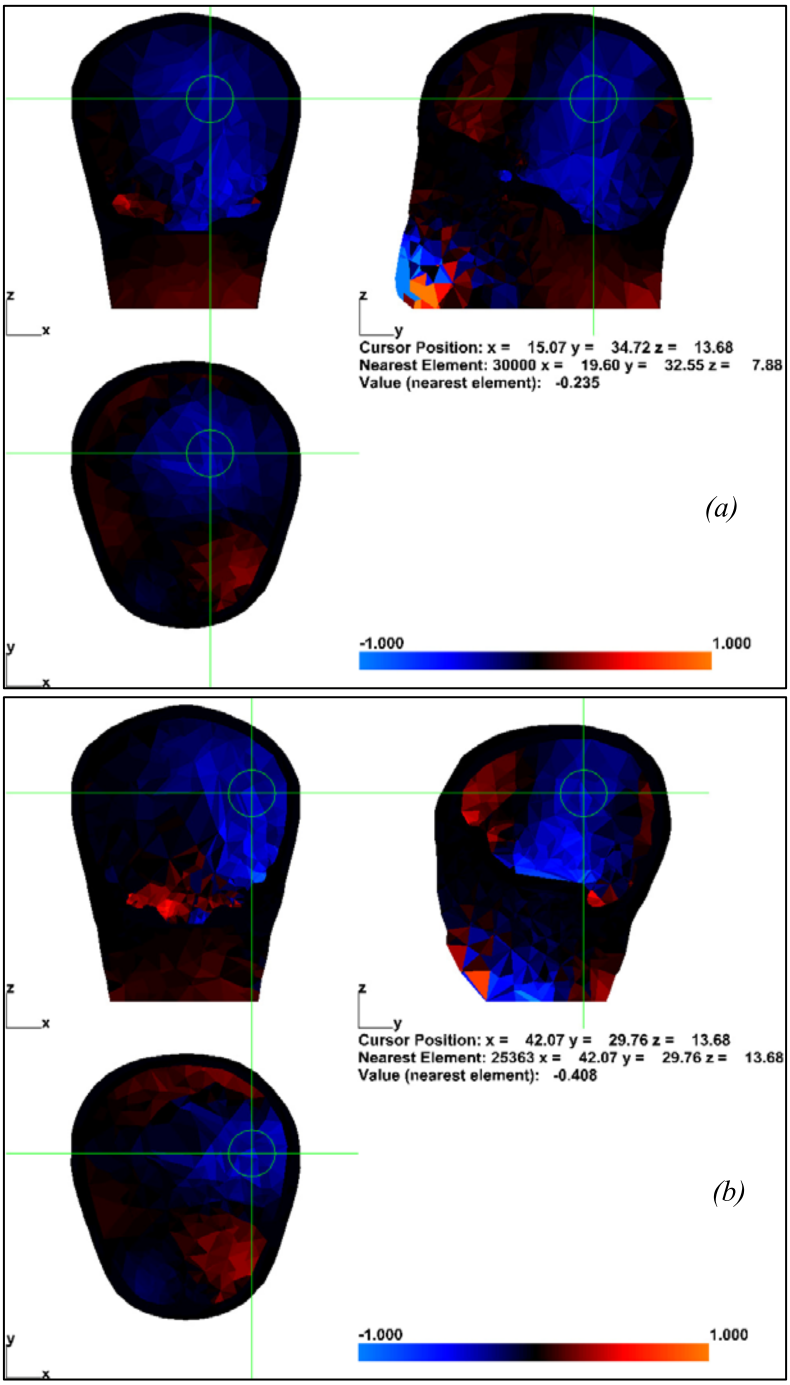

Figure 6.7: Raw images tank phantom data for perturbations at (a) x ≈ 15 mm and (b) x ≈ 35 mm reconstructed on TA031EL.

For the purpose of comparison, two of the sample images are chosen which constitute the best and worst of those in Figure 6.6 and Figure 6.7 in the opinion of the author. The image with the perturbation at $x \approx -15$, Figure 6.6(b), is almost completely clear of noise artefacts, particularly in the brain region whereas that where the perturbation is at $x \approx 35$, Figure 6.7(b), exhibits significantly higher amounts of noise.

The reconstruction of the same data on TA041 is shown in Figure 6.8. Although this model is anatomically similar to TA031EL, the electrode size, shape and positions are not. Therefore one would expect greater levels of noise artefacts. This expectation is largely upheld though any increase of noise is insignificant. There does, however, appear to be an improvement in the clarity of the perturbations; a fact not necessarily expected but one can speculate it is because the more accurate electrode modelling in TA031EL has caused elements within the brain to be of yet lower relative resolution than expected.

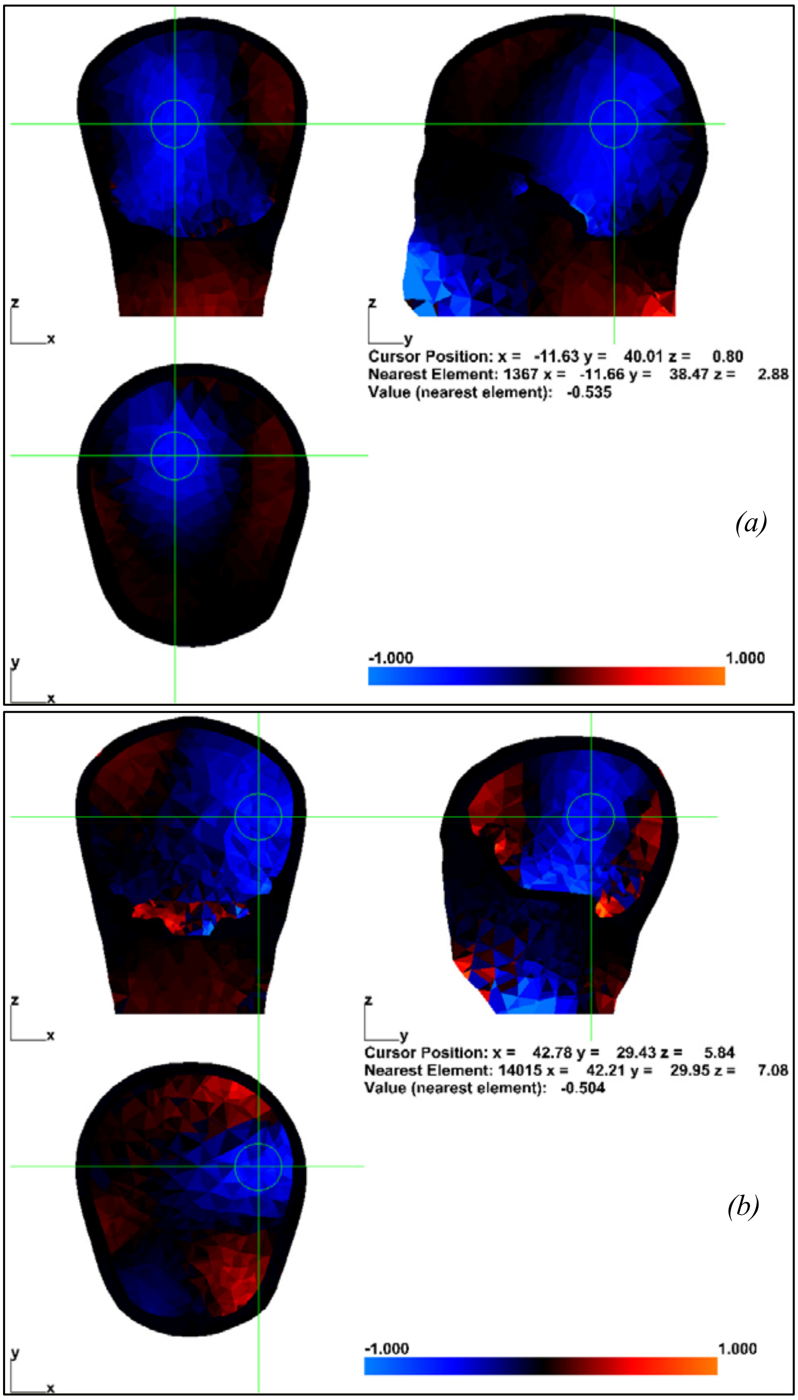

Figure 6.8: Raw images tank phantom data for perturbations at (a) x ≈ -15 mm and (b) x ≈ 35 mm reconstructed on TA041.

The same two reconstructed images on the affinely warped shelled sphere, SS040w, are shown in Figure 6.9. These images exhibit the significant increase of noise artefacts expected from such a mismatch of anatomical geometry particularly in the areas not served by the electrode array, namely the lower two quadrants of the *yz* plane. The peak conductivity increases are located accurately to within reasonable tolerance in the *x* and *y* directions but the *z* location is poor at $x \approx 35$ mm as is the clarity of the perturbed volume.

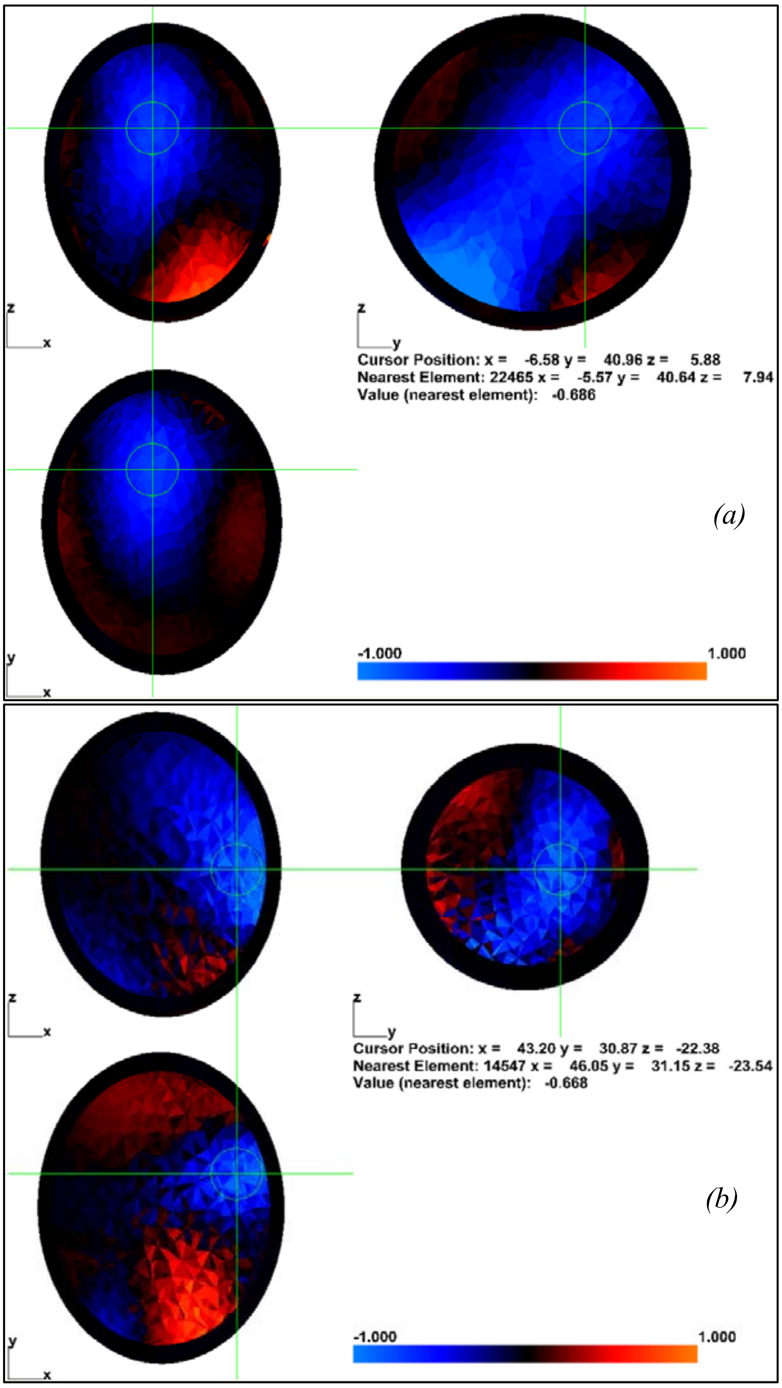

Figure 6.9: Raw images tank phantom data for perturbations at (a) $x \approx -15$ mm and (b) $x \approx 35$ mm reconstructed on SS040w.

As a direct comparison to these latter results, the reconstructed images of the data on the elastically warped sphere, SS040e, are shown in Figure 6.10. The level of noise artefacts for the image at $x \approx -15$ mm is could be assessed as marginally better but for that at $x \approx 35$ mm, it is noticeably worse. For the former, however, the clarity and shape of the perturbed volume, particularly in the *xy* plane, is arguably improved, the same can also be said for the latter, though to a significantly lesser extent.

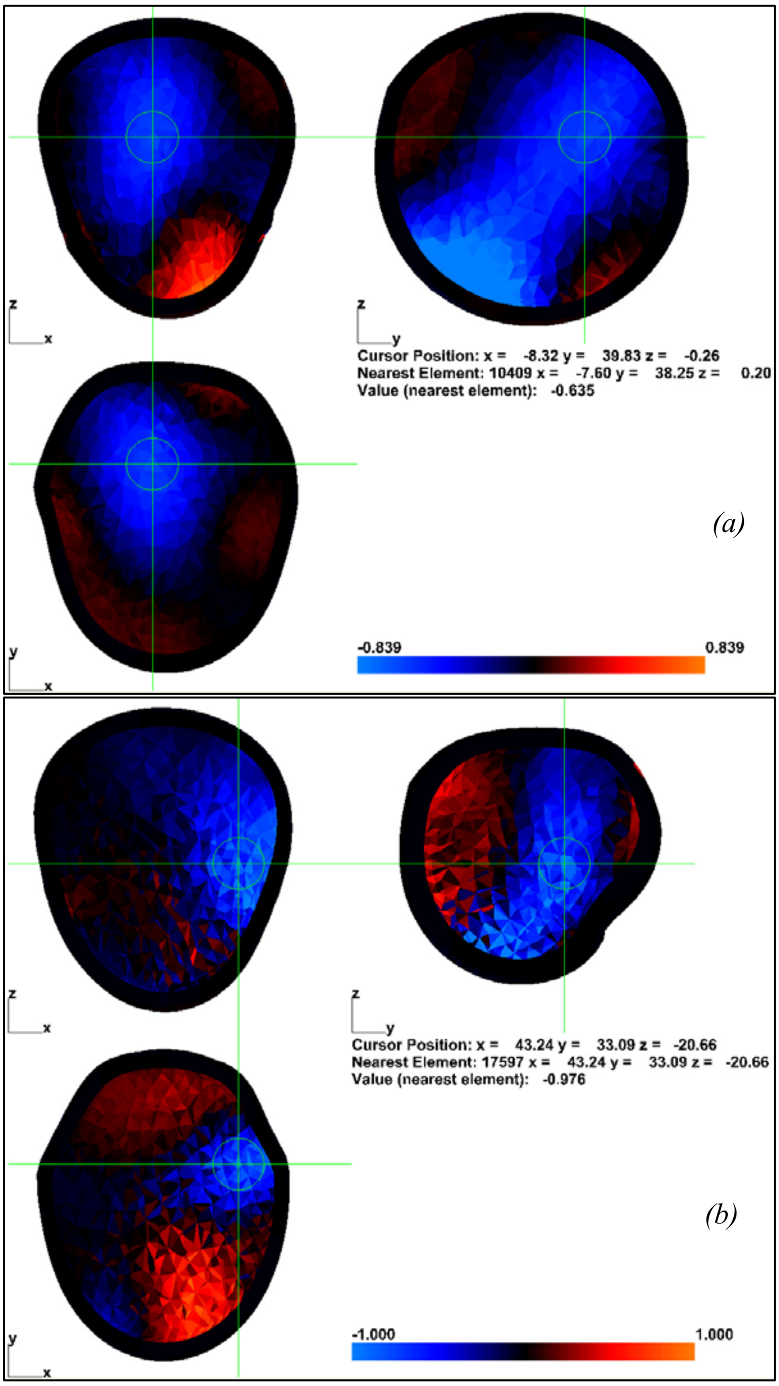

Figure 6.10: Raw images tank phantom data for perturbations at (a) x ≈ -15 mm and (b) x ≈ 35 mm reconstructed on SS040e.

The reconstructions on the canonical adult head mesh, SA035, are shown in Figure 6.11. The affinely warped version of these data is depicted in Figure 6.12 and the elastically warped data in Figure 6.13.

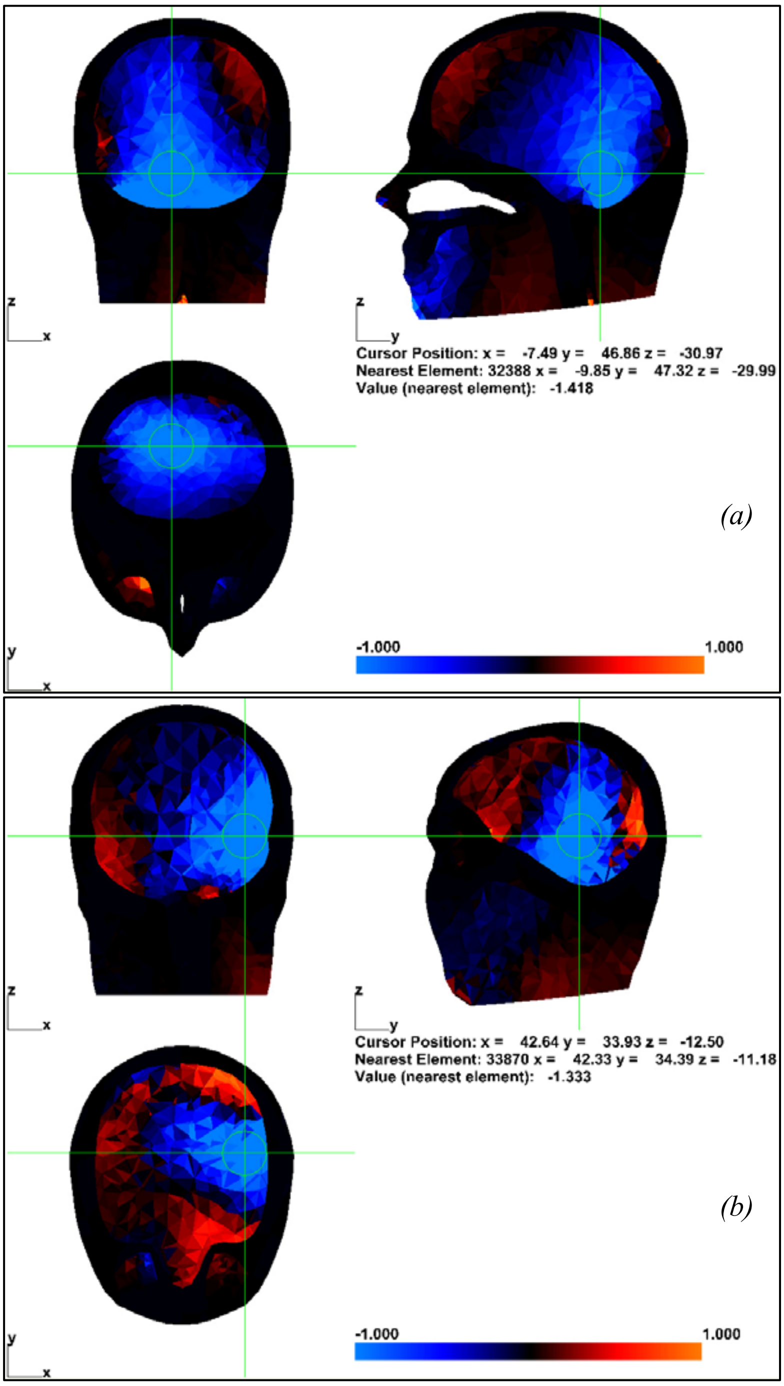

Figure 6.11: Raw images tank phantom data for perturbations at (a) x ≈ -15 mm and (b) x ≈ 35 mm reconstructed on SA035.

Noise artefacts are evident in all views of the canonical mesh, whereas in the images from the affinely warped and elastically warped meshes they are significantly reduced for both perturbation positions and almost completely eliminated in the sections defined by the *xz* plane of the perturbation at *x* ≈ -15 mm.

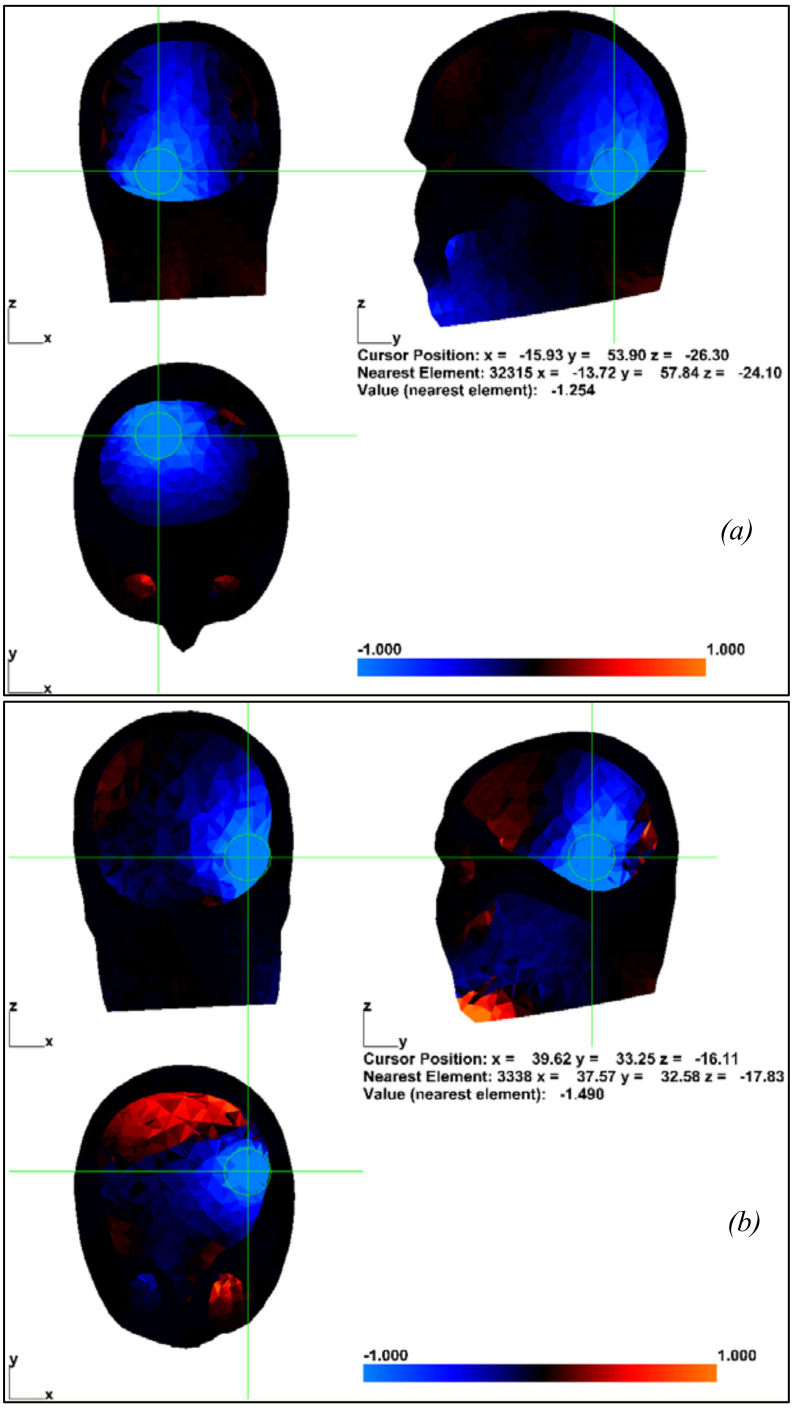

Cursor Position: x = -15.93 y = 53.90 z = -26.30
Nearest Element: 32315 x = -13.72 y = 57.84 z = -24.10
Value (nearest element): -1.254

Cursor Position: x = 39.62 y = 33.25 z = -16.11
Nearest Element: 3338 x = 37.57 y = 32.58 z = -17.83
Value (nearest element): -1.490

Figure 6.12: Raw images tank phantom data for perturbations at (a) x ≈ -15 mm and (b) x ≈ 35 mm reconstructed on SA035w.

After elastic warping, it could also be argued that there is a marginal improvement in noise levels and perturbation definition.

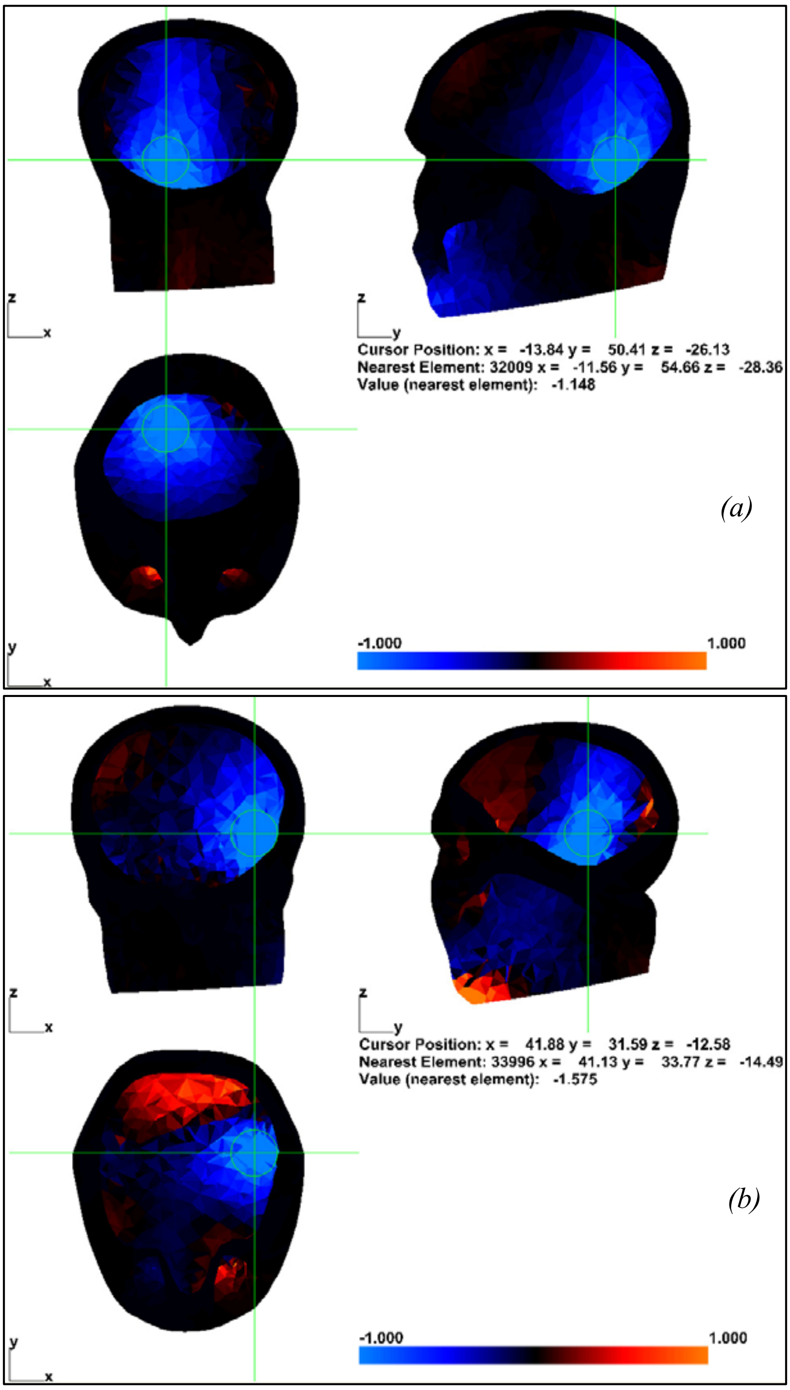

Figure 6.13: Raw images tank phantom data for perturbations at (a) x ≈ -15 mm and (b) x ≈ 35 mm reconstructed on SA035e.

6.2.3. Localisation of Conductivity Perturbations

Typical graphs of measured positions of the volumes of perturbed conductivity changes are shown in Figure 6.14. These are (a) the simulated data of the forward solution from TA031EL and (b) the experimental data from the phantom head-shaped tank with a real human skull, both reconstructed using the sensitivity matrix from TA031EL inverted using singular value decomposition truncated to 40 values. Therefore the former represents an *inverse crime*.

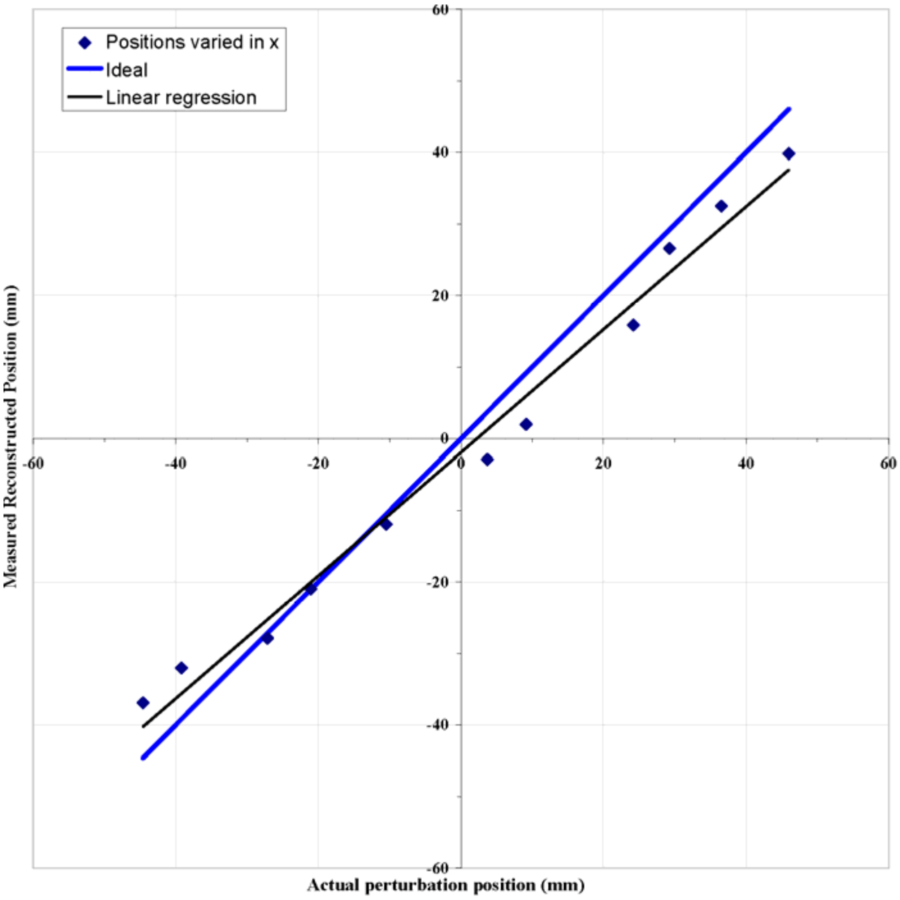

(a)

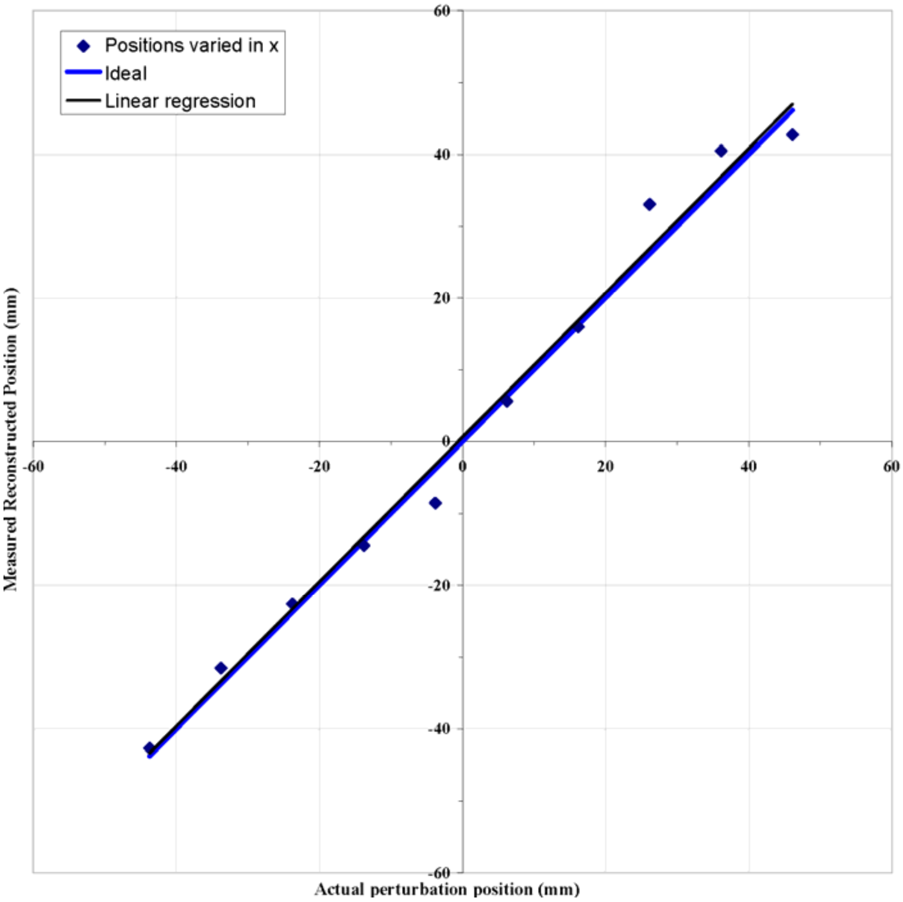

(b)

Figure 6.14: Graphs of measured conductivity perturbation positions in the x direction against actual experimental positions for (a) simulated data from TA031EL and (b) phantom tank data. Both are reconstructed using the forward model, TA031EL.

Localisation data are summarised in Table 6.4 for the simulated data and in Table 6.5 for the phantom tank data. For each target model, the slope of the least squares linear regression is given along with the offset, that is the intersection of the line of best fit with the measured position axis, and the coefficient of correlation R^2. Additionally, the mean absolute deviations between the measured and actual positions are given for all three spatial axes.

Table 6.4: Summary of localisation of perturbed volumes for simulated data from TA031EL

Target Model	x positions least squares linear regression			Absolute x deviations		Absolute y deviations		Absolute z deviations	
	Slope	Offset	R^2	mean	std	mean	std	mean	std
TA031EL	0.860	-1.938	0.986	4.7	3.0	6.7	5.0	10.2	5.2
TA041	0.987	-1.504	0.983	3.3	2.8	6.5	2.9	4.2	2.3
SS040w	0.625	-2.426	0.967	11.0	4.9	5.4	4.3	6.6	3.3
SS040e	0.854	-1.341	0.988	5.0	2.2	7.0	4.6	4.8	4.6
SA035	0.920	1.776	0.989	3.2	2.7	16.9	11.1	28.5	12.0
SA035w	0.832	-0.120	0.989	4.2	4.0	19.1	7.8	14.5	4.3
SA035e	0.907	2.451	0.991	3.2	3.3	16.3	8.5	18.4	4.7

It is interesting to note that the inverse crime, TA031EL, performed quite poorly with regard to the slope of the least squares regression when compared to the other head-shaped target models, namely: TA041 and SA035 and its warped derivatives. However, the mean absolute deviations of measured to actual positions in the x direction are comparable.

For the shelled sphere, there is a significant improvement in correlation for the elastically warped derivative which is born out by vastly reduced mean absolute deviation in the x direction. The mean absolute deviations in the other two spatial directions are within 2 mm, which when compared to the typical element sizes used with these resolutions – of the order of 10 mm – is not considerable.

For the shelled adult head, the act of affine and elastic warping appears to have degraded the linear regression of localisation in terms of slope but mean absolute deviation in the *x* direction is insignificantly different. For the other two spatial dimensions, the absolute deviations are high, though there is a considerable improvement in mean *z* localisation for the warped meshes. These high deviations could be attributed to the presence of the spinal column features in the shelled adult geometric model. It would be reasonable to speculate that this could be owing to the additional volume of features with low conductivity, such as the idealisation of the vertebrae.

The slope of the linear regression for reconstructions of phantom tank data on the models in significantly better than that of the simulated data. This is most likely to be because the accuracy of the simulated data is subject to inconsistencies in the discretization of TA031EL whereas the main sources of error in the phantom tank data is instrumentation noise and drift which is, as previously indicated, low with a signal to noise ratio of around 70 dB.

Table 6.5: Summary of localisation of perturbed volumes for phantom tank data

Target Model	x positions least squares linear regression			Absolute x deviations		Absolute y deviations		Absolute z deviations	
	Slope	Offset	R^2	mean	std	mean	std	mean	std
TA031EL	1.005	0.616	0.988	2.5	2.2	23.0	7.5	5.3	3.3
TA041	1.055	-0.543	0.993	2.2	2.1	23.1	5.4	4.9	5.9
SS040w	0.985	0.107	0.968	4.1	3.2	22.7	2.4	5.3	5.2
SS040e	1.105	0.596	0.987	4.3	2.2	22.8	3.6	6.4	5.0
SA035	1.010	2.917	0.994	3.2	1.9	13.7	5.2	13.0	7.4
SA035w	0.993	3.049	0.972	4.9	3.1	11.9	8.1	13.1	4.7
SA035e	0.986	3.162	0.977	4.5	3.0	15.8	7.1	12.3	5.1

With this is mind, it is difficult to determine from the data in Table 6.5 any significant benefits from affinely or elastically warping meshes to achieve better boundary shape. The main concern with these results is the consistent inaccuracy implied by the absolute y deviations. The fact that for the tank and sphere geometries, the error is highly consistent, may point more to the inaccuracy of supplied data than to issues with reconstruction. The positional data for the phantom tank experiments is described by Liston (2003) as being y = 43 mm and z = 2 mm relative to the line joining electrodes 13 and 17. It is also stated in the thesis that the position of the Perspex cylinder was measure relative to the foramen magnum and it is this inconsistency that may have given rise to the large error in the y values for the positions.

6.3. Conclusion

The goal of the exercises described in this Chapter was to establish whether warping a source finite element mesh such that it more accurately defines the geometry of a target subject, both in physical dimensions and for a significant area of the boundary surface, is a valid means of generating subject specific forward models for EIT. In the first instance, it is important to establish whether warping FE meshes in any way degrades the quality of the mesh such that it correspondingly degrades image reconstruction. This had already been addressed to some extent in Chapter 3 where the main goal was to establish whether element quality was substantially degraded as a result of warping spheres to ellipsoids and to examine the effects this might have on localisation of controlled perturbation positions. In this Chapter, the more important point of validating the elastic warping described in Chapter 5 in terms of its effects on image reconstruction has been attempted.

Boundary voltage data has re-established the now well-known fact that finite element models of spheres (SS040), actual subject geometry (TA031, TA041) and similar library geometry (SA035) can all provide reasonable forward models for EIT reconstruction. More importantly, however, it shows that little, if any, change is imposed on the relative voltage differences between measurements as a result of warping.

It has been established that both affine and elastic warping does not degrade the quality of reconstructed images. In fact in a number of cases presented, there is evidence to show that it is measurably improved both in the reduction of noise artefacts and the boundary shapes of known conductivity perturbations. However, while this evidence is insufficient to state conclusively that improved boundary shape through elastic warping generates correspondingly improved, less noisy images, it can be said that within the limitations of the data used that the results are encouraging.

This is, in some way, supported by the examination of the localisation of known conductivity perturbations in the reconstructed images, particularly when the simulated data is considered. The considerable improvement in localisation accuracy after warping the shelled sphere may indicate that when data subject to the inaccuracies that would be inherent from a discrete simulation is used then the use of more accurate boundary shape in the forward model will lessen its impact. This suggests a topic of further study in this field: by using a range of data with increasing levels of simulated noise, the point at which localisation inaccuracies become unacceptable in canonical and warped models could be established.

7. EVALUATION, DISCUSSION AND CONCLUSIONS

7.1. Geometric Modelling

There can be no doubt that significant advancements in the study of Electrical Impedance Tomography of the human brain have arisen from the outcomes of the work described in Chapter 2, which have been extensively used for a number of investigations by the group based in the Department of Clinical Neurophysiology at UCL and subsequently that at Middlesex University. The initial FE models and investigations of their benefits demonstrated that the layer of Cerebro-spinal fluid surrounding the brain, and other features such as the optic nerve played an important part in the accuracy of the forward model (Bayford *et al*, 2000; Bayford *et al*, 2001b; Bayford *et al*, 2001a; Bayford *et al*, 2002). After subsequent developments, the meshes were used in investigations previously cited to demonstrate the effectiveness of using a shelled accurate model of the adult head in improving image quality (Bagshaw *et al*, 2003; Liston *et al*, 2003). The underlying solid and surface modelling was used and acknowledged by Gibson *et al.* (2003), being work based on optical tomography in the Department of Medical Physics at UCL. It involved warping the adult head surface to fit points taken from optode positions on a neonate head using a thin-plate spline. The warped surface model was then used to generate a homogeneous mesh and demonstrated that this alternative strategy to warping produced simulated data which correlated well with that taken from the original neonate head model.

A range of other EIT studies that used the FE meshes followed. Ahadzi *et al.* (2004) used a three and four layer mesh based on the adult head for simulations to investigate current densities in the primary visual cortex. The mesh designated SA031 in Table 2.3 and Table 5.3 was used to evaluate and compare non-linear algorithms for Multi Frequency EIT (MFEIT) (Horesh *et al*, 2004). Fabrizi *et al.* (2005) carried out a study where seven epilepsy patients undergoing pre-surgical assessment were subjected to EEG and EIT and the EIT data was reconstructed on a similar mesh to that used by Bagshaw *et al.* (2003); the results suggesting that the problems in imaging epilepsy seizures could predominantly lie with instrumentation rather than the forward model. SA031 was again used in calibration studies for MFEIT of acute stroke (Romsauerova *et al*, 2005) and a denser further modified mesh consisting of regions defining grey matter, white matter, ventricles, eyes, optic nerve and internal ear canal was used to carry out feasibility of using EIT for stroke diagnosis (Horesh *et al*, 2005a). In another feasibility study, a high resolution mesh consisting of 136000 elements was used to simulate neuronal activity in the visual cortex for comparison with data taken from human volunteers (Gilad *et al*, 2005). A wide range of system sizes were used to investigate and evaluate solution algorithms for EIT and optical tomography (Horesh *et al*, 2005b). The neonate model has also been used in studies, for example Abascal *et al.* (2005). More recently, the models have been adapted for investigations into *Deep Brain Stimulation* (DBS). This is an area for further study by this research group at Middlesex University and initial work in the area has been presented (Bayford *et al*, 2005; Bayford *et al*, 2006b; Bayford *et al*, 2006a).

The models of the human head described in Chapter 2 represent significant improvements in anatomical accuracy over that hitherto used for EIT and related studies such as optical tomography, magnetic induction tomography (MIT), EEG and MEG. However, it cannot be claimed that they are as comprehensive as they could be; the only additional features other than scalp, skull CSF and brain modelled were the eyes and optic nerves, but these were not subsequently incorporated into models used in this thesis. In fact, the jaw bone was not present in most of the meshes in order to improve elemental resolution in the brain whilst maintaining modest system sizes for the sake of solution time. The brain is idealised by being modelled as one unit rather than make any attempt to represent the separate hemispheres and the *Corpus Callosum* between them. In fact, the idealisation is even more emphasised by the assumption of symmetry, one that is well known not to be true. The ventricles and internal ear canals have also been ignored, except for the one study mentioned above (Horesh *et al*, 2005a), as was the distinction between grey and white matter and the *sulcii* on the brain surface. One justification for such omissions is that only for clinical based work would such detail be of possible relevance and having established successfully the principle that computer-aided design tools are an effective means for carrying out such accurate modelling then it would be a simple matter to extend the strategy to incorporate additional anatomical features. Another justification has already been alluded to: that the finer detail would lead to higher system sizes (number of elements) in order to achieve adequately small element sizes in the inner regions of the brain. It will not be until improvement in execution times for forward and inverse modelling is achieved that the benefits of greater anatomical detail can be reaped. Such improvement will be the result of a number of developments such as more efficient matrix inversion strategies (Horesh *et al*, 2005b) and the use of the GRID (Fritschy *et al*, 2005).

The generation of the meshes was carried out exclusively using the software package I-DEAS (Integrated Design Engineering Analysis Software) which was developed and marketed by the Structural Dynamics Research Corporation (SDRC). Towards the end of the project SDRC was taken over by EDS (www.eds.com) who also acquired another popular engineering design system *Unigraphics*. The two packages have now been combined into one product and is marketed by the recently formed *UGS Corporation* (www.ugs.com, www.ugs.co.uk) under the name *UGS NX*. The use of stable releases of I-DEAS was maintained for the duration of the project however, as it was not clear what meshing features of I-DEAS were retained in the new product. It is important by way of conclusion that any meshing tool, commercial or otherwise, could be suitable for the work provided it meets the criteria essential for meshing the non-homogeneous models. The use of NETGEN (Schoberl, 1997) has already been discussed in

§2.1.2 as a suitable tool for homogeneous meshing but it is unable to utilise partitioned internal surfaces to generate a shelled mesh. The range of alternative commercial packages currently available on the market is too wide to discuss in detail here and none has been extensively trialled for suitability. Among them is *COSMOS Works* which is normally incorporated into *SolidWorks* (www.solidworks.com), a CAE package which is rapidly gaining popularity in the product design and engineering design sectors. Initial work with *SolidWorks* indicates that the production of shelled meshes might be possible using the assembly modelling feature of the product. If so, it may provide a suitable and possibly more cost effective future for mesh generation. Like I-DEAS, *Solidworks* also provides the functionality to generate surfaces from NURBS and, unlike I-DEAS, it also allows images to be imported so that the curves can be sculpted around their boundaries. The current release, however, still lacks the flexibility of curve manipulation offered by *Alias StudioTools* (now known as *Autodesk AliasStudio*) and until such a time that it does, then a dedicated surface modeller appears to be the most effective means of creating the initial underlying geometry to the precision achieved in these models. As stated in §2.4, the time taken to carry out the initial stages of producing a patient specific model is unacceptable for any time-critical clinical use. In addition to this impediment, none of the tools used is inexpensive and the level of operator specialism required is high. Thus it can be concluded that such methods are only suitable for generating a library of detailed models for close matching to a subject prior to warping.

7.2. Affine Warping

The need to investigate the effects of warping a finite element mesh was identified and this has been initially addressed in Chapter 3. The main focus of this exercise was to examine the extent of element distortion that would take place when warping a spherical mesh to an ellipsoid and test the effect this would have on reconstructed images. It was a very simple test generating results as expected for the homogeneous meshes but the main concern prior to undertaking the work was how the already elongated elements in the thinner shells would respond to such warping. As expected, the minimum stretch in the shelled mesh was significantly altered as indicated in Table 3.1, though it was still within acceptable limits being greater than 0.1. Reconstruction of simulated perturbations showed acceptable localisation even for the simulated data used, which was generated on a relatively coarse mesh and therefore likely to inherit errors in the boundary voltages. The work was presented to the EIT community (Tizzard *et al*, 2004), which generated some interest in the concept and the use of commercial CAE tools, namely I-DEAS, for meshing.

7.3. Surface Construction

With the principle established that warping a finite element mesh produced acceptable results with respect to element quality, the initial stages of that process have been addressed in Chapter 4. As reviewed in the Chapter, affine warping of triangulated surface models is common in EEG and MEG applications and free-form deformation (FFD) methods are becoming increasingly popular (Koikkalainen and Lotjonen, 2004). Such methods deform pre-existing surface models using registration points taken mostly from MRI datasets. Affine warping may just simply use the landmarks of nasion, inion and pre-auricular points whereas FFDs use larger point datasets from the MRI. The main aim of this study was to attempt to dispense with the need for MRI data leaving only the registration landmarks and electrode positions with which to work. The means of devising a scheme of parameterising the electrode positions in order to build knot vectors for the generation of a B-Spline surface patch is a novel approach to reconstructing geometry and proved to be highly successful. Moreover, the formulation of an iterative process to manipulate the surface such that it interpolated the electrode positions to a high degree of accuracy proved to be effective in terms of speed and final surface outcome. This was confirmed by the results of the surface quality evaluation in §4.4.2 where for around 90% of surface nodes covered by the B-Spline patch the distances between the nodes and the patch were within the expected 2 mm error. In fact this could be regarded as a conservative estimate of the expected error as three major factors contributed to it: the measurement of the electrode positions from a CT scan with a resolution of around 1 mm, the accuracy of positioning and scaling the image planes in the surface modeller, and the placement and manipulation of the underlying curves in the surface modeller. The degree of B-Spline surfaces generated was constrained to three and they still produced highly acceptable results. A fair evaluative comment on the work as is stands is that tests could have been carried out using surfaces of higher order to see if any further improvements could be made. Furthermore, the B-Splines were not rationalised which would have given greater local control thereby possibly improving convergence times. However, the algorithm would have been substantially more complex to achieve this as a strategy for evaluating weights would need to be devised and is a topic for further study. This work was also presented to the EIT community (Tizzard *et al*, 2005).

7.4. Elastic Deformation

The procedure described in Chapter 5 seemed a logical way forward for using the surface data from the previous Chapter to warp finite element models of the human head. The stress analysis techniques adopted are well established and robust for use in normal design situations and relatively easy to implement. What was not understood was how utilising such methods for large displacement deformation without resorting to non-linear solution methods would perform. As the author is unaware of other work which uses this approach to warp three-dimensional, non-homogeneous finite element models for the purpose of medical imaging, it could represent a novel application of the methodology. It was reasonably clear from the outset that the many variables defining the problem would need to be optimised and so a methodical empirical approach to investigating this was adopted to yield a successful outcome. It could be said, in retrospect, that the optimum values arrived at for *Poisson's ratio* and the choice of fully restrained nodes was not surprising. A value of $\nu = 0.3$ for *Poisson's ratio* is fairly typical for a wide range of elastic materials and fully restraining only one surface node allows maximum degree of freedom for all the unknown displacements in the model thus minimising element distortion. It could be said, however, that the optimum ratio of material stiffness between the shelled features of scalp, skull and CSF was somewhat surprising. Initial speculation would yield the expectation that higher ratios would result in significantly decreased change in shell thicknesses (measured as surface depths) and the fact that the changes varied insignificantly for values above 10:1 (Figure 5.3) was an interesting discovery. The fact that ratios higher than this resulted in significantly increased solutions times confirmed the final value chosen.

The warping algorithm could be said to be very successful within the limitations of the methods used. Figure 5.13 demonstrated conclusively that the approach is cost-effective in terms of time and this could be improved upon significantly with suggestions discussed in §5.6.2. The relative small amount of element distortion arising from the warping also confirms the effectiveness of the algorithm. The methodology is constrained by the specification that subject geometry must be obtained rapidly from the electrode positions and registration landmarks and so geometric accuracy of the subject-specific mesh is limited to the surface beneath the B-Spline patch. The work has been submitted and accepted for publication as a journal article (Tizzard and Bayford, 2007).

7.5. Validation

The results arising from the investigations described and presented in Chapter 6 go some way towards the validation of the warping approach to improving the forward model in EIT. The results for localisation of the conductivity perturbations from both simulated and laboratory data indicate that benefits can be drawn from having more accurate boundary shapes. Some improvements in localisation were observed but the correlation was too inconsistent to be conclusive though the results were encouraging, particularly when the mean absolute deviations from the ideal positions are considered. An even more important outcome from the validation, however, is the perceived improvement in image quality arising from the mesh warping. It is quite apparent that even affine warping of the adult head significantly improves the image quality and further improvements are perceived after elastic deformation. It can be said of the sphere that after elastic warping perturbation geometry is improved, though there artefacts in both sets of images and it is difficult to assert that they are reduced after deformation.

The results were limited to the data available and additional tests may generate a more substantial basis for conclusion but the focus of the thesis is mainly on the methodology and the validation stands as an acceptable demonstration that the approach is justified and worthy of further application, not just on models of the head but other regions of the body such as thorax as will be briefly introduced later. Another test that could have been included, for which data were available, would be from the Perspex cylinder moving from anterior to posterior in the tank phantom, though it is unlikely that the inclusion of such data would provide significant additional information. The use of Perspex as the perturbation may also be seen as a limitation in the results as it represents a 100% decrease in conductivity whereas for the majority of clinical cases the conductivity changes are significantly smaller. Also, because the method of reconstruction uses a linearised sensitivity algorithm, the conductivity change induced by an insulator would be outside the linear region and the resulting inverse solution could be said to be saturated. The results in Chapter 3, and particularly Figure 3.5, show the issues relating to attempting to image smaller conductivity changes using a shelled forward model and this is supported to some extent by Tidswell *et al.* (2001) who used a sponge soaked in a higher concentration saline solution to give rise to a 12% increase. The purpose and justification for using Perspex is that it generates clearer raw images with a strong enough contrast from which to assess the level of artefacts.

8. FURTHER WORK

8.1. Deep Brain Stimulation

A number of areas of further investigation arising from the surface modelling work described in Chapter 2 can be proposed. Some additional further work has already been identified and begun within the research group that represents an alternative application of the head models and that is within the field of Deep Brain Stimulation (§7.1). Initial activity has included modelling the electrode within the solid model of the human head in I-DEAS using MRI images of a subject with electrode surgically installed to help define position. The work highlights the need to extend the model of the brain still further to include at least the ventricles as their presence will strongly influence a forward solution of current injected into the deep brain region. Their influence on warping, and indeed that of the presence of the deep brain electrodes, will also need to be investigated. Figure 8.1 shows a section of the solid model of the human head with the deep brain probes included and a snapshot of a simulation showing current distribution around the left hand probe.

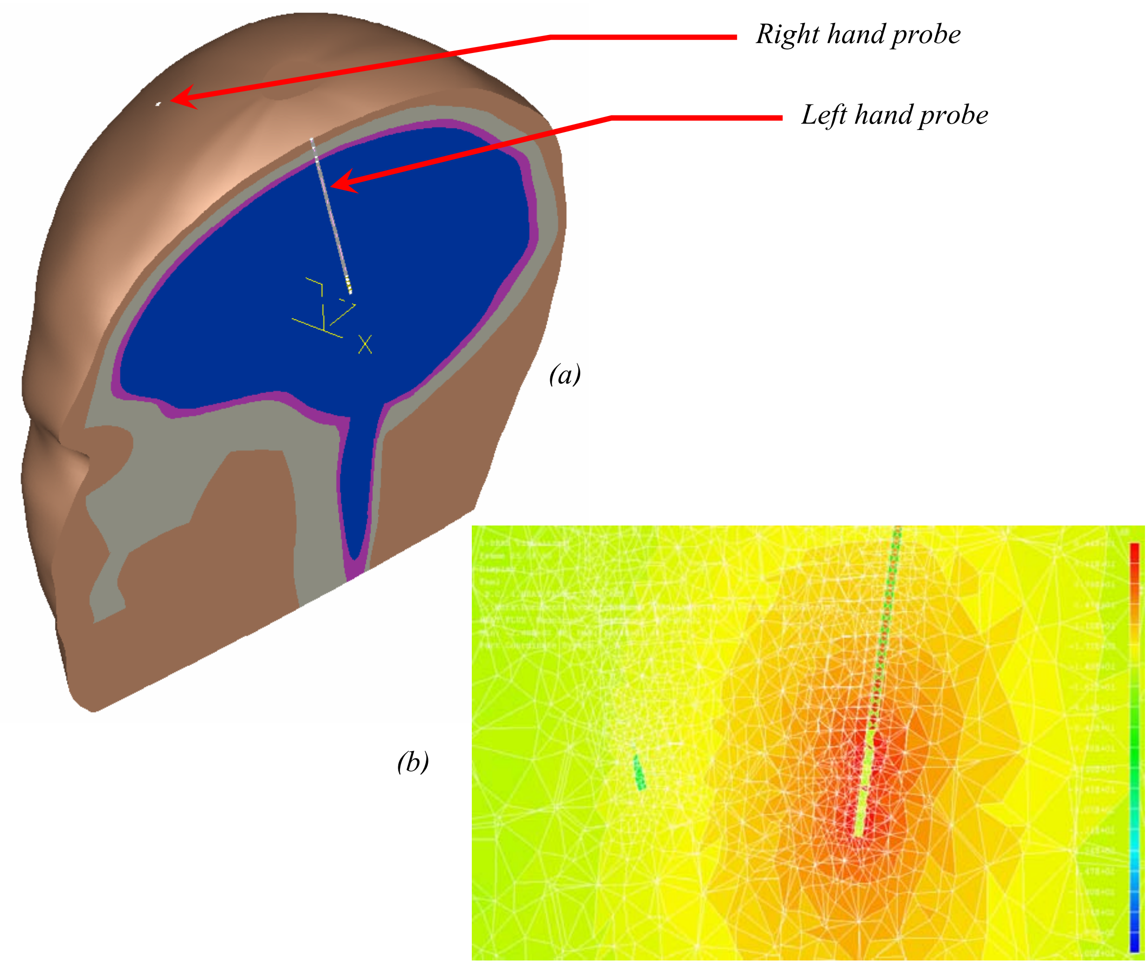

Figure 8.1: Example of initial DBS investigation showing (a) the head solid model with probes included and (b) simulation of current distribution around the left hand probe.

For the research group, it is the area of DBS that EIT of human brain function is likely to continue as it is perceived that there may be many benefits to be gained from combining the two technologies, particularly to assist the surgical procedures of electrode placement but also for the diagnosis and monitoring of the conditions such as Alzheimer's and Parkinson's disease that require the use of DBS.

For this and the other applications discussed in this thesis, further investigations into improving the forward model can be considered. One main area of interest in this respect in the use of hybrid models incorporating both Finite Elements and Boundary Elements. In such a BEM-FEM hybrid, the thin shells making up the thinner parts of the scalp and skull and the CSF layer around the brain continue to be modelled with finite elements while the regions of more substantial volume, such as the brain, can be modelled with boundary elements. Boundary element modelling is generally more computationally demanding due to fully populated and asymmetric matrices (Becker, 1992). There are also issues relating to accuracy when modelling thin shells with BEM (Karamanoglu, 1992).

8.2. Further Developments for Surface Reconstruction

In §7.3, the evaluation of the surface construction techniques raised the issue that greater control over the surface form for the B-Spline patch could be achieved through the use of Non-Uniform Rational B-Splines. For the head modelling example, the special case of the NURB was used namely that of the B-Spline. The B-Spline curve is defined by equation (4.1) and the NURBS by equation (8.1):

$$C(u) = \frac{\sum_{i=1}^{n} w_i V_i N_{i,k}(u)}{\sum_{i=1}^{n} w_i N_{i,k}(u)} \tag{8.1}$$

In this formulation, the term w_i represents weights assigned to the control points, V_i, and adjusting the weights has the effect of altering the influence that a control point has on the shape of the whole curve. The use of this modification to the algorithm described in Chapter 4 may have resulted in faster convergence towards the final surface through the electrode positions. However, a methodology would need to be established to evaluate the weights during the iterative process and it is uncertain at this stage whether this would result in any speed benefit. As the surface beneath the electrodes in the human head is relatively simple in terms of curvature changes, a simple degree 3 B-Spline did suffice, but for more complex boundary forms there may be a need to develop the process further.

Having established in principle that the electrode positions and registration landmarks can be used as the initial basis for patient geometry acquisition, the practical realities of obtaining the data in a clinical environment has yet to be established. It would be inappropriate to manually measure electrode coordinates using the experimental methods described, that is the use of a digitising arm, and so automatic means need to be investigated. One such approach could be to design the head net to incorporate localisation technology. Proposals could include the use of radio frequency transmitters and receivers to triangulate positions or strain measurement techniques within the fabric of the head net. The research group is embarking on a work programme to investigate such an approach but relating more to the imaging of lung function in pre-term neonates rather than the human head.

8.3. Monitoring Neonate Lung Function

Lung development can be severely arrested in preterm infants resulting in dysfunction and interrupted alveolarisation. Objective, non-invasive measures of lung maturity and development, oxygen requirements and lung function, suitable for use in small, unsedated infants, are urgently required to define the nature and severity of persisting lung disease, and to identify risk factors for developing chronic lung problems. EIT can provide such a means for continuous monitoring of lung function in an intensive care unit and the group is investigating techniques for this in conjunction with Great Ormond Street Hospital (GOSH) and in collaboration with City University and University College London. Figure 8.2 shows an electrode placement strategy currently in use at GOSH and it is proposed that for continuous monitoring an arrangement consisting of two or three rings of 8 electrodes each be incorporated.

Figure 8.2: Current electrode placement strategy for monitoring neonate lung function at Great Ormond Street Hospital

It is also proposed that the electrodes be applied by means of a wearable jacket to ease placement on the infant and ensure minimal disturbance to the system during routine physiotherapy. The jacket should also incorporate technology indicate in §8.2 above for the acquisition of electrode positions and other registration landmarks such as additional rings of dummy electrodes to increase the size of the dataset.

Initial tests on this work have been carried out. An approximate profile from one slice of a neonate CT scan supplied by GOSH has been used to generate a surface model of the thorax region. Electrode positions were evaluated to generate two B-Spline surface patches using an adapted form of the algorithm described in Chapter 4. One consisted of five rows of eight electrodes each and the second of five rows of 16 electrodes, in both cases equally spaced around the perimeter. These are shown with a render from the surface modeller of the original model in Figure 8.3.

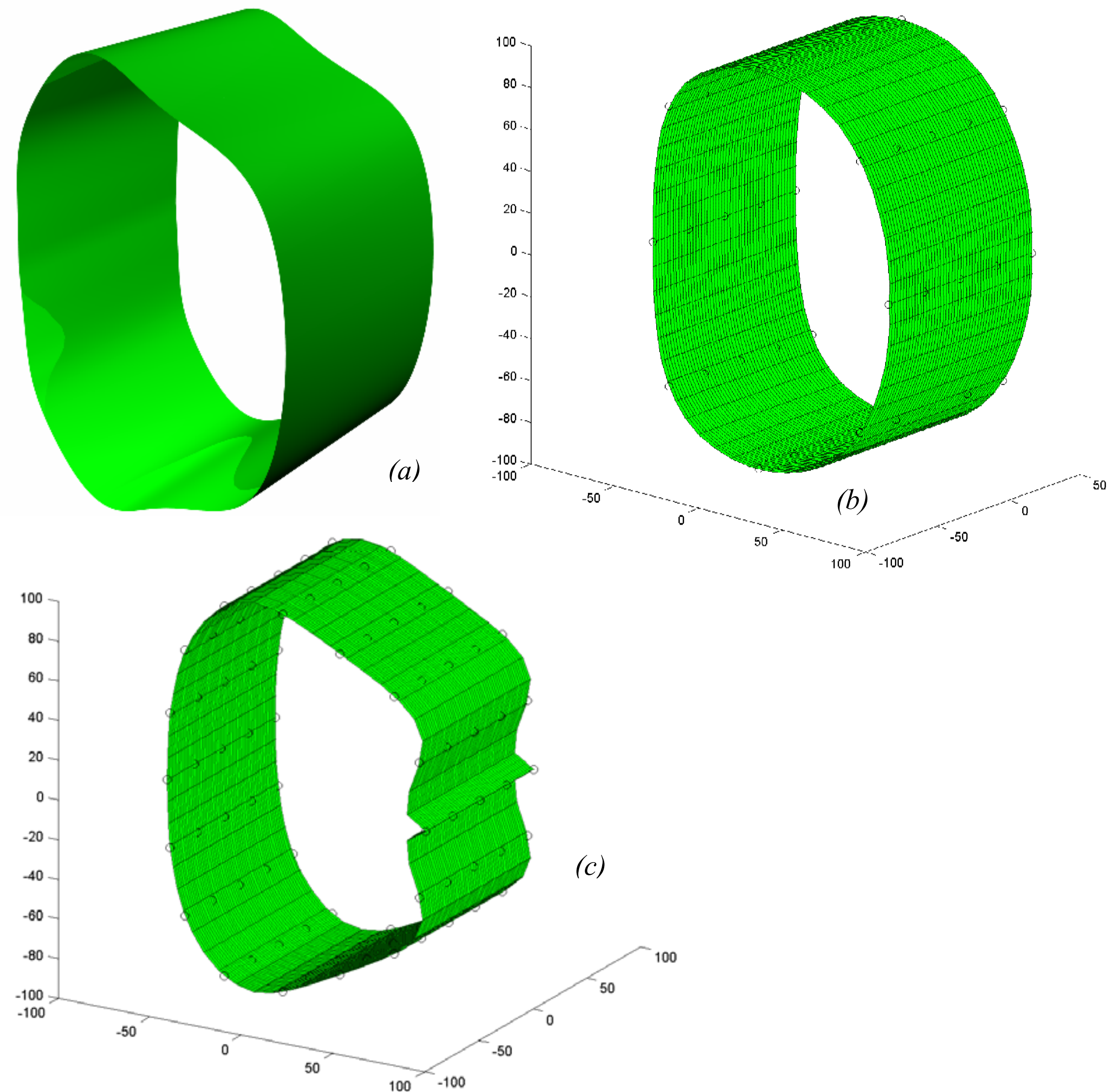

Figure 8.3: Initial tests on generating surface patches for an approximate neonate thorax region: (a) the original surface model, (b) B-Spline patch generated from 8 electrodes per row and (c) from 16 electrodes per row.

It is clear from visual inspection that the model incorporating eight electrodes per row poorly reflects the original shape whereas with 16 electrodes per row the shape is more accurately represented, except around the region defining the start and finish of the patch. For the latter issue, development of the algorithm needs to take place to enable the start and end gradients of the patch to be modified and may also incorporate the inclusion of rationalised B-Splines to allow for more accurate shaping. Thus, as an initial investigation it shows that the problem requires additional work over that already achieved for the human head but once achieved it is highly feasible that a cylinder could be warped to take on the surface form to improve image reconstruction.

8.4. Further Development of Warping Algorithm

It has already been discussed in §5.6.2 that execution time for the warping algorithm could be substantially improved by further investigation into the necessary matrix inversion techniques. In addition to this, however, is also the development of techniques to provide more accurate electrode modelling. As the surfaces are defined using electrode positions, then the nodes around the electrodes could be repositioned to ensure greater precision for both the location of the electrode and its geometry. This may introduce a range of issues regarding the quality of the ensuing mesh which could depend on the resolution of the surface triangles but such an outcome difficult to predict. However, if successful, it would provide further significant improvements to the forward model with relatively little time overhead.

REFERENCES

Abascal J F P J, Arridge S, Bayford R H and Holder D S. 2005. Selecting the regularisation parameter for linear electrical impedance tomography of brain function. *6th Conference on Biomedical Applications of Electrical Impedance Tomography.* (London: University College, London)

Adams V and Askenazi A. 1999. *Building Better Products with FInite Element Analysis*. (Santa Fe, NM: OnWord Press)

Adler A and Guardo R. 1996. Electrical impedance tomography: regularized imaging and contrast detection. *IEEE Trans. Med. Imaging* **15** 170-179.

Ahadzi G M, Gilad O, Horesh L, Bayford R H and Holder D S. 2004. An EIT electrode protocol for obtaining optimal current density in the primary visual cortex. *XII International Conference on Electrical Bioimpedance and V Electrical Impedance Tomography.* (Gdansk, Poland: Gdansk University of Technology) ed A Nowakowski, J Wtorek, A Bujnowski and A Janczulewicz.

Anand V B. 1993. *Computer Graphics and Geometrical Modelling for Engineers*. (New York: John Wiley & Sons)

Avis N J and Barber D C. 1994. Image Reconstruction Using Non-Adjacent Drive Configurations. *Physiol. Meas.* **15** A153-A160.

Bagshaw A, Liston A D, Bayford R H, Tizzard A, Gibson A, Tidswell A T, Sparkes M K, Dehghani H, Binnie C D and Holder D S. 2003. Electrical impedance tomography of human brain function using reconstruction algorithms based on the finite element method. *Neuroimage* **20** 752-64.

Baker A J and Pepper D W. 1991. *Finite Elements 1-2-3*. (London: McGraw-Hill)

Barber D C. 1989. A Review of Image Reconstruction Techniques for Electrical Impedance Tomography. *Med. Phys.* **16** 162-69.

Barber D C and Brown B H. 1988. Errors in Reconstruction of Resistivity Images Using a Linear Reconstruction Technique. *Clin. Phys. Physiol. Meas.* **9** A101-A104.

Barber D C and Seagar A D. 1987. Fast reconstruction of resistance images. *Clin. Phys. Physiol. Meas.* 8 47-54.

Baumann S B, Wozny D R, Kelly S K and Meno F M. 1997. The electrical conductivity of human cerebrospinal fluid at body temperature. *IEEE Trans. Biomed. Eng.* **44** 220-223.

Bayford R H. 2006. Bioimpedance tomography (Electrical Impedance Tomography). *Annual Review of Biomedical Engineering* **8** 63-91.

Bayford R H, Bagshaw A, Liston A D, Tizzard A and Holder D S. 2002. Development of algorithms to image impedance changes inside the human head. *The First Mummy Range Workshop on Electric Impedance Imaging.* (Colorado State University)

Bayford R H, Boone K G, Hanquan Y and Holder D S. 1996. Improvement of the positional accuracy of EIT images of the head using a Lagrange multiplier reconstruction algorithm with diametric excitation. *Physiol. Meas.* **17** A49-A57.

Bayford R H, Gibson A, Tizzard A and Holder D S. 2000. Modelling impedance changes in the human head using IDEAS. *World Congress on Medical Physics and Biomedical Engineering.* (Chicago)

Bayford R H, Gibson A, Tizzard A, Liston A D, Tidswell A T, Bagshaw A and Holder D S. 2001a. Modelling the effect of eye sockets in the human head using I-DEAS and its implication for imaging impedance change using Electrical Impedance Tomography. *XI International Conference on Electrical Bio-Impedance.* (Oslo) 391-96.

Bayford R H, Gibson A, Tizzard A, Tidswell T and Holder D S. 2001b. Solving the forward problem in electrical impedance tomography for the human head using IDEAS (integrated design engineering analysis software), a finite element modelling tool. *Physiol. Meas.* **22** 55-64.

Bayford R H, Tizzard A and Liu X. 2005. Dynamic modelling of electrical current distribution in the deep structure of the brain. *Proceedings of the 3rd IEE International Semiar on Medical Applications of Signal Processing.* (London, UK: Institute of Electrical Engineers) 131-34.

Bayford R H, Tizzard A and Liu X. 2006a. The Forward Model. *7th conference on Biomedical Applications of Electrical Impedance Tomography.* (Seoul, South Korea) 21.

Bayford R H, Tizzard A, Yousif N and Liu X. 2006b. Investigating the mechanism of deep brain stimulation using a dynamic complex model of the head incorporated with the complete model of electrode. *Clin. Neurophys.* **117** S219-S220.

Becker A A. 1992. *The Boundary Element Method in Engineering*. (London: McGraw-Hill)

Benham P P and Warnock F V. 1979. *Mechanics of Solids and Structures*. (London: Pitman)

Binnie C D, Rowan A J and Gutter T. 1982. *A Manual of Electroencephalographic Technology*. (Cambridge, UK: Cambridge University Press)

Boone K G and Holder D S. 1996. Current Approaches to Analogue Instrumentation Design in Electrical Impedance Tomography. *Physiol. Meas.* **17** 229-47.

Boone K G, Lewis A M and Holder D S. 1994. Imaging the Cortical Spreading Depression by EIT: Implications for Localization of Epileptic Foci. *Physiol. Meas.* **15** A189-A198.

Booth M J and Basarab-Horwath I. 1996. Comparing electrode configurations for electrical impedance tomography. *Electron. Lett.* **32** 648-49.

Bowden A E, Rabbitt R D and Weiss J A. 1998. Anatomical registration and segmentation by warping template finite element models. *Proc. SPIE* **3254** 469-76.

Breckon W R and Pidcock M K. 1987. Mathematical aspects of impedance imaging. *Clin. Phys. Physiol. Meas.* **8** A77-A84.

Brown B H and Barber D C. 1983. Applied potential tomography (apt) - a new in vivo medical imaging technique. *Clin. Phys. Physiol. Meas.* **4** 96.

Brown B H, Barber D C and Seagar A D. 1985. Applied Potential Tomography: Possible Clinical Applications. *Clin. Phys. Physiol. Meas.* **6** 109-21.

Buchner H, Knoll G, Fuchs M, Rienacker A, Beckmann R, Wagner M, Silny J and Pesch J. 1997. Inverse localization of electric dipole current sources in finite element models of the human head. *Electroencephalogr. Clin. Neurophysiol.* **102** 267-78.

Burger H C and Milaan J B, V. 1943. Measurements of the specific resistance of the human body to direct current. *Act. Med. Scand.* **114** 584-607.

Chapra S C and Canale P C. 1988. *Numerical Methods for Engineers. 2nd Ed.* (NY: McGraw-Hill)

Cheng K S, Chen B H and Tong H S. 1996. Electrical impedance image reconstruction using the genetic algorithm. *18th Annual International Conference of the IEEE Engineering in Medicine and Biology Society.* (IEEE)

Christensen G E, Rabbitt R D and Miller M I. 1996. Deformable templates using large deformation kinematics. *IEEE Transactions on Image Processing.* **5** 1435-47.

Clay M T and Ferree T C. 2002. Weighted regularization in electrical impedance tomography with applications to acute cerebral stroke. *IEEE Transactions on Medical Imaging.* **21** 629-37, Cohen F S, Ibrahim W and Pintavirooj C. 2000. Ordering and parameterizing scattered 3D data for B-spline surface approximation. *IEEE Trans. Pattern. Anal. Machine. Intelligence* **22** 642-48.

Cole K S and Cole R H. 1941. Dispersion and absorption in dielectrics. *J. Chem. Phys.* **9** 341-51.

Colton D L and Kress R. 1998. *Inverse acoustic and electromagnetic scattering theory*. (New York: Springer)

Corney J and Lim T. 2001. *3D Modelling with ACIS*. (Stirling: Saxe-Coburg)

Couteau B, Payan Y and Lavallee S. 2000. The mesh-matching algorithm: an automatic 3D mesh generator for finite element structures. *J. Biomech.* **33** 1005-9.

Dally J W and Riley W F. 1978. *Experimental Stress Analysis*. (Tokyo: McGraw-Hill)

Damadian R V. 1971. Tumor Detection by Nuclear Magnetic Resonance. *Science*

de Munck J C, Faes T J C and Heethaar R M. 2000. Boundary element method in the forward and inverse problem of electrical impedance tomography . *IEEE Trans. Biomed. Eng.* **47** 792-800.

Du Y, Liu Z and Cheng J. 1998. Weighted Newton-Raphson algorithm for electrical impedance tomography. *J. Beijing Univ. Aeronaut. Astronaut.* **24** 161-64.

Duraiswami R, Chahine G L and Sarkar K. 1997. Boundary element techniques for efficient 2-D and 3-D electrical impedance tomography. *Chem. Eng. Sci.* **52** 2185-96.

Duraiswami R, Sarkar K and Chahine G L. 1995. Efficient 2D and 3D electrical impedance tomography using dual reciprocity boundary element techniques. *Proceedings of the 1998 2nd European Boundary Element Method Symposium.* (Computational Mechanics Publ)

Eck M and Hoppe H. 1996. Automatic Reconstruction of B-Spline Surfaces of Arbitrary Topological Type. *Annual Conference on Computer Graphics.* (New Orleans, LA: ACM) 325-34.

Edic P M, Saulnier G J, Newell J C and Isaacson D. 1995. A Real Time Electrical Impedance Tomograph. *IEEE Trans. Biomed. Eng.* **42** 849-59.

EDS. 2003. I-DEAS Help Library.

Fabrizi L, Sparkes M, Abascal J F P J, Horesh L and Holder D S. 2005. Electrical Impedance Tomography in epilepsy - not an easy task. *6th Conference on Biomedical Applications of Electrical Impedance Tomography.* (London: University College, London)

Foley J D and Van Dam A. 1982. *Fundamentals of Interactive Computer Graphics*. (Reading, MA: Addison-Wesley)

Frey P J, Borouchaki H and George P-L. 1998. 3D Delaunay mesh generation coupled with an advancing-front approach. *Computer Methods in Applied Mechanics & Engineering* **157** 115-31.

Fritschy J, Horesh L, Bayford R H and Holder D S. 2005. Applications of GRID in clinical neurophysiology and electrical Impedance tomography of brain function. *6th Conference on Biomedical Applications of Electrical Impedance Tomography.* (London: University College, London)

Gamba H R, Bayford R and Holder D. 1999. Measurement of electrical current density distribution in a simple head phantom with magnetic resonance imaging. *Phys. Med. Biol.* **44** 281-91.

Geddes L A and Baker L E. 1967. The specific resistance of biological material- a compendium of data for the biomedical engineer and physiologist. *Med. Biol. Eng. Comput.* **5** 271-93.

Geselowitz D B. 1971. An Application of Electrocardiographic Lead Theory to Impedance Plethysmography. *IEEE Trans. Biomed. Eng.* **18** 38-41.

Gibson A, Riley J, Schweiger M, Hebden J, Arridge S and Delpy D. 2003. A method for generating patient-specific finite element meshes for head modelling. *Phys. Med. Biol.* **48** 481-95.

Gilad O, Horesh L, Ahadzi G E, Bayford R H and Holder D S. 2005. Could synchronized neuronal activity be imaged using low frequency electrical impedance tomography (LFEIT)? *6th Conference on Biomedical Applications of Electrical Impedance Tomography.* (London: University College, London)

Grabowski H A, Brief J, Hassfeld S, Krempien R, Raczkowsky J, Rembold U and Worn H. 1998. Model-based registration of medical images using finite element meshes. *Proceeding of 12th International Symposium on Computer Assisted Radiology and Surgery.* (Tokyo: Elsevier Science) ed H U Lemke, M W Vannier, K Inamura and A G Farman. 159-63.

Guardo R, Boulay C, Murray B and Bertrand M. 1991. An Experimental Study in Electrical Impedance Tomography Using Backprojection Reconstruction. *IEEE Trans. Biomed. Eng.* **38** 617-27.

Guoya D, Zou J, Bayford R H, Xinshan M, Shankai G, Weili Y and Manling G. 2005. The comparison between FVM and FEM for EIT forward problem. *IEEE Trans. Magnetics*. **41** 1468-71.

Hansen J H and Olsen C E. 1980. Brain extracellular space during spreading depression and ischaemia. *Act. Physiol. Scand.* **108** 355-65.

Harris N D, Suggett A J, Barber D C and Brown B H. 1987. Applications of Applied Potential Tomography (APT) in Respiratory Medicine. *Clin. Phys. Physiol. Meas.* **8** A155-A165.

Harris N D, Suggett A J, Brown B H and Barber D C. 1988. Applied potential tomography: a new technique for monitoring pulmonary function. *Clin. Phys. Physiol. Meas.* **9** A79-A86.

Holder D S. 1992. Electrical Impedance Tomography (EIT) of Brain Function. *Brain Topog.* **5** 87-93.

Holder D S. 1998. Electrical impedance tomography in epilepsy. *Electron. Eng.* **70** 69-70.

Holder D S, Rao A and Hanquan Y. 1996. Imaging of physiologically evoked responses by electrical impedance tomography with cortical electrodes in the anaesthetised rabbit. *Physiol. Meas.* **17** 179-86.

Hoppe H. 1994. Surface Reconstruction from Unorganized Points. PhD. University of Washington.

Horesh L, Bayford R H, Yerworth R J, Tizzard A, Ahadzi G E and Holder D S. 2004. Beyond the linear domain - the way forward in MFEIT reconstruction of the human head. *XII International Conference on Electrical Bioimpedance and V Electrical Impedance Tomography.* (Gdansk, Poland: Gdansk University of Technology) ed A Nowakowski, J Wtorek, A Bujnowski and A Janczulewicz. 683-86.

Horesh L, Gilad O, Romsauerova A, Arridge S and Holder D S. 2005a. Stroke type detection by mulit-frequency electrical impedance tomography (MFEIT) - a feasibility study. *6th Conference on Biomedical Applications of Electrical Impedance Tomography.* (London: University College, London)

Horesh L, Schweiger M, Bollhofer M, Douri A, Holder D S and Arridge S. 2005b. Multilevel Preconditioning For 3D Large-Scale Soft-Field Medical Applications Modelling. *Int. J. Inf. Syst. Sci.* **1** 1-24.

Hornak J P. 1998. Partial Matrix of Imaging Systems. *The Encyclopaedia of Imaging Science and Technology.* http://www.cis.rit.edu/htbooks/eist/

Hounsfield G N. 1973. Computerized transverse axial scanning (tomography). 1. Description of system. *Brit. J. Radiol.* **46** 1016-22.

Hu S-M and Wallner J. 2005. A second order algorithm for orthogonal projection onto curves and surfaces. *Comput. Aided Geom. Design* **22** 241-60.

Isaacson D, Mueller J L, Newell J C and Siltanen S. 2004. Reconstructions of chest phantoms by the D-bar method for electrical impedance tomography. *Medical Imaging, IEEE Transactions on* **23** 821-28.

Isaacson D, Mueller J L, Newell J C and Siltanen S. 2006. Imaging cardiac activity by the D-bar method for electrical impedance tomography. *Physiol. Meas.* **27** S43-S50.

Jain H, Isaacson D, Edic P M and Newell J C. 1997. Electrical impedance tomography of complex conductivity distributions with noncircular boundary. *IEEE Trans. Biomed. Eng.* **44** 1051-60.

Karamanoglu M. 1992. Boundary Element Analysis of Spherical and Radome Shells. PhD Thesis. Middlesex University.

Kiber M A, Barber D C and Brown B H. 1990. Estimation of Object Boundary Shape from the Voltage Gradient Measurements. *Electrical Impedance Tomography EEC Workshop.* (Copenhagen

Kim Y and Woo H W. 1987. A prototype system and reconstruction algorithms for electrical impedance technique in medical body imaging. *Clin. Phys. Physiol. Meas.* **8** 63-70

Kim Y, Woo H W, Brooks T J and Elliot S O. 1987. Electrical Impedance Techniques in imaging: a feasibility study. *J. Clin. Eng.* **12** 221-31.

Koikkalainen J and Lotjonen J. 2004. Reconstruction of 3-D head geometry from digitized point sets: an evaluation study. *Information Technology in Biomedicine, IEEE Transactions on* **8** 377-86.

Lamm C, Windischberger C, Leodolter U, Moser E and Bauer H. 2001. Co-Registration of EEG and MRI Data Using Matching of Spline Interpolated and MRI-Segmented Reconstructions of the Scalp Surface. *Brain Topog.* **14** 93-100.

Law. 1993. Thickness and resistivity variations over the surface of the human skull. *Brain Topog.* **6** 99-109.

Lawry M H. 1999. *I-DEAS Master Series. Student Guide*. (Milford, OH: Structural Dynamics Research Corporation)

Lehr J. 1972. A Vector Derivation Useful in Impedance Plethysmographic Field Calculations. *IEEE Trans. Biomed. Eng.* **19** 156-57.

Li J H, Joppek C and Faust U. 1996. In vivo EIT electrode system with 32 interlaced active electrodes. *Med. Biol. Eng. Comput.* **34** 253-56.

Liston A D. 2003. Models and Image Reconstruction in Electrical Impedance Tomography of Human Brain Function. PhD Thesis. Middlesex University, London, UK.

Liston A D, Bagshaw A, Bayford R H, Tizzard A, Tidswell A T, Dehghani H and Holder D S. 2003. Effects of modelling layers and realistic geometry in reconstruction algorithms for EIT of brain function. *4th Conference on Biomedical Applications of Electrical Impedance Tomography.* (Manchester, UK: UMIST)

Liston A D, Bayford R H, Tidswell A T and Holder D S. 2001. A multi-shell algorithm to reconstruct EIT images of brain function. *Physiol. Meas.* **23** 105-19.

Maekawa T and Ko K H. 2003. Surface construction by fitting unorganized curves. *Graphical Models* **64** 316-32.

Malvimuo J and Plonsey R. 1995. *Bioelectromagnetism: Principles and Applications of Bioelectric and Biomagnetic Fields*. (New York: Oxford University Press)

Maurer C R, Jr., Aboutanos G B, Dawant B M, Maciunas R J and Fitzpatrick J M. 1996. Registration of 3-D images using weighted geometrical features. *Medical Imaging, IEEE Transactions on* **15** 836-49.

Meier D S, Fisher E, Tkach J A, Masaryk T J, Cohen J A and Cornhill J F. 1998. Automated anatomical labeling of MRI brain data using spatial atlas warping in a finite element framework. *Medical Imaging 1998: Image Processing.* 1234-45.

Mengxing T, Xiuzhen D, Mingxin Q, Feng F, Xuetao S and Fusheng Y. 1998. Electrical impedance tomography reconstruction algorithm based on general inversion theory and finite element method. *Med. Biol. Eng. Comput.* **36** 395-98.

Metherall P. 1998. Three-Dimensional Electrical Impedance Tomography of the Human Thorax. PhD Thesis. Sheffield University.

Mottram J T and Shaw C T. 1996. *Using Finite Elements in Mechanical Design*. McGraw-Hill McGraw-Hill)

Murai T and Kagawa Y. 1985. Electrical Impedance Computerised Tomography Based on a Finite Element Model. *IEEE Trans. Biomed. Eng.* **32** 177-84.

Olmi R, Bini M and Priori S. 2000. Genetic algorithm approach to image reconstruction in electrical impedance tomography. *IEEE Trans. Evol. Comput.* **4** 83-88.

Onwubiko C. 1989. *Foundations of Computer-Aided Design*. (St Paul, MN: West)

Pinheiro P A T and Dickin F J. 1997. Sparse matrix methods for use in electrical impedance tomography. *Int. J. Numer. Meth. Eng.* **40** 439-51.

Polydorides N and Lionheart W R B. 2002. A Matlab toolkit for three-dimensional electrical impedance tomography: a contribution to the Electrical Impedance and Diffuse Optical Reconstruction Software project. *Meas. Sci. Technol.* **13** 1871-83.

Pottmann H and Leopoldseder S. 2003. A concept for parametric surface fitting which avoids the parametrization problem. *Comput. Aided Geom. Design* **20** 343-62.

Radovitzky R and Ortiz M. 2000. Tetrahedral mesh generation based on node insertion in crystal lattice arrangements and advancing-front-Delaunay triangulation. *Computer Methods in Applied Mechanics & Engineering* **187** 543-69.

Romsauerova A, Yerworth R, Horesh L, Abascal J F P J and Holder D S. 2005. Calibration and preliminary human measurements for multifrequency EIT of the human head. *6th Conference on Biomedical Applications of Electrical Impedance Tomography.* (London: University College, London)

Schoberl J. 1997. NETGEN An advancing front 2D/3D-mesh generator based on abstract rules. *Computing and Visualization in Science* **1** 41-52.

Soleimani M, Abascal J F P J and Lionheart W R B. 2004. Simultaneous Reconstruction of the boundary shape and conductivity in 3d electrical impedance tomography. *XII International Conference on Electrical Bioimpedance and V Electrical Impedance Tomography.* (Gdansk, Poland: Gdansk University of Technology) ed A Nowakowski, J Wtorek, A Bujnowski and A Janczulewicz. 475-78.

Soleimani M, Powell C E and Polydorides N. 2005. Improving the forward solver for the complete electrode model in EIT using algebraic multigrid. *IEEE Transactions on Medical Imaging.* **24** 577-83.

Somersalo E, Cheney M, Isaacson D and Isaacson E. 1991. Layer stripping: a direct numerical method for impedance imaging. *Inverse Prob.* **7** 899-926.

Tarvainen M, Vauhkonen M, Savolainen T and Kaipio J P. 2001. Boundary element method and internal electrodes in electrical impedance tomography. *Int. J. Numer. Meth. Eng.* **50** 809-24.

Tidswell A T, Gibson A, Bayford R H and Holder D S. 2001. Validation of a 3D reconstruction algorithm for EIT of human brain function in a realistic head-shaped tank. *Physiol. Meas.* **22** 177-85.

Tizzard A. 1994. *An Introduction to Computer-Aided Engineering.* (London: McGraw-Hill)

Tizzard A, Bayford R H, Horesh L, Yerworth R J and Holder D S. 2004. Effects of Warping Finite-Element Meshes for the Forward Model of the Head in EIT. *XII International Conference on Electrical Bioimpedance & V Electrical Impedance Tomography.* (Gdansk, Poland Gdansk University of Technology) ed A Nowakowski, J Wtorek, A Bujnowski and A Janczulewicz. 495-98.

Tizzard A, Horesh L, Yerworth R J, Holder D S and Bayford R H. 2005. Generating accurate finite element meshes for the forward model of the human head in EIT. *Physiol. Meas.* **26** S251-S261.

Tizzard A, Holder D S and Bayford R H. 2005. Generating surfaces for registration and warping FE meshes for the forward model in EIT of brain function. *EMBEC05: The 3rd European Medical and Biological Engineering Conference.* (Prague, Cz : IFMBE)

Tizzard A and Bayford R H. 2007. Improving the finite element forward model of the human head by warping using elastic deformation. *Physiol. Meas.* **28** S163-S182 doi:10.1088/0967-3334/28/7/S13

Vauhkonen P J, Vauhkonen M and Kaipio J P. 2000. Errors due to the truncation of the computational domain in static three-dimensional electrical impedance tomography. Physiological Measurement. **21** 125-35

Walker R C, Purnell G L, Jones-Jackson L B, Thomas K L, Brito J A and Ferris E J. 2004. Introduction to PET imaging with emphasis on biomedical research. *Neurotoxicology*. **25** 533-42.

Warfield S K, Ferrant M, Gallez X, Nabavi A, Jolesz F A and Kikinis R. 2000. Real-Time Biomechanical Simulation of Volumetric Brain Deformation for Image Guided Neurosurgery. *SC 2000: High Performance Networking and Computing Conference.* (Dallas, USA) 1-16.

Weinstein D M, Johnson C R and Schmidt J A. 1995. Effects of adaptive refinements on the inverse EEG solution. Experimental and numerical methods for solving ill-posed inverse problems. *Proc. SPIE* **2570** 2-11.

Yerworth R J, Bayford R H, Cusick G, Conway M and Holder D S. 2002. Design and performance of the UCLH Mark 1b 64 channel electrical impedance tomography (EIT) system, optimized for imaging human brain function. *Physiol. Meas.* **23** 149-58.

Yorkey T J and Webster J G. 1987. A comparison of impedance tomographic reconstruction algorithms. *Clin. Phys. Physiol. Meas.* **8** 55-62.

Yvert B, Bertrand O, Echallier J F and Pernier J. 1995. Improved forward EEG calculations using local mesh refinement of realistic head geometries. *Electroencephalogr. Clin. Neurophysiol.* **95** 381-92.

A. APPENDIX

References Arising Directly from this Thesis

Bagshaw A, Liston A D, Bayford R H, Tizzard A, Gibson A, Tidswell A T, Sparkes M K, Dehghani H, Binnie C D and Holder D S. 2003. Electrical impedance tomography of human brain function using reconstruction algorithms based on the finite element method. *Neuroimage* **20** 752-64.

Bayford R H, Bagshaw A, Liston A D, Tizzard A and Holder D S. 2002. Development of algorithms to image impedance changes inside the human head. *The First Mummy Range Workshop on Electric Impedance Imaging.* (Colorado State University)

Bayford R H, Gibson A, Tizzard A and Holder D S. 2000. Modelling impedance changes in the human head using IDEAS. *World Congress on Medical Physics and Biomedical Engineering.* (Chicago)

Bayford R H, Gibson A, Tizzard A, Liston A D, Tidswell A T, Bagshaw A and Holder D S. 2001a. Modelling the effect of eye sockets in the human head using I-DEAS and its implication for imaging impedance change using Electrical Impedance Tomography. *XI International Conference on Electrical Bio-Impedance.* (Oslo) 391-96.

Bayford R H, Gibson A, Tizzard A, Tidswell T and Holder D S. 2001b. Solving the forward problem in electrical impedance tomography for the human head using IDEAS (integrated design engineering analysis software), a finite element modelling tool. *Physiol. Meas.* **22** 55-64.

Bayford R H, Tizzard A and Liu X. 2005. Dynamic modelling of electrical current distribution in the deep structure of the brain. *Proceedings of the 3rd IEE International Semiar on Medical Applications of Signal Processing.* (London, UK: Institute of Electrical Engineers) 131-34.

Bayford R H, Tizzard A and Liu X. 2006a. The Forward Model. *7th conference on Biomedical Applications of Electrical Impedance Tomography.* (Seoul, South Korea) 21.

Bayford R H, Tizzard A, Yousif N and Liu X. 2006b. Investigating the mechanism of deep brain stimulation using a dynamic complex model of the head incorporated with the complete model of electrode. *Clin. Neurophys.* **117** S219-S220.

Horesh L, Bayford R H, Yerworth R J, Tizzard A, Ahadzi G E and Holder D S. 2004. Beyond the linear domain - the way forward in MFEIT reconstruction of the human head. *XII International Conference on Electrical Bioimpedance and V Electrical Impedance Tomography.* (Gdansk, Poland: Gdansk University of Technology) ed A Nowakowski, J Wtorek, A Bujnowski and A Janczulewicz. 683-86.

Liston A D, Bagshaw A, Bayford R H, Tizzard A, Tidswell A T, Dehghani H and Holder D S. 2003. Effects of modelling layers and realistic geometry in reconstruction algorithms for EIT of brain function. *4th Conference on Biomedical Applications of Electrical Impedance Tomography.* (Manchester, UK: UMIST)

Tizzard A, Bayford R H, Horesh L, Yerworth R J and Holder D S. 2004. Effects of Warping Finite-Element Meshes for the Forward Model of the Head in EIT. *XII International Conference on Electrical Bioimpedance & V Electrical Impedance Tomography.* (Gdansk, Poland Gdansk University of Technology) ed A Nowakowski, J Wtorek, A Bujnowski and A Janczulewicz. 495-98.

Tizzard A, Horesh L, Yerworth R J, Holder D S and Bayford R H. 2005. Generating accurate finite element meshes for the forward model of the human head in EIT. *Physiol. Meas.* **26** S251-S261.

Tizzard A, Holder D S and Bayford R H. 2005. Generating surfaces for registration and warping FE meshes for the forward model in EIT of brain function. *EMBEC05: The 3rd European Medical and Biological Engineering Conference.* (Prague, Cz : IFMBE)

Tizzard A and Bayford R H. 2007. Improving the Finite Element Forward Model of the Human Head by Warping using Elastic Deformation. *Physiol. Meas.* **28** S163-S182 doi:10.1088/0967-3334/28/7/S13